FABRICATION AND TESTING OF PVDF BASED PENG DEVICES FOR IoT APPLICATIONS

A Thesis Submitted in

Partial Fulfillment of the Requirements

for the Degree of

DOCTOR OF PHILOSOPHY

By

NIKHIL DILIP KULKARNI

(Roll No.196103019)

DEPARTMENT OF MECHANICAL ENGINEERING

INDIAN INSTITUTE OF TECHNOLOGY GUWAHATI

GUWAHATI (ASSAM)-781039

JULY 2024

Dedicated to my beloved parents Mr. Dilip Dattatraya Kulkarni and Yashashree Dilip Kulkarni, wife Shruti, and fellow researchers who are working tirelessly for the betterment of society

Certificate

This is to certify that the thesis entitled "**Fabrication and testing of PVDF based PENG devices for IoT applications**" being submitted by **Mr. Nikhil Dilip Kulkarni** to the Indian Institute of Technology, Guwahati, for the award of the degree of Doctor of Philosophy in Mechanical Engineering is a record of original bonafide research work carried out by him under my supervision and guidance. The thesis work, in my opinion, has reached the requisite standard fulfilling the requirements for the degree of Doctor of Philosophy.

The results contained in this thesis have not been submitted in part or full to any other University or Institute for the award of any degree or diploma.

Dr. Poonam Kumari

Associate Professor

Department of Mechanical Engineering

Indian Institute of Technology Guwahati

Guwahati - 781039

Declaration

I, Nikhil Dilip Kulkarni (Roll no: 196103019) declare that the present written submission is my thoughts in my own words. I have adequately cited and referenced the original sources, where other's ideas have been involved. I also declare that I have adhered to all principles of academic honesty and integrity and have neither fabricated nor falsified any idea/data/fact/source in my submission. I understand that any violation of the above will be cause for disciplinary action by the Institute and can also evoke penal action from the sources which have thus not been properly cited or from whom proper permission has not been taken when needed.

(Nikhil Dilip Kulkarni)

Date: Roll No. 196103019

Acknowledgements

First and foremost, I want to express my sincere gratitude toward my Ph.D. supervisor, Dr. Poonam Kumari, for providing me an opportunity to work under her supervision. I am grateful to her for her consistent guidance, motivation, patience, kindness and family support as well, over these years. She has always made available herself for discussions besides her busy schedules. Her enthusiasm, sublime work ethics, analytical abilities, and never-say-die attitude toward research and life as well, has natured my scientific skills and also inspired me immensely to work hard. I am proud to have her as my Ph.D. supervisor. Thank you, Ma'am, for all your help, advice, and support. I am thankful to Dr. V.N. Kulkarni for his consistant academic as well as emotional support which made my PhD journey relaxing.

I want to thank my doctoral committee members, Prof. K. S. R. Krishna Murthy, Dr. Atanu Banerjee, and Dr. Sweta Tiwari for their encouragement, insightful comments, and suggestions which have helped me to refine and widen my research from various perspectives. My sincere gratitude also goes to the Head of Department of Mechanical Engineering, Prof. K. S. R. Krishna Murthy, for providing all the resources needed for my research. I also thankful to all faculty and staff members of the Mechanical Engineering department who help me whenever I needed. Without their help, it would not have been possible to conduct my research. It is an honor for me to thank the Indian Institute of Technology Guwahati for giving me such an excellent opportunity for undergoing my research. I am grateful to technical officers of Department of Mechanical Engineering, IIT Guwahati, Mr. Sanjib Kumar Sarma and Saifuddin Ahemed for helping me out with UTM tests and rheological measurements respectively. Furthermore, I extend my appreciation for Dr. Momita Das for her valuable time and expertise in carrying out FESEM plots which have facilitated the smooth progress of my research endeavors. I am thankful to Ms. Shashipriya (Department of physics) for

allowing me to perform P-E loop testing. I am also grateful to Mr. Amir Suhail and Mr. Jaharlaal Pati, a research scholars from Centre of Nanotechnology, IIT Guwahati for helping me carrying out sputtering and thermal evaporation processes. I am grateful to the Central instrument facility (CIF), Indian Institute of technology Guwahati (IITG), for providing XRD, DSC, TGA, Raman, and AFM characterization facilities. I am also thankful to North East Centre for Biological Sciences and Healthcare Engineering (NECBH), IIT Guwahati and Department of Biotechnology (DBT), Govt. of India for Project No. BT/COE/34/SP28408/2018 for the FESEM facility. I gratefully acknowledge the Department of Science and Technology (DST) and NEWGEN IEDC, India for providing financial support through grant TDP/BDTD/03/2021(G) and IEDC/2021-22/PK2 to support this research work. I am also thankful to the Ministry of Education (MOE), Government of India for providing me financial support during my Ph.D. at IIT Guwahati.

I want to thank my seniors, Dr. Agyapal Singh, Dr. Sharnish Kar, Dr. Mukesh Kumar, Dr. Viwek Singh, and Dr. Sathish Kumar R. for their mentorship related to make things done and hand-holding whenever I got stuck during the research. I should also mention about Mr. Dhirendra kumar Verma, Ms. Mridusmita, Mrs. Vaishnavi, Vaibhav, and Abhimanyu for their timely help, suggestions, and encouragements. It was fun to work with the PG students (Saurabh and Akash) whose contributions showed new dimension to this research. I would like to extend my sincere gratitude to my colleague and friend, Abir Saha, for his invaluable assistance and support throughout the development of this thesis. I appreciate Abir's dedication and collaborative spirit, which made working together both enjoyable and productive. I am indebted to my friends, Abhishek, Armaan, Prateechee, Rupresha, Ashok, Rahul, Shivani, Suraj, Omkar, and Dhruv who made this journey along with me creating a memorable campus life. In the midst of academic demands and stress, these guys provided a haven of comfort and understanding. Whether it was sharing a laughter-filled coffee break or offering a listening ear during moments of frustration, they all played an indispensable role in maintaining my sanity and balance. I would like to extend my heartfelt gratitude to my extended family for their unwavering support and understanding during the pursuit of my doctoral studies. Your belief in my abilities and the countless moments of understanding during family gatherings made this journey more manageable. I am fortunate to

belong to a family that values education and intellectual pursuits. Thank you for being a crucial part of my academic adventure.

I would like to express my deepest gratitude to my parents, Dilip Dattatraya Kulkarni and Yashashree Dilip Kulkarni, whose unwavering support and encouragement, have been the foundation upon which my academic journey has been built. Their belief in my abilities, even during moments of self-doubt, has been a constant source of motivation. This thesis is as much a reflection of their sacrifices as it is of my own efforts. Thank you, Mom and Dad, for being my pillars of support and for making this achievement possible.

I am also profoundly grateful to my wife, Shruti, for her patience, understanding, and steadfast support. Her encouragement has been a source of strength during the highs and lows of this demanding academic pursuit. Her sacrifices and belief in my goals have been instrumental in achieving this milestone. I extend my heartfelt gratitude to my cousins, Unmesh, Abhishek, Anuprita, Dinesh, Kaustubh, Anurag, Rishikesh and Tanaya, for their unwavering support and encouragement throughout my Ph.D. journey. Their support extended beyond family ties, creating a sense of camaraderie that eased the challenges of the doctoral process. My family, teachers, and friends are the backbone of my happiness, and I dedicate my thesis to them.

Finally, I thank God for always being with me.

Nikhil Dilip Kulkarni

Abstract

Increasing environmental pollution and battery durability have redirected energy research toward eco-friendly renewable technologies. There is a pressing need to create energy conversion and power supply devices that are both high-performing and sustainable due to the rapid development of wearable electronics and the Internet of Things (IoT). The rapid development of polymer based flexible piezoelectric sensors have attracted considerable attention due to their promising applications in nanogenerators. PVDF thin films have a wide prospect in energy harvesting applications due to flexible design and presence of electroactive phase. Despite massive work in this domain, commercial applications are very rare since PVDF based thin films have low piezo response. Composite film samples are fabricated using DMF as a solvent through low cost solvent casting approach. This research work focuses on the fabrication and testing of flexible PENG devices made up of PVDF-based composites with enhanced mechanical, dielectric, and piezoelectric response for energy scavenging purposes. PVDF-TiO_2 composite films are fabricated to assess their piezoelectric performance for energy scavenging. Effect of varying rGO content on energy scavenging capacity of PVDF-TiO_2 composite films is then studied. Further, the MCDM-based TODIM technique is used to select the best piezoelectric material from the samples available. Role of reinforcement of rGO in PVDF-BTO composites for enhanced mechanical and piezoelectric performance is then studied. Further, naturally available bio-compatible filler materials are explored to develop sustainable piezoelectric energy harvesters. PVDF composites based on treated BMP are tested for their suitability as impact sensor under a variety of impact loading conditions. After that, PVDF-FS based bio based energy scavenging device interacting with human body parts to monitor real-time physiological signals is developed. The surface morphology, beta phase fraction, thermal stability, mechanical behaviour, and dielectric response of all the nanocomposite structures are examined.

Conductive electrodes are deposited on the top and bottom surfaces of fabricated composite films to create a PENG device. The device is then put through a series of bio-mechanical operations, including tapping, thumb pressing, film twisting, and bending, to measure piezo response.These kind of flexible piezo devices prove to be ideal for mechanical energy harvesters used in sensing applications due to their excellent overall properties and good cost-performance balance.

Contents

List of Figures

List of Tables

List of Abbreviation

DMF = Dimethylformamide
PVDF = Poly(vinylidene-fluoride)
DMF = N, N-dimethyl formamide
rGO = Reduced graphene oxide
$BaTiO_3$ = Barium titanate
TiO_2 = Titanium oxide
FESEM = Field emission scanning electron microscopy
EDS = Energy-dispersive spectroscopy
AFM = Atomic force microscopy
XRD = X-ray diffraction test
ATR = Attenuated total reflectance
FTIR = Fourier transform infrared spectroscopy
DSC = Differential scanning calorimetry
UTM = Universal testing machine
DMA = Dynamic mechanical analysis
TGA = Thermo-gravimetric analysis
DSO = Digital storage oscilloscope
PET = Polyethylene terephthalate
PDMS = Polydimethylsiloxane
MCDM = Multi criteria decision making

Chapter 1

INTRODUCTION

1.1 BACKGROUND AND MOTIVATION

PENGs are gaining significant attention nowadays as micro/nano energy systems in various application domains like wearable devices, implantable medical devices, robotics, and Internet of things (IoT). A smartwatch can, for instance, monitor heart rate to ensure overall health; IoT can enhance living and working conditions and propel progress in industry and agriculture. Nowadays, rechargeable batteries are primarily used to power these gadgets. Because of their limited capacity and lifespan, batteries must be constantly checked, recharged, and replaced. This makes wearable devices extremely frustrating and impractical for use in the workplace. Fortunately, the environment and biomechanical movement contain abundant energy. Therefore, harvesting these energies into electricity would extend the life of the above-mentioned devices or even eliminate batteries by forming self-powered systems. At present, the flexible PENG stands out as a promising option. It has the potential to seamlessly integrate with personal electronics and wireless sensors, providing sustainable energy for prolonged durations thanks to its exceptional mechanical properties, environmental adaptability, and impressive energy harvesting performance. PENG devices convert mechanical signals like vibrations, acoustics, sound, and human body motions into useful electrical energy. PENGs are preferred because of its high coupling coefficient, durability, and easier fabrication.

This research work aims to examine the impact of reinforcing various nanofillers into PVDF to produce highly flexible nanocomposite films through solvent casting. These films will be evaluated for their suitability in energy scavenging and applications in wearable devices.

1.2 OVERVIEW OF RESEARCH GAPS IN PVDF BASED PENG DEVICES

PVDF and its co-polymers have attracted considerable attention in the domain of PENGs because of their piezoelectricity, flexible nature, and chemical stability. However, several research gaps must be addressed to further the development and application of PVDF-based PENGs. The following is an overview of these research gaps:

- PVDF and its co-polymers exhibit enhanced piezoelectric performance, but further research is needed to optimize their composition and processing conditions. Further, nanofillers (such as CNTs, graphene, and BTO) can improve PVDF composite performance, but their dispersion and interaction mechanisms need to be better understood.
- It is crucial to evaluate the ecological consequences and sustainability of PVDF-based PENGs throughout their lifecycle. Research into environmentally friendly materials and processes is necessary.
- Lowering the cost of materials and fabrication processes while preserving high performance is essential for the commercialization of PVDF-based PENGs.
- Despite advancements, the energy conversion efficiency of PVDF-based PENGs remains relatively low. Innovative strategies, including optimizing mechanical properties and electrical output, are needed to improve this efficiency.

1.3 PROBLEM FORMULATION

Piezoelectric materials have attracted considerable interest in self-powered systems due to their ability to convert mechanical energy into electrical energy. Among these, piezoelectric polymers are notable for their ability to withstand higher strains, strain rates, and impact stresses compared to inorganic materials despite having a lower piezoelectric coefficient and Young's modulus. While ceramic materials exhibit excellent piezoelectric and dielectric properties, they are not ideal for energy harvesting applications due to their brittleness, non-biocompatibility, rigidity, and high fabrication costs. In contrast, piezoelectric polymers offer higher tensile strength and greater flexibility, making them ideal for applications requiring substantial bending and twisting. PVDF is a

promising electroactive polymer recognized for its flexible design, environmental friendliness, biocompatibility, chemical inertness, low acoustic impedance, and high piezoelectric properties. These attributes make PVDF suitable for various sensors and energy-harvesting devices. The piezoelectric properties of PVDF result from the dipole polarization of its long-chain molecules, which is further enhanced by stretching and poling the polymer sheets to induce the formation of the β phase [1]. The research aims to develop PVDF-based flexible nanocomposite PENGs by integrating various nanofillers to improve their mechanical, dielectric, and piezoelectric properties for energy-scavenging applications.

1.4 SOLUTIONS EXPLORED IN THE THESIS

The present research focuses on developing PVDF-based flexible nanocomposite films to address the challenges posed by piezoelectric materials in self-powered systems and enhance the performance of PVDF-based PENGs. The developed films incorporate various nanofillers to improve mechanical, dielectric, and piezoelectric properties, making them more effective for energy-scavenging applications. The various solutions explored in this thesis are summarized below:

- The thesis focuses on improving PVDF-based PENGs by integrating different nanofillers. One approach involves PVDF-TiO_2 composite films, aiming to boost PVDF's piezoelectric performance through TiO_2 nanoparticles. The developed films are solvent-cast with optimized TiO_2 content for enhanced dielectric, mechanical, and piezoelectric properties, resulting in improved energy harvesting capabilities suitable for self-powered sensors.

- Another strategy is fabricating PVDF-rGO-TiO_2 hybrid nanocomposites, combining rGO and TiO_2 to enhance PVDF's mechanical and piezoelectric characteristics. Hybrid films with varying rGO content and fixed TiO_2 concentrations exhibit superior performance, showcasing synergistic effects for advanced energy scavenging applications.

- Additionally, PVDF-BTO-rGO nanocomposites are developed using BTO and rGO to further enhance PVDF's mechanical and piezoelectric properties. Optimal rGO content in solvent-cast films enhances mechanical strength, modulus, and energy harvesting capabilities, offering

robust solutions for flexible energy devices.

- The thesis explores sustainable PVDF composites, utilizing biocompatible bamboo fibers to improve flexibility and energy harvesting efficiency. Similarly, reinforced PVDF composites demonstrate enhanced mechanical and piezoelectric properties, which are suitable for bioenergy scavenging from human-body interactions.

- Currently, there is a significant research gap regarding the fabrication of bamboo fiber-reinforced PVDF composites and the analysis of their dielectric, mechanical, and piezoelectric response. PVDF composites for impact sensors have also been developed, employing treated BMP to enhance mechanical durability and piezoelectric response under dynamic conditions.

- Lastly, a PVDF-FS bioenergy scavenging device is created for real-time physiological signal monitoring, demonstrating effective energy harvesting from human interactions.

These solutions aim to overcome piezoelectric material limitations in energy harvesting, leveraging PVDF's unique properties and nanofillers to enhance flexibility, mechanical strength, and piezoelectric performance for diverse self-powered sensing and energy harvesting applications.

1.5 KEY ADVANCEMENTS FROM THE THESIS

The key pieces of new knowledge that emerged from the thesis, with a focus on IoT-based technologies for wearable devices, are summarized below:

- **Development of PVDF-based Nanocomposites:** Development of PVDF-based nanocomposites: The thesis successfully developed PVDF-based nanocomposites by integrating various nanofillers such as TiO_2, rGO, BTO, bamboo fibers, and fish scales. These composites exhibit improved mechanical, dielectric, and piezoelectric properties, enhancing their suitability for energy harvesting applications.

- **Specific Nanofiller Contributions:** Specific Nanofiller Contributions: Each nanofiller—TiO_2 for enhanced piezoelectric performance, rGO for mechanical reinforcement and piezoelectric enhancement, BTO for mechanical strength and energy harvesting capabilities, BMP for

biocompatibility and flexibility, and fish scales for bioenergy scavenging—was strategically utilized to maximize composite performance.

- **Fabrication Techniques:** The thesis employed solvent casting and optimization techniques to fabricate PVDF-based films with tailored nanofiller concentrations. This approach ensured optimal mechanical strength, flexibility, and energy-harvesting efficiency across various applications.

- **Synergistic Effects:** Hybrid nanocomposites like PVDF-TiO_2-rGO and PVDF-BTO-rGO showed synergistic effects, combining the strengths of different nanofillers to achieve superior mechanical and piezoelectric properties, thereby advancing the field of flexible energy harvesting technologies. Overall, this thesis marks a substantial contribution to PVDF-based nanocomposite technology, tackling crucial challenges in energy harvesting applications and setting the stage for future advancements in self-powered systems and sensor technologies.

These advancements aim to overcome piezoelectric material limitations in energy harvesting, leveraging PVDF's unique properties and nanofillers to enhance flexibility, mechanical strength, and piezoelectric performance for diverse self-powered sensing and energy harvesting applications.

1.6 NEW KNOWLEDGE EMERGED FROM THE THESIS

The key new insights from this study, which significantly contribute to the development of next-generation IoT-based wearable devices are summarized below:

- The thesis introduced novel PVDF-based nanocomposites with advanced nanofillers such as TiO_2, rGO, BTO, BMP, and FS, enhancing the mechanical flexibility and piezoelectric properties essential for wearable IoT devices.

- The thesis emphasized the synergistic effects of combining multiple nanofillers in PVDF, such as rGO, BTO, and TiO_2. This combination demonstrated superior mechanical, thermal, dielectric, and piezoelectric properties compared to single-filler composites, revealing the potential for developing more efficient energy harvesting materials through hybridization.

- The investigation into natural and biocompatible fillers, such as BMP and FS, introduced sustainable alternatives for reinforcing PVDF composites. This research showed that these natural fillers could enhance PVDF's flexibility and energy harvesting capabilities, paving the way for environmentally friendly and biocompatible piezoelectric sensors.

- The thesis explores bamboo fiber-reinforced PVDF composites, utilizing bio-compatible bamboo fibers to improve flexibility and energy harvesting efficiency. Similarly, FS-reinforced PVDF composites demonstrate enhanced mechanical and piezoelectric properties, suitable for bioenergy scavenging from human-body interactions.

- Developing PVDF based composites as a sustainable impact sensor showcased how wearable devices can monitor and react to diverse physical activities and impacts, thereby broadening the capabilities of IoT wearables.

- The research provided a scalable approach to fabricating PVDF-based nanocomposites, paving the way for mass production of cost-effective, high-performance nanogenerator devices.

These advancements make a substantial contribution to advancing next-generation IoT-based wearable devices, introducing novel insights and technologies that enhance health monitoring, energy harvesting, and interactive capabilities in wearable technology.

1.7 ORGANIZATION OF THESIS

The complete work presented in the thesis has been organized into eight chapters. The following is a brief outline of each chapter's contents. Chapter 1 provides the background and motivation for the current work, formulates the problem, and identifies research gaps. It offers a brief overview of the solution explored in the thesis and highlights key advancements presented.

Chapter 2 provides a comprehensive introduction to piezoelectricity, including various types of piezoelectric materials and the electroactive polymer PVDF. It explores the principle of piezoelectric energy harvesting and discusses different techniques for fabricating PVDF-based composites and imparting piezoelectric behavior to PVDF. The pros and cons of PENG devices and their applications are also briefly covered. Additionally, Chapter 2 presents a detailed literature review on

the current status of PVDF-based flexible piezo nanogenerators for mechanical energy scavenging. Based on this extensive review, the objectives of the present study are outlined and framed in this chapter.

In chapter 3, fabrication of highly flexible PVDF-TiO_2 nanocomposites through solvent casting process for nanogenerator applications is presented. Effect of TiO_2 loading on electroactive β phase of PVDF is examined through characterization tools like XRD and FTIR. The structural and morphological behavior of PVDF-TiO_2 nanocomposites is also studied. The β phase of PVDF is enhanced by simply adding TiO_2 nanofillers to the PVDF matrix without any further mechanical (hot pressing, stretching) or electrical treatment (electrospinning, thermal poling). The piezoelectric performance is then investigated by recording output voltage generated by fabricated PENGs for nanogenerator applications.

Chapter 4 explores the impact of a fixed TiO_2 concentration and varying levels of rGO loading on mechanical, dielectric and piezoelectric performance of PVDF. A PENG device based on PVDF-rGO-TiO_2 hybrid structure is fabricated and subjected to continuous finger tapping using human hand to record and analyse piezoelectric output voltage response. Further, MCDM based TODIM technique is utilized and and a sensitivity study is carried out to select the best material for mechanical energy to select best material combination for energy harvesting purposes.

In Chapter 5, the influence of rGO loading on the mechanical, dielectric, and piezoelectric characteristics of PVDF-BTO composite structures is demonstrated. Structural properties along with average crystalline size and lattice strain of PVDF-BTO-rGO nanocomposites were calculated using XRD technique with Williamson-Hall approach. he impact of increased rGO reinforcement (beyond 0.45 wt.%) on the energy harvesting performance of PVDF-BTO composite was investigated for the first time through a combination of solvent casting and electrode poling processes. Piezo responses of poled and unpoled PENG devices for different loading conditions is tested and compared.

Chapter 6 involves gathering residual BMP, which is subsequently incorporated in different proportions into PVDF to produce bio-compatible composite piezo-energy harvesters. Leftover bamboo micro particles (BMP) from bamboo factories were collected an used as fillers with PVDF matrix in varying concentrations (1, 3, 5, 7, and 9 wt.%) to fabricate low-cost composite films using sol-

vent casting route for mechanical energy harvesting purpose. The composite with the best overall performance is selected for a chemical treatment of BMP to further assess its behavior. The treated BMP-based composite is checked for its structural, dielectric, and mechanical behavior. PENG devices are fabricated to test their piezoelectric performance under various loading conditions using a human hand (finger tapping, palm tapping, film twisting, and wrist pressing). PVDF-treated BMP composites are then examined for its performance as a potential impact sensor. The recorded results are subjected to statistical analysis employing the Weibull distribution method, aimed at addressing output voltage fluctuations for individual test loads. The utilization of a cost-effective, highly sensitive piezoelectric impact sensor fabricated from FS significantly enhances the potential for sustainability and circular economies.

In Chapter 7, FS particles are utilized to create bio-compatible piezoelectric impact sensors for structural health monitoring applications. The remaining FS obtained from local food canteens are gathered and treated, then incorporated into different proportions into PVDF to create flexible composites via solvent casting followed by thermal poling. Morphology, size, structure, and different phases of FS structures are examined through FESEM, XRD, and FTIR tools. Sustainable composite films based on PVDF-FS are assessed for both mechanical properties and piezo response. The composite film exhibiting the best performance is then chosen to investigate the effect of different impact loads on the generated piezoelectric voltage.

Finally, Chapter 8 summarizes the major conclusions and suggestions for future research.

Chapter 2

LITERATURE REVIEW

2.1 INTRODUCTION

In recent years, portable and wearable electronic devices have undergone tremendous development. Personalized devices like smart glasses and smartwatches have become prevalent, greatly enhancing convenience in people's lives. Concurrently, advancements in flexible electronics, big data, and artificial intelligence have driven these devices towards greater flexibility, integration, and intelligence, enabling diverse applications such as human-machine interaction, health monitoring, and the IoT. A significant challenge for portable and wearable devices is their energy supply. Replaceable batteries are currently the primary power source, but their rigid nature restricts the flexibility of these devices. Moreover, the limited lifespan of batteries and their potential environmental impact are inconsistent with sustainable development principles. Therefore, extensive efforts have been made to explore new, eco-friendly, renewable energy sources for these devices.

The self-powered technology is a viable solution for the supply of sustainable energy in portable and wearable devices. This technology allows devices to operate independently by harvesting energy from their environment, without relying on an external power source. The ability to effectively capture various forms of environmental energy is crucial for the success of self-powered technology.

Portable and wearable electronic devices have access to a wide array of energy sources, including chemical, thermal, mechanical, and solar energy. Energy harvesting systems tailored to these energy forms have garnered significant attention. For instance, triboelectricity is generated during the contact-separation process of two distinct materials. Piezoelectricity arises from the mechanical deformation of piezoelectric materials, while electromagnetic power is produced when a conductor

moves through a stationary magnetic field. All these mechanisms convert mechanical energy into electrical energy. Consequently, triboelectric, piezoelectric, and electromagnetic energy harvesters are well-suited for capturing mechanical energy from human motion. Additionally, biofuel cells use enzymes or microbes as catalysts to transform chemical energy into electrical energy.

2.2 PIEZOELECTRICITY

This section outlines the historical background and basic scientific concepts related to piezoelectricity, which serve as the foundation for the current research.

2.2.1 Fundamentals of piezoelectric effect

A piezoelectric effect was discovered in 1880 by young French scientists Pierre and Jacques Curie [2]. In response to external mechanical input, the crystal breaks its central symmetry structure, generating the piezo potential. Due to their anisotropic dielectric responses, piezoelectric materials can convert mechanical energy into electrical energy. Fig. 2.1 illustrates the different stages of piezoelectric technology development as discussed by Mohith et. al [3]. The principle of piezoelectricity involves the electromechanical interaction within a particular set of materials, linking their elastic and electrical behaviors. The imposition of external stimuli, either in the form of mechanical stress or electrical potential, on polarized piezoelectric materials leads to the generation of electrical charge (direct piezoelectric effect, or mechanical strain (inverse piezoelectric effect), as illustrated in Fig. 2.2 by Mishra et.al [4].

The principle of piezoelectricity involves the electromechanical interaction within a distinct set of materials, bridging the gap between elastic and electrical behaviors. By subjecting piezoelectric materials to high temperatures and applying a strong electric field in a specific direction, polarization occurs, leading to an organized alignment of initially randomly oriented electric dipoles. This, in turn, initiates the piezoelectric effect. The fundamental concept behind the piezoelectric effect is explained in Fig. 2.3 as discussed by Mohith et. al [3]. The fundamental governing equations for direct as well as indirect piezoelectric effect are given in equations 2.1 and 2.2:

$$D = dT + \epsilon E \tag{2.1}$$

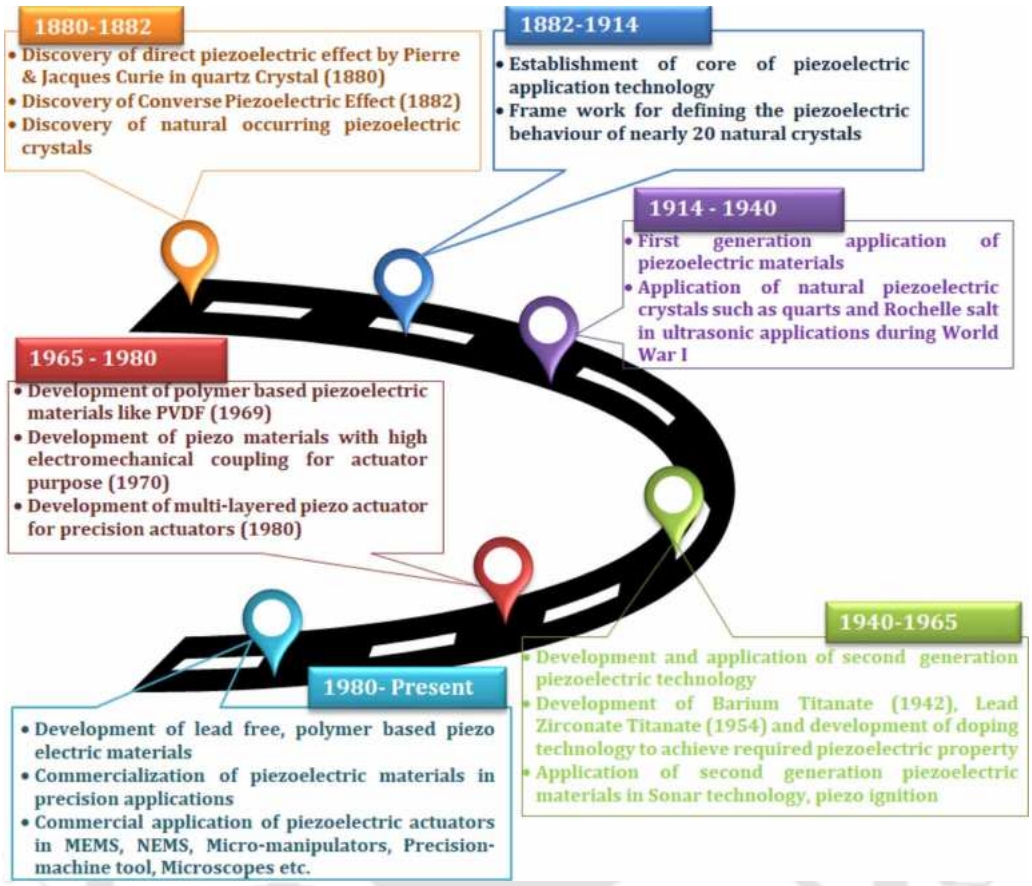

Fig. 2.1: A roadmap for the progress and application of piezoelectric technology [3].

$$X = sT + dE \tag{2.2}$$

where D is electrical displacement, T stress, d piezo coeficient, s compliance, X strain, E electric field. Direct and converse effects can be used for a variety of applications; direct effect, as sensors, while converse effect, as actuators.

2.2.2 Types of piezoelectric materials

The effectiveness and suitability of the piezoelectric energy harvesters are predominantly influenced by the selection of materials. Piezoelectric ceramics are polycrystalline materials comprising irregularly arranged small grains, prepared through a solid-state reaction and sintering process. When subjected to an electrical field during poling, the initially disordered spontaneous polarization in piezoelectric ceramics can be reoriented, maintaining a remnant polarization even after the external field is removed. This imparts a macropiezoelectric property to the ceramics. However, the inclusion of lead limits its application in biomedical and related fields. Lead-free ceramics are

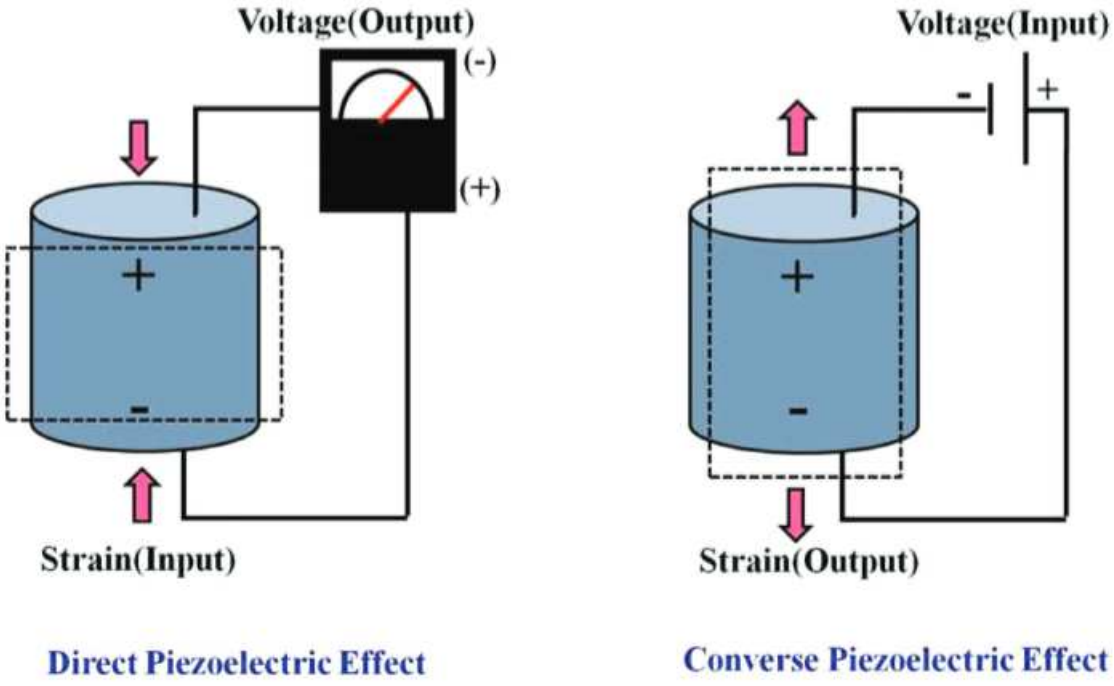

Fig. 2.2: Schematic of direct and inverse piezoelectric effect [4].

.

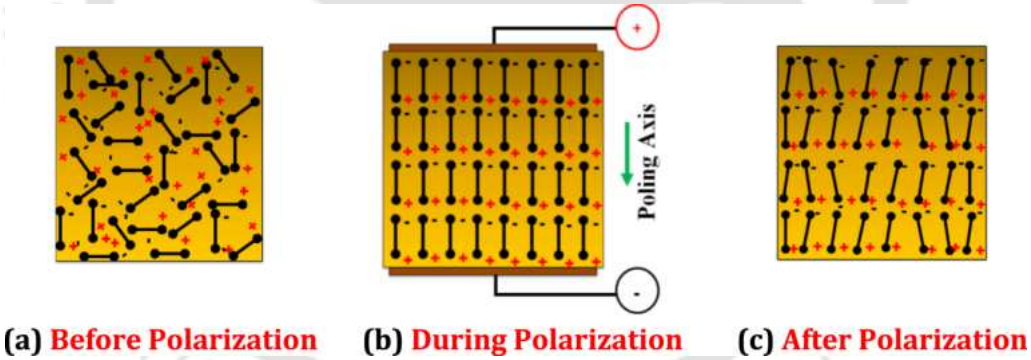

Fig. 2.3: Poling process depicting mechanism of piezoelectric effect. (a) Before polarization (b) During polarization (c) After polarization [3].

being employed as alternatives, but their efficiency is not as comparable to their counterparts. Piezo-ceramics, despite possessing high piezoelectric properties, are being avoided due to their brittleness, rigidity, high density, and lack of flexibility. The single crystals are next-generation piezoelectric materials for high-performance devices and systems, encompassing applications such as underwater communication sonars, ultrasound medical imaging probes, and sensors/actuators. Nonetheless, the precise control of shape and size during the growth process of these piezoelectric single crystals proves challenging, limiting their practical applications in various fields, including

micro-scaled actuators and composite meta-materials. Additionally, single crystals have a tendency to loose its piezoelectric properties when subjected to elevated electric fields. Moreover, piezoelectric polymers like PVDF, known for their high flexibility, low density, high dielectric breakdown, and low fabrication cost have garnered significant attention in recent years. Unlike single crystal and ceramic based piezo materials, polymers feature intertwined long-chain molecules that attract and repel each other when subjected to an electric field. Typical piezoelectric polymers include PVDF and its copolymers, nylon, and cellulose. Among these polymers, PVDF stands out for its exceptional piezoelectric properties, attributed to its molecular configuration and crystal structure. In general, piezoelectric polymers have a lower piezoelectric strain constant (d_{31}) than piezoelectric ceramics. The piezoelectric stress constant (g_{31}) for piezoelectric polymers, in contrast to piezoelectric ceramics, are significantly higher. The piezoelectric materials are categorized as per their material classes in the table 2.1 below.

Table 2.1: Types of piezoelectric materials.

Class of material	Examples
Natural crystals	Topaz, Rochelle salt, berlinite, quartz
Synthetic crystals	Lithium niobate, langasite, gallium orthophosphate
Ceramics (lead based)	Lead titanate, PMN-PT, lead zirconate titanate, PZN-PT
Ceramics (lead-free)	ZnO, $ZnSO_3$, $BiFeO_3$, $BaTiO_3$, $(K,Na)NbO_3$
Biomaterials	Collagen, cellulose, bone, silk, DNA
Polymer based	PVDF and its copolymers, polyamide

2.3 PVDF

PVDF is a semi-crystalline thermoplastic polymer synthesized through the polymerization of vinylidene difluoride. In 1969, Kawai [5] identified the piezoelectric effect of PVDF and initially measured its g_{31} and d_{31} coefficients, which were at least one order of magnitude higher than those of other polymers. Two years later, Bergman et al. [6] discovered the pyroelectric properties of PVDF. Since then, PVDF and its copolymers have been extensively researched for their applications in

pyroelectric and piezoelectric technologies. PVDF shows a complex semi-crystalline crystal structure consisting of five crystalline phases α, γ, β, ϵ and δ in which γ, β, ϵ and δ are polar phases while α is non-polar phase. The α-polymorph is characterized by a monoclinic unit cell featuring the TGTG conformation, rendering it piezoelectrically inactive. Conversely, the β-polymorph adopts an orthorhombic unit cell with the TTTT conformation, making it piezoelectrically active. Theγ-polymorph, exhibiting an orthorhombic unit cell with the T3GT3G conformation, occupies an intermediate state. On the other hand, the δ-polymorph serves as the polar counterpart of the α-form, while the ϵ-polymorph serves as the anti-polar counterpart of the δ-form. Numerous noteworthy properties of PVDF, particularly those associated with its application as a sensor or actuator, stem from the substantial electrical dipole moment inherent in the PVDF monomer unit. The β phase is particularly interesting for energy harvesting applications due to its electroactive polar crystalline nature. As compared with the other phases, the effective dipole moment in the β phase structure is the highest (due to the parallel arrangement of $-CF_2$ and $-CH_2$ bonds) and remains perpendicular to the carbon chain. In PVDF or its copolymer samples, the formation of the β-phase and the transition from α- to β-phase are crucial for achieving optimal piezoelectric properties. Exceptional ferroelectric, piezoelectric, and pyroelectric nature make PVDF an excellent choice in the domain of energy harvesting. The different semi-crystalline phases of PVDF as analysed by Wu et. al [7] are shown in Fig. 2.4.

2.4 FABRICATION TECHNIQUES OF PVDF BASED PIEZOELECTRIC COMPOSITES

The preparation process significantly influences the piezoelectric characteristics of PVDF based composites. Nowadays, numerous studies indicate that the primary factors influencing the piezoelectric properties of PVDF piezoelectric films include crystallinity content, molecular orientation, dipole orientation aligned with the electric field direction, electric field intensity, heat treatment, polarization temperature, and its duration, among others. Nevertheless, the pivotal factor affecting the efficacy of PVDF piezoelectric nanogenerator is their manufacturing process. Commonly, the preparation techniques encompass spin coating, solvent casting, hot pressing, electrospinning, and

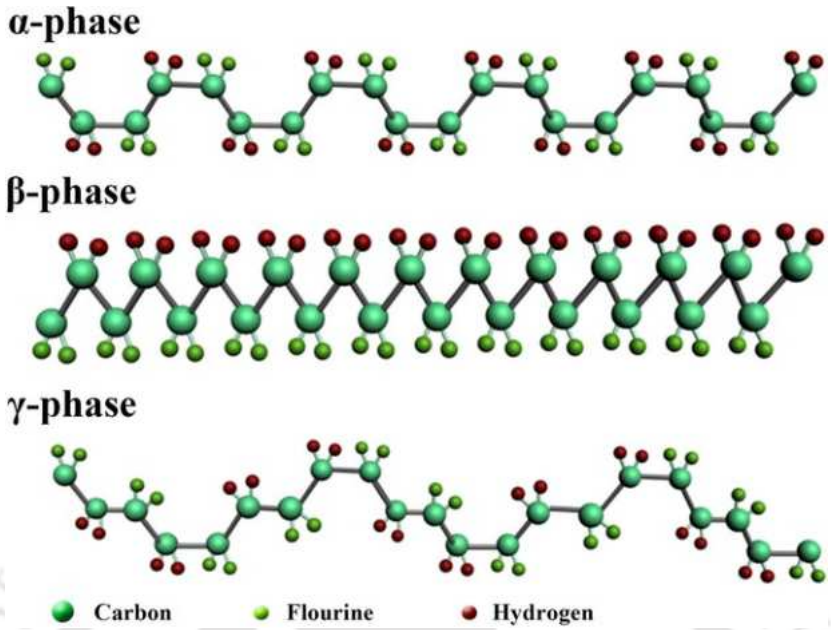

Fig. 2.4: α, β, and γ phases of semi-crystalline PVDF [7].

similar methods.

2.4.1 Solvent casting

The solution casting technique is extensively employed for fabricating films based on PVDF and its copolymers. The solution casting method, also recognized as the direct casting method, stands as one of the most prevalent techniques for producing polymeric films. This method, straightforward in its approach, has been employed for an extended duration in the development of polymeric film systems, hence earning the label of the conventional solution casting method by numerous authors. The process entails dissolving polymers in suitable solvents. These polymeric solutions, potentially incorporating various additives undergo degassing. Degassing can be achieved through vacuum application at a slightly elevated temperature or by ultrasonication. Subsequently, the degassed solutions are poured into molds positioned on a leveled surface and dried under controlled environmental conditions of specific temperature and humidity. Typically, the molds are composed of non-adhesive materials (e.g., Teflon, glass), facilitating easy removal of the films once dried. Following this, if necessary, the peeled-off films are subjected to curing before being stored for future use. Given the relative simplicity of this method, it has been extensively utilized by researchers in developing films for sensing, actuation, biomedical, and food packaging applications with notable

effectiveness.

2.4.2 Hot press

PVDF or its copolymers films can alternatively be prepared using a hot press. While solution casting offers advantages such as cost-effectiveness and simplicity, incomplete evaporation and susceptibility to environmental influences can be significant drawbacks. Hence, a hot press method has been developed to produce PVDF films through thorough evaporation or without the need for dissolution in organic solvents. A typical hot press setup for PVDF film preparation involves a high-temperature pressing stage followed by high-pressure cooling [8–10]. The critical factors in the hot press operation include temperature, pressure, and duration. Typically, temperatures in hot press processes exceed 150°C, occasionally reaching even higher levels surpassing 200°C. Elevated temperatures ensure the thorough melting of the PVDF matrix. Pressure levels in the hot press vary according to experimental conditions. Based on published reports, the lowest pressure recorded exceeds 5 MPa, while the highest pressure reaches 30 MPa [11]. The application of high temperature and pressure in a hot press can effectively remove voids within the matrix by inducing rolling of the material.

2.4.3 Electrospinning

Electrospinning is one of the widely used technique to fabricate PVDF films with high electroactive phase content. This process synthesizes thin fiber mats through the combination of mechanical stretching and poling. The charged jet of polymer solution is ejected when a high DC voltage is supplied to the solution due to the potential difference. After the low boiling point solvents evaporate, an electrically charged jet of the polymer solution is sprayed across the rotating or fixed collector. The polymer solution and collector plate are subjected to a high electric field, which causes the Taylor cone to develop at the spinneret's tip. Surface tension and viscosity are overcome by the electrostatic forces operating on the polymer solution, creating a thin spray jet of the polymer solution that produces high-quality, polymeric fibers. The determinants affecting electrospinning comprise solution parameters (such as solution concentration, type of solvent, and molecular weight of PVDF and its copolymers), voltage, tip-to-collect distance, collector rotation

speed, temperature, humidity, needle diameter, and the incorporation of nanofillers. In contrast to alternative methods, electrospinning presents a distinct advantage: the strain exerted during injection on the mixed solution prompts the uni-axial elongation of PVDF molecular chains along the fiber axis, resulting in the formation of the β-phase.

Typically, in initially prepared PVDF films, the α-phase prevails, given its stable thermal characteristics. Conversely, forming the β phase proves challenging due to the elevated energy barriers associated with the all-trans conformation [12]. However, the piezoelectric properties of PVDF or copolymers rely on the electroactive phase, particularly the β phase. Consequently, several techniques have been devised to enhance the formation of the β-phase or facilitate the α-to-β phase transformation.

2.5 TECHNIQUES TO IMPART PIEZOELECTRIC BEHAVIOR TO PVDF

Various approaches has been tried to enhance piezoelectric behavior of PVDF. The enhancement in piezo response can be achieved through increasing β phase content of PVDF. There are various ways to get this electroactive β phase. A few techniques consist of mechanical stretching, Electric poling, melt quenching, heat treatment, hot press and electrospinning. The details of these techniques are elaborated in the following subsections.

2.5.1 Addition of nanofillers

Developing polymer based nanocomposites using nanomaterials as reinforcing fillers has proven to be a successful method of improving the piezoelectric activity. The introduction of electroactive fillers induces the formation of the piezoelectric phase by promoting the nucleation of the crystalline β phase within the polymer. Various electroactive fillers, including carbon-based, inorganic, and bio-based materials have been incorporated into PVDF to increase the polar phase content, resulting in an enhancement of its piezoelectric properties. Achieving a uniform distribution is crucial in composites because the aggregation of nanofillers can lead to both crystal defects and a reduced degree of crystallinity. Different nanofillers like CNT, graphene, GO (graphene oxide), CNF, and CB (carbon black) serve as strengthening additives. Achieving uniform distribution is of paramount

importance in composites because the clustering of nanofillers not only leads to crystal defects but also diminishes the degree of crystallinity. Conversely, uniform dispersion can enhance properties or elevate the overall crystallinity. Researchers have drawn consistent conclusions regarding the roles of nanofillers as given below:

- The nanofillers can act as nucleating agents during the initial crystallization process, thereby enhancing the formation of the β-phase.
- The stress accumulation resulting from the inclusion of fillers can provide the energy needed for the transformation from theα-phase to the β-phase during the stretching process.
- Moderately electrically conductive nanofillers have the potential to establish a conductive network, inducing alignment of dipole moments during the subsequent poling process.

2.5.2 Mechanical stretching

Stretching is typically employed to enhance the transformation from the α-phase to the β-phase and reorganize the molecular chains of the β-phase, leading to a significant improvement in voltage output capability. Various parameters, such as stretching speed, elongation ratio, and temperature, affect the stretching process outcome. In non-stretched samples, the crystal area is primarily characterized by the α-phase (spherical structure). However, during the stretching process, the applied force prompts a transformation from the spherical structure to a fibrillar-like structure, resulting in the all-trans-planar zigzag conformation (TT), which is characteristic of the β-phase molecular chains. Simultaneously, the dipole moments align along the normal direction of stretching. The stretching ratio plays a crucial role, and high stretching ratios can result in significant elongation and a complete change in the crystal structure. Studies indicate that the elongation ratio should exceed 4 to achieve nearly pure β-phase samples. The anti-parallel structure is disrupted and polymer chains are aligned through mechanical stretching. PVDF films upon uni-axial stretching causes longitudinal deformation of molecular chains resulting in formation of more densely packed structure [13]. Given that the β phase has largest density among the PVDF's crystalline phases, it might be the polymorph that is most anticipated to occur during the stretching

process. Stretching at a high temperature of 80°C further enhances the chain mobility, which made it easier to align dipoles along the stretching direction [14].

2.5.3 Electric poling

As previously noted, introducing nanofillers and applying stretching can generate a significant proportion of the β-phase through evaporation and crystallization without the need for poling [15, 16]. In this scenario, the dipole moments are dispersed randomly within the matrix, resulting in mutual offset throughout the material. Consequently, the overall piezoelectricity is absent. To align the dipole moments in a specific direction for optimal piezoelectric performance, the process of poling is employed. Electroactive polar phase can be induced in PVDF with the help of electric poling process. In this technique, dipoles are aligned in particular direction with the help of externally applied electric field usually at elevated temperatures. Upon applying an electric field to the polymer structure, spontaneous polarization occurs subsequent to breaching the curie temperature, resulting in unidirectional dipole alignment. Due to this alignment, the dipoles are oriented in a way that, when the external electric field is removed, locking them into place and causes the polymer to become permanently polarized. Several poling methods exist, including (i) DC electrode poling, and (ii) Corona discharge poling. The commonly employed techniques are DC electrode and Corona discharge poling, while AC electrode poling is a more recent introduction. Subsequent sections will provide detailed discussions on each poling process, highlighting their advantages and disadvantages.

2.5.3.1 DC poling

Electrode poling represents a direct poling approach, characterized by its relatively simple and long-standing nature compared to other methods such as Corona poling and AC poling. In electrode poling, metal electrodes are deposited onto piezoelectric material using techniques like electrospinning [49] or sputtering [50], or the sample can be placed between two electrodes in the form of copper or aluminum tape, or coated with silver paint, with glass slides serving as sample holders. Close proximity between the electrodes and piezoelectric material is crucial to enhance dipole polarization. Thermal excitation requires heating the material, where temperature plays a key role

in the poling process. Electrode poling typically occurs in an insulating medium like a silicone oil bath or inert atmosphere to prevent excessive electric discharge and maintain a constant temperature. The process begins by immersing the electrodes in the oil bath and gradually increasing the temperature toward the material's Curie point, ensuring material activity is not compromised (d_{33} value decreases beyond the Curie temperature). Subsequently, DC voltage is incrementally raised until the electric field (typically ranging from 5 to 1000 kV/cm) [17, 18] across the sample aligns with the specified saturation polarization values. This voltage is sustained for a brief duration, followed by slow cooling of the sample to room temperature while maintaining a constant electric field. Finally, the high voltage source is deactivated.

2.5.3.2 Corona discharge poling

The conventional DC method used for poling piezoelectric samples exhibits several limitations. This technique necessitates electrode coating on both the top and bottom surfaces of the specimen, restricting its applicability to small samples. In contrast, Corona poling requires metallization on only one side of the piezoelectric material and does not require a vacuum environment. However, the Corona discharge process, which utilizes the breakdown of dry air or inert gas [17, 19], to polarize the piezoelectric material, is significantly more complex than electrode poling. Breakdown occurs at localized weak points such as pinholes, leading to electrode short-circuiting and impeding additional polarization. Despite this complexity, the Corona poling process has been successfully employed for manufacturing large film samples. During Corona poling, charges from the corona point (needle) disperse across the exposed surface of the sample (uncovered by electrodes), creating an electric field between the sample surfaces. Surface potential assessment can be conducted using an electrostatic kilovoltmeter [20] or a comparison method [21]. Notably, the absence of electrodes in weaker regions prevents sample short-circuiting, making Corona poling a more refined technique.

2.5.4 Heat treatment

Temperature plays a crucial role in shaping the crystal structure of PVDF films. Heat treatment serves to facilitate solvent evaporation and elevate the crystallinity degree of the β-phase. Consequently, implementing appropriate heat treatment proves to be an effective strategy for generating

samples with a substantial fraction of the β-phase. Three critical parameters that impact the outcomes of heat treatment are temperature, duration of operation, and the rate of both heating up and cooling down. Of these factors, temperature holds the utmost significance, with the effective annealing temperature falling within the range of 60 to 150°C [22]. While annealing can enhance the transition from the nonpolar α-phase to the polar β- and γ-phases during initial crystallization and promote the formation of more polar phases within the amorphous region of PVDF chains, its effectiveness is constrained by the adverse impact of reduced crystallinity degree. Annealing is recommended to occur within the temperature range bounded by the Curie temperature (T_c) and the melting temperature (T_m). During this process, thermal energy facilitates the reorientation and repositioning of polymer chains, resulting in increased crystallinity during subsequent cooling. Corresponding findings suggest that annealing temperatures below 100°C are suitable to β-phase formation [23, 24].

2.6 PRINCIPLE OF ENERGY HARVESTING

Mechanical energy is the most prevalent ambient form of energy that can be harnessed and transformed into useful electric power. Piezoelectric energy harvesting is a mechanism of collecting ambient mechanical energy and converting it into the useful electrical energy. Mechanical energy is mostly wasted, so different options have been investigated to convert it into other useful forms of power. Yang et.al [25] discussed potentiality of piezoelectric energy harvesting system of converting ambient mechanical signals such as industrial machines and transportation, bridge and building oscillations, power shoes, human actions such as walking, running, hand and leg motions and heart movement within the body etc. into useful electrical signal as shown in Fig. 2.5. Piezoelectric energy harvesting proves to be a highly convenient method for capturing ambient mechanical energy and transforming it into electrical power. This is because the piezoelectric effect relies solely on the intrinsic polarization of the material, eliminating the need for an external voltage source, magnetic field, or contact with another material, as is the case with electrostatic, electromagnetic, and triboelectric energy harvesting, respectively. Piezoelectric nanogenerators are characterized by their durability, reliability, high sensitivity to small strains, and an enhanced power output density

(approximately 3–5 folds higher), along with higher voltage output, in comparison to alternative energy harvesting methods [26, 27]. Additionally, piezoelectric generators can be fabricated in compact dimensions and small structures, making them easily integrable into microelectromechanical systems. Moreover, they remain unaffected by environmental factors such as humidity [28, 29]. Prof. Wang first introduced the idea for a piezoelectric nanogenerator in 2006 while sweeping the tip of an atomic force microscope through vertically produced ZnO nanowires [30]. This endeavor established the groundwork for the technological evolution and utilization of nanogenerators. In contemporary times, PZT (lead zirconate titanate) stands out as the most frequently utilized

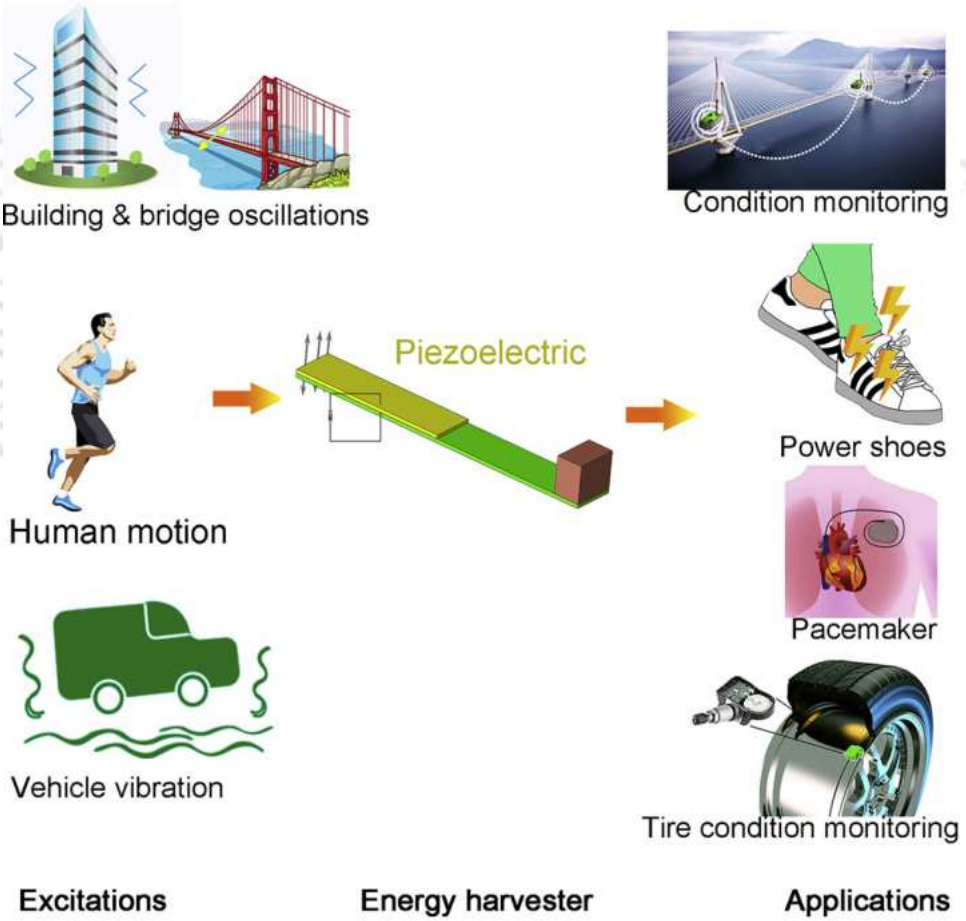

Fig. 2.5: Different ways of harvesting mechanical energy [25].

piezoelectric material due to its notable piezoelectric constant and electromechanical coupling factor. Nevertheless, its progress is impeded by factors such as high cost, fragility, high density, and environmental hazards [31, 32]. Conversely, PVDF and its copolymers offer numerous advantages,

including excellent flexibility, eco-friendliness, high resistance to halogens and acids, lightweight nature, and commendable biocompatibility. Notably, these materials can be shaped into complex, curved structures, thus presenting promising alternatives to PZT in certain applications.

Piezoelectricity arises from the highly organized dipole moments within crystalline polymers, which is influenced by the following four factors.

- The fraction of β-phase: The β-phase demonstrates superior piezoelectric properties compared to the more common α-phase. Hence, a key objective is to enhance the formation of the β-phase and the transition from α- to β-phase.
- Crystallinity degree: Piezoelectricity is only exhibited by the crystalline portion of the polymer, while the amorphous region does not contribute. Consequently, certain processes may increase the β-phase fraction but decrease the overall crystallinity degree. It's essential to carefully optimize parameters to strike a balance between these effects.
- Alignment of molecular chains: In initial crystallization, the orientation of molecular chains within the matrix is random, resulting in weak electrical output capability.
- The arrangement of dipole moments: In films lacking stretching or poling, the dipole moments within the polymer or composites typically remain disorganized. Consequently, these samples exhibit extremely weak or even negligible piezoelectricity, attributed to the mutual cancellation of dipole moments in opposing directions.

2.7 TYPES OF ENERGY HARVESTERS

Wearable technology demands clean, renewable, and sustainable energy to be practical and eco-friendly. Various types of energies are available in the environment, including those emanating from the human body and the surroundings. Human mechanical motions such as walking, running, and finger movements generate substantial mechanical energy daily, as shown in Fig. 2.6 as discussed by Huang et. al [33]. Efficiently capturing this mechanical energy is challenging. Wearable energy harvesting transforms ambient and human body energy into usable electrical energy. Transduction

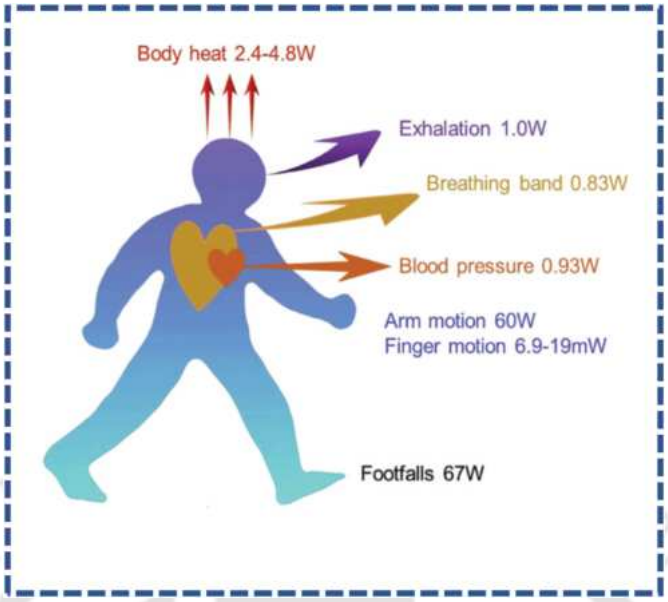

Fig. 2.6: Power generation via human activities [33].

mechanisms convert energy from one form to another, such as kinetic to electric energy. Piezoelectric and triboelectric generators are the two most widely used methods for capturing mechanical energy from human movement [34]. However, triboelectric nanogenerators (TENGs) face reliability, stability, and dependability issues. Further research on power management reliability and resistance to environmental conditions like humidity and temperature is needed. Piezoelectric generators, a conventional method of mechanical energy harvesting, have attracted significant interest due to their high energy density and more comprehensible physical mechanism. In biomechanical energy harvesting, PENGs are crucial for intelligent footwear [35], implantable technology [36], and intelligent fabrics [37]. PENGs may be limited by the variety of available materials compared to TENGs. However, their advantages of higher output current, straightforward design, and operational mode make piezoelectric generators essential for energy harvesting. Another useful energy source is the heat energy produced by the human body. There is a temperature gradient between the body and the outside environment, while the body temperature remains constant. Thus, continuous energy harvesting is possible with thermoelectric generators, which operate on the Seebeck effect—the diffusion of holes and electrons caused by a temperature gradient. Thermoelectric generators (TG), due to their insufficient energy conversion efficiency, cannot meet the power requirements of wearable devices. However, their stable energy source allows for continuous and prolonged energy

collection without human movement. The human body can also generate chemical energy, alongside bio mechanical and thermal energy. Bio-fuel cells, an energy-harvesting device, can capture chemical energy from the human body and convert it into electrical energy. Combining human energy harvesters with various energy-collecting techniques enhances energy efficiency. Solar energy, a clean, renewable energy type, is significant in energy harvesting. Self-powered systems, built on energy harvesting technologies, can operate without an external energy source [34]. A classification of different types of wearable energy harvesters in presented in Fig. 2.7 as discussed by Huang et. al [33].

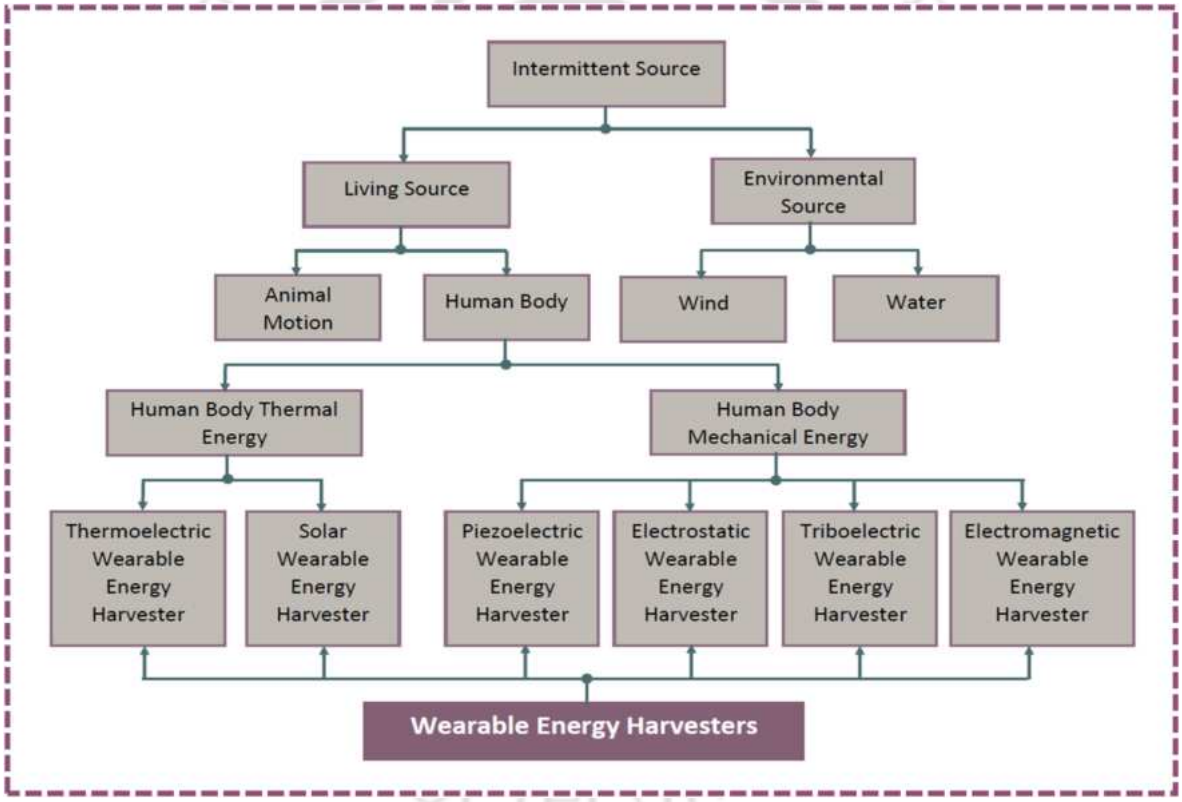

Fig. 2.7: Flow chart describing types of wearable energy harvesters [33].

PENGs stand out from other harvesters such as TENGs, Photovoltaic (solar) energy harvesters, and TEGs due to their superior power density, compatibility with various environments, and versatility across different applications.

2.8 SUITABILITY OF PENGs FOR IoT APPLICATIONS

PENGs are gaining increasing attention for IoT applications due to their unique capabilities. They convert mechanical energy from vibrations, motions, or pressure into electrical energy, offering a renewable and sustainable power solution in IoT, where many devices rely on batteries or need autonomous energy sources. The compact size of nanoscale PENGs allows for integration into small IoT devices and structures, crucial for the miniaturization requirements of IoT technology. These generators operate effectively at low frequencies and amplitudes of mechanical input, making them suitable for harvesting energy from ambient vibrations and movements typical in IoT environments. Piezoelectric materials, known for their durability and reliability over extended periods, can withstand harsh environmental conditions, making them suitable for outdoor and rugged IoT applications. As the IoT landscape expands, there is a growing demand for cost-effective energy solutions, and PENGs offer a promising method to power IoT sensors and devices without relying solely on batteries. Moreover, PENGs can be fabricated using various materials and techniques, allowing customization to meet specific IoT application requirements such as sensitivity to different mechanical stimuli.

PENGs are especially targeted in this thesis for IoT-based wearable health devices, as they can harvest energy from natural body movements like walking, running, or even subtle motions. A typical wearable device, such as a smartwatch, requires energy in the range of 10-100 mW [38]. A polymer-based PENG device, with a typical power density in the range of 1-30 mW/cm^2, can easily power these wearable devices. In healthcare domain, sensors embedded in or worn on the body are used to collect physiological data such as temperature, pressure rate, electrocardiograms (ECG), and electroencephalograms (EEG) from patients [39]. Additionally, environmental data like temperature, humidity, date, and time can also be recorded. These type of data help make accurate and meaningful inferences about patients' health conditions. Data storage and accessibility are crucial in the IoT system, as a large amount of data is acquired from various sources, including mobile phones, sensors, emails, software, and various applications. This information is made available to doctors, caregivers, and authorized parties, and sharing it through the servers or cloud

enables quick diagnosis and medical intervention if necessary. Effective and secure transmission is maintained through cooperation between users, patients, and the communication module. Most IoT systems feature a user interface that acts as a dashboard for medical caregivers, providing user control, data visualization, and interpretation. Extensive research has documented the progress of IoT systems in healthcare monitoring, control, security, and privacy, highlighting their effectiveness and promising future in the healthcare sector. However, designing an IoT device requires careful consideration of quality service metrics, including privacy, security, cost, reliability, and availability.

PENGs have the potential to fulfill the energy requirements of low to moderate-power wearable healthcare devices, particularly those with intermittent operation and low-duty cycles. For high-power devices, hybrid systems that combine multiple energy harvesting technologies with efficient energy storage and power management strategies are likely to be more effective.

However, challenges such as optimizing efficiency, scaling up manufacturing processes, and integrating PENGs into existing IoT architectures remain. Despite these obstacles, the potential of PENGs to provide sustainable, self-powered solutions aligns well with the evolving needs of IoT, particularly in applications such as remote monitoring, environmental sensing, and smart infrastructure.

2.9 ADVANTAGES 0F PENG DEVICES

PENGs present numerous benefits, making them appealing for a variety of applications. Here are some key advantages:

- **Miniaturization:** With their nanometer-scale dimensions, PENGs can be integrated into microelectronic devices, facilitating the development of self-powered nanosystems and driving advancements in nanoelectronics and wearable technology.

- **Flexibility and Versatility:** PENGs can be fabricated using flexible materials, allowing their incorporation into various substrates and surfaces, including flexible and wearable electronics.

- **Scalability:** The fabrication processes for PENGs, such as electrospinning, solvent casting,

and melt extrusion are scalable, enabling mass production and widespread adoption in various applications.

- **Integration with Existing Systems:** PENGs can be seamlessly integrated with existing electronic systems and components, enhancing the functionality and efficiency of a wide range of devices, from medical implants to environmental sensors.

2.10 DISADVANTAGES 0F PENG DEVICES

PENGs have attracted significant interest due to their capability to convert mechanical energy into electrical energy at the nanoscale. However, various challenges and limitations must be overcome to enable their wider application and optimization. Below are some of the main drawbacks of PENG devices:

- **Limited Output Power:** PENGs typically generate low power output, which may be inadequate for many practical applications. The harvested energy might not suffice to power larger electronic devices without substantial energy storage and management systems.
- **Material Limitations:** The performance of PENGs is highly dependent on the piezoelectric material used. Common materials like PZT are toxic and environmentally hazardous. There is a need to develop new materials that are both efficient and eco-friendly.
- **Mechanical Fatigue:** Piezoelectric materials can experience mechanical fatigue over time, especially under continuous or cyclic loading, leading to performance and reliability degradation.
- **Environmental Stability:** The performance of PENGs can be affected by environmental factors such as temperature, humidity, and exposure to chemicals. Ensuring stability and longevity in various environmental conditions is crucial.

2.11 APPLICATIONS OF PENG DEVICES

Piezoelectric nanogenerators are employed in diverse fields owing to their capacity to harness energy from surrounding mechanical vibrations and motions. The following are examples of appli-

cations for piezoelectric nanogenerators:

Wearable devices: Integrating piezoelectric nanogenerators into wearable gadgets allow for the extraction of energy from the wearer's body motions. This harvested energy can be utilized to power various sensors and other electronic elements in health monitoring devices.

Biomedical Implants: PENG devices can be used in powering biomedical implants, such as pacemakers, drug delivery systems, tissue engineering and ultrasonic imaging. These devices can capture energy from the mechanical movements of organs or muscles, ensuring a continuous and sustainable power source for the implants.

Energy Harvesting in IoT Devices: Internet of Things (IoT) devices generally function in areas where frequent battery replacement is inconvenient or impractical. The utilization of piezoelectric nanogenerators allows for the extraction of energy from the surroundings, facilitating the creation of self-powered IoT devices capable of extended operation without the need for external power sources.

Smart Fabrics and Textiles: Incorporating piezoelectric nanogenerators into fabrics and textiles enables the production of electrical power through body movements or external forces. This generated energy can then be harnessed to supply power to small electronic components embedded in clothing, such as communication devices or health monitoring sensors.

Environmental Monitoring: PENGs offer advantages to remote environmental monitoring stations by extracting energy from wind, vibrations, or other natural sources. This capability facilitates the deployment of energy-efficient, self-sustaining monitoring systems in distant or hard-to-reach locations.

2.12 LITERATURE REVIEW OF PVDF BASED FLEXIBLE PENG DEVICES

Various material combinations have been used by researchers for piezoelectric energy harvesting, including ceramic ferroelectrics, such as PZT [40], KNN [41], and BTO [42], piezoelectric semiconductors, such as GaN [43], CdS [44] and ZnO [30] as well as ferroelectric polymers, such as PVDF [45]. Ferroelectric polymers are lighter and more flexible than ceramic and semiconductor based piezoelectric materials. This research work is focused on PVDF based piezo energy har-

vesters. Various nanofiller combinations are reinforced in PVDF to enhance its piezo response for PENG device fabrication as given in Fig. 2.8.

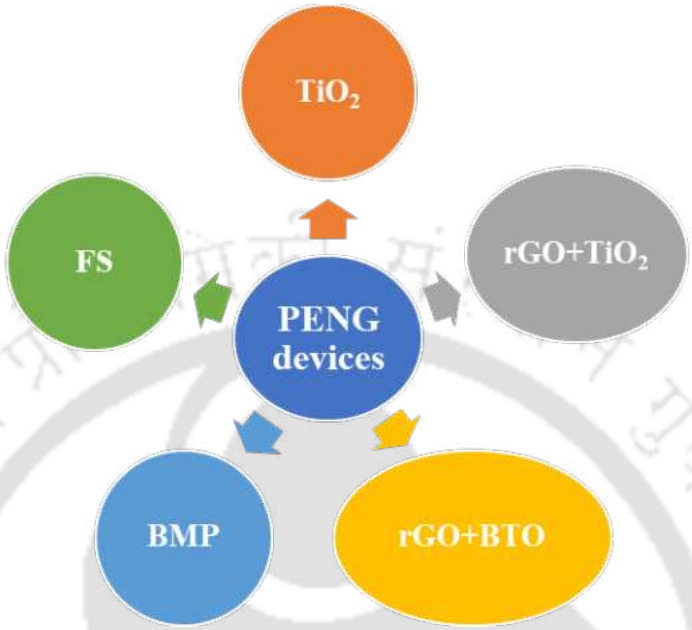

Fig. 2.8: Nanofiller combinations used with PVDF for PENG device development.

2.12.1 PVDF-TiO_2 nanocomposite based piezoelectric energy harvesters

Different types of fillers are doped into PVDF to induce electroactive phases and improve dielectric and mechanical properties.TiO_2 nanoparticles can be used as fillers in PVDF matrix for their high chemical and thermal stability as well as higher dipole moment. TiO_2 is best suited for nanofiller as it enhances the electrical and mechanical properties of PVDF. TiO_2 significantly enhances the electroactive β phase and piezoelectric properties of PVDF [46–48]. Alam et al. [49] developed spin coated PVDF-TiO_2 nanocomposite films for energy harvesting purposes that produced open circuit voltages of about 5 V under continuous finger imparting condition. Later, [46] recorded day to day human activities and acoustic vibrations into useful electrical energy by fabricating PVDF-TiO_2 based electrospun nanofibers.An open circuit voltage of approximately 11.5 V is observed under conditions of repeated finger touching. Zhu et al. [50] prepared PVDF-TiO_2 nanofibers for enhancing piezo behaviour of PVDF to use in geophone applications. The highest piezoelectric output voltage of 3.85 V was observed for 2 wt.% PVDF-TiO_2 nanofibers for finger tapping conditions. Abdolrasouli et al. [51] developed electrospun nanofiber mats of PVDF-based

graphene oxide supported TiO_2-Fe_3O_4 hybrid nanoparticle-nanosheets, which showed remarkable piezo response with 79% enhancement in β phase content and maximum voltage generation of 4.63 V at 2 wt.% of TiO_2-Fe_3O_4-GO addition. Further, Liu et al. [52] fabricated dopamine (DA) coated PVDF-TiO_2 thin films with using the solvothermal technique. DA treated TiO_2 reinforced PVDF films showed a β phase content of 84% as opposed to 36% for neat PVDF film. Later, Arunguvai et al. [53] studied the role of TiO_2 and ZrO_2 nanofillers for enhancing energy harvesting capacity of PVDF-TrFE and reported enhanced output voltage of around 8.2 V for nanocomposite thin film as compared to pure PVDF-TrFE. Liu et al. [54] enhanced piezoelectric behaviour of PVDF through corona poling and increased β phase up to 86.1% by adding 0.5 wt.% TiO_2. A voltage reading of approximately 3.5 V is achieved for applied pressure of 1 MPa using a mechanical test system. Kum-Onsa et al. [55] improved dielectric behaviour of PVDF by incorporating TiO_2 nanorods assisted by dispersion and hot pressing. The highest recorded dielectric constant is 66, observed when incorporating a 0.5% loading of TiO_2. Nevertheless, no information is provided in the above-mentioned reports regarding the effect of TiO_2 content on PVDF's mechanical properties. Most of the works mentioned in the literature have followed electrospinning approach for nanocomposite fabrication, but few studies were conducted on PVDF-TiO_2 thin films fabricated using solvent cast process.

2.12.2 PVDF-TiO_2-rGO based three phase energy harvesters

Different techniques have been tried to enhance energy harvesting performance of ceramic reinforced PVDF nanocomposites. The addition of a carbon-based conductive filler to polymer-ceramic based nanocomposites can further improve its dielectric strength and piezoelectric properties, allowing the nanogenerator to harvest more energy [56, 57]. rGO is a conductive nanoparticle which consists of a more surface area and excellent thermal as well as mechanical stability. A higher surface area of rGO leads to improved dipole formation and enhanced charge storage in the nanocomposite. In addition, oxygen functional groups present in the basal plane of rGO enhance polymer crystallinity by engaging and arranging chains in a single direction. Saygh et al. [58] fabricated GO-TiO_2-PVDF based hybrid nanocomposites by simple solution mixing process for the first time

for pressure sensor application. Maximum tensile strength of 46.91 MPa was obtained for PVDF based hybrid nanocomposite. Later, Ishaq et al. [59] reported enhanced dielectric values for rGO and TiO_2 loaded PVDF nanocomposites which were fabricated using solvent casting process. A maximum dielectric constant of 70.4 was recorded. Ponnamma et al. [60] synthesized PVDF based nanocomposites with a binary nanofiller combination of TiO_2 and rGO for sensing applications through the solution mixing process. The nanocomposite films displayed enhanced thermal and dielectric properties. There are very few research studies on three phase PVDF nanocomposites based on rGO and TiO_2. According to literature data, no detailed information is available on the optimal loading percentage of rGO in PVDF-TiO_2 matrix for maximum dielectric, mechanical, and piezoelectric performance.

2.12.3 PVDF-rGO-BTO based three phase energy harvesters

In recent years, BTO has gained significant attention because it possesses strong piezoelectric properties, is simple to prepare, and is relatively cheap. The rGO addition facilitates uniform dispersion of BTO nanoparticles into the polymer solution. Reinforcing conductive fillers create several micro-capacitor models inside the composite structure, enhancing overall dielectric properties. It also stabilizes the β phase content of PVDF [56]. Yaqoob et al. [61] reported role of graphene oxide on ferroelectric and dielectric behaviour of PVDF-BTO composites for prospective energy harvester applications. The nanocomposite films were coated on $Pt/TiO_2/SiO_2/Si$ substrate. The study highlights a maximum dielectric constant of 98, coupled with a relatively lower dielectric loss of 0.081 at 1 MHz for 0.3 wt.% of rGO loading in PVDF-BTO composite. Later, Yaqoob et al. [62] synthesized flexible PENG devices by spin coating composite solution on Cu/PET substrate followed by polydimethylsiloxane (PDMS) encapsulation. A peak-to-peak voltage of 8.5 V under a 2N force on loading a 0.5% of rGO was recorded. Yaqoob et al. [63] further enhanced the piezo response by fabricating a tri-layer PENG structure which recorded a peak to peak voltage of 10 V for an applied force of 2 N. Shi et al. [64] studied synergistic behaviour of graphene and BTO nanofillers on energy harvesting performance of electrospun PVDF nanofibers. The fabricated PENG device generated 112 V during finger pressing-releasing process. Bakar et al. [65] reinforced graphene

quantum dots in PVDF-BTO composites to check its energy harvesting capability. A peak-to-peak voltage of 4.6 V was obtained. Luo et al. [66] fabricated flexible wearable pressure sensor device for electronic skin applications. PVDF-BTO-rGO thin films were fabricated using near- field electro hydrodynamic direct-writing method. Li et al. [67] synthesized multi-layer PVDF-BTO-rGO based ternary PENG device having rGO loading up to 0.45 wt.%. A maximum voltage of 16.91 V is reported for finger joint bending conditions at various angular positions. However, very limited study on energy harvesting performance of PVDF-BTO-rGO nanocomposites fabricated through solvent casting is available.

2.12.4 BMP based sustainable impact sensor

Some of the piezoelectric ceramics are toxic, highly brittle, and non-biocompatible, which limits their use in nanogenerators and flexible electronics. Moreover, improper disposal of these materials can result in serious ecological degradation. Therefore, it is necessary to switch the focus toward developing energy scavenging devices made of naturally available biocompatible piezoelectric materials [68]. Bamboo is a naturally occurring functional material having excellent mechanical strength, high stiffness, less density, and high growth rate. High crystallinity and presence of polar hydroxyl group in bamboo makes it piezoelectric. Singh et al. [69] fabricated mustard seeds-PVDF based triboelectric nanogenerator using electrospinning technique with an output voltage and power density of 84 V and 334 mW/m^2 respectively for an impact force of 40 N. Maiti et al. [70] fabricated energy efficient onion skin based piezoelectric energy harvester that could generate around 18 V voltage and 166 nA current under repetitive human fingers hitting and releasing as an applied loading condition. Saqib et al. [71, 72] at first developed tomato peel based piezoelectric nanogenerator, followed by natural sea grass based spray coatable triboelectric device, for energy harvesting applications. The seagrass-based device generated an instantaneous power of 1.69 mW. Badatya et al. [73] developed a piezoelectric biodegradable eggshell membrane combined with a PVDF layer nanogenerator through a solution-based method. The fabricated nanogenerator device recorded a substantial output voltage of 15 V and a current of 150 nA, even in the absence of electrical poling. Sun et al. [74] developed chemically treated wood sponge based nanogenerator with 0.06

V output voltage for finger tapping loading condition for energy harvesting purposes. Sahu et al. [75] incorporated coconut husk (CH) powder in PVDF to fabricate flexible PENG devices to monitor the breathing pattern using solvent casting process. 7 % CH in PVDF composition showed a maximum voltage of 14 V, a current of 50 nA and a power density of 0.35 $\mu W/cm^2$ using a linear motor at a constant frequency. But, the problem with these devices is that, they do not possess enough mechanical strength and flexibility. There are few reports available regarding piezoelectricity of bamboo [76–78]. Due to its low piezo response and rigid nature, BMP is not suitable for commercial use. It is, therefore, crucial to reinforce these materials with PVDF so that the energy harvester device is structurally sturdy and has improved piezoelectric performance. Furthermore, energy harvesters based on BMP have not been explored thus far.

2.12.5 Bio-piezoelectric nanogenerators

Collagen (type I) is most abundant piezo biomaterial found in animal tissues (skin, cartilage, tendon, bone). The cost-effective source of this collagen is fish constituents (skin, maws, fins, and swim bladder). Fish is mainly considered a bio waste material as it is consumed in large proportion across the world [79]. These bio wastes on disposal cause increasing environmental pollution. The recycling of fish constituents (typically scales) into the fabrication of sustainable piezo sensors is excellent solution. The presence hydrogen bonding motifs (with polar uni-axial orientation) between the poly peptide chains behaves as molecular dipoles that results in spontaneous polarization and piezoelectric nature [80]. Ghosh et al. [81, 82] for the first-time reported fish scale based piezoelectric bio energy harvester with an output voltage, power density and sensitivity of 4 V, 1.14 $\mu W/cm^2$ and 23.5 $\mu V/Pa$. Later, a fish skin-based pressure sensor with a sensitivity of 27 mV/N was developed by the same group. Marimuthu et al. [83] constructed piezo capacitor based on waste fisheries for energy conversion and storage purposes. The powder of fish scales and bones were reinforced into PVA to fabricate PENG device film using doctors blade instrument. The piezo capacitor reported a maximum voltage of 6 V for a mechanical force of 1 N. Under the impact of palm tapping and mechanical force, the capacitor demonstrated a self-charging capacity, reaching 1.23 V and 6 mA within a 10-second time frame. To further enhance its output response, Kumar et al. [84] reinforced

fish scales into the PVDF polymer matrix. The device exhibited a voltage of 22 V with a power density of 28.5 $\mu W/cm^2$ for finger pressing condition. Most of the published work has focused solely on the piezoelectric behavior of FS, with little research being done on role of FS as a reinforcing element in PVDF matrix. Moreover, for a commercial sensor development, a PENG device needs to have good piezo response and enough mechanical strength. No work has been reported yet on studying mechanical properties of FS based devices.

2.13 RESEARCH GAPS

The following research gaps have been identified based on the above literature:

- According to literature data, no detailed information is available on the optimal loading percentage of TiO_2 in PVDF matrix for maximum dielectric, mechanical, and piezoelectric performance. The mechanical energy harvesting behaviour of PVDF-TiO_2 nanocomposite thin films containing higher TiO_2 loading in PVDF matrix has not yet been investigated.

- The effect of varying rGO and fixed TiO_2 concentration on mechanical and piezoelectric response of PVDF is not yet studied. Additionally, no research work has reported the energy harvesting behaviour of rGO-TiO_2 loaded PVDF based hybrid nanocomposites.

- Very few reports are available on mechanical properties of PVDF-BTO-rGO nanocomposites. Yet, there is no research on the optimal rGO content in PVDF-BTO nanocomposites to achieve maximum tensile strength, toughness, elastic modulus, and hardness.

- There has not been much research on the energy harvesting behaviour of PVDF-BTO-rGO nanocomposite films made by solvent casting, as most research works have focused on electrospun or spin coated films.

- Since bamboo fibers exhibit piezo properties, there has been no research to assess their piezoelectric response. Currently, there is a significant research gap regarding fabrication of bamboo fiber reinforced PVDF composites and analysis of its dielectric, mechanical, and piezoelectric response.

- The studies on fabrication of FS based PVDF composites are still limited. Moreover, the effect of varying FS concentration on mechanical, dielectric and piezoelectric properties of PVDF is not yet explored.

2.14 OBJECTIVES

Based on the literature survey, following objectives are proposed for the present research work:

- Fabrication and characterization of highly flexible PVDF-TiO_2 based nanocomposites using solvent casting technique for energy harvesting applications.
- Application of MCDM based material selection and optimization technique called TODIM followed by a sensitivity study to select the best material for mechanical energy harvesting applications for PVDF-TiO_2-rGO hybrid composites.
- To study the effect of rGO loading on mechanical and piezoelectric performance of PVDF-BTO nanocomposites prospective PENG device fabrication for energy scavenging.
- The development of a low-cost, sustainable BMP based flexible bio composite for impact sensing and mechanical energy harvesting applications.
- Development of FS based bio compatible piezoelectric impact sensor.

Chapter 3

PVDF-TiO_2 nanocomposite based piezoelectric energy harvesters

3.1 INTRODUCTION

PVDF thin films have a wide prospect in energy harvesting applications due to flexible design and presence of electroactive phase. Despite massive work in this domain, commercial applications are very rare since PVDF based thin films have low piezoresponse. In this chapter, the piezoelectric output voltage of the PVDF films is further enhanced by loading TiO_2 nanofillers into the viscous PVDF solution using solvent casting approach. TiO_2 nanoparticles are ideal fillers for PVDF matrices due to their exceptional chemical and thermal stability, along with a high dipole moment. Incorporating TiO_2 enhances both the electrical and mechanical characteristics of PVDF. Moreover, TiO_2 significantly boosts the electroactive β phase and piezoelectric properties of PVDF. The materials used along with nanocomposite fabrication is discussed in sec.3.2. Different weight concentration (0, 0.5, 1, 2, 5, 7, and 10 wt.%) of TiO_2 nanofillers are added in the respective PVDF solution, and the resulting solutions are casted on glass petri dish to obtain highly flexible composite films. Sec.3.3 explores the analysis of fabricated nanocomposite films using various characterization tools such as FTIR, FESEM, and XRD. Additionally, presence of the β phase, thermal behavior, surface roughness, mechanical properties, and piezoelectric performance are investigated. The tensile strength, elastic modulus, and storage modulus of PVDF-TiO_2 nanocomposite films showed significant enhancement compared to pure PVDF. PVDF-TiO_2 films showed about 143% increment in ϵ and 214% increment in σ_{ac} than pure PVDF. TiO_2 loaded PVDF films showed enhanced P_r values which indicates increased piezoelectric performance. The piezoelectric test is performed on

seven PENG devices. The piezoelectric output voltage of TiO_2 reinforced nanocomposite films also showed significant improvement. The open circuit voltage reached 5.45 V, which provide a solid foundation for energy harvesting applications. At last, a conclusive summary of the current work is provided in sec.3.4.

3.2 EXPERIMENTAL

3.2.1 Materials

PVDF pellets (molecular weight of 530,000), DMF (anhydrous, 99.8%) solvent and TiO_2 nanoparticles (<100 nm particle size, 99.5% trace metals basis) are ordered from Sigma Aldrich, USA.

3.2.2 Synthesis of nanocomposite films

The PVDF-TiO_2 nanocomposite films are fabricated with the help of a solvent casting technique . Solvent casting process consists of dispersion of nanofiller in a polymer solution by energetic agitation, controlled evaporation of solvent, and finally composite film casting. Agitation can be accomplished by magnetic stirring followed by sonication [85]. Initially, the PVDF pellets (2 g) are added to 10 ml of polar DMF solvent. The amount of solvent is crucial here since it determines the uniformity and agglomeration possibilities of the sample. Different weight concentration (0, 0.5, 1, 2, 5 and 10 wt.%) of TiO_2 nanofillers are added in the respective solution, and the resulting solutions are named as PVDF, PVDF-0.5T, PVDF-1T, PVDF-2T, PVDF-5T, PVDF-7T and PVDF-10T respectively. TiO_2 loading above 10% causes severe filler agglomeration in the PVDF matrix, leading to film breakage due to increased brittleness. Therefore, TiO_2 loading is limited to 10%. The wt.% of TiO_2 nanoparticles can be obtained with the help of equation 3.1:

$$W_{TNP} = \frac{W_{TiO_2}}{W_{TiO_2} + W_{PVDF}} \tag{3.1}$$

Where $W_{\mathrm{TiO_2}}$ and W_{PVDF} are weights of TiO_2 and PVDF in g respectively. A list of the exact amounts of each mixture ratio is provided in Table 3.1.

To get uniform dispersion, the resulting mixture is magnetically stirred for 4 hours at 60 °C. As soon as the solution is ready, it is subjected to an ultrasonication process, ensuring uniform and thorough dispersion of the matrix and fillers. The solution is kept in a sonicator for about 1 hour,

Table 3.1: Weight percentages of different nanocomposite films.

Sample name	Weight of PVDF (g)	Weight of TiO_2 (g)	DMF volume (mL)
PVDF	2	-	10
PVDF-0.5T	2	0.01	10
PVDF-1T	2	0.02	10
PVDF-2T	2	0.04	10
PVDF-5T	2	0.1	10
PVDF-7T	2	0.15	10
PVDF-10T	2	0.23	10

depending on the nanofiller reinforcement. The nanocomposite solution has a viscosity of around 738 Pa.s, as measured by a rheometer (Physica MCR 301, Anton Paar) at 1 Hz and 25 °C. The mixture is then poured in a glass petri dish. The obtained solution is then placed in a furnace at 65 °C for 12 hours to eliminate solvent and moisture content to get free standing nanocomposite films (90 mm diameter). Further, the sample is kept in a vacuum desiccator for 48 hours for its thorough drying. Fig. 3.1a presents the schematic representation of nanocomposite synthesis using solvent casting process. The actual nanocomposite films post fabrication are shown in Fig. 3.1b-c. Once the fabrication is completed, nanocomposite films are subjected to compression press to adjust its thickness value. Further, the final thickness value is confirmed using a digital micrometer (Mitutoyo 293-240-30 μm).

3.2.3 Material characterization

The surface morphologies are captured using a FESEM (GeminiSEM 500, ZEISS) followed by a quantitative constituent analysis and element mapping with the help of EDS.The crystal structure, size, and associated lattice strains are analyzed using XRD (Rigaku technologies, Japan) using Cu-Kα radiation (1.54 Å). The measurement is performed for the 2θ range from 15° to 60° with a scanning rate of 4°/min. The piezoelectric phase enhancement of the nanocomposite sample is confirmed by FTIR (PerkinElmer, Singapore) with ATR mode over the wavenumber span of 600-1000

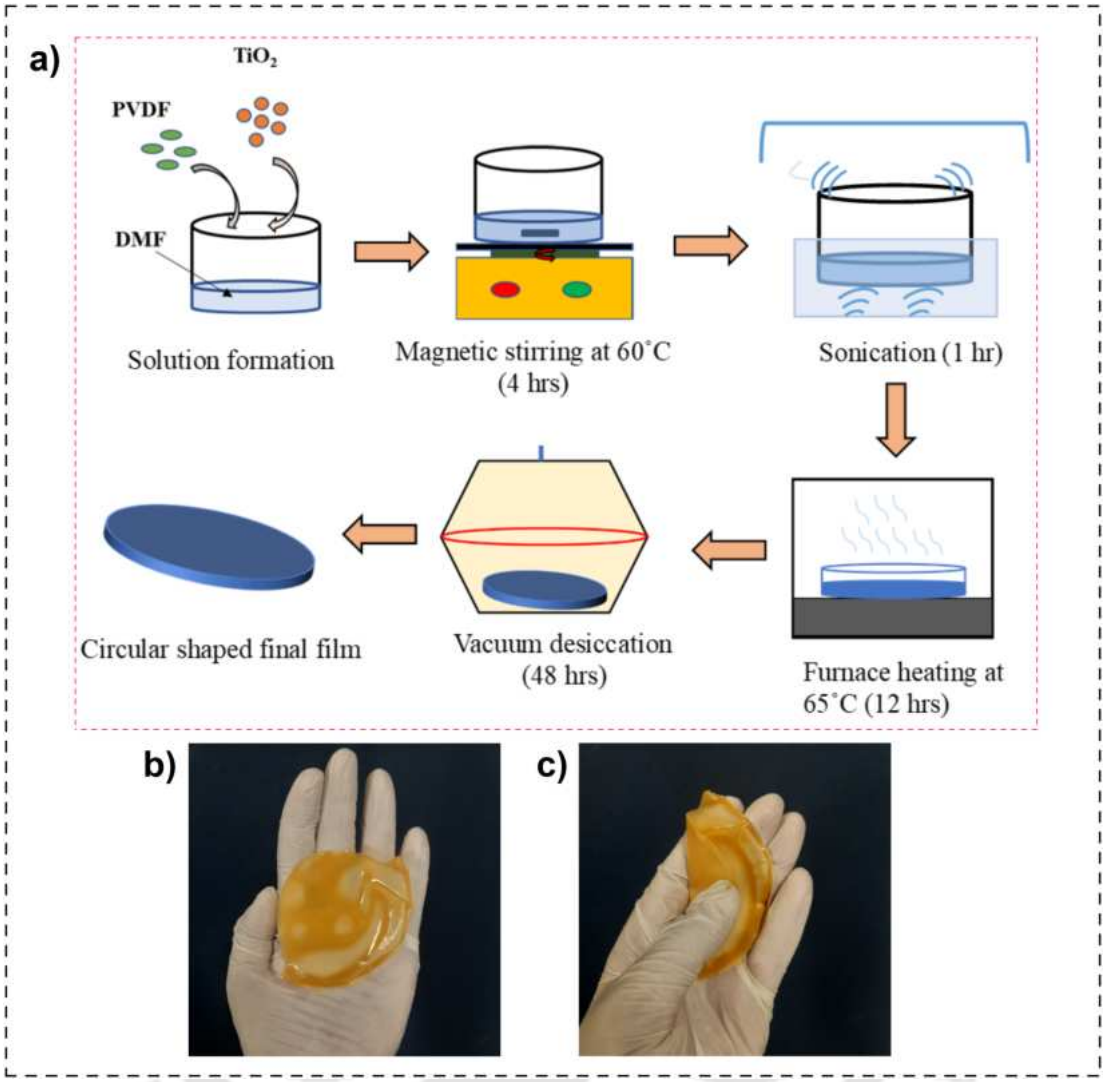

Fig. 3.1: a) Fabrication of nanocomposites using solvent casting process, b) nanocomposite films (post fabrication), and c) nanocomposite film displaying its flexibility.

cm^{-1}. The roughness nanocomposite films is checked using AFM (Cypher, Oxford) with tapping mode. UV-VIS spectroscopy (PerkinElmer, Lambda 950) is used to measure the nanocomposites' absorbance and optical band gap over the wavelength range of 200-700 nm. Differential scanning calorimetry (DSC) (Netzsch, STA449F3A00) is carried out from 25 °C-200 °C with a heating rate of 10 °C/min. The dielectric measurement is carried out using Impedance and material analyzer (IMA) (Novocontrol, BDS 2300) from 1 MHz to 3 GHz at room temperature. For the test, samples are cut into circular shapes of about 5 mm diameter followed by aluminium (Al) electrode coating (about 200 nm thick) on both sides using the thermal evaporation technique. The viscoelastic properties of the sample are recorded using a dynamic mechanical analyser (DMA) (Physica MCR

702, Anton Paar) under tensile mode on a 40 × 10 mm sample size. The samples are subjected to a temperature sweep from 25 °C-200 °C at 1 Hz with a heating rate of 8°/min and change in frequency from 0.1 to 70 Hz at room temperature. The mechanical properties (tensile strength and elastic modulus) of the sample are obtained using a 100 kN universal testing machine (UTM) (Instron, dynamic UTM 8801) with a strain rate of 1mm/min. Before conducting the test, the samples are prepared according to the ASTM standard D882. The Polarization–electric field (P-E) loop study of nanocomposite samples (around 5 mm of diameter) is carried out using a ferroelectric tester (Radiant technologies, USA). The piezoelectric voltage of the piezoelectric nanogenerators (PENGs) is measured using DSO (GWInSTEK, GDS-2102A).

3.3 RESULTS AND DISCUSSION

3.3.1 FESEM and EDS

The morphological characteristics and structure of the prepared nanocomposite films are studied using FESEM. We analyzed seven samples in this study. Uniform grain structures of PVDF are presented in Fig. 3.2a. Fig. 3.2b-g shows that TiO_2 nanofillers are uniformly distributed in the PVDF without much agglomeration, as shown by the dotted red colored circles and rectangles. The presence of Fluorine (F), Carbon (C), Oxygen (O), and Titanium (Ti) in EDS and elemental mapping spectra for PVDF-7T confirms the PVDF-TiO_2 nanocomposite formation, as presented in Fig. 3.3. The elemental mapping data indicates a uniform distribution of each element throughout the composite sample. Ti molecule is present at 4.4 keV energy level in PVDF-TiO_2 sample. The energy levels at 0.5 keV, 0.6 keV, and 0.24 keV, respectively, confirm F, O, and C elements corresponding to the polymer matrix [86].

3.3.2 XRD analysis

XRD analysis is performed on seven samples to verify the presence of TiO_2 in the PVDF matrix. It also helped to determine the electroactive β phase of crystal structure. The diffraction peaks obtained (Fig. 3.4a) at $2\theta = 18.21°$ and $20.22°$ represents α phase and β phase of PVDF respectively [87], while the peaks at 27.42°, 36.08°, 44.2°, and 56.51° belongs to miller indices of (110),

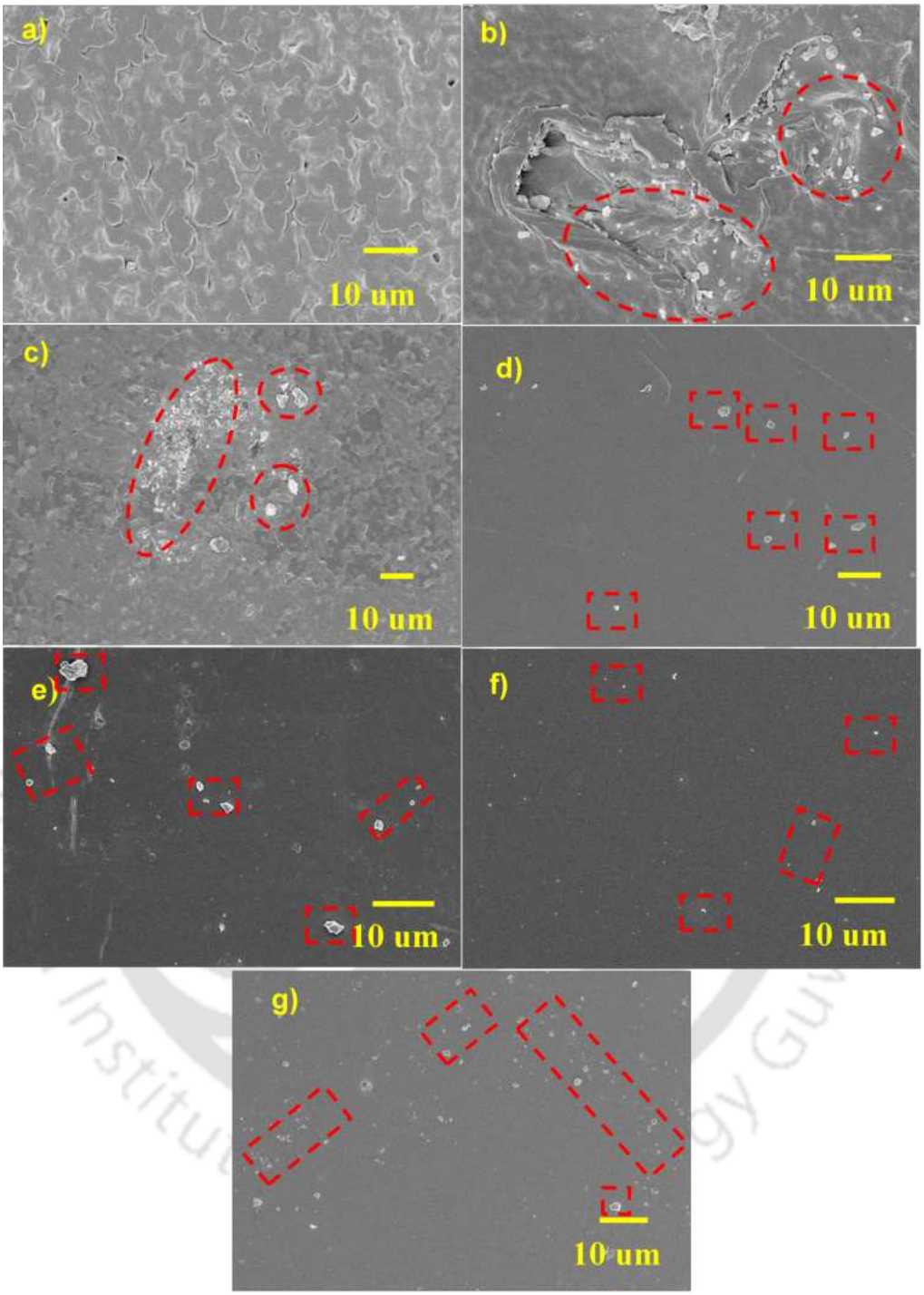

Fig. 3.2: FESEM plots of PVDF and its nanocomposites: a) PVDF, b) PVDF-0.5T, c) PVDF-1T, d) PVDF-2T, e) PVDF-5T, f) PVDF-7T and g) PVDF-10T.

(200), (211), and (220) respectively, which corresponds to the rutile phase of TiO_2 [88]. Fig. 3.4b shows that with increasing TiO_2 concentration, the intensity of β phase of PVDF also increases. As a result, the PVDF matrix exhibits enhanced piezoelectric activity.

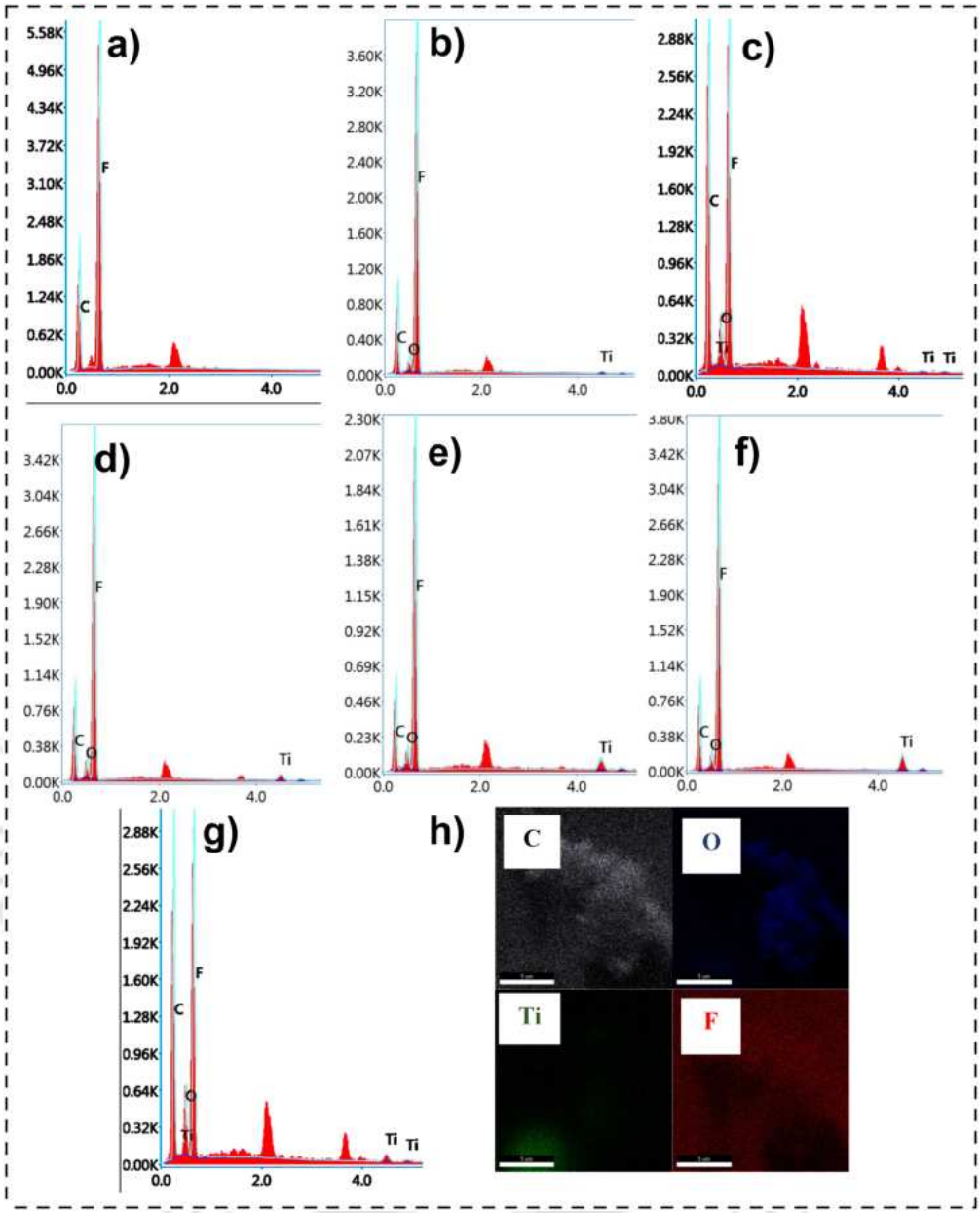

Fig. 3.3: EDS images of PVDF and its nanocomposites: a) PVDF, b) PVDF-0.5T, c) PVDF-1T, d) PVDF-2T, e) PVDF-5T, f) PVDF-7T, g) PVDF-10T and h) EDS elemental mapping of Ti, O, F, and C elements for PVDF-7T.

3.3.3 FTIR spectra

FTIR study is carried out to identify the phases of PVDF (particularly β phase) and its nanocomposite. Fig. 3.5a shows that peaks corresponding to 841 (CH_2 rocking), 1288 (Trans band), and 1400 (CH_2 Wagging) cm^{-1} belongs to the β phase of the nanocomposite [89], while absorption peaks at 614, 763, and 976 cm^{-1} represents α phase of PVDF [90]. The β phase fraction in the

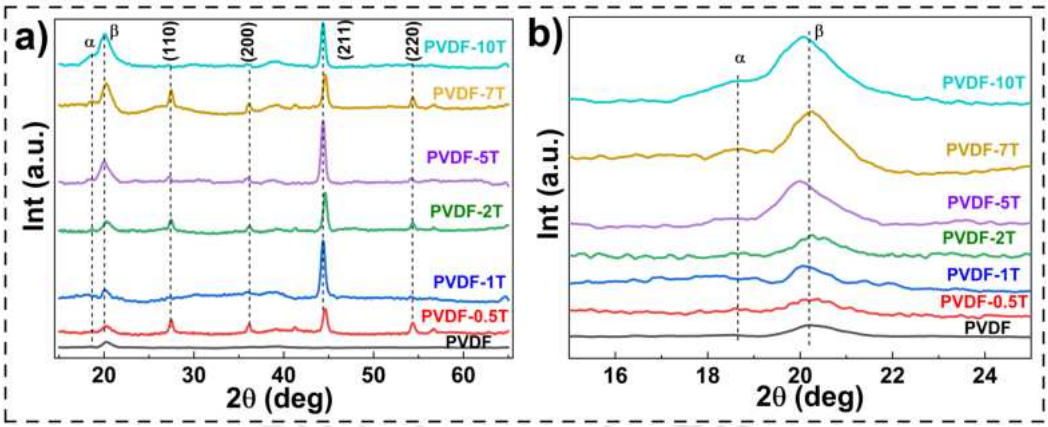

Fig. 3.4: XRD plots of PVDF and its nanocomposites: a) crystalline phases with miller indices and b) β phase enhancement of PVDF-TiO_2 nanocomposite films.

fabricated samples is calculated using Gregorio relation [91] as given in equation 3.2:

$$F(\beta) = \frac{A_{841}}{A_{841} + 1.26A_{763}} \tag{3.2}$$

Where A_{841} and A_{763} are absorption intensity values for α and β phases, respectively. Fraction of electroactive β phase obtained using above relation are 52, 63, 71, 78, 85, 86, and 89% corresponding to samples with TiO_2 reinforcement of 0, 0.5, 1, 2, 5, 7, and 10 wt.% respectively as presented in Fig. 3.5b. It can be seen clearly in Fig. 3.5b that TiO_2 reinforcement enhanced the electroactive β phase of PVDF, further its piezoelectric activity also enhanced. A maximum β phase content of 89% is obtained for 10 wt.% TiO_2 concentration. Filler loading has a positive effect on β phase content, nevertheless, at greater concentrations, the value decreases due to filler agglomeration and networking.

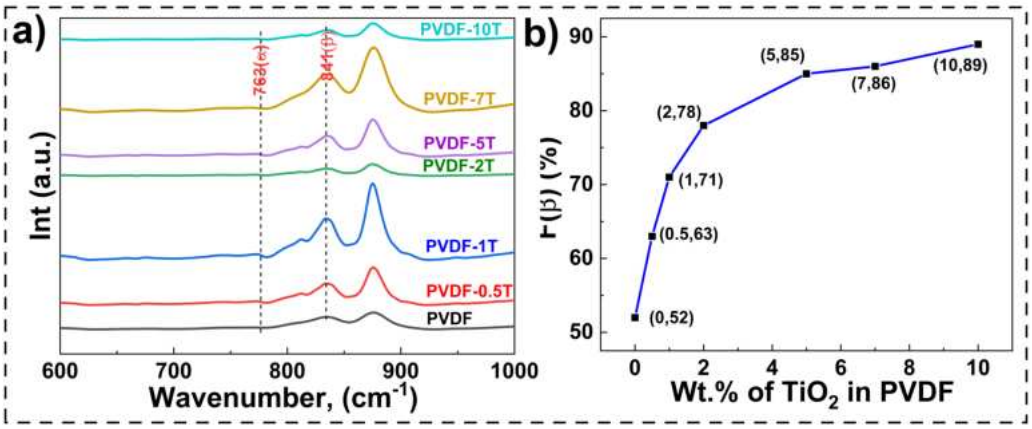

Fig. 3.5: FTIR test details: a) FTIR spectra and b) variation in electroactive β phase content against increasing TiO_2 reinforcement.

3.3.4 AFM measurement

PVDF-TiO_2 thin film surface height is captured using AFM spectroscopy (see Fig. 3.6). Four samples are studied under AFM (PVDF, PVDF-2T, PVDF-5T, and PVDF-10T). Average surface roughness (S_a), root mean square roughness (S_q), maximum peak height (S_p), and average maximum height (S_z) of these samples are measured using Gwyddion software. The reinforcement of TiO_2 nanofillers in the PVDF has increased the surface roughness of samples than pure PVDF. The increment in surface roughness causes higher friction which leads to higher β phase. The higher β phase is responsible for enhanced piezoelectricity [92]. The surface roughness parameters are presented in Table 3.2.

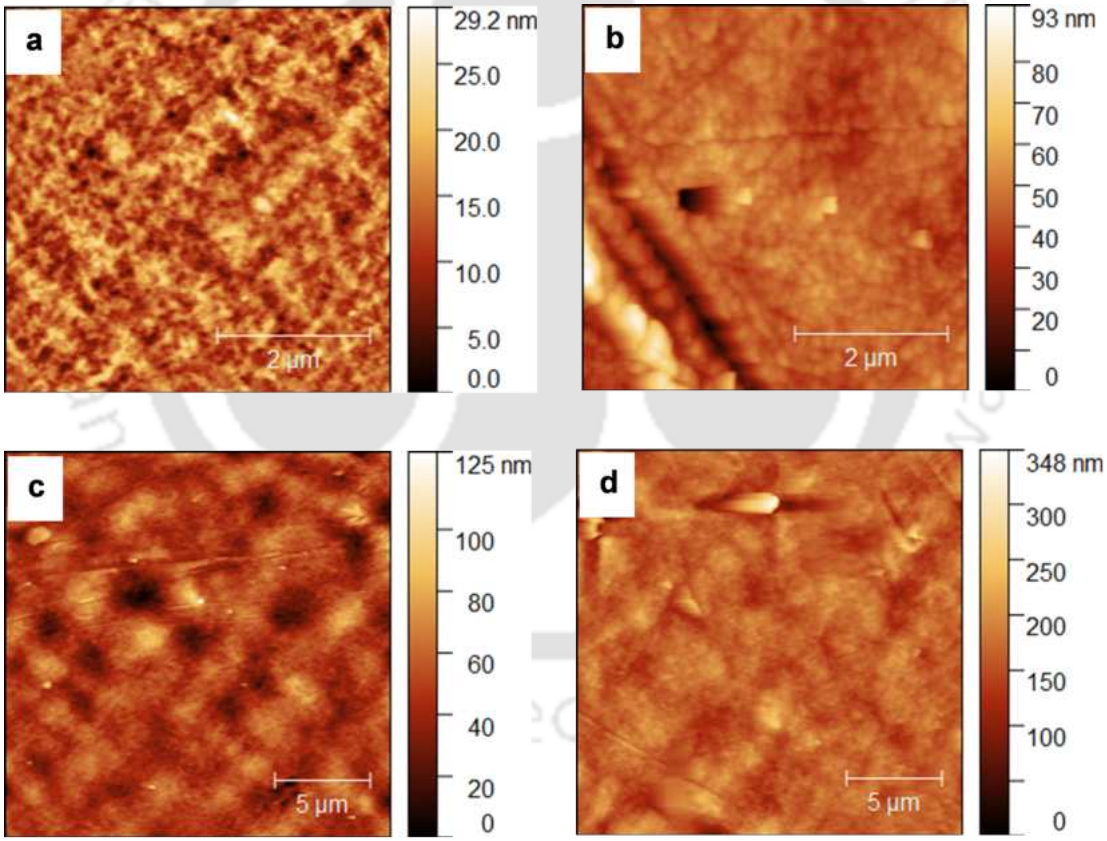

Fig. 3.6: AFM images of PVDF and its composites: a) PVDF, b) PVDF-2T, c) PVDF-5T, and d) PVDF-10T.

3.3.5 UV-Vis spectroscopy

UV-Vis spectroscopy test is conducted to measure the optical properties of PVDF and PVDF-TiO_2 nanocomposites. Fig. 3.7 depicts the absorbance spectra for neat PVDF and PVDF-TiO_2

Table 3.2: Surface roughness parameters.

Sample name	S_a (nm)	S_q (nm)	S_p (nm)	S_z (nm)
PVDF	13.823	3.461	15.4	29.223
PVDF-2T	43.26	8.801	50.2	93.46
PVDF-5T	48.128	11.53	76.72	124.84
PVDF-10T	164.31	22.821	184.119	348.43

films. The spectra show that PVDF does not absorb in the visible spectrum while TiO_2 presents a band at 380 nm (3.26 eV), which is consistent with the literature values [93, 94]. With an increasing TiO_2 content, the absorption value also increases. The peaks at Fig. 3.7b-c depicts tauc graphs for

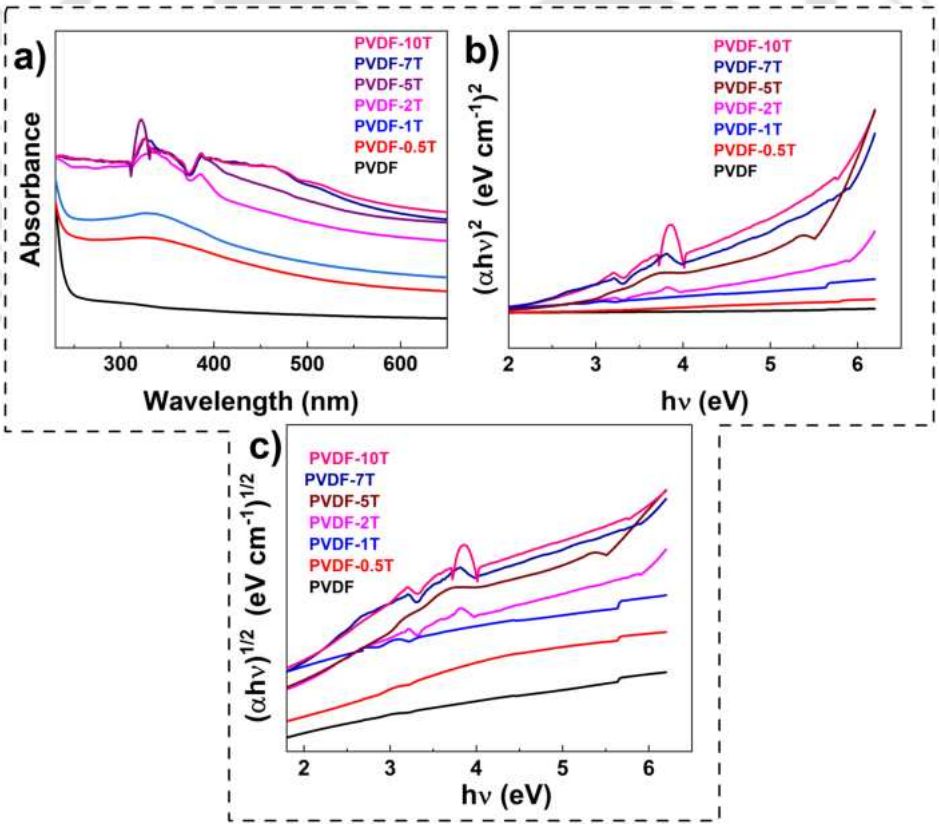

Fig. 3.7: Optical properties of PVDF and its nanocomposites: a) UV-Vis absorption plot, tauc plots of b) direct and c) indirect band gap.

direct and indirect band gap of test samples using the equation 3.3:

$$\alpha = 2.303 \times \frac{A_b}{\mathrm{d}} \tag{3.3}$$

Where A_b is the absorbance and d is the thickness of the prepared samples.

$$\alpha(\nu) = \frac{(h\nu - E)^n}{h\nu} \tag{3.4}$$

Where the exponent n = 0.5 for indirect transition and n = 2 for direct transition. Therefore, tauc plots are used for the indirect and direct band gap calculation. At $\alpha = 0$, the extrapolated line intersects the photon energy axis, yielding an optical band gap value. The reduction in the band gap value with increment in TiO_2 nanofillers is explained by the defect formation, which enhance the density of localized states in the band gap and, consequently, increase the grain size of the film. In nanocomposite films, a reduction in the energy band gap increases electrical conductivity and affects their optical properties [95]. The direct and indirect band gap values are presented in Table 3.3.

Table 3.3: Direct and indirect band gap values of PVDF and PVDF/TiO_2 films.

Sample name	Direct band gap (eV)	Indirect band gap (eV)
PVDF	5.56	4.96
PVDF-0.5T	5.18	4.83
PVDF-1T	4.99	4.72
PVDF-2T	4.92	4.23
PVDF-5T	4.81	3.9
PVDF-7T	4.24	3.84
PVDF-10T	3.89	3.5

3.3.6 DSC analysis

With the use of DSC, the thermal behaviour and percentage crystallinity (X_c) of nanocomposites are examined. A total of three samples are analyzed (pure PVDF, PVDF-5T, and PVDF-10T). Fig. 3.8 shows the typical DSC thermographs for these samples. The X_c value can be obtained with the help of equation 3.5.

$$X_c = \frac{\Delta H_m}{\Delta H_{100\%}} \times 100 \tag{3.5}$$

Where ΔH_m and $\Delta H_{100\%}$ are the melting enthalpies of nanocomposite films and perfectly crystalline PVDF (104.7 J/g), respectively [96]. The melting temperature (T_m) for pure PVDF is 167.25°C. However, with the addition of TiO_2 nanoparticles, a slight increase is observed for PVDF-5T and PVDF-10T, respectively, as tabulated in Table 3.4. It is due to the excellent thermal properties of TiO_2, and the decomposition temperature of nanocomposite structures [97]. The X_c values of nanocomposite increase in comparison with pure PVDF. When TiO_2 nanofillers are added in pure PVDF, heterogeneous nucleation of PVDF matrix takes place, thereby causing increased crystallinity [52]. Additionally, changes in nanofiller size, filler reinforcement, and the interfacial interactions between nano TiO_2 and PVDF matrix are responsible for the increment in crystallinity values [98, 99].

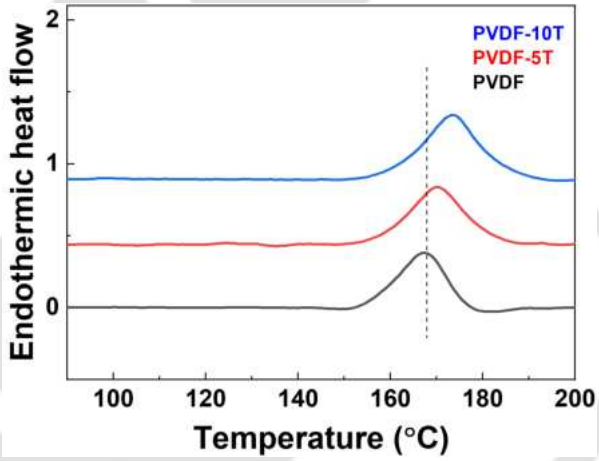

Fig. 3.8: DSC results of PVDF and PVDF/TiO_2 nanocomposite films.

Table 3.4: Melting temperature and crystallinity values of PVDF and PVDF-TiO_2 films.

Sample name	T_m (°C)	ΔH_m (J/g)	X_c %
PVDF	167.25	28.044	26.78
PVDF-5T	170.14	32.23	30.78
PVDF-10T	173.58	40.02	38.22

3.3.7 Dielectric measurement

Fig. 3.9a shows thermally evaporated circular nanocomposite films for dielectric measurement. Fig. 3.9b shows the variation of ϵ and ϵ' over frequency for PVDF-TiO_2 nanocomposites. Dielectric performance of PVDF polymer is greatly influenced by TiO_2 content. It is observed that the maximum ϵ of 23 is obtained for the PVDF-10T sample, which is 2.42 times higher than neat PVDF film. So, 143% increment in ϵ is observed for 10 wt.% of TiO_2 addition. It is observed that a steadily increasing ϵ and ϵ' is seen as TiO_2 nanofillers are incorporated into the PVDF matrix. This substantial increment in dielectric values is explained based on Maxwell- Wagner-Sillars (MWS) polarization mechanism [100]. In the MWS theory, the concept of dielectric polarization is demonstrated, which predicts that under slowly changing electric fields, charge accumulation, redistribution of the electric field, and enhanced polarization will occur at interfaces between constituents with different permittivity such as in a blend or composite dielectric material [101–103]. This charge accumulation at the interfacial location induces interfacial polarization causing increment in ϵ and ϵ' values owing to the presence of two heterogeneous systems having distinct dielectric constants [104]. Furthermore, the dielectric constants for all samples show a decreasing tendency as frequency increases, as dipoles cannot rotate at higher frequencies, thereby lowering the polarization and dielectric constant [105]. Fig. 3.9c-d denotes variation of ac conductivity (σ_{ac}) of nanocomposite films over a frequency range. It is observed that σ_{ac} values of PVDF-TiO_2 nanocomposite films increased exponentially over the increasing TiO_2 content. The maximum value of σ_{ac} is obtained for the PVDF-10T sample, which is 0.0186 S/cm, 3.14 times that of PVDF. Table 4 gives values of ϵ, ϵ' and σ_{ac} at 1MHz for PVDF-TiO_2 based nanocomposite films.

3.3.8 DMA analysis

DMA can study the interaction of nanofillers with polymers in nanocomposites films. Compared to pure PVDF, nanocomposites are more effective at transferring the interfacial stress and restricting the segmental motion of polymer chains [106]. However, the storage modulus starts to decrease at a higher filler concentration (10 wt.%), due to the agglomeration of TiO_2 nanofillers within the PVDF matrix. With increasing temperature, the storage modulus reduces and becomes

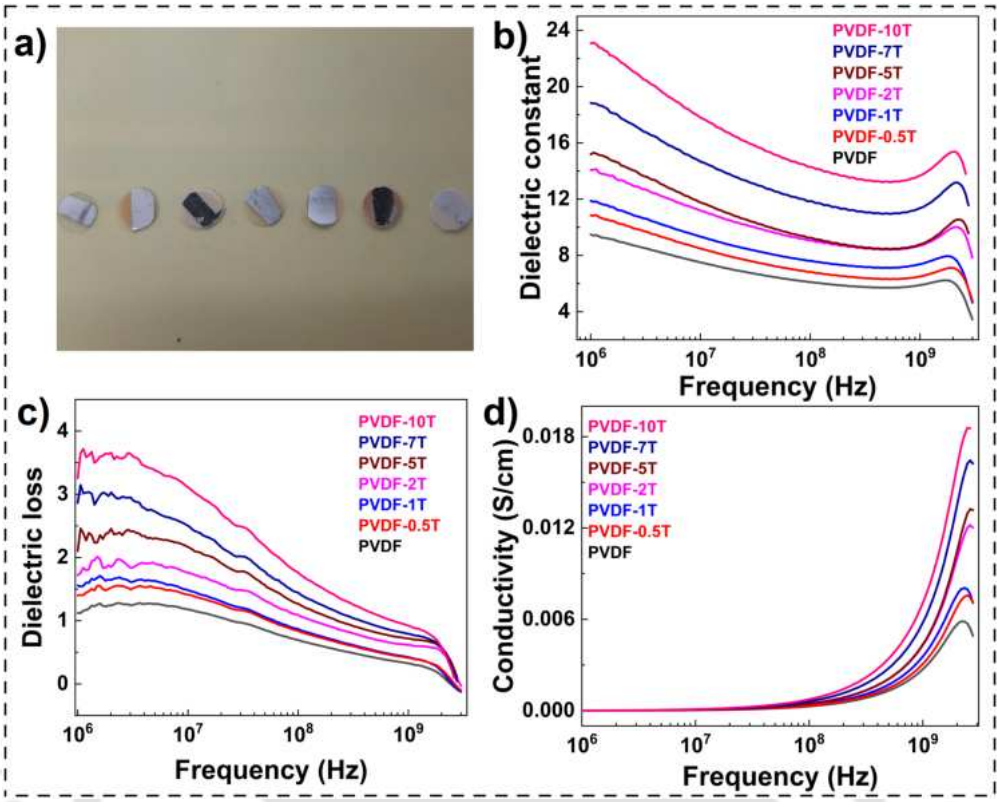

Fig. 3.9: Al coated samples for dielectric test, b) dielectric constant, c) dielectric loss and d) conductivity of pure PVDF and PVDF/TiO_2 nanocomposite films.

Table 3.5: Melting temperature and crystallinity values of PVDF and PVDF-TiO_2 films.

Sample name	ϵ	ϵ'	σ_{ac} (S/cm)
PVDF	9.48	1.12	0.0059
PVDF-0.5T	10.86	1.39	0.0076
PVDF-1T	11.87	1.56	0.0081
PVDF-2T	14.07	1.72	0.0123
PVDF-5T	15.17	2.10	0.0134
PVDF-7T	18.83	2.87	0.0165
PVDF-10T	23.06	3.26	0.0186

constant after a certain temperature is reached for all nanocomposites. The increase in temperature increases the kinetic energy of molecules, resulting in increased molecular mobility (oscillation of molecules in polymer). This reduces the storage modulus by increasing the free volume between

molecular segments [107]. The loss modulus of the nanocomposites is higher compared to pure PVDF at room temperature. The loss modulus of the nanocomposites decreased with increasing temperature. DMA plots for temperature and frequency sweep conditions are presented in Fig. 3.10.

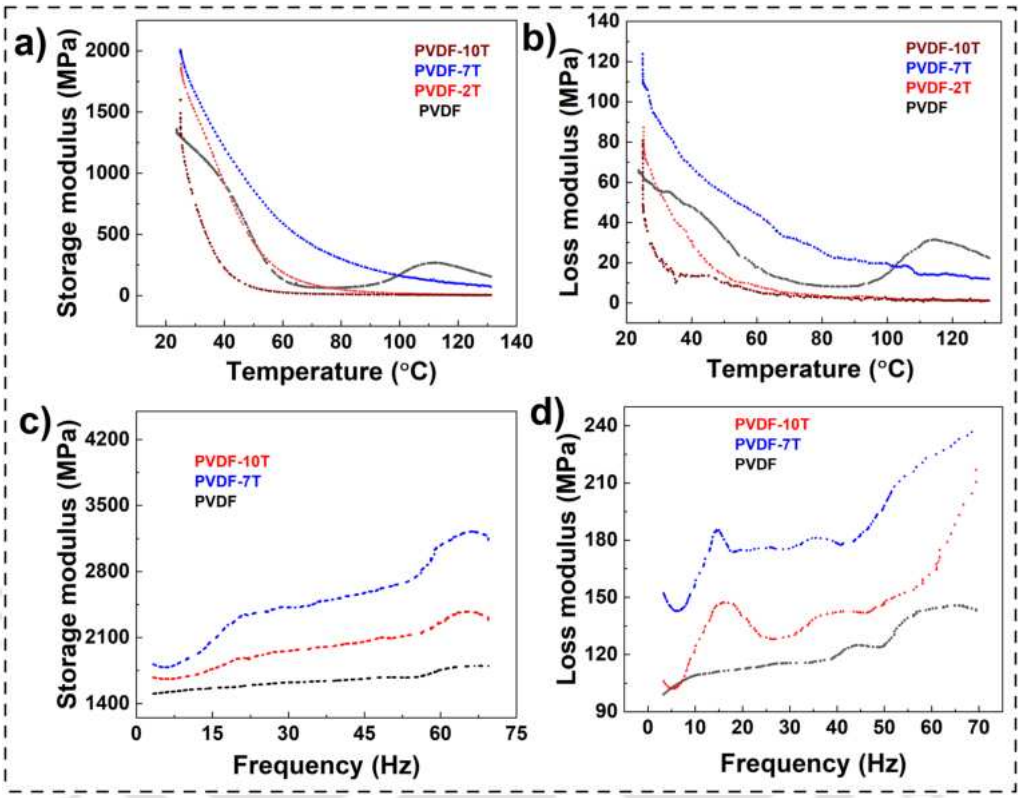

Fig. 3.10: DMA plots of PVDF and its nanocomposites: a) storage modulus, and b) loss modulus over temperature, c) storage modulus, and d) loss modulus over frequency.

3.3.9 UTM testing

The tensile strength and elastic modulus for PVDF-TiO_2 nanocomposite samples are calculated as shown in Fig. 3.11a-b. By increasing TiO_2 concentration, nanocomposites exhibit enhanced tensile strength and elastic modulus. Tensile strength values for PVDF, PVDF-0.5T, PVDF-1T, PVDF-2T, PVDF-5T, PVDF-7T and PVDF-10T nanocomposite films are 35.90, 39.17, 42.36, 46.62, 50.28, 34.45 and 21.08 MPa respectively. Elastic modulus obtained are 1175.3, 1187.3, 1384.1, 1421.1, 1592.2, 1150.2 and 648.2 MPa corresponding to samples with TiO_2 reinforcement of 0, 0.5, 1, 2, 5, 7, and 10 wt.% respectively. Compared with pure PVDF, the nanocomposite with 5wt.% TiO_2 has the maximum value of tensile strength and elastic modulus, where there is an increase of

40% and 36% respectively. The introduction of TiO_2 particles led to reduction of macro-voids and enhanced interactions between inorganic particles and polymers, contributing to the heightened mechanical strength of the composite structure [108]. While with a further increase of TiO_2 above 5 wt.%, a reduction in mechanical strength is observed. The higher content of TiO_2 particles slows down dispersion, causing agglomeration. The agglomerated particles tend to create defects, causing stresses to accumulate within nanocomposite, resulting in a decreased tensile strength and elastic modulus [109].

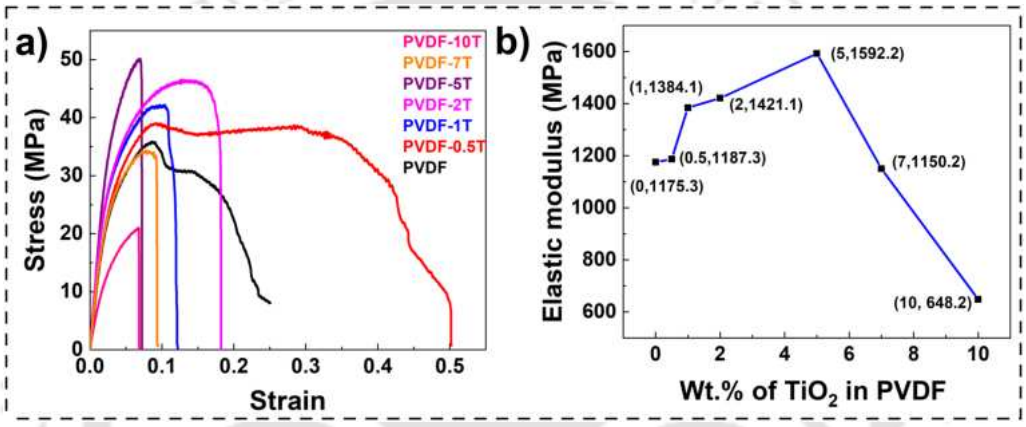

Fig. 3.11: Tensile test results of PVDF based nanocomposites: a) Stress vs. strain curve and b) elastic modulus variation over different TiO_2 concentration.

3.3.10 Ferroelectric measurements

The P-E loop test has been conducted to confirm the enhanced ferroelectric properties of PVDF-TiO_2 nanocomposite films. Fig. 3.12 shows the P-E loop plot without any poling treatment. The area of all the samples was fixed at 0.1963 cm^2. The remnant polarization (P_r) values for nanocomposite films are 0.00475, 0.00587, 0.00678, 0.00957, 0.0101, 0.0152 and 0.0174 $\mu C/cm^2$, respectively, under an applied electric field of 40 kV/cm. PVDF-10T nanocomposite film has been found to have a maximum P_r value of 0.0174 $\mu C/cm^2$, which is 267% higher than pure PVDF film. Materials with higher remnant polarization are expected to have higher piezoelectric properties and generate higher voltage signals in nanogenerators [110]. This result confirms the enhanced piezoelectric behaviour of nanocomposite films due to TiO_2 reinforcement in the PVDF matrix. Variation of P_r with TiO_2 nanofiller loading is presented in Fig. 3.12b.

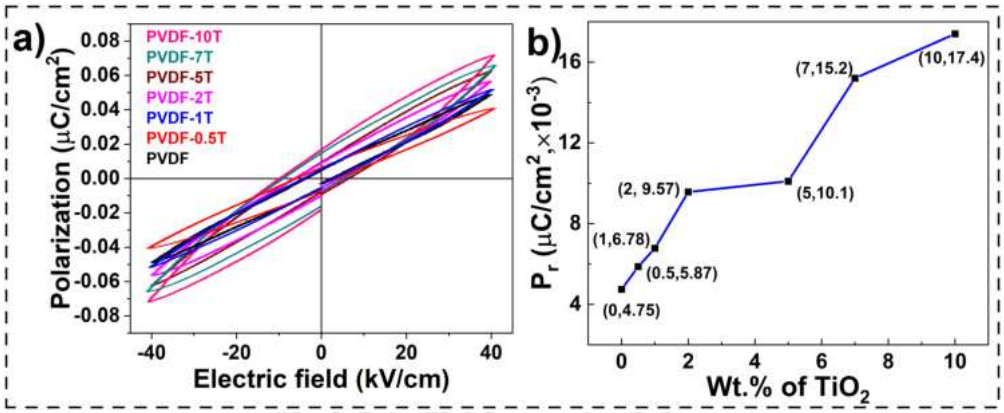

Fig. 3.12: Ferroelectric properties of nanocomposite films: a) P-E loop, b) P_r values for different nanofiller concentrations.

3.3.11 Voltage measurement of PENG device

The nanocomposite films have been fabricated into piezoelectric energy harvesting nanogenerators to test their output voltage for energy harvesting purposes. The schematic representation of PENG device along with fabricated piezoelectric sensor is presented in Fig. 3.13. The piezoelectric test is performed on seven PENG devices. PENG devices are fabricated by thermally evaporating Al electrodes (about 200 nm thick) on top and bottom portions of nanocomposite films. The device is sealed with PET films on both sides to protect it from environmental noise and damage. In all devices, the effective area of the nanogenerator is kept at 25 mm^2. All devices have been subjected to continuous finger tapping to measure peak to peak voltage (V_{pp}). The V_{pp} values for PVDF, PVDF-0.5T, PVDF-1T, PVDF-2T, PVDF-5T, PVDF-7T and PVDF-10T nanocomposite films are 2.08, 2.34, 3.21, 3.36, 4.39, 4.78 and 5.45 V respectively as shown in Fig. 3.14. The maximum piezoresponse voltage is observed in a nanocomposite with 10wt.% TiO_2 loading. Nanocomposites with increased piezoelectric voltage are attributed to an increased β phase percentage and dipole-dipole interactions between nanofiller and matrix [51]. The voltage values as recorded by DSO for different test samples are presented in Table 3.6.

3.4 SUMMARY

Highly flexible PVDF-TiO_2 nanocomposite films are successfully fabricated through solvent casting. The uniform dispersion of TiO_2 nanofiller is confirmed by FESEM and EDS spectra. The

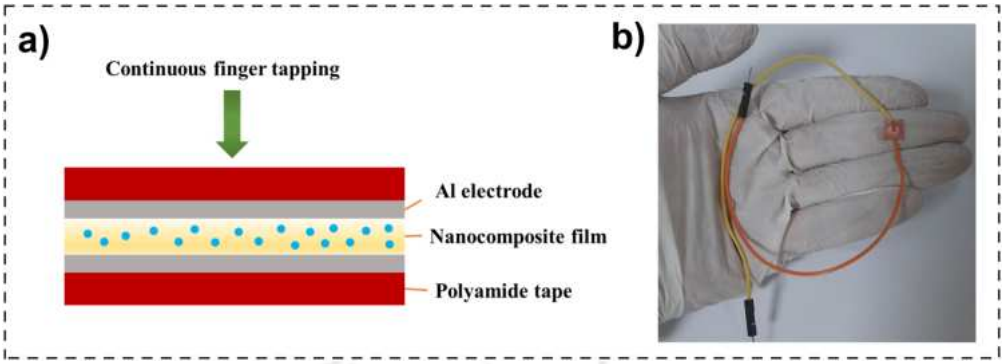

Fig. 3.13: a) Schematic representation and b) actual picture of PENG sensor device.

Table 3.6: Piezoelectric voltage values recorded for nanocomposite samples.

Sample name	o/p voltage (V)
PVDF	2.08
PVDF-0.5T	2.34
PVDF-1T	3.21
PVDF-2T	3.36
PVDF-5T	4.39
PVDF-7T	4.78
PVDF-10T	5.45

electroactive β phase is confirmed by FTIR study. In contrast to pure PVDF, the nanocomposite containing 5 wt.% TiO_2 demonstrated the highest tensile strength and elastic modulus, exhibiting an increase of 40% and 36%, respectively. However, when the TiO_2 content exceeded 5 wt.%, a decline in mechanical strength is noted. The elevated concentration of TiO_2 particles impeded dispersion, leading to agglomeration. These agglomerated particles introduced defects, contributing to the accumulation of stresses within the nanocomposite, consequently reducing both tensile strength and elastic modulus. The PVDF-10T sample demonstrated the highest ϵ value, reaching 23, which is 2.42 times greater than that of the pure PVDF film. This corresponds to a remarkable 143% increase in ϵ with the addition of 10 wt.% TiO_2. The piezoelectric test is conducted on seven PENG devices. These devices are created by thermally evaporating aluminum electrodes onto the upper

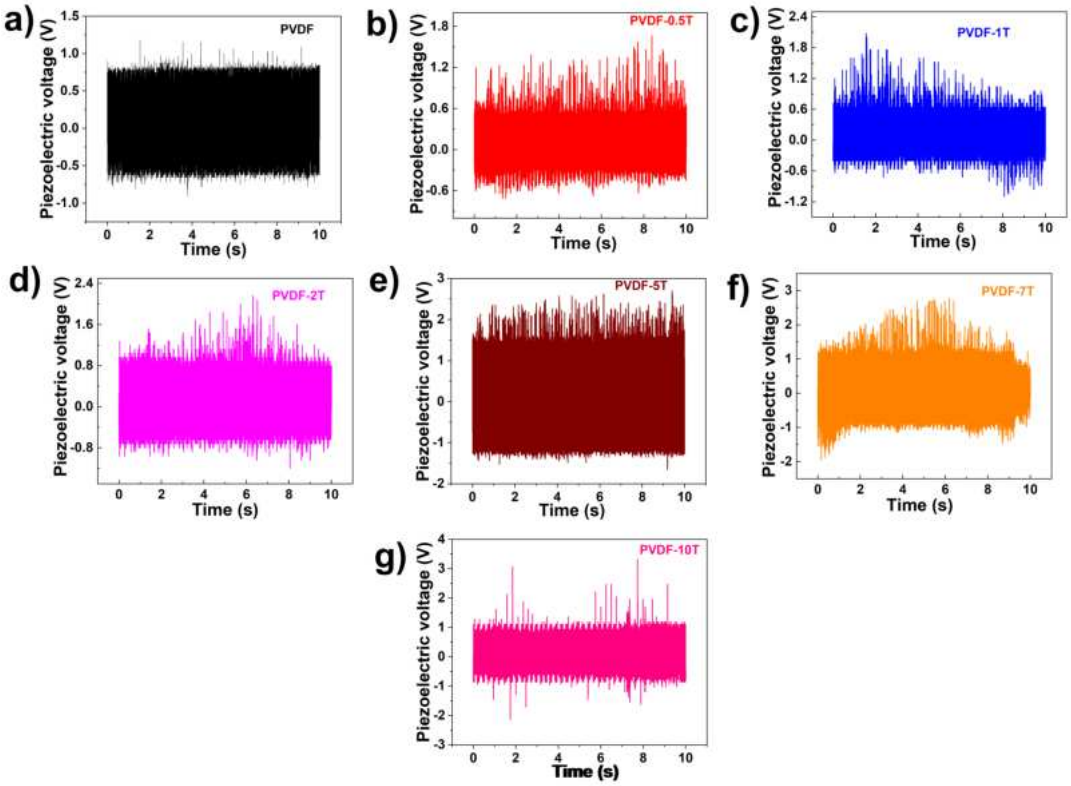

Fig. 3.14: Voltage output from nanocomposite films subjected to continuous finger tapping: a) PVDF, b) PVDF-0.5T, c) PVDF-1T, d) PVDF-2T, e) PVDF-5T, f) PVDF-7T, and g) PVDF-10T

and lower sections of nanocomposite films. To safeguard the device from environmental interference and potential harm, it is enclosed with PET films on both sides. The nanocomposite containing 10 wt.% TiO_2 loading exhibited the highest piezoresponse voltage. The increased piezoelectric voltage in these nanocomposites is ascribed to an augmented β phase percentage and enhanced dipole-dipole interactions between the nanofiller and the matrix. Such flexible nanocomposite films demonstrate suitability for mechanical energy harvesting in sensing applications, owing to their outstanding properties and favorable cost-performance ratio.

Chapter 4

MCDM based material selection using TODIM technique for PVDF-TiO_2-rGO hybrid nanocomposites

4.1 INTRODUCTION

Flexible and cost-effective PVDF based composites having excellent piezo performance are quite interesting for developing actuators, sensors, and nanogenerators. Based on the findings of the previous chapter, a 10 wt.% loading of TiO_2 in PVDF yields the maximum piezoelectric response. Consequently, in this chapter, a hybrid PVDF-based nanocomposite consisting of a fixed quantity (10 wt.%) of TiO_2 and varying quantities of rGO (up to 1.5 wt.%) for increased mechanical and piezoelectric performance is reported. The discussion of the materials employed and the fabrication of the nanocomposite can be found in sec.4.2. A 10 wt.% of TiO_2 and varying concentration of rGO (up to 1.5 wt.%) are added to PVDF-DMF solution to synthesize hybrid nanocomposite using solvent casting approach. Sec.4.3 explores the fabrication of hybrid nanocomposite films through FESEM, FTIR, and XRD. Additionally, presence of the β phase, thermal behavior, dielectric response, mechanical properties, and piezoelectric performance are investigated. Compared to pure PVDF, there is a significant enhancement in mechanical properties for hybrid nanocomposites. A highest piezoelectric voltage as well as current values of 10.2 V and 0.78 µA is recorded for a hybrid nanocomposite containing 1 wt.% of rGO for continuous finger-tapping operation. Sec.4.4 discuses MCDM based optimization technique called TODIM to select best material from available options for energy scavenging applications. Furthermore, a sensitivity study is conducted to examine how

this technique behaves under various attenuation factors, assessing its robustness for the desired application. S5 type of nanocomposite sample is the most suitable material according to the TODIM approach. Finally, a comprehensive summary of the present study is presented in sec.4.5.

4.2 EXPERIMENTAL

4.2.1 Materials

PVDF pellets (M_w of 530,000), N, N-dimethyl formamide (DMF) (anhydrous, 99.8%) solvent, and BTO nanoparticles (<100 nm size, 99% trace metals basis) are ordered from Sigma Aldrich, USA. rGO powder (purity >99%, 3-5 layers) is supplied by Techinstro industries, Nagpur.

4.2.2 Fabrication of nanocomposites

The nanocomposite films are synthesized using solvent casting approach. PVDF (2 g) is mixed with DMF (15 ml) solvent. It is then subjected to magnetic stirring at 60 °C for 3 hours. A fixed quantity of TiO_2 powder (10 wt.%) is then added to 5 ml of DMF followed by magnetic stirring at room temperature. Simultaneously, varying quantities of rGO sheets (0.5, 0.75, 1, 1.25, and 1.5 wt.%) are sonicated in 5ml DMF for 15 minutes. After the sonication, TiO_2 and rGO solutions are mixed and stirred for another 30 minutes Once the resulting solution becomes homogeneous, it is added into the PVDF solution. The resulting PVDF-TiO_2-rGO solution is magnetically stirred at 60 °C for another 4 hours. Then the obtained solution is vacuum desiccated for half hour (30 minutes) to eliminate bubbles that are present in the solution. After degassing, it is poured into a glass plate and is placed in the furnace at 65 °C for 12 hours. Free-standing nanocomposite films (90 mm diameter) are obtained after heating. The samples are then kept in a desiccator for 48 hours to make them completely dry. Similar steps are followed for fabricating pure PVDF and PVDF-TiO_2 composite samples. The weight fraction of rGO is calculated using equation 4.1:

$$W_{rGO} = \frac{W_{rGO}}{W_{rGO} + W_{\mathrm{TiO_2}} + W_{PVDF}} \tag{4.1}$$

W_{PVDF}, W_{rGO}, and W_{TiO_2} are mass (in g) of PVDF, rGO and TiO_2 respectively. After removing bubbles, the solution is poured on the clean and dried glass petri dish and kept in a furnace at around 60 °C for 12 hours. Free-standing, highly flexible films are obtained on the complete removal

of solvent. They are kept in vacuum desiccator for around 48 hours to dry them further. Before fabricating the PENG devices, the respective samples are subjected to electric poling using DC poling unit (50 kV, 5 mA, Ujwal Electronics) to impart piezoelectric nature. For convenience, the samples are given the following names: P (neat PVDF), PT (PVDF-TiO_2), PTR0.5 (PVDF-TiO_2-0.5% of rGO), PTR0.75 (PVDF-TiO_2-0.75% of rGO), PTR1 (PVDF-TiO_2-1% of rGO), PTR1.25 (PVDF-TiO_2-1.25% of rGO), PTR1.5 (PVDF-TiO_2-1.5% of rGO). The fabrication process of the poled hybrid nanocomposites is presented in Fig. 4.1. The weight percentage of constituents for nanocomposite samples is presented in Table 4.1.

Table 4.1: Weight percentages of different nanocomposite films.

Sample name	Weight of PVDF (g)	Weight of TiO_2 (g)	Weight of rGO (g)
P	2	-	-
PT	2	0.36	-
PTR0.5	2	0.36	0.01
PTR0.75	2	0.36	0.015
PTR1	2	0.36	0.02
PTR1.25	2	0.36	0.025
PTR1.5	2	0.36	0.03

4.2.3 Material characterization

The surface structure along with morphology of fabricated samples are studied using the FESEM instrument (Gemini SEM 500, make: ZEISS) with an accelerating voltage of 5 kV. The phases of PVDF are identified using FTIR (make: PerkinElmer) study for the wavelength of 400 to 4000 cm^{-1}. The crystal structure and phase information is obtained using XRD instrument (smartlab, make: Rigaku technologies) for the 2θ values of 15-65° with 4°/min scanning rate. Raman analysis of fabricated films is recorded using Laser Micro Raman System (532 mm wavelength laser) (LabRam HR, make: Horiba) with an integration time of 5 s. Thermal behavior of fabricated film samples is analysed using a Thermogravimetric analysis (TGA) instrument (spectrum two, make:

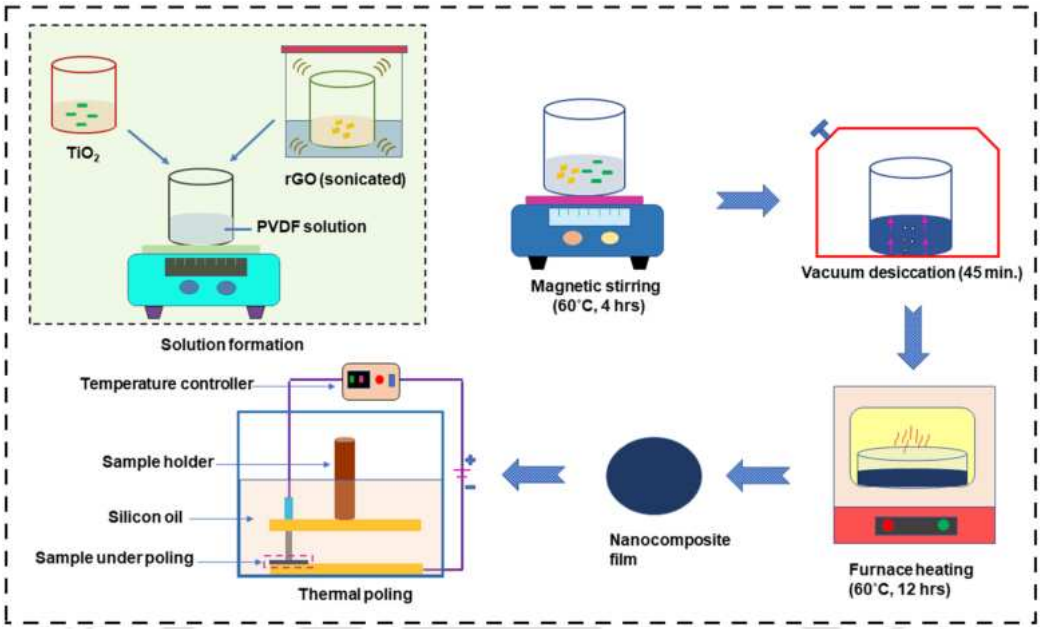

Fig. 4.1: Fabrication process of hybrid nanocomposites.

PerkinElmer). A measurement is made over the temperature span of 40-700 °C under a nitrogen gas environment with a constant heating rate (10 °/min). The samples' elastic modulus and tensile strength are calculated using UTM (AGX-V, make: Shimadzu) with 1 kN load cell capacity. ASTM standard D 882 is followed for testing each sample. A cross-head speed of 1 mm/min. is used in every test. Each sample of the same concentration is tested five times. Hardness of fabricated films are calculated with a micro-hardness testing equipment (MVH-II, make: Omni Tech) using 0.2 kgf load with 20 s dwell time. Every sample is examined five times. The dielectric performance are recorded with LCR meter (IM3536, make: Hioki) from 1 kHz to 1 MHz at room temperature. The top and bottom surface of the prospective PENG sample is coated with thin aluminum layer (200 nm thickness) using thermal evaporation method. Polyamide tape is wrapped on both sides to protect the film from physical damage. The final PENG device of size 2.5 cm x 2.5 cm is then subjected to continuous finger tapping to record piezoelectric voltage and current on a digital storage oscilloscope (GDS-2102 A, make: GWInSTEK).

4.3 RESULTS AND DISCUSSION

4.3.1 FESEM

The surface information of samples is recorded using FESEM instrument. The structure of TiO_2 is spherical, whereas that of rGO is sheet-like. According to SEM results, average size of TiO_2 nanoparticles is about 63.74±14.9 nm. SEM plots of TiO_2 and rGO, along with particle size distribution for TiO_2 particles, are shown in Fig. 4.2a-c. PVDF matrix grain structure is observed in Fig. 4.3a. rGO and TiO_2 fillers are visible and are uniformly dispersed into the PVDF, as depicted in Fig. 4.4b-f. TiO_2 particles loaded in the PVDF matrix are indicated by yellow dotted rectangles, whereas rGO sheets loaded in PVDF-TiO_2 composites are indicated by cyan colored dotted circles. rGO sheets at higher loading (above 1 wt.%) are seen agglomerated (dotted blue colored circle) in PVDF-TiO_2 composite structures (see Fig. 4.3e-f.).

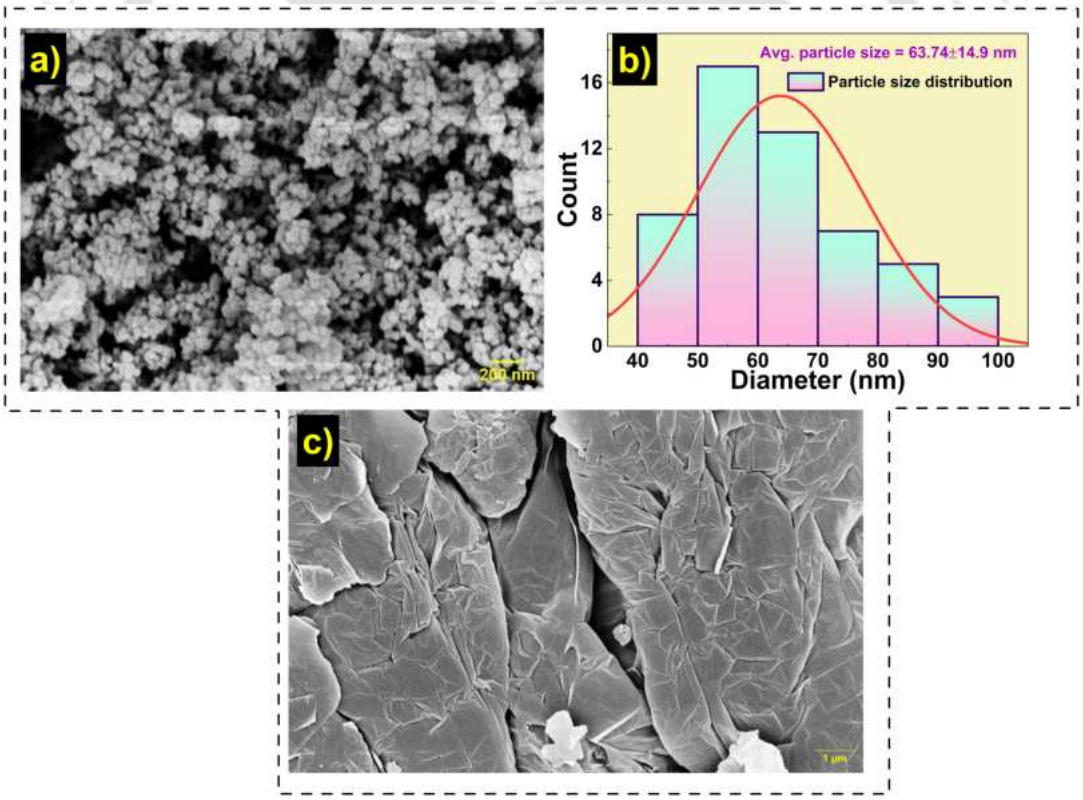

Fig. 4.2: a) SEM image and particle size distribution of TiO_2 nanoparticles, and c) SEM image of rGO nanosheets

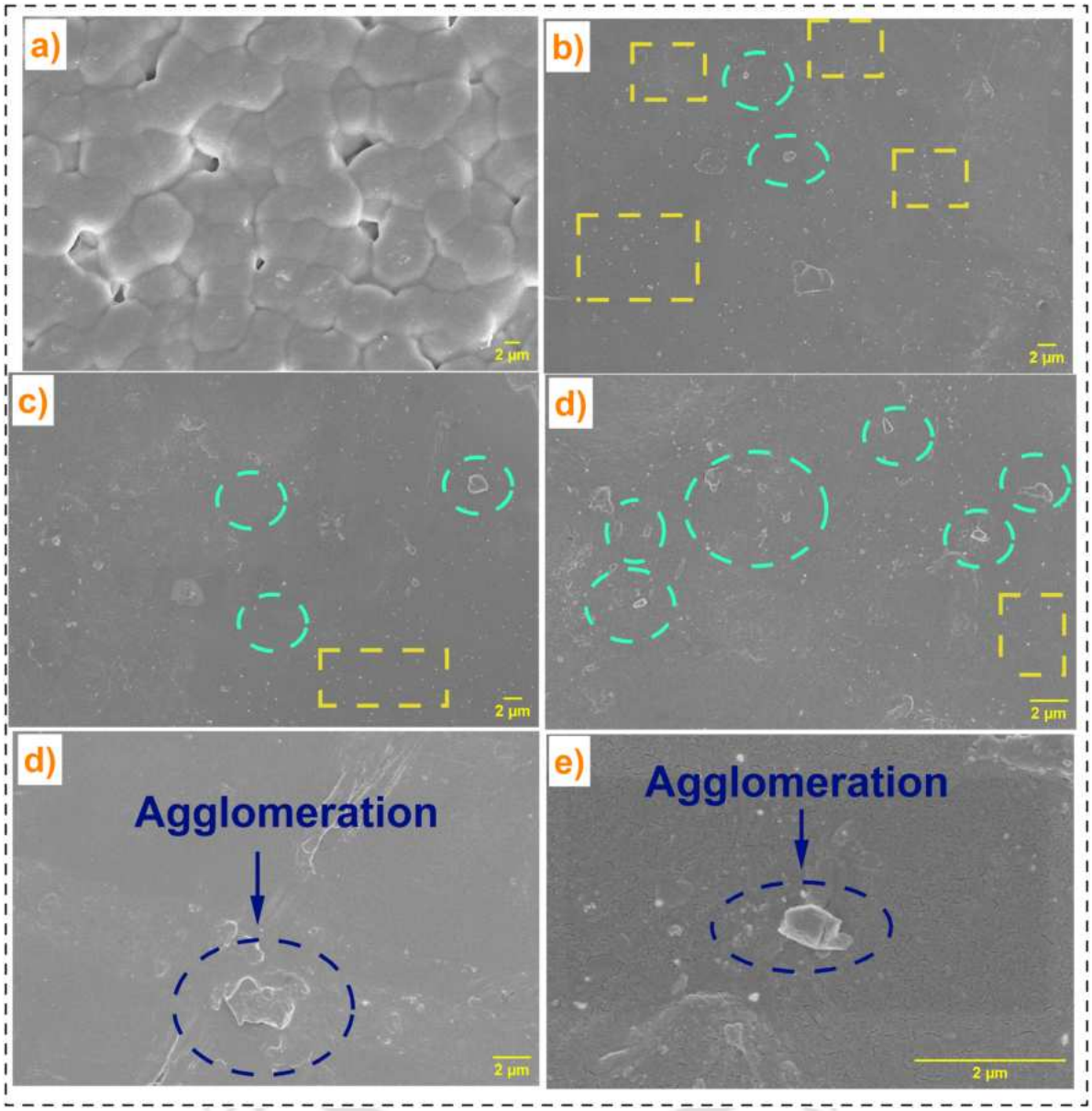

Fig. 4.3: FESEM images of fabricated samples. a) P, b) PTR0.5, c) PTR0.75, d) PTR1, e) PTR1.25, and f) PTR1.5.

4.3.2 XRD

XRD plots of pure PVDF and composite samples are presented in Fig. 4.4a. The peaks at obtained 19° and 21° corresponds to α and β phase of PVDF, respectively. The XRD analysis confirms the piezoelectric behaviour of PVDF by identifying the β phase of the material. The characteristic TiO_2 peaks at 27°, 36°, 44°, and 56° correspond to miller indices (110), (200), (211), and (220), respectively [88]. The β phase present in PVDF material is because of dipole movement of polar DMF solvent [111]. Thus, PVDF exhibits α as well as β phase in its XRD spectra. An

increment in β phase intensity is observed up to 1 wt.% of rGO addition. This shows that rGO helps nucleate the β phase of PVDF, causing to increased piezoelectric performance [104].

4.3.3 Raman spectroscopy

Raman spectroscopy is an effective tool for the structure identification of fabricated films. Raman plots displaying the structure of neat PVDF film and one selected hybrid nanocomposite (P and PTR0.75) are presented in Fig. 4.4b. The peaks corresponding to 1431 and 2977 cm^{-1} belong to PVDF. Additionally, the band belonging to 839 cm^{-1} corresponds to the β phase of PVDF [59]. The weak band at 431 and intense one at 2977 cm^{-1} show -CH_2 and C-H bond vibrations, respectively. The peaks at 515 and 638 cm^{-1} in the composite film sample correspond to TiO_2 [112]. Peaks appeared at 1356 and 1592 cm^{-1} representing D and G bands of rGO, respectively. While the D peak is linked with dangling bonds, defects, and wrinkles in carbon-based structures, the G peak is linked with the vibrations (in-plane) corresponding to sp2 carbon structures. The presence of TiO_2 and rGO bands confirms the successful fabrication of a hybrid nanocomposite.

4.3.4 FTIR measurement

The phase formation of the PVDF matrix is identified using the FTIR technique as presented in Fig. 4.4c. The peak present at 763 cm^{-1} belongs to α phase of PVDF, whereas peaks at 841, 1288 and 1400 cm^{-1} correspond to β phase of PVDF [89]. Points 1, 2, 3, 4, 5, 6, and 7 in Fig. 4.4d represent P, PT, PTR0.5, PTR0.75, PTR1, PTR1.25, and PTR1.5, respectively. The electroactive phase content fraction (F(β)) values are calculated using equation 4.2:

$$F(\beta) = \frac{A_{841}}{A_{841} + 1.26A_{763}} \tag{4.2}$$

Where, A_{841} and A_{763} are absorption intensity values for α and β phases, respectively. TiO_2 addition in the PVDF matrix increased F(β) value from 68% to 71%. Further, on rGO addition, significant F(β) enhancement is observed from 73% to 82% up to 1 wt.% loading. This increment may be attributed to the rGO's function as a nucleating agent, which plays a prominent role in polar β phase formation [104]. Additionally, interactions between fluorine atoms of macromolecular PVDF chains and π bond of rGO cause the formation of the β phase. However, F(β) values are

reduced from 82% to 75% when rGO loading increased from 1.25 wt.% to 1.5 wt.%. This effect arises due to the agglomeration of rGO sheets inside the PVDF matrix, which constrains molecular chain motion. These findings show that including rGO significantly affects the polar phase of PVDF in PVDF-TiO_2 composites. The F(β) values of fabricated samples are presented in Table 4.2:

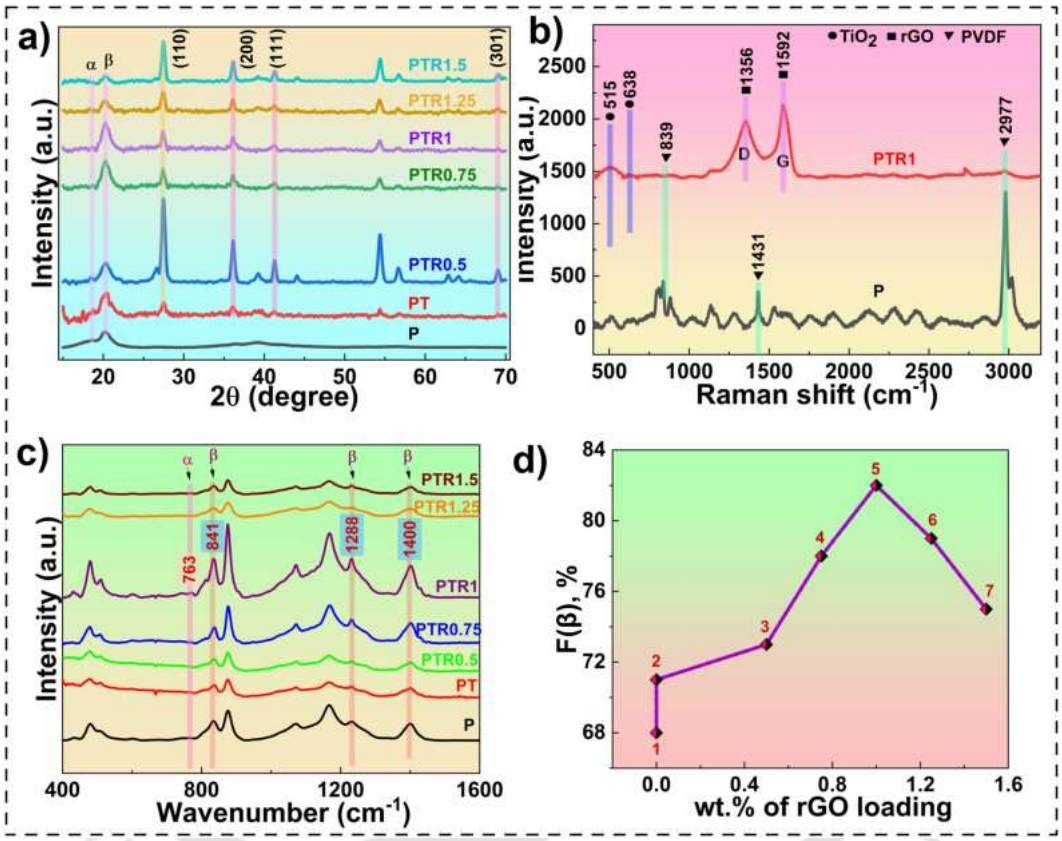

Fig. 4.4: a) XRD graphs of PVDF and its composites, b) Raman plots of samples P and PTR0.75, c) FTIR graph, and d) β phase Fraction of fabricated films.

4.3.5 TGA

The role of rGO nanosheets on the thermal behavior of PVDF-TiO_2 films is studied with the help of TGA analysis as shown in Fig. 4.5. PVDF showed melting (endothermic) at around 155 °C followed by sudden decomposition at around 430 °C. The thermal stability of PVDF matrix is enhanced upon TiO_2 loading. This could be attributed to strong interaction of distributed TiO_2 with polymer matrix PVDF. Coordinate bonding between polymer chains and TiO_2 constrains thermal effect on macromolecules causing increased macromolecular chains rigidity. This increases the required thermal energy for the polymer chain movement and its breakage [113]. A large aspect

Table 4.2: Fraction of electroactive phase content values for different fabricated samples.

Sample name	F(β) %
P	68
PT	71
PTR0.5	73
PTR0.75	78
PTR1	82
PTR1.25	78
PTR1.5	75

ratio of rGO makes it an effective thermal barrier and inhibits PVDF degradation [114]. When rGO sheets adhere to the PVDF chains, they exhibit a stabilizing effect due to the shielding against heat and the radical-trapping property. This, in turn, leads to a delayed degradation of PVDF at elevated temperatures. Decomposition temperature (T_{od}) increases till 1.25 wt.% of rGO loading and then reduces. Sample PTR 1.25 displayed a maximum Tod of 480 °C. Our results indicated that the loading of rGO in PVDF-TiO_2 composites reduces overall thermal degradation and enhances residual mass compared to neat PVDF and PVDF-TiO_2 composites.

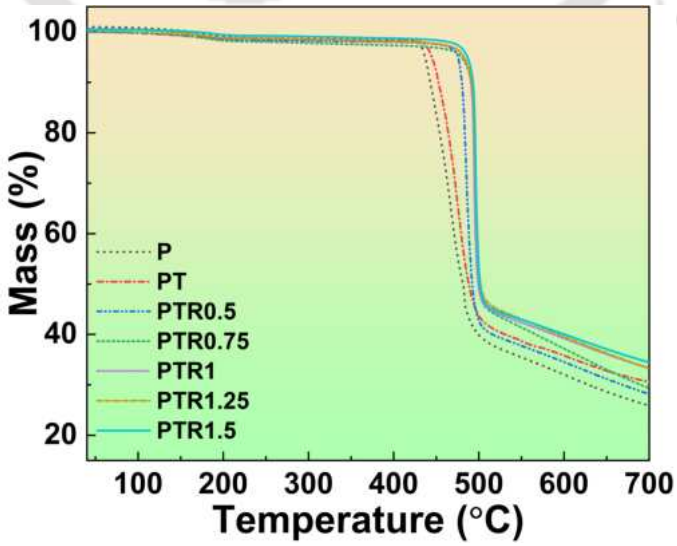

Fig. 4.5: TGA plot of PVDF and its nanocomposites.

4.3.6 UTM

A piezoelectric material must possess excellent mechanical properties for energy harvesting. The mechanical performance of the pure PVDF and its nanocomposites is evaluated by performing tensile testing, as shown in Fig. 4.6a-d. Numbers 1, 2, 3, 4, 5, 6, and 7 in Fig. 4.6b-e represent test films P, PT, PTR0.5, PTR0.75, PTR1, PTR1.25, and PTR1.5, respectively. PT showed increased, UTS and E compared to pure PVDF samples. Further increment in E and UTS of PVDF-TiO_2 nanocomposites is observed up to 1 wt.% rGO loading. Sample PTR1 showed a maximum value of UTS and E, around 88% and 104% higher than pure PVDF, respectively. rGO loading in PVDF-TiO_2 composite structure interrupts the propagation of crack growth resulting restriction to crack flow, thereby enhancing mechanical properties. Higher loading of rGO (>1wt.%) causes a significant reduction in mechanical properties. Poor dispersion of rGO sheets at higher concentrations creates defects and nanoscale voids, resulting in stress concentration in different areas of the PVDF [115]. PVDF showed a maximum toughness value (10.4 MJ/m^3) among all test samples. Toughness values of test samples are determined by measuring the area under stress vs. strain curves till fracture limit. PVDF-TiO_2 nanocomposite toughness value decreased to 1.87 MJ/m^3 after TiO_2 addition. Further reinforcement of rGO increases toughness values for hybrid composite samples PTR0.5 and PTR1. Toughness values started decreasing again above 1 wt.% of rGO. The increased toughness observed in composite PVDF fibers is attributed to the mobility and ease of energy absorption by the small β crystallites generated by the filler. The mechanical properties of the fabricated nanocomposites are presented in Table 4.3.

4.3.7 Hardness measurement

The hardness plot of test films is presented in Fig. 4.7. Incorporation of TiO_2 showed an excellent synergy effect in enhancing the surface hardness of PVDF matrix. Sample PT showed a hardness value of 11±1.2 against 7±1.64 of pure PVDF. rGO loading further enhanced the hardness of nanocomposite films. Graphene is known to be the hardest material on the earth. So, after its incorporation into the PVDF matrix, significant improvement in hardness is observed. Sample PTR1 showed a maximum hardness value of 25±2.5, around 2.5 times higher than PVDF. RGO helps

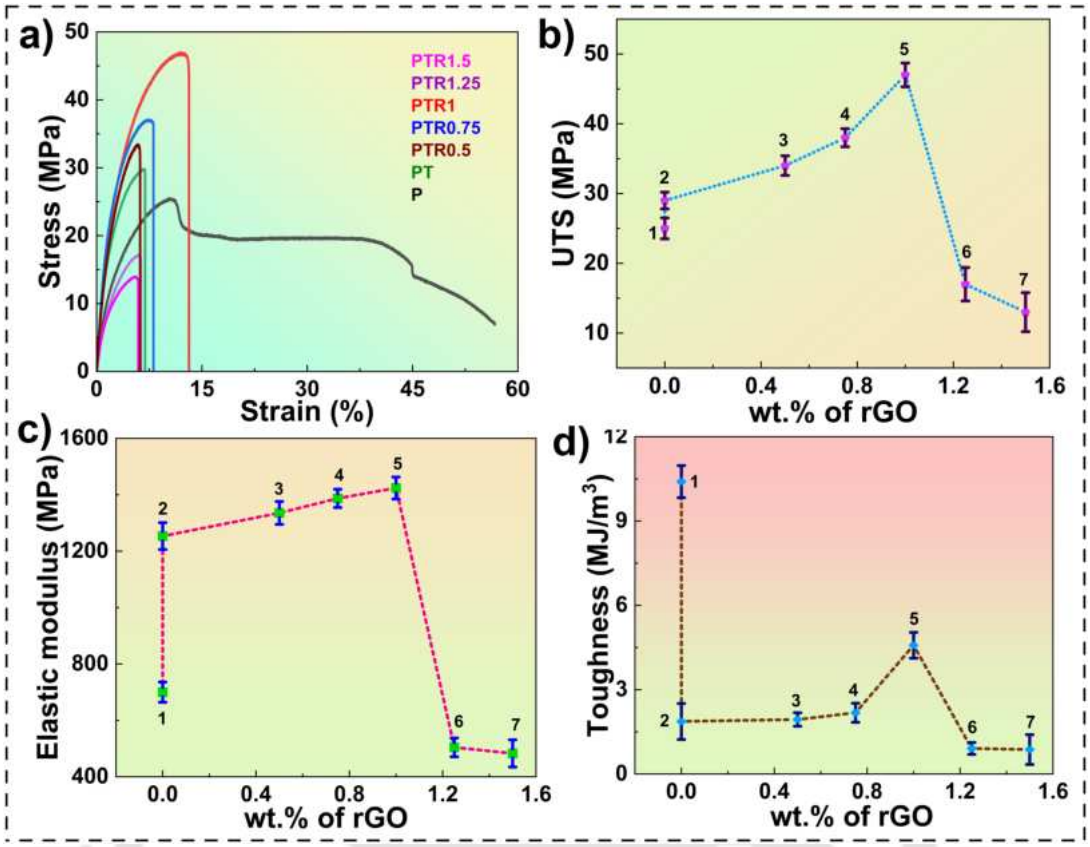

Fig. 4.6: Mechanical properties of fabricated samples. a) stress vs. strain plot, variation of b) breaking stress, c) elastic modulus, and d) toughness.

Table 4.3: Mechanical properties of PVDF and its composites.

Sample name	UTS (MPa)	E (MPa)	T (MJ/m^3)
P	25±1.5	700±35.68	10.4±0.57
PT	29±1.2	1253.7±47.56	1.87±0.64
PTR0.5	34±1.4	1335.6±40.57	1.94±0.24
PTR0.75	38±1.3	1387.2±32.5	2.18±0.34
PTR1	47±1.7	1424±38.78	4.58±0.46
PTR1.25	17±2.4	504.2±33.24	0.91±0.21
PTR1.5	13±2.8	483±48.21	0.87±0.53

,

lock PVDF macromolecular chains, thereby restricting chain mobility when the load is applied. A higher force, therefore, is required for surface indentation. Several other studies reported improved

hardness of polymers upon adding rGO sheets [116, 117]. This occurs due to the presence of the hard phase of rGO sheets within the PVDF matrix. The rGO effectively interlocks the molecular chains of PVDF, consequently restricting chain mobility when subjected to a load [118]. However, rGO reinforcement beyond 1 wt.% causes a reduction in hardness values. This can be due to agglomeration of rGO sheets in PVDF-TiO_2 composites, causing a reduction in micro hardness. The hardness values of nanocomposite films are tabulated in Table 4.4.

Table 4.4: Hardness values of nanocomposites.

Sample name	Hardness values (HV)
P	7±1.2
PT	12±1.1
PTR0.5	16±1.7
PTR0.75	19±1.4
PTR1	23±1.8
PTR1.25	29±1.2
PTR1.5	21±1.5

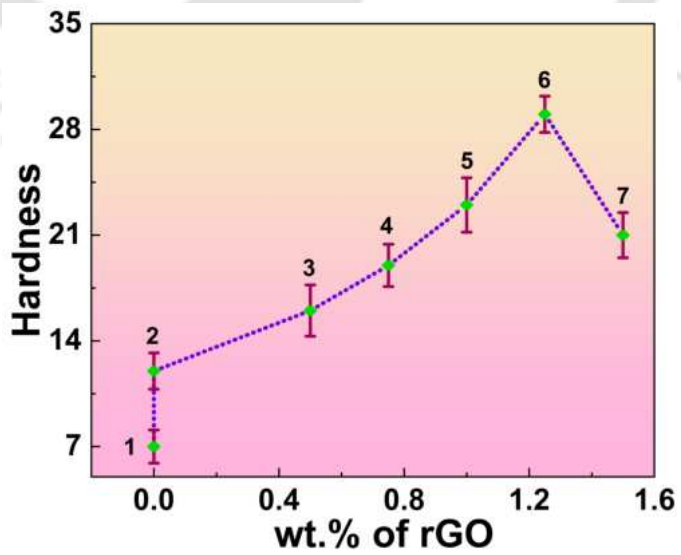

Fig. 4.7: Hardness plot of PVDF and its nanocomposites.

4.3.8 Dielectric measurement

The behavior of the ϵ over frequency is presented in Fig. 4.8a. ϵ value is found to be enhanced on TiO_2 loading. Further increments in ϵ values are observed for all the test samples with increasing rGO reinforcement. ϵ is more at lesser frequency values because of the Maxwell Wagner Sillar (MWS) effect, which ensures perfect alignment of permanent and induced dipoles causing interfacial polarization (IP). In contrast, due to the short alignment time, dipoles are unable to perform IP as frequency values increase. This process is known as the polarization relaxation phenomenon. The highly conducting nature of rGO increases IP resulting in enhanced ϵ values. Increased loading of rGO sheets causes a higher accumulation of free charges at the interfacial locations creating a greater number of dipoles. A homogeneous filler distribution along with enhanced interfacial area increases IP values [59]. In the presently fabricated hybrid composites, rGO behaves as an electrode, whereas TiO_2 and PVDF matrix acts as a micro capacitor's dielectric medium. Increasing rGO loading further enhances micro-capacitor numbers. A dielectric constant of 43 (at 10^3 Hz) is observed for sample PTR1.5, which is about 300% and 200% higher than PT and P, respectively. The σ_{ac} plots of fabricated films are presented in Fig. 4.8b. Rise in σ_{ac} values on rGO addition is attributed to the creation of conductive routes. The increment rate in σ_{ac} is less at lower frequencies, but at higher frequencies, it is significantly greater. The variation in σ_{ac} over lower frequency values is separately presented in Fig. 4.8c for better understanding. The dielectric performance of PVDF is considerably improved on TiO_2 and rGO addition. The values of dielectric constant at 1 KHz is presented in Table 4.5.

4.3.9 Voltage measurement

The films are subjected to a DC voltage of 3 kV at 120 °C for 3 hours to impart piezoelectric properties. The setup is submerged in silicon oil to avoid electric arcing during poling (see Fig. 4.9).To check the piezo response, all the fabricated devices are subjected to continuous mechanical loading through finger tapping (see Fig. 4.10a for actual PENG device). The V_{oc} and I_{sc} of all the fabricated PENG devices are recorded through finger tapping, shown in Fig. 4.10b-c. Increments in V_{oc} and I_{sc} values are observed with increased rGO loading. The increment ceases for sample PTR1.25,

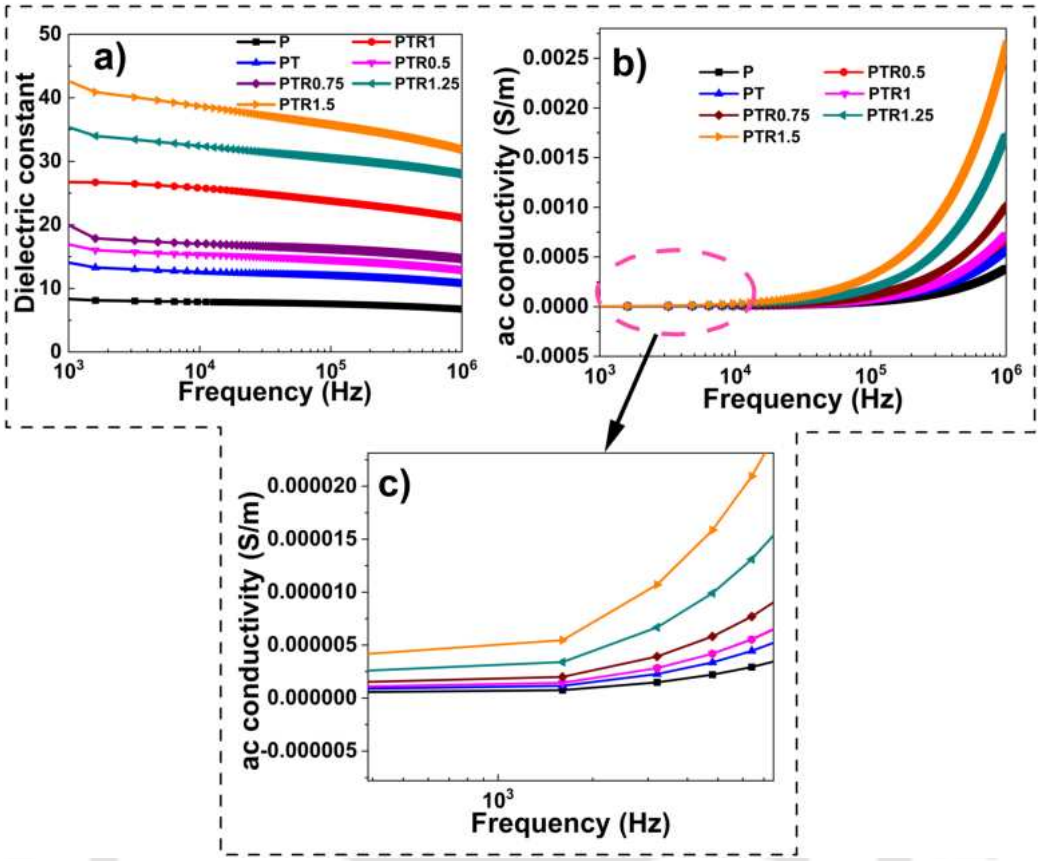

Fig. 4.8: Dielectric parameters measurement of PVDF and its nanocomposites. a) ϵ, b) σ_{ac}, and c) σ_{ac} (zoomed version).

Table 4.5: Dielectric constant values of PVDF based hybrid nanocomposites.

Sample name	ϵ
P	8
PT	14
PTR0.5	17
PTR0.75	20
PTR1	26
PTR1.25	35
PTR1.5	43

where a reduction in piezo response is observed. Therefore, maximizing piezoelectric output from a PENG device requires optimum rGO quantity. PTR1 showed maximum V_{oc} (12 V) and I_{sc} (0.56

μA) values compared to other samples. The variation of V_{oc} and I_{sc} for fabricated samples over rGO loading is presented in Fig4.10d. PENG device's enhanced piezoelectric performance is attributed to the nanocomposite film's enhanced charge generation and storage capability. Moreover, rGO sheets promote alignment of dipole inside PVDF and help in multiple micro-capacitor creation within the nanocomposite. In ceramic-based polymer composites, free charges on the surface of rGO sheets accumulate by dipoles from PVDF and TiO_2 nanoparticles, creating new dipoles in that specific position. This ultimately enhances charge generation and storage [62]. The formation of numerous nanocapacitors in the film by rGO nanosheets allows for the accumulation of more electrons, leading to increased output. The introduction of an optimal rGO loading resulted in increased nucleation of the β phase, a finding confirmed through FTIR spectrum analysis. The information presented above confirms that rGO loading considerably improves energy scavenging capacity of PENG device. We believe that the reduction in piezoelectric response after a certain

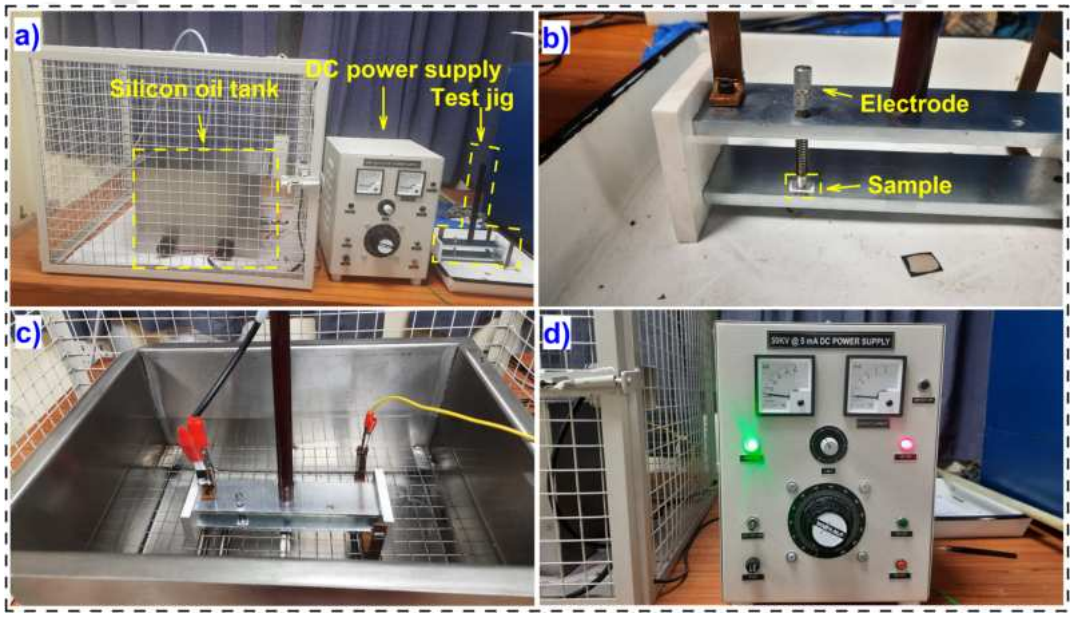

Fig. 4.9: a) Electrode poling setup, b) sample under loading condition, c) electrical connections before poling, d) ongoing poling operation.

quantity of rGO loading is due to the agglomeration effect of a large number of rGO nanosheets in PVDF-TiO_2 composites. The V_{oc} and I_{sc} values for fabricated films are enlisted below in Table 4.6. The comparison of V_{oc} values of previously reported hybrid PENG devices containing rGO and/or TiO_2 nanofillers with the current study is listed in Table 4.7.

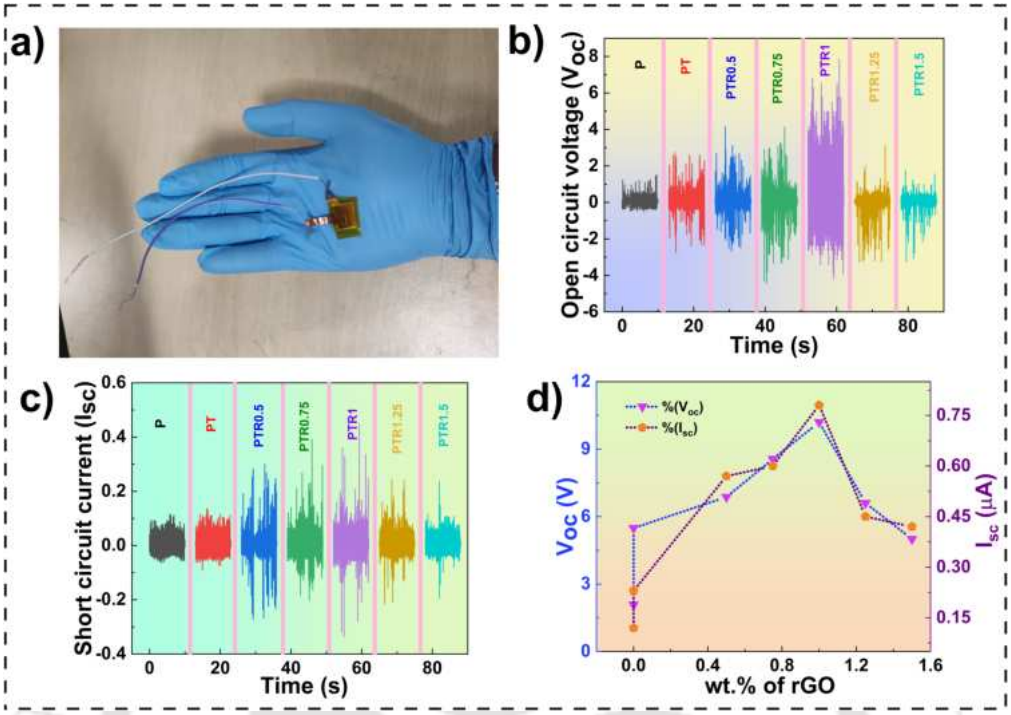

Fig. 4.10: a) Fabricated PENG device, b) piezoelectric voltage plot, c) current plot, and d) variation of V_{oc} and I_{sc} with respect to rGO loading quantity.

Table 4.6: Piezoelectric parameters for PENG devices.

Sample name	V_{oc} (V)	I_{sc} (μA)
P	2.08	0.13
PT	5.49	0.23
PTR0.5	6.87	0.57
PTR0.75	8.56	0.61
PTR1	10.2	0.78
PTR1.25	6.6	0.45
PTR1.5	5	0.42

Table 4.7: Overview of piezoelectric output voltage recorded for hybrid PENG devices.

Material name	Fabrication process	o/p voltage (V)	References
PVDF/rGO/TiO_2	Solution casting	10.2	This work
PVDF/TiO_2/MoS_2	Drop casting	17.4	[119]
PVDF/ZnO/MWCNT	Solution casting	1.32	[120]
P(VDF-TrFE)/TiO_2/ZnO	Electrospinning	23	[121]
PVDF/rGO/BTO	Solvent casting	2.3	[122]
PVDF/(BCT-BZT)/rGO	Solution casting + hot pressing	4	[123]
PVDF/BF33BT/GO	Solution casting	3.9	[124]
PVDF/$NaNbO_3$/RGO	Solution casting	2.16	[125]
P(VDF-TrFE)/rGO/$BaTiO_3$	Spin coating	8.5	[62]
P(VDF-TrFE)/rGO/ZnO	Electrospinning	0.84	[126]
P(VDF-TrFE)/GO/PZT	Solution blending	60	[127]

4.4 MCDM approach

4.4.1 MCDM based optimization

MCDM analysis proves valuable in complex decision scenarios with numerous alternatives and criteria. The process commences by assigning weights to criteria, drawing on expert insights, experience, and/or available data relevant to the decision problem [128]. Many industries, including retail, logistics, engineering, and others, use MCDM tools to provide real-world outcomes. MCDM analyses are frequently employed in scenarios lacking a definitive 'correct' solution, aiming to identify the optimal outcome within specified constraints. While various MCDM methods exist, they share common steps. Initially, criteria are defined and quantified. Subsequently, the significance of each criterion is assessed. Next, alternatives are created and appraised against the criteria. Ultimately, a decision is reached based on the evaluation result [129]. To calculate the weightage of criteria and rank the material alternatives, the Shannon entropy weightage method is applied. Using prospect theory as the basis, TODIM is a discrete MCDM technique. Every MCDM technique is predicated on the notion in which the decision making would often look towards a solution that

maximizes global measure of value. In contrast, TODIM consists of implementing the prospect theory paradigm by adapting a global measurement of value. TODIM is based on a prospect value function that measures the degree to which each alternative is dominant over the others. Therefore, how people formulate risk-averse decisions is described empirically and is incorporated into this method. Based on this method, each alternative is ranked according to its partial and overall dominance over the remaining alternatives. The steps involved in entropy and TODIM methods are described below:

Step 1: Formulation of decision matrix TODIM method begins with generating a decision matrix, B, according to equation 4.3:

$$B = [b_{ij}]_{m\times n} = \begin{bmatrix} b_{11} & b_{11} & \dots & b_{1n} \\ b_{21} & b_{22} & \dots & b_{2n} \\ \dots & \dots & \dots & \dots \\ b_{m1} & b_{m2} & \dots & b_{mm} \end{bmatrix}. \tag{4.3}$$

can be varied as 1,2,3,4...up to m, and j can be varied as 1,2,3,4...up to n. Therefore, m is the total number of material alternatives, and n is the number of decision criteria.

Step 2: Normalization of decision matrix The normalization of the decision matrix has been done as per equation 4.4 for beneficial criteria and equation 4.5 for non-beneficial criteria. The normalized data outcome is denoted as P_{ij}.

$$P_{ij} = \frac{b_{ij}}{\sum_{i=1}^{m} b_{ij}} \tag{4.4}$$

$$P_{ij} = \frac{\frac{1}{b_{ij}}}{\sum_{i=1}^{m} \frac{1}{b_{ij}}} \tag{4.5}$$

where P_{ij} is the normalized value of b_{ij}.

Step 3: Entropy computation Entropy weights are calculated using Shannon's entropy method, which is created and evaluated by several scientists to determine the weight of specific criteria. According to the weightage calculations, a preference is given to the higher value over the lower one. The subsequent section outlines the procedure used to calculate the weights in this study. The entropy of each criterion is calculated using equation 4.6:

$$E_j = -k \sum_{i=1}^{m} P_{ij} P_{ij} \tag{4.6}$$

where $k = \frac{1}{\ln(m)}$, where m is the total number of material options.

Step 4: Weightage calculation The criteria's weightage is calculated using equation 4.7:

$$w_j = \frac{1 - E_j}{\sum_{j=1}^{n} (1 - E_j)} \tag{4.7}$$

Step 5: Calculation of relative weightage The relative weightage of the criteria is calculated using the equation 4.8.

$$w_{ct} = \frac{w_j}{w_r} \tag{4.8}$$

Here w_{j} is the reference weightage criteria, w_{r} is the weightage reference criteria (selected as the weightage of the criteria with maximum value), and w_{ct} is relative weight criteria.

Step 6: Dominance degree of alternative calculation The dominance degree of alternatives of A_{i} over A_{j} is calculated as per equation 4.9.

$$\delta(A_i, A_j) = \int_{c=1}^{n} \phi_c(A_i, A_j) \tag{4.9}$$

A_{i} over A_{j} is evaluated as per equation 4.10.

$$\delta(A_i, A_j) = \left\{ \begin{array}{ll} \sqrt{\frac{w_{cr}(P_{ic} - P_{jc})}{\sum_{c=1}^{n} w_{ct}}} & \text{if } (P_{ic} - P_{jc}) > 0 \\ 0 & \text{if } (P_{ic} - P_{jc}) = 0 \\ \frac{-1}{\theta}\sqrt{\frac{(\sum_{c=1}^{n} w_{ct})(P_{ic} - P_{jc})}{w_{ct}}} & \text{if } (P_{ic} - P_{jc}) < 0 \end{array} \right\} \tag{4.10}$$

The gaining and loosing of i^{th} alternative over j^{th} alternative is denoted as $P_{\mathrm{ic}} - P_{\mathrm{jc}} > 0$ and $P_{\mathrm{ic}} - P_{\mathrm{jc}} > 0$. θ belongs to factor of attenuation for the losses. Depending on the θ value, the form of the prospect theoretical value function in the negative quadrant may vary.

Step 7: Calculation of overall dominance degree of alternative The overall dominance degree of the alternative is calculated as per the equation 4.11.

$$\xi_i = \frac{\sum_{j=1}^{m} \delta(A_i, A_j) - \min \sum_{j=1}^{m} \delta(A_i, A_j)}{\max \sum_{j=1}^{m} \delta(A_i, A_j) - \min \sum_{j=1}^{m} \delta(A_i, A_j)} \tag{4.11}$$

Step 8: Ranking of alternative Finally, the alternatives are sorted in descending manner by dominance score, with the alternative with the greatest dominance score being the best.

Step 9: Sensitivity analysis of the process Different θ values analysed the sensitivity of the process varied from 1 to 10. Further, the rank of the alternative materials is compared to understand the robustness of the computation technique.

4.4.2 Ranking and TODIM method

The decision matrix for the process has been presented in Table 2. The samples P, PT, PTR0.5, PTR0.75, PTR1, PTR1.25, and PTR1.5 have been labelled S1, S2, S3, S4, S5, S6, and S7 for further convenience in analysis. Table 3 represents the weightage of different criteria. The relative weightage criteria have been presented in Table 4. Furthermore, the overall dominance degree of alternative for is presented in Table 5. According to the material selection and optimization process, the S5 type of material is the best alternative, followed by S4, S3, S6, S7, S2, and S1. Table 6 represents the overall dominance degree and Ranking of the materials for different θ values varied from 1 to 10. The variation of θ value is significantly called the sensitivity analysis of the process. The Ranking of all the material alternatives for all θ values remain the same (see Table 6). Material ranking consistency indicates the robustness of the method. The ranking of available material alternatives with different values of attenuation factors is presented in 4.11.

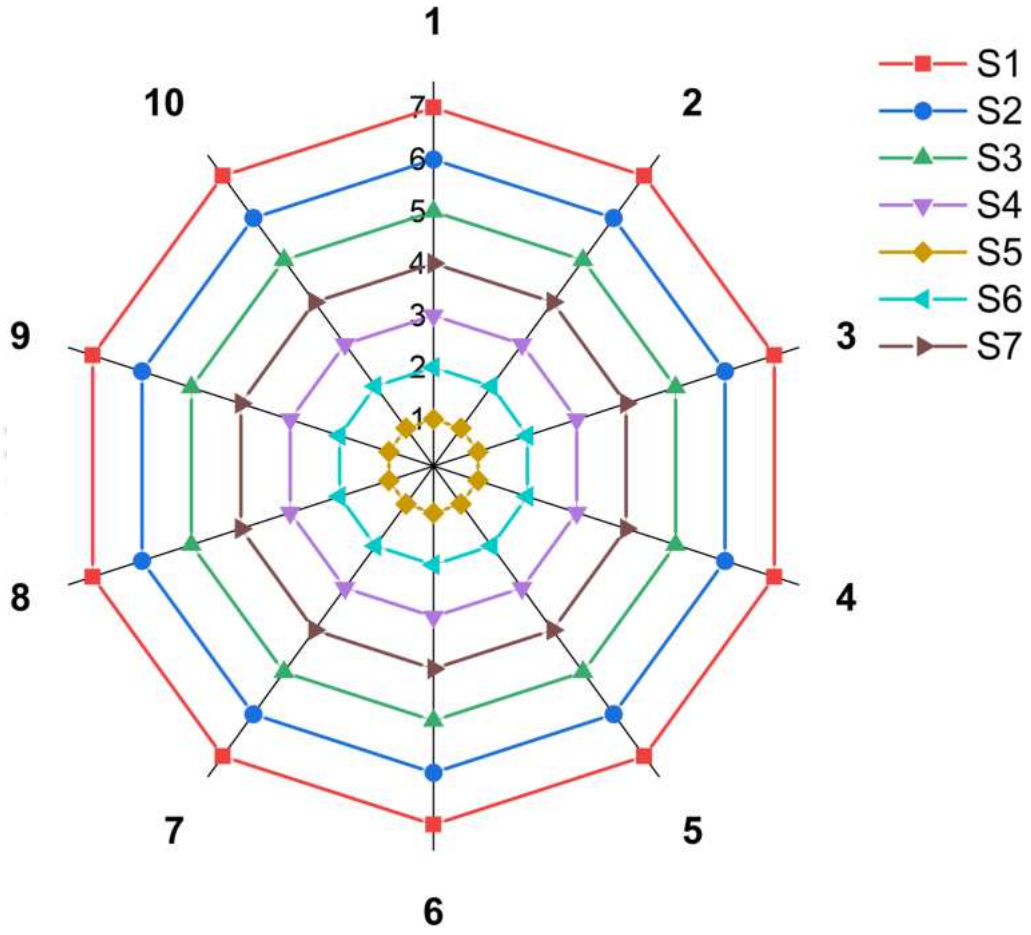

Fig. 4.11: Rankings with varying values of attenuation factor.

Table 4.8: Decision matrix.

	$F(\beta)$ (%)	UTS (MPa)	E (MPa)	Toughness (MJ/m^3)	Hardness (HV)	V_{oc} (V)	m_r (%)	T_{onset} (°C)	ϵ	I_{sc} A
	(CR_1)	(CR_2)	(CR_3)	(CR_4)	(CR_5)	(CR_6)	(CR_7)	(CR_8)	(CR_9)	(CR_{10})
Samples	Beneficial	Beneficial	Beneficial	Beneficial	Beneficial	Beneficial	Beneficial	Beneficial	Beneficial	Beneficial
P (S1)	68	25	700	10.4	7	2.08	431	25.8	8	0.13
PT (S2)	71	29	1253	1.87	12	5.49	435	30.6	14	0.23
PTR0.5 (S3)	73	34	1335	1.94	16	6.87	468	28.17	17	0.57
PTR0.75 (S4)	78	38	1387	2.18	19	8.56	476	29.18	21	0.61
PTR1 (S5)	82	47	1424	4.58	23	10.2	481	33.27	27	0.78
PTR1.25 (S6)	79	17	504	0.91	29	6.6	484	33.5	35	0.45
PTR1.5 (S7)	75	13	483	0.87	21	5	487	34.8	43	0.42

Table 4.9: Weightage of different criteria.

	(CR_1)	(CR_2)	(CR_3)	(CR_4)	(CR_5)	(CR_6)	(CR_7)	(CR_8)	(CR_9)	(CR_{10})
Weightage	0.00196	0.08095	0.09066	0.40318	0.07999	0.08519	0.00118	0.00529	0.12772	0.12386

Table 4.10: Relative weightage of different criteria.

	(CR_1)	(CR_2)	(CR_3)	(CR_4)	(CR_5)	(CR_6)	(CR_7)	(CR_8)	(CR_9)	(CR_{10})
Weightage	0.004873	0.20078	0.224868	1	0.198406	0.211298	0.002938	0.013116	0.316787	0.3072

Table 4.11: Relative weightage of different criteria.

Material alternatives	$\sum_{i=1}^{m} \delta(A_i, A_j)$	ξ_i	Ranking
S1	-77.617	0.000	7
S2	-54.621	0.307	6
S3	-34.460	0.576	5
S4	-26.703	0.679	3
S5	-2.638	1.000	1
S6	-19.501	0.775	2
S7	-26.903	0.676	4

4.5 SUMMARY

A three-phase nanocomposite comprising PVDF-TiO_2-rGO is created through a solvent casting method, maintaining a constant quantity of TiO_2 and varying the amount of rGO. The incorporation of rGO significantly improves the mechanical, dielectric, and thermal properties of PVDF-BTO composites. Conductive rGO increases interfacial polarization resulting in enhanced ϵ values. Beyond a 1% loading quantity, rGO sheets exhibit agglomeration, causing reduction in mechanical, thermal and piezoelectric performance. The output voltage is measured by constructing a PENG device using the synthesized nanocomposite films. The presence of numerous nanocapacitors in the film, facilitated by rGO nanosheets, enables the accumulation of a greater number of electrons, thereby enhancing the piezoelectric output voltage. The incorporation of an optimal loading of rGO contributes to increased nucleation of the β phase, a conclusion supported by FTIR spectrum analysis. The details provided affirm that the introduction of rGO loading significantly enhances the energy scavenging capacity of the PENG device. Increments in Voc and Isc values were observed with increased rGO loading. The increment ceases for sample PTR1.25, where a reduction in piezo response is observed. Therefore, maximizing piezoelectric output from a PENG device requires optimum rGO quantity.PENG device showed maximum V_{oc} and I_{sc} of 12 V and 0.56 μA values respectively. To identify the optimal material for energy harvesting, a MCDM-based TODIM technique is employed, evaluating and ranking material performance across various attenuation factors.

The TODIM technique provides a comprehensive and effective approach to decision-making in intricate situations. It incorporates elements like risk, ambiguity, and decision-makers' preferences, offering a robust framework to evaluate options and make informed decisions. The consistency in material ranking across all combinations attests to the robustness of the decision-making technique.

Chapter 5

Effect of rGO reinforcement on mechanical and piezoelectric properties of PVDF-BTO nanocomposites

5.1 INTRODUCTION

The low-cost and highly flexible PENGs have potential applications in mechanical energy harvesting and low-power electronics. The primary objective of this chapter is to investigate whether BTO could provide distinct or enhanced mechanisms for improving the piezoelectric performance of PVDF films compared to TiO_2. BTO has garnered significant attention due to its strong piezoelectric properties, ease of preparation, and cost-effectiveness. Additionally, the inclusion of rGO promotes the uniform dispersion of BTO nanoparticles within the polymer solution. The incorporation of conductive fillers forms multiple micro-capacitor models within the composite structure, thereby enhancing the overall dielectric properties and stabilizing the β phase content of PVDF. The materials used and fabrication of nanocomposite films are discussed in sec.5.2. PVDF is reinforced with a fixed quantity of BTO and varying concentrations of rGO to enhance the piezoelectric behavior of PVDF films using solvent casting approach. Sec.5.3 investigates the characterization and testing of three phase hybrid nanocomposite films. Structural and morphological investigation of hybrid composites is carried out using Raman, FTIR, FESEM, and XRD tools. Moreover, effect of rGO loading on dielectric, mechanical and piezoelectric behavior is discussed in this section. An increment in electroactive β phase from 54 to 73% has been observed by loading rGO in PVDF-BTO nanocomposite. Mechanical properties such as Young's modulus, tensile strength, breaking strain,

storage modulus, viscosity, and hardness of PVDF-BTO-rGO films showed remarkable increment compared to PVDF-BTO nanocomposite respectively. The PENG devices are subjected to continuous finger tapping, film twisting, and thumb pressing using human hand to record piezoelectric output for poled and unpoled samples. The PENG devices displayed significant enhancement in piezoelectric output voltage from 0.98 V for pure PVDF to 4.1 V for PVDF-BTO-rGO when rGO content is 1.25 wt.% for finger tapping condition. The overall summary of this chapter is presented in sec.5.4.

5.2 EXPERIMENTAL

5.2.1 Materials

PVDF pellets (M_w of 530,000), N, N-dimethyl formamide (DMF) (anhydrous, 99.8%) solvent, and BTO nanoparticles (<100 nm size, 99% trace metals basis) are ordered from Sigma Aldrich, USA. rGO powder (purity >99%, 3-5 layers) is supplied by Techinstro industries, Nagpur.

5.2.2 Preparation of PVDF-BTO-rGO hybrid composite

The nanocomposite films are fabricated using solvent casting process as presented in Fig. 5.1. Initially, 2 g of PVDF is added to DMF (10ml) solvent under magnetic stirring for 3 hours at 60 °C. A 15 wt.% BTO is then added to PVDF solution and the resulting mixture is further stirred for another 2 hours. Different amount of rGO is added into PVDF-BTO solutions to get 0.5, 0.75, 1, 1.25, and 1.5 wt.% of PVDF-BTO-rGO solutions. The prepared solutions are again magnetically stirred at 500 rpm for 4 hours. before being sonicated for 1 hour Then, the resulting solutions are kept in a vacuum desiccator for 30 minutes to remove bubbles from the solution. The same procedure is followed for pure PVDF and PVDF-BTO nanocomposite formation. The degassed solutions are then poured into the petri dish and kept at 70 °C for 12 hours in muffle furnace to evaporate the solvent. The free-standing nanocomposite films are obtained once the solvent is removed completely. The resulting films are then compressed between two square-shaped aluminium plates and annealed at 120 °C for approximately 1 hour resulting in dense composite

with less porosity. The weight fraction of rGO is calculated using equation 5.1:

$$W_{rGO} = \frac{W_{rGO}}{W_{rGO} + W_{\mathrm{BTO}} + W_{PVDF}} \tag{5.1}$$

W_{PVDF}, W_{rGO}, and W_{BTO} are mass (in g) of PVDF, rGO and BTO respectively. The fabricated nanocomposite film is presented in Fig. 5.2a. The as-prepared nanocomposite films are given the

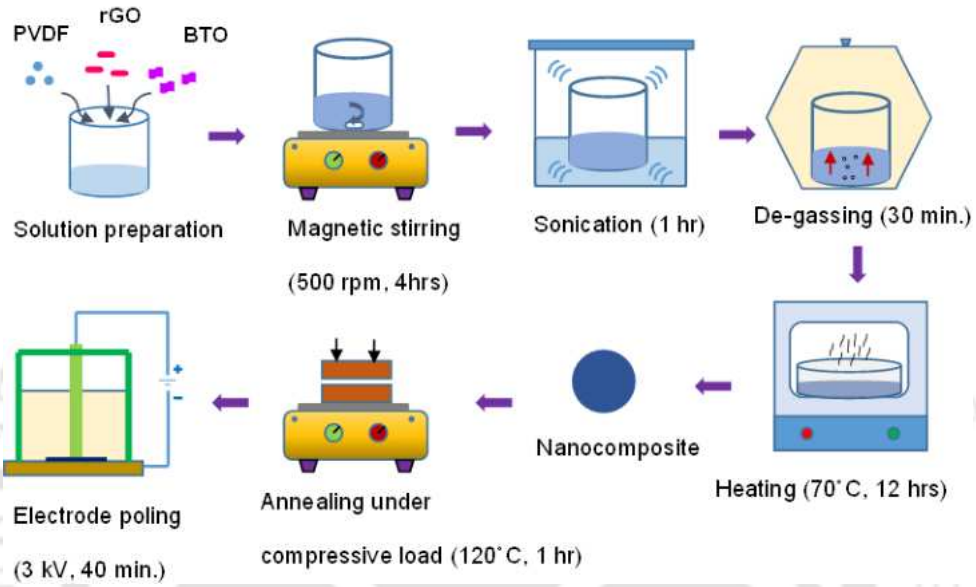

Fig. 5.1: Step by step process for nanocomposite fabrication using solvent casting approach.

following names for convenience: A (pure PVDF), AB (PVDF-BTO), ABC 0.5, (PVDF-BTO-0.5wt.% rGO), ABC 0.75 (PVDF-BTO-0.75wt.% rGO), ABC 1 (PVDF-BTO-1wt.%rGO), ABC 1.25 (PVDF-BTO-1.25wt.% rGO), ABC 1.5 (PVDF-BTO-1.5wt.% rGO). After the nanocomposite fabrication, the samples are subjected to electric poling process, to further enhance piezoelectric behavior. At first, Al electrodes (200 nm thick) are thermally evaporated on both sides of nanocomposite films. Al coated samples are then placed in between the spring-loaded copper electrode of the poling jig. To prevent any electrical arcing, the test samples are immersed in the silicon oil. A sandwich structure is cut into 3 cm x 1.5 cm pieces, which are then wrapped in PET sheets to protect them from damage as shown in Fig. 5.2b. The weight percentage of constituents for nanocomposite samples is presented in Table 5.1.

Table 5.1: Weight percentages of different nanocomposite films.

Sample name	Weight of PVDF (g)	Weight of BTO (g)	Weight of rGO (g)
A	2	-	-
AB	2	0.36	-
ABC0.5	2	0.36	0.01
ABC0.75	2	0.36	0.015
ABC1	2	0.36	0.02
ABC1.25	2	0.36	0.025
ABC1.5	2	0.36	0.03

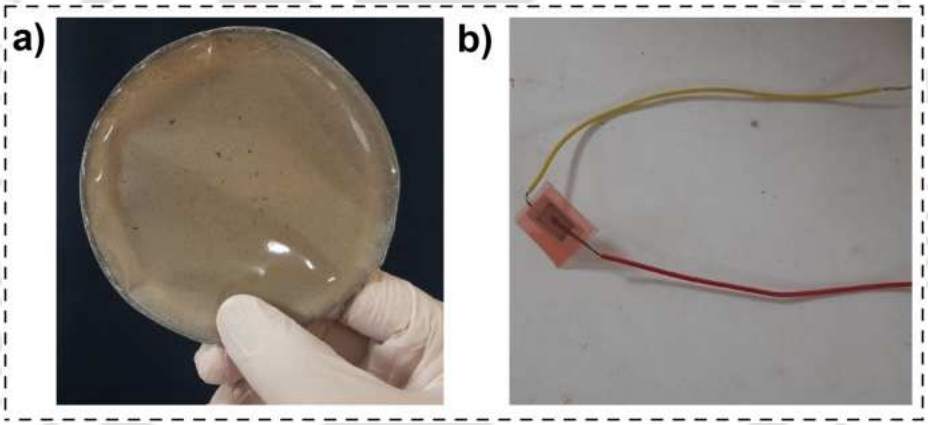

Fig. 5.2: a) Solvent cast nanocomposite film, b) fabricated PENG device.

5.2.3 Material characterization

The microstructure and surface morphology of solvent cast films are examined with the help of FESEM (GeminiSEM 500, ZEISS) followed by elemental analysis and distribution study using EDS. Raman spectra of nanocomposite films are recorded with the help of Laser Micro Raman System (LabRam HR, Horiba JobinYvon) having 532 nm laser wavelength with 5 seconds integration time. FTIR (PerkinElmer, Singapore) of the nanocomposite films are performed over the wavenumber range of 400-3500 cm^{-1} in ATR mode. Phase and crystal plane analysis is performed using XRD (Rigaku, Japan) having Cu Kα radiation with 1.54 Åwavelength over the 2θ span from 15-80° with a scan rate of 4°/min. Thermal stability and residual mass of nanocomposite films are analyzed

from 20 °C-800 °C at 10 °C/min using TGA instrument (TGA 4000, PerkinElmer). Nanocomposite films are heated from 25 °C-250 °C at 10 °C/min for DSC test (STA449F3A00, Netzsch) under Argon gas atmosphere. Mechanical properties (elastic modulus, tensile strength, and toughness) of the nanocomposite films are determined with an Instron dynamic UTM 8801 (100 kN) machine at a velocity of 1 mm/min. To prepare the samples for the tests, ASTM standard D882 is followed. The viscosity is measured using (Physica MCR 301, Anton Paar) rheometer at room temperature with a fixed strain of 1%. The viscoelastic behaviour of the nanocomposite films is studied using a DMA (Physica MCR 702, Anton Paar) in tensile mode on a 40 × 10 mm sample size. The films are subjected to a frequency sweep from 0.1 Hz to 100 Hz at room temperature conditions. The hardness values of the nanocomposite samples are determined using Vickers micro hardness test using micro hardness tester (Omni tech, MVH-II). Each sample is subjected to a load of 0.2 kgf for 20 seconds. The dielectric property measurement is performed using LCR meter (Hioki, IM 3536) from 1 kHz–1 MHz at room temperature. The piezo response of fabricated PENGs is recorded using digital storage oscilloscope (GWInSTEK, GDS-2102A).

5.3 RESULTS AND DISCUSSION

5.3.1 FESEM and EDS

FESEM plots of rGO and BTO nanoparticles are shown in Fig. 5.3a-b respectively. BTO displays a spherical structure whereas rGO shows a sheet-like structure. The diameter distribution spectra presented in Fig. 5.3c show that BTO nanoparticles have an average particle size of 75.86±20 nm. Fig. 5.3d-e shows grain structure of pure PVDF and BTO loaded PVDF matrix respectively. rGO and BTO particles are completely dispersed and well covered in PVDF. Dense rGO sheets with embedded BTO particles at certain locations can be found in Fig. 5.3f. EDS spectra in Fig. 5.4a-d indicate fluorine (F), oxygen (O), carbon (C), titanium (Ti), and barium (Ba) elements are mainly present in the sample, which confirms the successful fabrication of PVDF-BTO-rGO nanocomposite films. The energy levels of F, Ba, Ti, O, and C elements in the polymer matrix are 0.5 keV, 4.46 keV, 4.5 keV, 0.6 keV, and 0.24 keV, respectively [130, 131]. Elemental mapping as shown in Fig. 5.4e-f confirms uniform distribution of the constituent elements inside PVDF matrix.

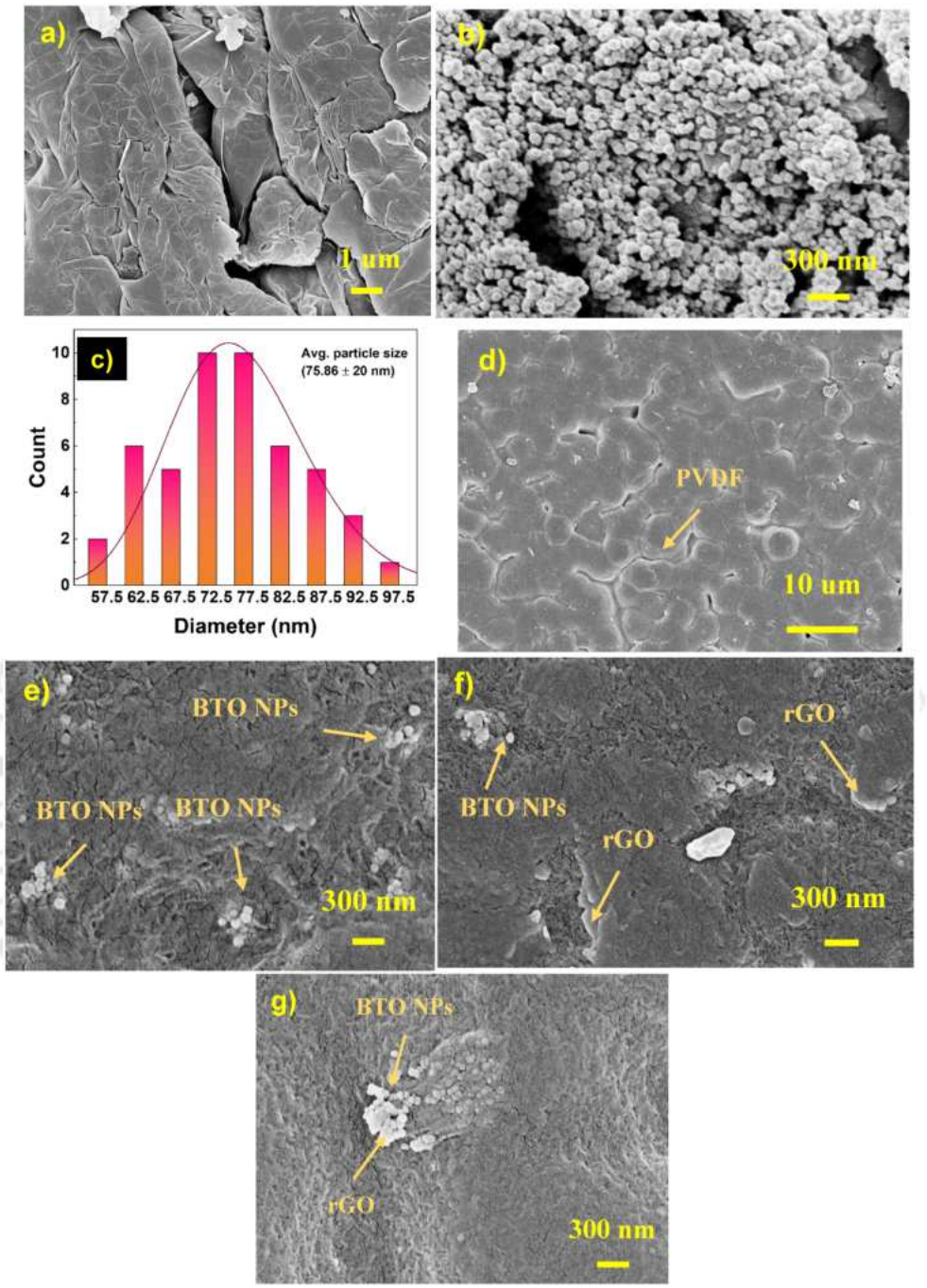

Fig. 5.3: FESEM images of a) rGO nanosheets, b) BTO nanoparticles, c) BTO nanoparticle size distribution, and samples d) A, e) AB, f) ABC 0.75, and g) ABC 1.5.

5.3.2 Raman spectroscopy

Fig. 5.5a-b shows Raman spectra for pure rGO and rGO loaded polymer composites. Raman spectroscopy is helpful in characterization of material structure and defects in rGO based materials. The intense peak at 308 cm^{-1} and small peak at 720 cm^{-1} corresponds to tetragonal crystal structure of BTO [132]. The peaks at 1431 and 2974 cm^{-1} belongs to PVDF matrix [133]. A D

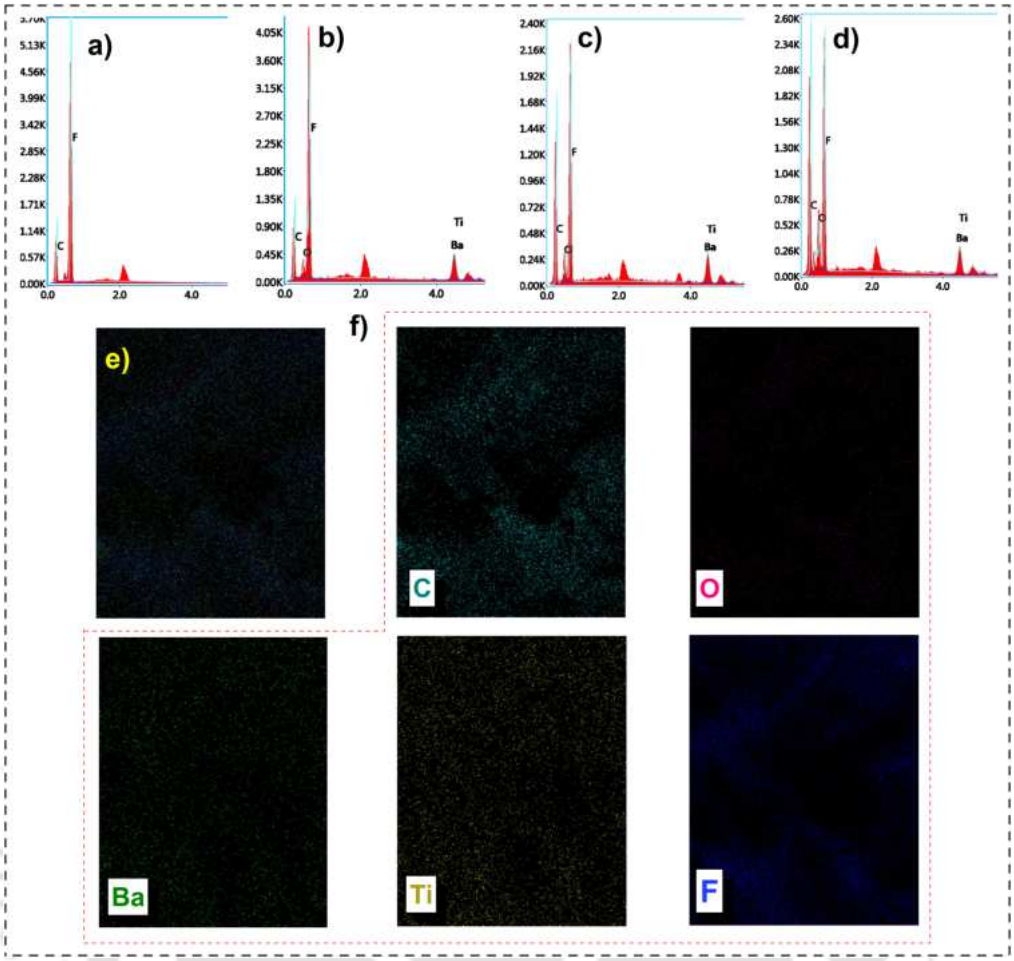

Fig. 5.4: EDS spectra for sample a) A, b) AB, c) ABC 0.75, and d) ABC 1.5. e) all the mapping elements. f) mapping image of each constituent element for ABC 0.75.

peak at 1326 cm^{-1} and a G peak at 1573 cm^{-1} are observed for rGO which specifies defects and sp2 carbon networks of the samples under test. The intense peak at 2974 cm^{-1} and weak peak at 1431 cm^{-1} represents C-H and $–CH_2$ bond vibrations respectively. The D and G peaks of ABC 0.5 are not as intense due to the lower filler content of rGO. ABC 1 showed maximum intensity for D band, thereby signaling more defects on rGO sheets. The intensity ratio (I_r) values shown by different nanocomposite samples are presented in Table 5.2.

5.3.3 FTIR spectroscopy

The FTIR plot shown in Fig. 5.5c is utilized to explore PVDF's crystalline forms in more detail. The vibrational bands at 763 cm^{-1} and 976 cm^{-1} are associated with the non-polar α phase [90], while the characteristic peaks at 841 cm^{-1} and 1231 cm^{-1} are associated with the electroactive β phase [134, 135]. Symmetric tensile vibrations of $–CF_2$ and C–C produce the absorption peaks at

Table 5.2: Intensity ratio values for different nanocomposite samples.

Sample name	I_r
ABC 0.5	0.36
ABC 0.75	0.23
ABC 1	0.94
ABC 1.25	0.65
ABC 1.5	0.93

842 and 1288 cm^{-1}, whereas $-CH_2$ swing antisymmetric stretching of C–C produces the absorption peak at 1400 cm^{-1}. The electroactive phase content fraction (F(β)) values are calculated using equation 5.2:

$$F(\beta) = \frac{A_{841}}{A_{841} + 1.26A_{763}} \tag{5.2}$$

Where, A_{841} and A_{763} are absorption intensity values for α and β phases, respectively. It can be observed that β phase content in nanocomposite films, especially in rGO reinforced films, is higher than neat PVDF films. As rGO loading increases, the increment in β phase content continues until the loading reaches 1.25 wt.%, followed by a drastic reduction. β phase content of 54, 58, 66, 69, 73, and 70% is obtained corresponding to samples with rGO reinforcement of 0, 0.5, 0.75, 1, 1.25, and 1.5 wt.% respectively as presented in Fig. 5.5d. The significantly enhanced β phase content results from the improved interaction between the local electric field surrounding the nanofiller and PVDF dipoles, where the rGO sheets act as nucleating agents to facilitate β phase formation [64, 104]. The reduction in β phase content value may be attributed to agglomeration of rGO sheets causing hindrance to PVDF molecular chains motion. The F(β) values of fabricated samples are presented in Table 5.3:

5.3.4 XRD spectra

The effect of rGO loading on the phases and structure of nanocomposite films is investigated using XRD analysis. Diffraction peaks of rGO and BTO powder are presented in Fig. 5.6a-b. A

Table 5.3: Fraction of electroactive phase content values for different fabricated samples.

Sample name	F(β) %
A	54
ABC 0.5	58
ABC 0.75	66
ABC 1	69
ABC 1.25	73
ABC 1.5	70

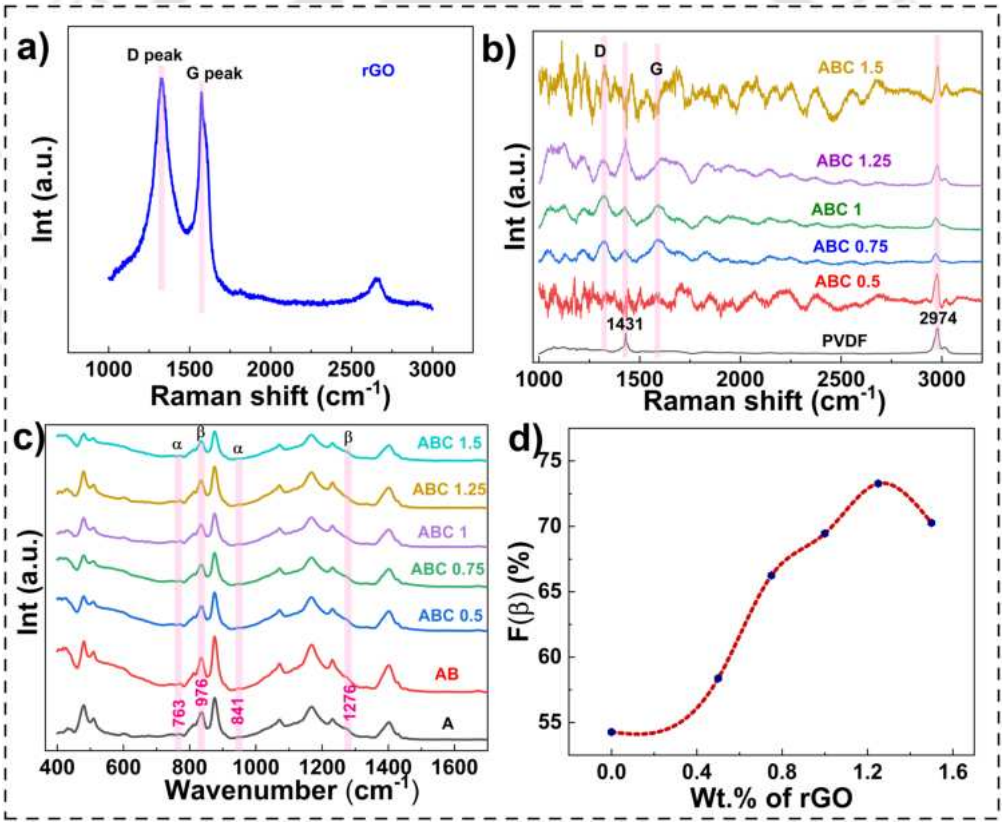

Fig. 5.5: Raman plot of a) pure rGO and b) PVDF-BTO-rGO nanocomposite films for different rGO content, c) FTIR spectra and d) fraction of electroactive β phase content against varying rGO content for PVDF-BTO-rGO nanocomposite films.

diffraction peak at 20.36° represents electroactive β phase of PVDF that occurred due to diffraction of (200) and (110) crystal planes [136]. The peaks shown at 2θ = 22.07°, 31.53°, 38.89°, 45.23°, 50.98°, 56.17°, 65.89°, 70.46°, 74.88°, and 79.16° belong to miller planes of (100), (110), (111), (200),

(210), (211), (320), (300), (310), and (311) respectively. The peak at $2\theta = 26.51°$ corresponds to rGO. The interaction between PVDF and rGO has a direct effect on β phase content of PVDF. On rGO addition, -CF_2 dipole of PVDF matrix and –CH_2 dipole of rGO orientate with each other which causes enhancement of polar β phase of PVDF matrix [137]. The XRD plots of PVDF-BTO-rGO nanocomposites are shown in Fig. 5.6c-d. Further, Williamson-Hall (W-H) method with uniform deformation model (UDM) is applied to calculate the average crystalline size and lattice strain induced in the sample. UDM only considers isotropic strain, which generally affects the physical broadening of the XRD profile. The equation 5.3 used to calculate the crystal parameters is given as:

$$\delta_{\mathrm{hkl}} \cdot cos\theta = \frac{0.9\lambda}{D} + 4\mu sin\theta \tag{5.3}$$

where δ_{hkl} is full width at half of the maximum intensity (FWHM) for different planes, D is average crystalline size, μ is lattice strain, and λ is the wavelength. Crystalline size and strain values are calculated by plotting ($4\sin\theta$) along X-axis and ($\beta_{\mathrm{hkl}}\cos\theta$) along Y-axis, followed by straight-line fit ($R^2 = 0.8954$). The slope represents lattice strain in this straight line, while the intercept represents crystal size. Average crystalline size of BTO nanoparticles is found to be 65 nm, as shown in Fig. 5.6e. Calculated structural parameters are given in Table 5.4.

Table 5.4: XRD structural parameters for nanocomposites.

Sample name	Crystalline size (nm)	Lattice strain
AB	26.5	0.00254
ABC 0.5	29.68	0.00247
ABC 0.75	32.74	0.00213
ABC 1	33.67	0.00194
ABC 1.25	37.48	0.00169
ABC 1.5	40.38	0.00158

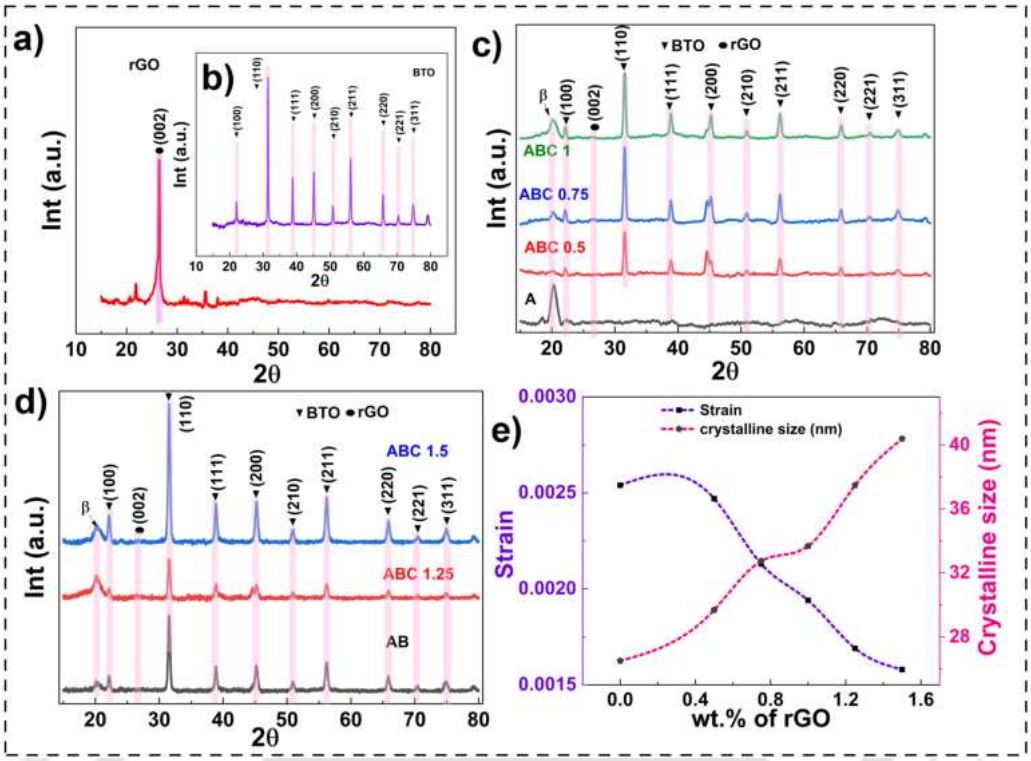

Fig. 5.6: XRD patterns of a) rGO nanosheets, b) BTO nanoparticles, c) A, ABC 0.5, ABC 0.75, ABC 1, and d) AB, ABC 1.25 and ABC 1.5 nanocomposite films, e) crystalline size and induced strain.

5.3.5 TGA and DSC analysis

Role of presence of nanofillers on thermal stability of PVDF matrix is analysed using TGA study as shown in Fig. 5.7a. For pure PVDF, sudden thermal decomposition at around 425 °C is observed leading to weight loss of about 60% at around 490 °C followed by more gradual thermal degradation. Incorporation of BTO nanoparticles (20 wt.%) in the PVDF matrix shows significant enhancement in thermal stability. BTO nanoparticles and the PVDF matrix have a large surface area of contact, which restricts the thermal breakdown of the PVDF chain. In addition, PVDF-BTO nanocomposites are reinforced with secondary rGO nanofillers to test their thermal stability. A further increase in thermal stability is observed as rGO content is increased. The enhanced thermal stability is attributed to the barrier effect of rGO, which restricts thermodegradation [138]. As a result of their synergistic effect, BTO and rGO reduce thermal degradation rate, thereby improving the thermal performance of PVDF-BTO-rGO nanocomposite. Additionally, better dispersion of nanofillers into the PVDF matrix can increase the activation energy for thermal degradation.

Increment in onset temperature (T_{onset}) has been observed on reinforcing BTO particles whereas in nanocomposites added with rGO, T_{onset} values enhance significantly. Sample ABC 1.5 showed maximum T_{onset} of 480.47 °C, an increase of 44 °C compared to PVDF. Increased percentage of residual mass (m_r) on nanofiller addition also confirms the enhanced thermal stability of nanocomposite samples. Sample ABC 1.5 showed a maximum residual mass of 32.25% at 750 °C. The thermal behavior of nanocomposites is further studied using DSC tests as shown in Fig. 5.7b. The analysis comprised four samples (A, AB, ABC 1.25, and ABC 1.5). Gradual increment in melting temperature is observed with increasing rGO content in PVDF-BTO nanocomposites. The large surface area of rGO sheets makes them ideal nucleating agents because of their ability to adsorb PVDF chains and cause nucleation as a result [138]. Degree of crystallinity (X_c) of nanocomposite samples are calculated using following equation 5.4:

$$X_c = \frac{\Delta H_{mt}}{\Delta H_{100\%}} \times 100 \tag{5.4}$$

where, ΔH_{mt} is enthalpy associated with melting, $\Delta H_{100\%}$ is enthalpy associated with 100% crystalline PVDF (104.7 J/g) [96]. BTO reinforcement increases the crystallinity of PVDF matrix. The crystallinity values of PVDF-BTO nanocomposites are further enhanced by adding rGO as a secondary nanofiller. Increasing crystallinity is caused by changes in filler reinforcement, nanofiller size, and interfacial interactions of nanofillers with PVDF matrix [98, 99]. The values of different thermal parameters calculated using TGA and DSC are listed in Table 5.5.

5.3.6 UTM testing

An excellent piezoelectric material must possess good mechanical properties if it is to be used in energy harvesting, self-powering device applications. Effect of rGO loading on mechanical properties of PVDF-BTO nanocomposites is studied in tensile measurements as shown in Fig. 5.8a-c. It is observed that, on increasing the rGO concentration up to certain extent, tensile strength and elastic modulus are also increased. A drastic reduction in strength and elastic modulus is observed for 1.5 wt.% of rGO loading. This is caused by agglomeration of rGO sheets in a PVDF-BTO heterogeneous system. A maximum tensile strength and elastic modulus of 41.43 MPa and 1215.2 MPa are observed for ABC 1.25 sample.

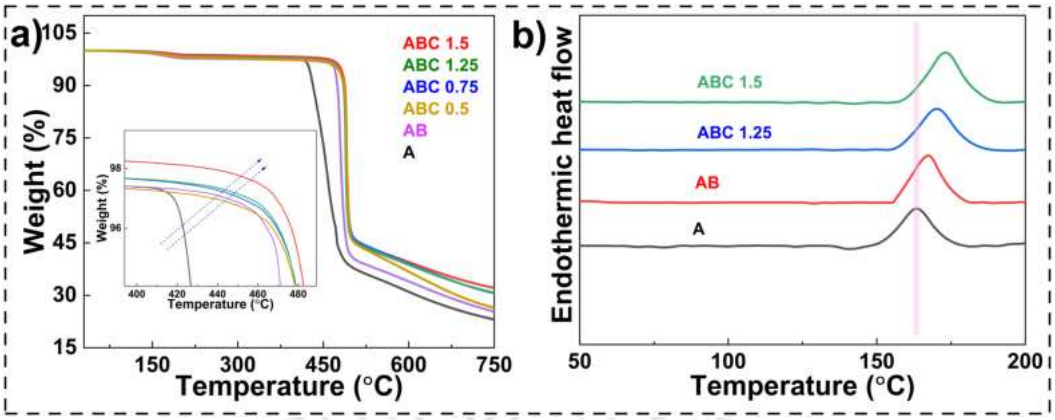

Fig. 5.7: a) TGA and b) DSC plots for nanocomposite samples.

Table 5.5: TGA and DSC parameters for PVDF nanocomposites.

Sample name	T_{onset} (°C)	m_r (%)	ΔH_{mt} (J/g)	X_c (%)	T_m (°C)
A	430.19	23.14	24.23	23.15	163.4
AB	469.58	25.37	25.2	24.06	167.37
ABC 0.5	474.5	26.47	-	-	-
ABC 0.75	475.65	30.59	-	-	-
ABC 1.25	475.75	30.73	25.89	24.72	170.24
ABC 1.5	480.47	32.25	30.09	28.73	173.23

Reduction in the breaking strain is observed for higher concentrations of rGO, confirming ductile to brittle transformation of nanocomposite films. The poor dispersion of rGO and BTO fillers leads to micro-nanoscale voids and defects causing stress concentration at different locations in the PVDF matrix. This leads to enhanced brittleness and reduction in breaking stress and strain values [115]. Maximum breaking strain of 0.36 is observed for sample A. For all samples, toughness values are calculated by following the area under the stress-strain curve up to breaking point. The toughness value increased for sample AB, and then decreased for samples with rGO content. Sample AB showed a maximum toughness value (6.08±0.2). A summary of mechanical properties is presented in Table 5.6. Values of toughness, breaking strain and max. tensile strength obtained is considerably higher than previously reported result [139].

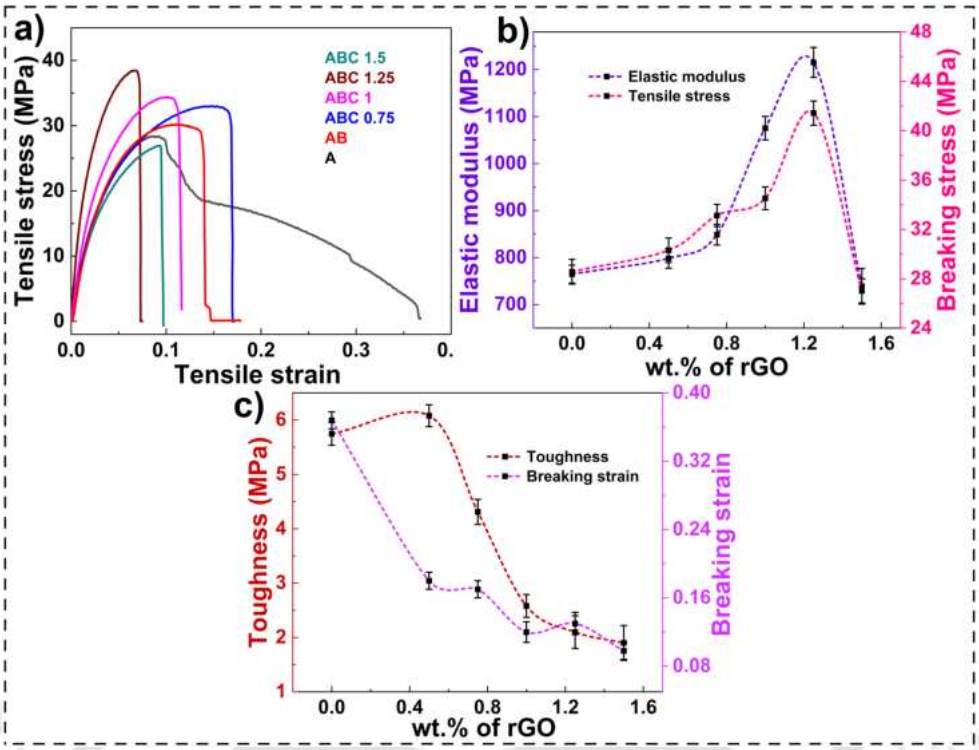

Fig. 5.8: a) Stress-strain plot, effect of rGO concentration on b) elastic modulus, c) tensile stress, d) breaking strain, and e) toughness of PVDF-BTO-rGO nanocomposite films.

Table 5.6: Mechanical properties of nanocomposites.

Sample name	Max. tensile stress (MPa)	Breaking strain	Elastic modulus (MPa)	Toughness (MJ/m^3)
A	28.57±1	0.36±0.01	764.82±19	5.74±0.21
AB	30.31±0.99	0.18±0.01	798.36±21	6.08±0.2
ABC 0.75	33.13±0.91	0.17±0.01	848.73±22	4.31±0.23
ABC 1	34.52±0.92	0.12±0.012	1075.4±25	2.58±0.21
ABC 1.25	41.43±0.98	0.13±0.013	1215.2±32	2.1±0.3
ABC 1.5	27.02±0.98	0.09±0.01	739.08±38	1.9±0.32

5.3.7 DMA analysis

The dynamic mechanical analysis can be used to explore interactions between nanoparticles and polymer matrix in nanocomposites. Mechanical properties like storage and loss moduli over desired frequency ranges are evaluated using this test. Fig. 5.9a shows rectangular nanocomposite films for DMA measurement, whereas Fig. 5.9b presents state of the sample (as shown by dotted red

lines) under prospective loading condition for dynamic response measurement. The plot of storage modulus vs frequency as shown in Fig. 5.9c demonstrates the effect of nanofillers on storage modulus values. Nanocomposites are better at distributing interfacial stress and limiting the segmental motion of polymer matrix chains than pure PVDF [106]. It is observed that all the nanocomposite samples displayed enhanced storage modulus values compared to pure PVDF. The high elastic modulus and high strength of rGO and BTO nanofillers are responsible for the enhancement of storage modulus. This increment in storage modulus is attributed to the reinforcing effect of nanofillers in PVDF matrix. Sample ABC 1.25 showed a maximum storage modulus value, whereas sample ABC 1.5 showed drastic reduction as compared to other nanocomposites in storage modulus. The agglomerates formed by the accumulation of heavily reinforced nanofillers may be responsible for this reduction. The behaviour of damping factor (tanδ) against frequency values is shown in Fig. 5.9d. A slight increment in tanδ values is observed for nanocomposites with increasing nanofiller content. The increase is ascribed to the nanocomposites' less elastic nature as a result of the development of multiple filler networks inside the composites [60]. As a result, rGO optimized storage modulus values for PVDF-BTO nanocomposites up to 1 wt.% reinforcement, leading to drastic reductions at higher loadings.

5.3.8 Hardness measurement

The nature of polymer-nanofiller interface determines the micro hardness of nanocomposite samples. Surface indentation plots of the nanocomposite samples are presented in Fig. 5.10a-g. Points 1, 2, 3, 4, 5, 6, and 7 in Fig. 5.10h corresponds to samples A, AB, ABC 0.5, ABC 0.75, ABC 1, ABC 1.25, and ABC 1.5 respectively. BTO addition in PVDF matrix enhances the overall hardness value of PVDF-BTO nanocomposite. The reason behind this increment in micro hardness value may be due to better interfacial adhesion between polymer and nanofiller. On rGO addition, micro hardness value increased further up to 1.25 wt.% of rGO loading, then reduced. rGO nanosheets are among the hardest materials on earth. As a result, it improved the polymer's hardness when it is incorporated into a PVDF matrix. Additionally, rGO sheets have been found to improve the hardness of polymers in various other studies [116, 117]. This is because of the hard phase

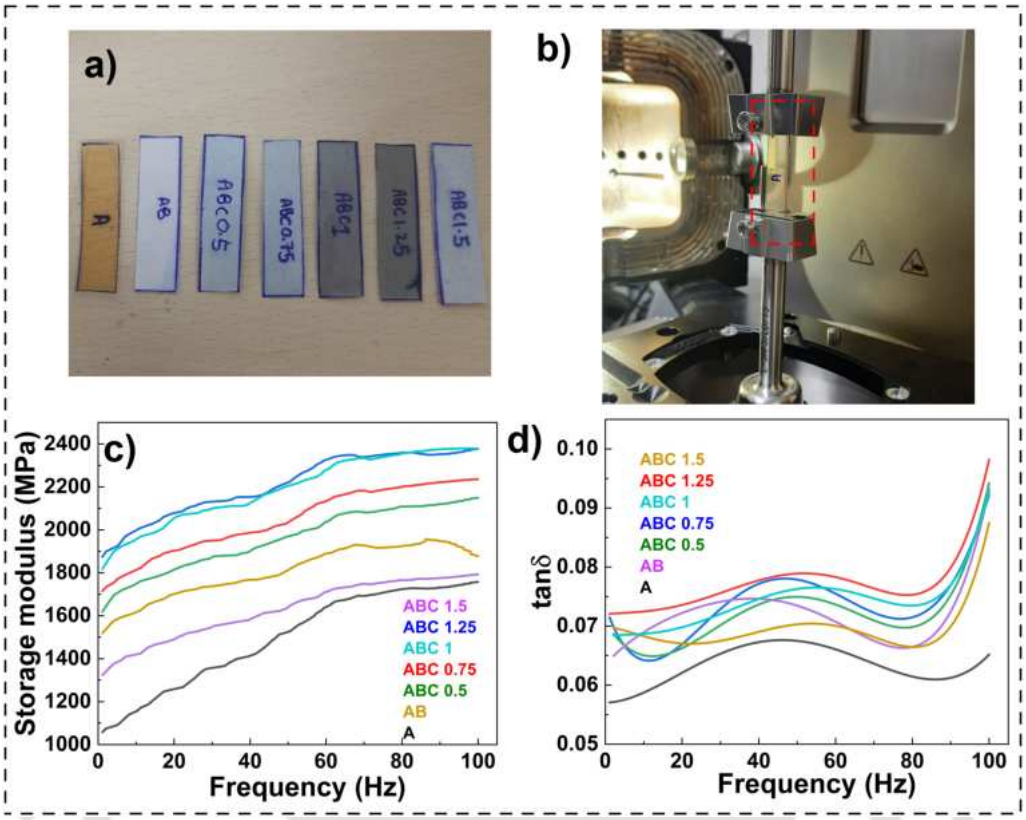

Fig. 5.9: a) Samples to be analysed for DMA, b) sample loading position under dynamic loading condition, DMA results of variation of c) storage modulus, and d) damping factor over specified frequency range.

of rGO sheets present in the PVDF matrix. The rGO interlocks the molecular chains of PVDF, thereby constraining the chain mobility when load is applied [118]. But, at higher rGO loading, this interaction starts degrading due to agglomeration of nanofillers in the PVDF matrix, resulting in reduction in micro-hardness value. As mentioned in tensile test measurements, agglomeration occurs at higher filler loading, which has adverse impact on the hardness values. The hardness values of nanocomposite films are presented in Table 5.7.

5.3.9 Dielectric measurement

The variation in dielectric behaviour of PVDF-rGO-BTO nanocomposites over the frequency range is studied as shown in Fig. 5.11a. Dielectric properties of PVDF-BTO nanocomposites are significantly affected by rGO loading. The ϵ increases as the rGO content increases. A sample ABC 1.5 showed a maximum ϵ value of 61 at 1 kHz, gradually decreasing to 37 at 1 MHz. At lower

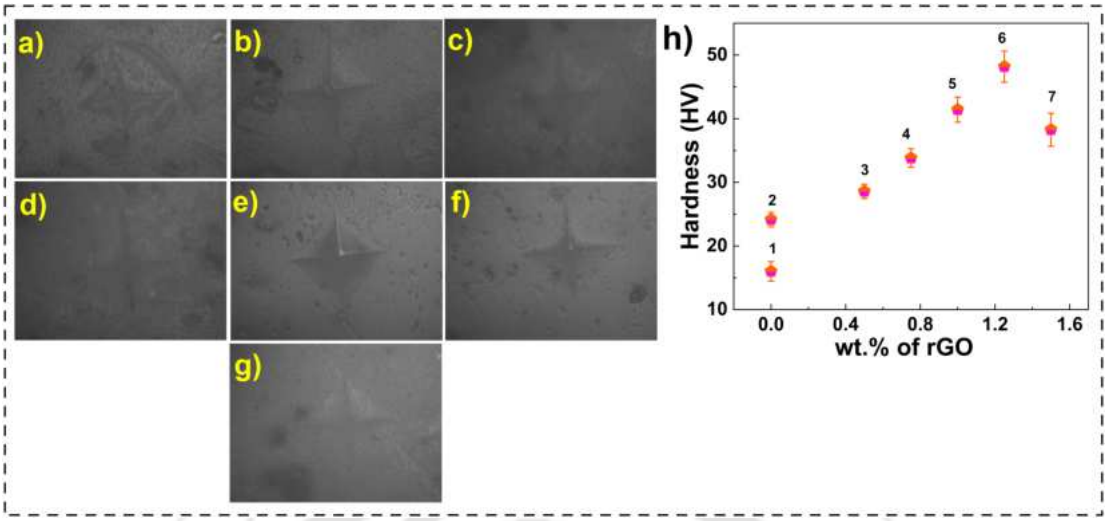

Fig. 5.10: Surface image after micro indentation for a) A, b) AB, c) ABC 0.5, d) ABC 0.75, e) ABC 1, f) ABC 1.25, and g) ABC 1.5. h) micro-hardness values for nanocomposite samples.

Table 5.7: Hardness values of nanocomposites.

Sample name	Hardness values (HV)
A	16±1.54
AB	24.13±1.14
ABC 0.5	28.57±1.12
ABC 0.75	33.82±1.45
ABC 1	41.42±1.98
ABC 1.25	48.18±2.45
ABC 1.5	38.26±2.6

frequencies, high ϵ values are caused by the Maxwell-Wagner-Sillars (MWS) theory of interfacial polarization (IP) at the insulator-conductor interface [104]. On the contrary, due to the brief alignment duration, dipoles cannot polarize effectively at the interface as frequency values rise. This phenomenon is referred to as the polarization relaxation phenomenon. The high conductivity of rGO amplifies the interfacial polarization, leading to improved ϵ values. Elevated loading of rGO sheets results in a greater accumulation of free charges at the interface, thereby generating a larger number of dipoles. An even distribution of fillers coupled with an increased interfacial area further boosts interfacial polarization values. In the presently fabricated hybrid composites, rGO behaves

as an electrode, whereas BTO and PVDF matrix acts as a micro capacitor's dielectric medium. Increasing rGO loading further enhances micro-capacitor numbers. However, at higher frequencies, electric dipoles do not get enough time for their alignment because of rapidly increased electric field causing reduction in dielectric values [140]. Lower dielectric loss is observed at lower frequencies, followed by an increment at higher frequencies. The behaviour of σ_{ac} of nanocomposites is presented in Fig. 5.11b. rGO being highly conductive, improves the overall conductivity of nanocomposite samples upon its addition. Sample ABC 1.5 showed maximum σ_{ac} of 4.18 μS/m at 1 kHz. The values of dielectric constant at 1 KHz is presented in Table 5.8.

Table 5.8: Dielectric constant values of PVDF based hybrid nanocomposites.

Sample name	ϵ
A	8
AB	13
ABC 0.5	16
ABC 0.75	18
ABC 1	23
ABC 1.25	37
ABC 1.5	61

5.3.10 Piezoelectric measurement

Before fabricating the PENG devices, the respective samples are subjected to electric poling using DC poling unit. A voltage of 3 kV is used for about 40 minutes to align ferroelectric dipoles of BTO and PVDF. A total of seven PENG devices are fabricated and tested under soft tapping, twisting, and thumb pressing conditions as presented in Fig. 5.12. On testing, it is observed that output voltage shown by nanocomposite films is significantly enhanced due to nanofiller addition. Initially, on BTO addition, increment in piezo voltage is observed. But, in addition to secondary nanofiller rGO, piezo voltage and current is enhanced further with increasing rGO loading. rGO facilitates dipole alignment of PVDF matrix and allows micro-capacitor model formation inside

the nanocomposite. Carbonyl and carboxyl groups in the rGO basal plane play an important role in aligning polymer chains by attracting fluorine atoms. rGO sheets have a large number of free charges on their surfaces as a result of their high mobility. Dipoles generated by PVDF and BTO fillers accumulate these free charges in ceramic-polymer composites, generating new dipoles there. Consequently, the sheet will generate and store more charge as a result of the increased number of dipoles. In conclusion, RGO nanofiller enhances the energy harvesting capacity of PENG device [141]. It is noticed that a maximum o/p voltage of 4.1 V is obtained for finger tapping condition for rGO concentration of 1.25 wt.%. Finger tapping and twisting yielded substantially greater output voltage for increased rGO loading compared to thumb pressing conditions. The enhanced output signals are attributed to increment in β phase of PVDF, as confirmed in FTIR results. Poling process maximizes electric dipole alignment of β phase. However, this increment is stopped for ABC 1.5 showing a reduction in piezo response. An overview of piezo voltage behaviour for nanocomposites under different loading conditions concerning changing rGO loading is presented in Fig. 5.13a. To confirm the effectiveness of electrode poling operation, piezo responses of poled and unpoled samples of a same concentration are compared under soft tapping, twisting and thumb pressing conditions as shown in Table 5.9. A significant increment in output voltage is observed for all the nanocomposite samples after electrode poling process under different loading conditions as presented in Fig. 5.13b-d.

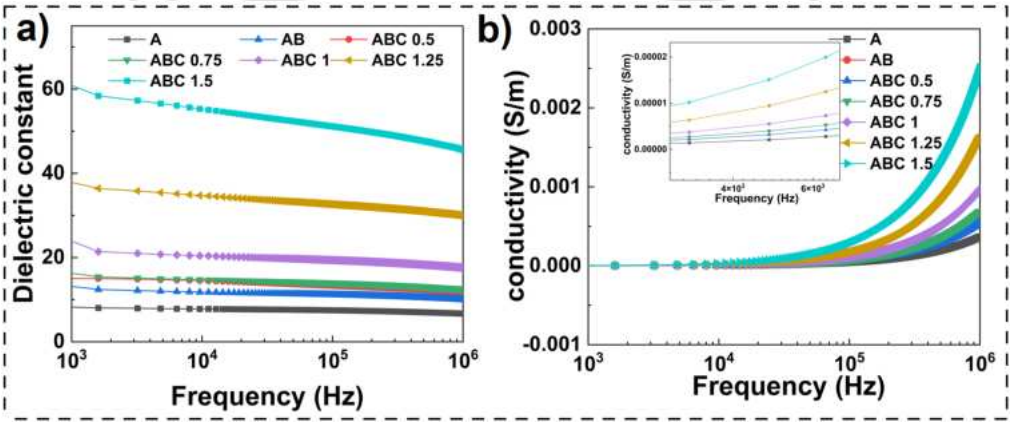

Fig. 5.11: Variation of a) ϵ, and b) σ_{ac} for pure PVDF and nanocomposite samples.

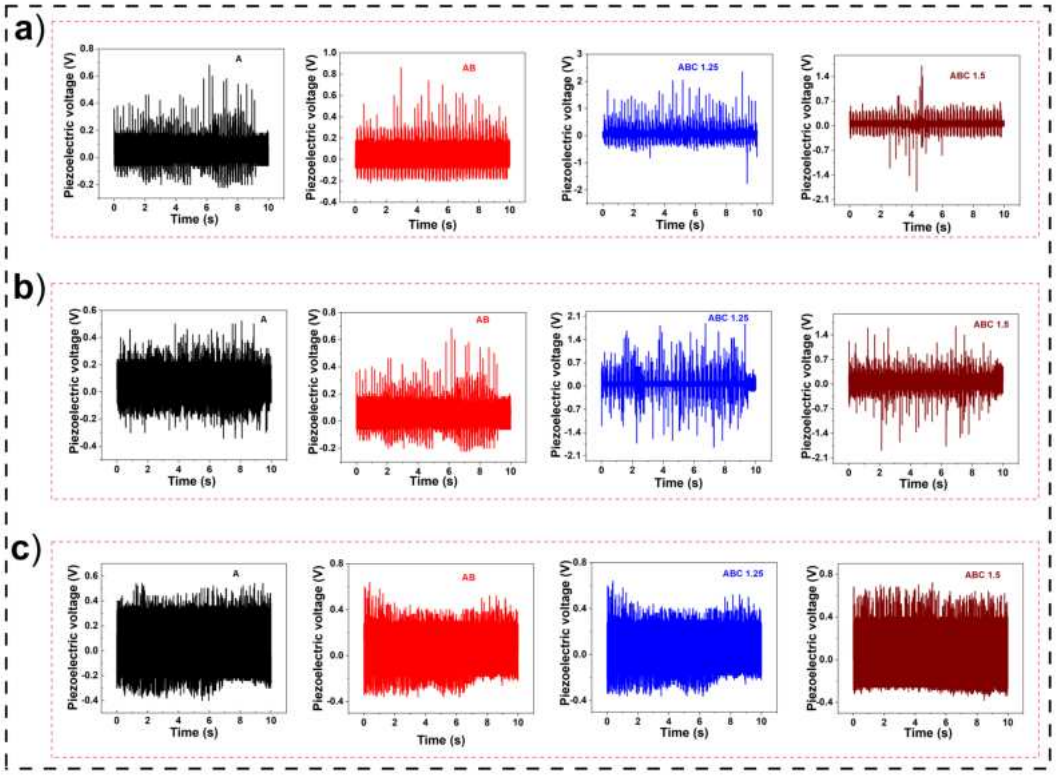

Fig. 5.12: Piezo voltage of A, AB, ABC 1.25, and ABC 1.5 for a) finger tapping, b) twisting, and c) thumb pressing conditions, after electrode poling.

Table 5.9: Voltage measured on test samples for different loading conditions.

Sample	Finger tapping		Twisting		Thumb pressing	
name	poled	unpoled	poled	unpoled	poled	unpoled
A	0.98	0.3	0.86	0.4	0.94	0.25
AB	1.08	0.38	0.98	0.32	1	0.41
ABC 0.5	1.64	0.42	1.1	0.41	0.98	0.2
ABC 0.75	2.18	0.5	1.08	0.47	1.16	0.47
ABC 1	3.14	0.57	1.15	0.58	1.32	0.38
ABC 1.25	4.1	0.62	3.72	0.73	1.44	0.73
ABC 1.5	3.56	0.64	3.6	0.29	1.12	0.64

5.4 SUMMARY

This chapter explores the investigation of the piezoelectric and mechanical characteristics of composites based on PVDF with varying levels of rGO loading. The focus is on the investigation

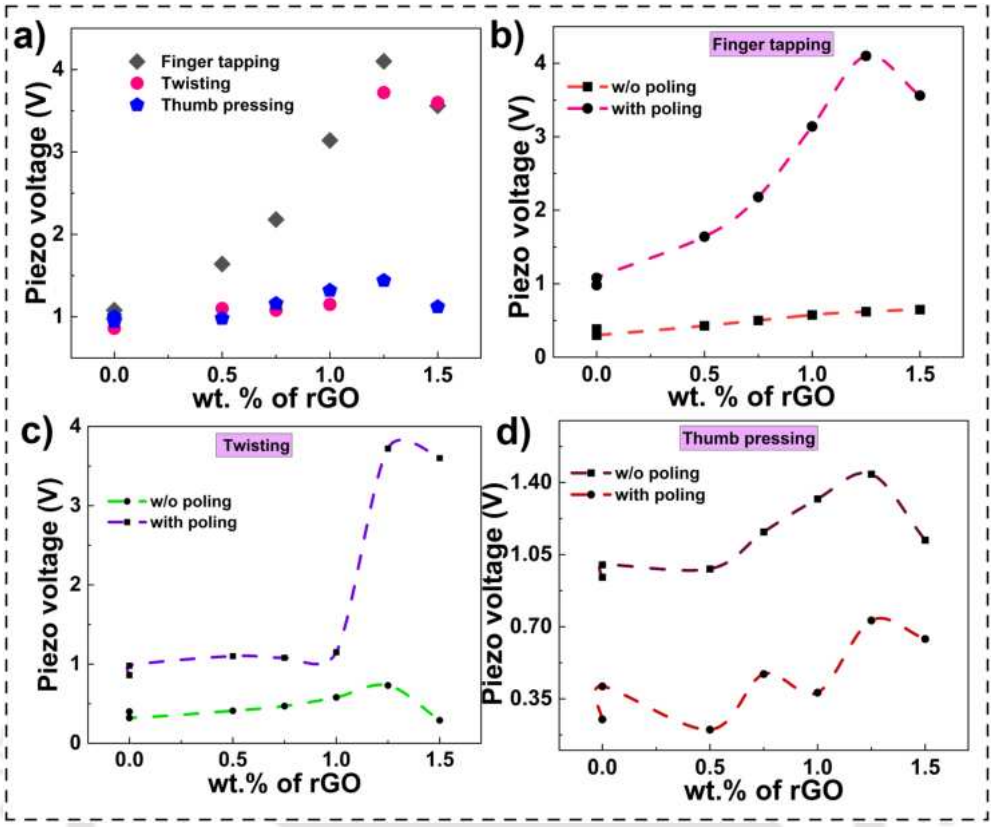

Fig. 5.13: Comparison of o/p voltage generated for nanocomposite samples a) under different loading conditions, for poled and unpoled samples under b) finger tapping condition, c) twisting condition, d) thumb pressing condition.

of the response of highly flexible hybrid composite films, with an additional enhancement of their piezoelectric properties through thermal poling. The successful creation of a three-phase composite material is verified using FESEM and XRD tools. The chapter reveals that at higher loading levels, the agglomeration of rGO sheets occurs, leading to a reduction in the overall properties of the hybrid composites. The role of rGO sheets as nucleating agents is identified, fostering improved interaction between the dipoles of PVDF and nanofillers. This interaction results in an augmentation of the electroactive phase content. The combination of BTO and rGO demonstrates a synergistic effect that reduces the thermal degradation rate and enhances the thermal performance of PVDF-BTO-rGO composites. The mechanical properties, including Young's modulus, tensile strength, breaking strain, storage modulus, and viscosity exhibited a significant increase in PVDF-BTO-rGO films when compared to PVDF-BTO nanocomposites. Furthermore, the chapter discusses how rGO sheets contribute to increased hardness in polymers by interlocking molecular chains

of PVDF, thereby restricting chain mobility under load applications. The piezoelectric voltage response of both poled and unpoled nanocomposite samples is recorded and compared. The poled sample, subjected to finger tapping conditions, exhibits the maximum piezoresponse. Initially, the addition of BTO resulted in an increase in piezo voltage. However, upon introducing the secondary nanofiller rGO, both piezo voltage and current were further enhanced with increasing rGO loading. The presence of rGO facilitates the alignment of dipoles within the PVDF matrix and promotes the formation of a micro-capacitor model within the nanocomposite. Carbonyl and carboxyl groups on the basal plane of rGO play a crucial role in aligning polymer chains by attracting fluorine atoms. Additionally, rGO sheets possess a high mobility, leading to a large number of free charges on their surfaces. These free charges are accumulated in ceramic-polymer composites by the dipoles generated from PVDF and BTO fillers, resulting in the creation of new dipoles. Consequently, the sheet generates and stores more charge due to the increased number of dipoles. In summary, the inclusion of rGO nanofiller enhances the energy harvesting capacity of the PENG device. The heightened piezoelectric voltage post-poling holds potential for powering various electronic devices in diverse applications.

Chapter 6

BMP based piezoelectric energy harvesters for impact sensing

6.1 INTRODUCTION

Global energy consumption is increasing continuously bringing about an escalation in energy prices and volatility. Around 80% of the energy generated is derived from non-renewable sources such as fossil fuels, oil, and nuclear power, with renewable sources such as wind, solar, hydrothermal, geothermal, and wave energy constituting the remaining 20%. An increasing trend in creating materials with a greater extent of sustainability from an ecological and financial perspective involves the usage of bioresources and industrial residues. The increasing exhaustion of fossil fuels and serious environment pollution have inspired researchers to look for alternative and sustainable sources of energy. The development of PVDF-BMP composites, alongside TiO_2 and BTO-based materials for PENGs, is guided by a multifaceted approach aimed at balancing eco-friendliness and material performance. Incorporating BMP as an additional filler in PVDF aimed to evaluate its potential as an environmentally friendly alternative with suitable performance metrics, expanding the material library and providing a comparative analysis. Sec.6.2 discusses the synthesis of BMP particles, its chemical treatment, and its characterization followed by PVDF-BMP composite fabrication. Leftover BMP from bamboo factories is collected and used as fillers in varying concentrations (1, 3, 5, 7, and 9 wt.%) with PVDF matrix to fabricate low-cost composite films using solvent casting route for mechanical energy harvesting purposes. Sec.6.3 explores characterization techniques and tests used after composite fabrication. Sec.6.4 provides a comprehensive discussion of the results obtained from the characterization tests conducted. Out of the prepared samples, PVDF with 5

wt.% BMP showed maximum electroactive phase content (82%), tensile strength (34.23 MPa), and piezoelectric voltage (6.5 V) amongst the untreated samples. PVDF with 5 wt.% BMP is then subjected to NaOH treatment for further enhancement in overall performance. PVDF with 5 wt.% treated BMP showed 467% increment in output voltage and 235% increment in output current as compared to pure PVDF. Sec.6.5 investigates the potential of the treated BMP-PVDF-based composite as an impact sensor. The piezoelectric output voltage of PVDF with 5 wt.% treated BMP is then measured under impact loading conditions to determine its suitability as an impact sensor. A bamboo-based piezoelectric impact sensor that is highly sensitive and cost-effective opens enormous possibilities for sustainability and circular economies.

6.2 EXPERIMENTAL

6.2.1 Materials

PVDF powder (M_w of 5,34,000 by GPC), and DMF (anhydrous, 99.8%) solvent are purchased from Sigma Aldrich, USA. BMP is a iste product produced after the cutting and shaping of bamboo. With the aid of a powerful magnet, bamboo particles are further screened. As a result of this process, small iron particles are removed from the bamboo dust. The main challenge is to extract minute non-ferrous metal pieces, soil particles, and grease. The removal of these types of materials is accomplished through a multi-step cleaning procedure, beginning with multiple washes with water and acetone and finishing with a magnetic stirring. After washing, the sample is dried in the hot furnace for 8 hours at 60 °C. The ball milling process is performed after drying for 30 minutes followed by the sieving process in descending (from 300 to 25 µm sieve size) order for obtaining the desired dimensions.

6.2.2 BMP synthesis and its chemical treatment

Natural fibers have very poor interfacial properties. The bonding between PVDF matrix and bamboo particles is improved by alkaline treatment. Bamboo particles are subjected to NaOH treatment which removed hemicellulose, lignin, fat, and wax content from their surface followed by depolymerization of lignocellulose [142, 143]. The process of transforming bamboo biomass

to usable bamboo microparticles is schematically presented in Fig. 6.1. Mechanical properties of bamboo particles are enhanced due to depolymerization process. PVDF with 5 wt.% of BMP is selected for chemical treatment as it showed maximum mechanical, thermal, and piezoelectric properties. The treated and untreated composite films with the same filler concentration are then compared. For the chemical treatment, 6 wt.% aqueous solution is taken in a beaker and subjected to magnetic stirring at 48 °C for about 8 hours with 800 rpm. In the next step, acetone is used to wash the obtained solution, followed by distilled water until it reached a pH value of 7. After being treated, the bamboo particles are dried in a muffle furnace at 60 °C for about 6 hours. Through a two-step reaction process, sodium (Na) is implanted into bamboo particles. In the first step, NaOH is ionized into Na^+ and OH^- ions due to the polarity of H_2O molecules. In the second step, a nucleophilic reaction may allow Na cations to graft to cellulose by forming a covalent bond. Na ions and lower weight polymers are removed from bamboo particles through multiple washings with H_2O [144–146].

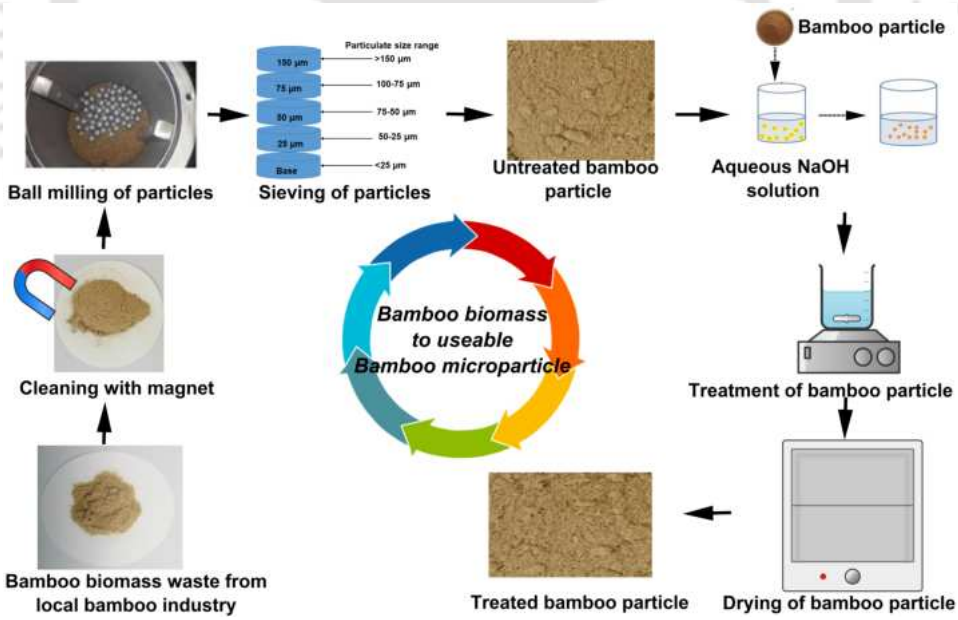

Fig. 6.1: Flow diagram of BMP recycling, processing, and its chemical treatment.

6.2.3 Characterization of BMP

BMP particle size and its morphology are two important factors deciding mechanical and thermal properties of its composites. Through NaOH treatment, the surface roughness of particles is

increased, thereby improving the interfacial bond between the filler and the matrix. BMP particles are reduced in size after chemical treatment (see Fig. 6.2a-b). It is discovered that the average particle diameter of untreated particles is 27.45 µm, compared to 18.35 µm for treated particles. XRD plots of untreated and treated BMP are presented in Fig. 6.2c. A total of 3 peaks are observed (two broad and one sharp) at 2θ values of 15.88°, 22.32°, and 34.79°, corresponding to crystal planes of (1 1 0), (0 0 2) and (0 4 0) respectively [147, 148]. The occurrence of these mentioned peaks indicates presence of native cellulose in the BMP. Further, crystallinity index (CI) of the BMP is calculated using equation 6.1:

$$CI(\%) = \frac{A_C}{A_C + A_A} \times 100 \tag{6.1}$$

where A_A is amorphous region area, and A_C is crystalline region area under XRD plot. Untreated BMP has been found to have a crystallinity of about 60.041%, whereas treated BMP has a crystallinity of 76.78%. After the crystallinity calculations, average crystalline size (D) of the BMP has been calculated using Debye-Scherrer formula as given below in equation 6.2:

$$D = \frac{k\lambda}{\gamma \cos\theta} \tag{6.2}$$

where k,λ, γ, and θ are Scherrer's constant, wavelength of incident radiation, FWHM, and Bragg's angle respectively. Average crystalline size for untreated and treated samples is found to be 2.489 nm and 2.806 nm respectively. FTIR spectra for untreated and treated BMP are presented in Fig6.2d. Some peaks change in intensity after chemical treatment, while others vanish altogether. NaOH treatment of BMP results in a reduction in lignin and hemicellulose content. The detailed information regarding peak assignment and its location for treated and untreated particles is given in Table 6.1.

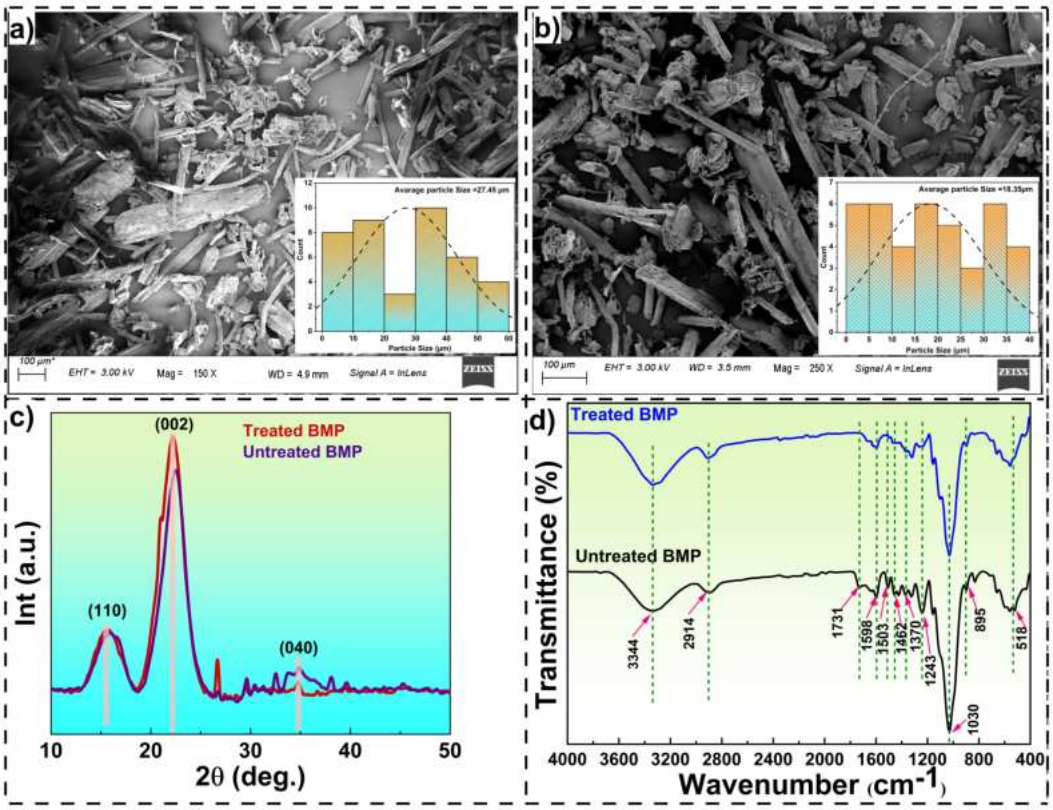

Fig. 6.2: FESEM images of a) untreated and b) treated BMP, XRD plot of c) untreated and treated BMP, FTIR spectra of d) untreated and treated BMP.

Table 6.1: Transmittance band assignment in FTIR plot.

Wavenumber (cm^{-1})	Assignment	References	Untreated	Treated
3344	Stretching vibration of O-H groups present in lignin, Cellulose, and hemicellulose	[149]	P	P
2914	Stretching vibration of C-H group of lignin and cellulose	[150]	P	P
1731	Stretching vibrations of C=O group of hemicellulose	[150]	P	A
1643	Water absorption	[151]	P	A
1598	C=C bond vibrations of aromatic lignin group	[152]	P	P (small)
1503	Vibration of C-O bond of lignin	[153]	P	A
1462	C-H and C-O bond stretching and bending vibration of lignin	[154]	P	A
1419	Bending vibration of $-CH_2$ group of lignin	[155]	P	A
1370	C-H_2 bending vibrations of hemicellulose	[154]	P	A
1320	C-H group bending vibrations of cellulose	[155]	P	P
1243	C=O bond stretching vibrations present in lignin and extractive	[156]	P	A
1030	C-O/C-C bond stretching vibration of cellulose	[153]	P	P
895	C-H group bending vibrations of cellulose	[157]	P	P
662	O-H group vibrations of cellulose	[154]	P	P
566	p-hydroxyphenyl of propene in lignin vibrations	[157]	P	P (small)

6.2.4 Preparation of PVDF-BMP bio-composites

PVDF-BMP composites are synthesized using solvent casting process. 2 g of PVDF powder is weighed on weighing balance machine and then added to 10 ml of DMF solvent. The resulting mixture is then subjected to magnetic stirring on a hot plate for short span (about 15 minutes) to get uniformly dissolved PVDF solution. Then, different weighed quantities (1, 3, 5, 7, and 9 wt.%) of BMP are added into obtained solution followed by continuous magnetic stirring for 4 hours at 65 °C. Once the uniform PVDF-BMP solution is obtained, it is placed in vacuum desiccator to remove any bubbles present in the solution. The desiccation process is carried out for about 1 hour. Once the bubbles are removed completely, the resulting solution is cast on glass petri dish and kept in furnace for drying for about 12 hours at 60 °C. The resulting free standing PVDF-BMP composite films are then kept in desiccator for about 48 hours for complete removal of moisture. Once the films are completely dried, they are placed between two steel dies and are subjected to annealing for 1 hour at 120 °C. The compressed annealing helps in reducing porosity thereby making the sample dense which is essential for electric poling process as it prevents any spark generation and sample failure. The step-by-step fabrication process of composites is presented in Fig. 6.3. The fabricated composite samples are given following names for the convenience- PV (neat PVDF), 1BPV (PVDF-1 wt.% BMP), 3BPV (PVDF-3 wt.% BMP), 5BPV (PVDF-5 wt.% BMP), 7BPV (PVDF-7 wt.% BMP), 9BPV (PVDF-9 wt.% BMP) and 5BPVT (PVDF-5 wt.% treated BMP). The required quantities of BMP particles are calculated using equation 6.3. The weighted quantities of BMP in PVDF matrix are listed in Table 6.2.

$$\text{wt. of BMP } (\%) = \frac{W_{BF}}{W_{BF} + W_{PVDF}} \tag{6.3}$$

6.3 CHARACTERIZATION

Structural analysis of PVDF-BMP composite films is carried out using XRD (Smartlab, Rigaku Technologies, Japan) using CU-kα rays for the 2θ span of 10-60° with step size of 4° /min. The surface morphology study is performed using FESEM (Gemini 500, ZEISS). FTIR spectroscopy

Table 6.2: Composition details of filler and matrix materials.

Sample name	Weight of PVDF (g)	Weight of BMP (g)	DMF volume (mL)
PV	2	-	10
1BPV	2	0.02	10
3BPV	2	0.06	10
5BPV	2	0.1	10
7BPV	2	0.15	10
9BPV	2	0.19	10
5BPVT	2	0.1	10

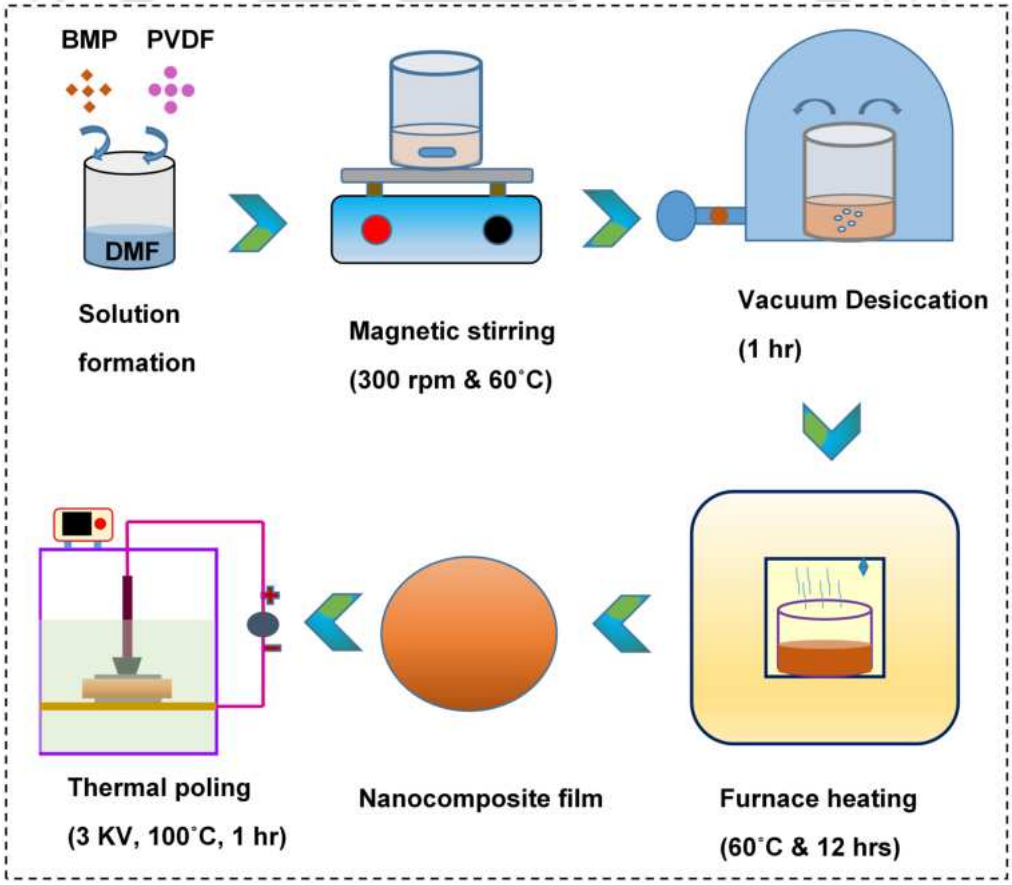

Fig. 6.3: Fabrication process of BMP composites through solvent casting route.

(PerkinElmer, Singapore) is recorded in the range of 400-1700 cm^{-1} with ATR mode. Thermal stability of the composites is studied using TGA instrument (TGA 4000, PerkinElmer) in the temperature of 20-600 °C with heating rate of 10°/min. Tensile strength of PVDF-BMP composites

is calculated using 100 kN UTM machine (dynamic 8801, Instron) with a velocity of 1mm/min. Samples for UTM are prepared according to ASTM D 882 standard. Micro-hardness values of composite films are obtained using hardness tester (MVH- II, Omni tech). A load of 0.2 kgf with dwell time of 20 seconds. is used for every test sample. Each sample is tested 6 times. Dielectric parameters are measured using LCR meter (IM 3536, Hioki) in the frequency range of 1 KHz to 1 MHz at room temperature. The piezoelectric response of the fabricated PENG device in the form of voltage and current is recorded using DSO (GDS-2102A, GWInSTEK).

6.4 RESULTS AND DISCUSSION

6.4.1 XRD analysis

XRD analysis is particularly performed to study effect of bamboo reinforcement on β phase of PVDF. A total of seven samples are considered for XRD testing. The peaks at 18.23° and 20.23° confirm the presence of α (020) and β (200) phases respectively. Electroactive β phase is essential for piezo response of PVDF matrix [158]. It can be observed from Fig. 6.4 that, β phase intensity increases up to 5 wt.% of BMP reinforcement followed by reduction at higher loading. It is observed that, 5BPV sample after undergoing chemical treatment further enhanced the intensity of electroactive β phase. Amongst the available samples, 5BPVT displayed maximum intensity of β phase. The β phase increment results in enhancement in piezo response of PVDF [104]. The XRD results confirm the maximum piezoresponse of sample 5BPVT.

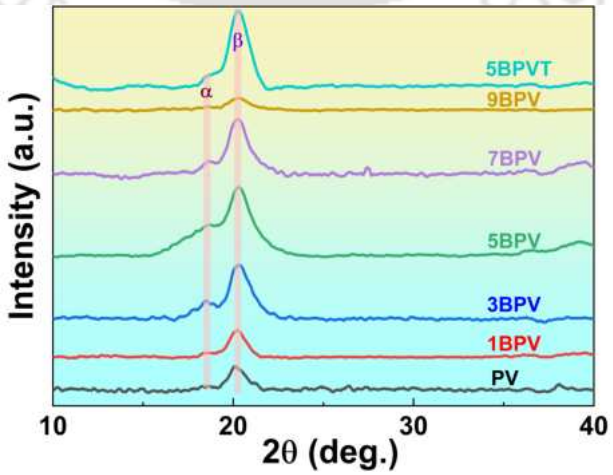

Fig. 6.4: XRD plot of PVDF and BMP based composites.

6.4.2 FESEM

Uniform dispersion of filler materials into the polymer matrix is important parameter in assessing the quality of composite. The surface morphology along with filler dispersion is investigated using FESEM results as presented in Fig. 6.5. A uniform grain structure of neat PVDF film is shown in Fig. 6.5a. It is found that BMP are uniformly dispersed (as shown in dotted light green colored rectangles) in PVDF matrix up to 5 wt.%, which ensures successful fabrication of composite. It is observed that, above 5% reinforcement, BMP starts agglomerating inside PVDF matrix, as shown in the light green colored dotted circles in Fig. 6.5e-f.

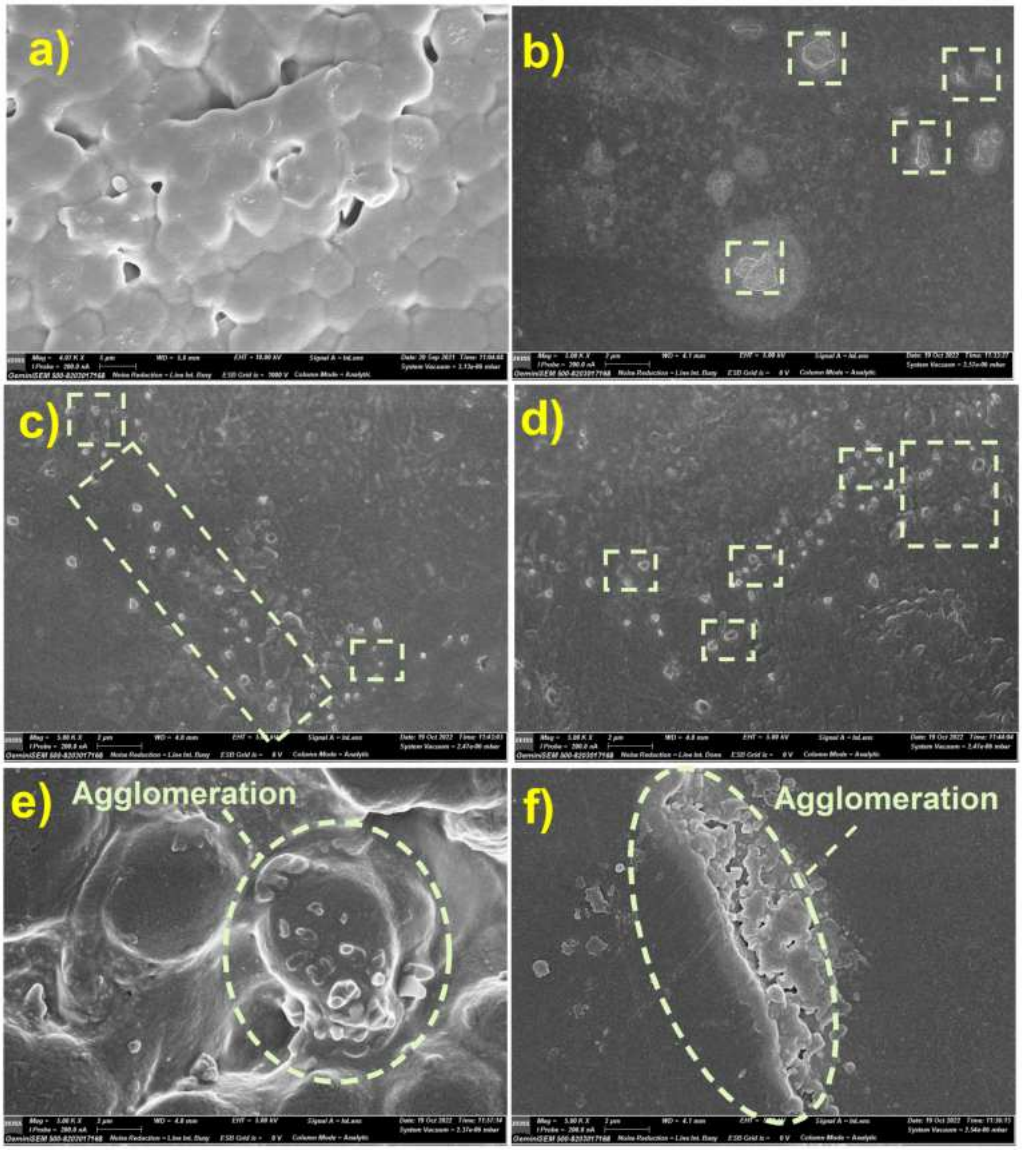

Fig. 6.5: FESEM images of a) PV, b) 1BPV, c) 3BPV, d) 5BPV, e) 7BPV, and f) 9BPV.

6.4.3 FTIR

FTIR analysis is performed to identify the different crystal phases of PVDF and its content (particularly β phase). Peaks corresponding to wavenumbers of 841 (CH_2 rocking), 1288 (Trans band) and 1400 (CH_2) cm^{-1} corresponds to electroactive β phase of PVDF matrix [89], whereas peaks at 614 and 763 cm^{-1} corresponds to α phase of PVDF, as presented in Fig. 6.6a. It is observed that BMP reinforcement has a positive impact on enhancing piezo response of PVDF matrix up to certain loading amount, by enhancing the overall electroactive phase content. However, at reinforcement above 5 wt.%, β phase content reduced, which may be due to filler-matrix aggregation. 5BPVT showed maximum β phase fraction of 86% among all the samples. This is due to chemical treatment of BMP. The values of electroactive phase content for composite with varying BMP concentration are presented in Fig. 6.6b.

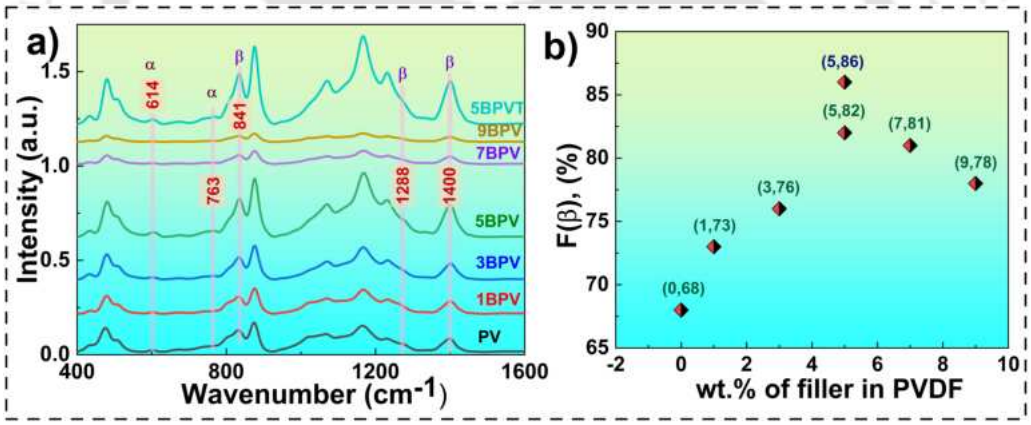

Fig. 6.6: FTIR spectra of a) PVDF-BMP composites, b) β phase variation concerning BMP filler content of composite samples.

6.4.4 TGA analysis

TGA analysis is used to examine the effect of reinforcement of treated and untreated BMP on PVDF's thermal stability as shown in Fig. 6.7. PVDF displayed endothermic melting at 150 °C followed by sudden exothermic/endothermic decomposition at 422 °C[159]. Six composite samples are analyzed to study thermal performance. Untreated BMP addition leads to an increment in decomposition temperature (T_{onset}) values, followed by a reduction when loading content exceeds 5 wt.%. sample 5BPVT showed maximum TT_{onset} of 488 °C, which is 16% higher than pure PVDF.

A similar trend can be seen in variation of residual mass (m_r) over changing BMP content. Sample 5BPVT showed maximum m_r value of 25.7%. The increased thermal stability of treated BMP composites is associated with covalent bonding of Na^+ ions with BMP. Through graft copolymerization, the hydroxyl group and other hydrophilic functional groups of treated filler are replaced by Na grafted ionic groups, improving thermal stability [160]. Due to the chemical treatment of BMP, cellulose-I has been converted to cellulose-II which is more thermally stable with better crystalline structure [150, 161, 162]. Thus, 5BPVT exhibits better thermal stability with lower mass loss at elevated temperatures. However, above 5 wt. % of BMP loading, considerable reduction in thermal degradation temperature and residual mass takes place. This can be attributed to poor interfacial bonding due to agglomeration of BMP particles into the PVDF matrix. The thermal decomposition temperature and residual mass values for pure PVDF and composite films are presented in Table 6.3.

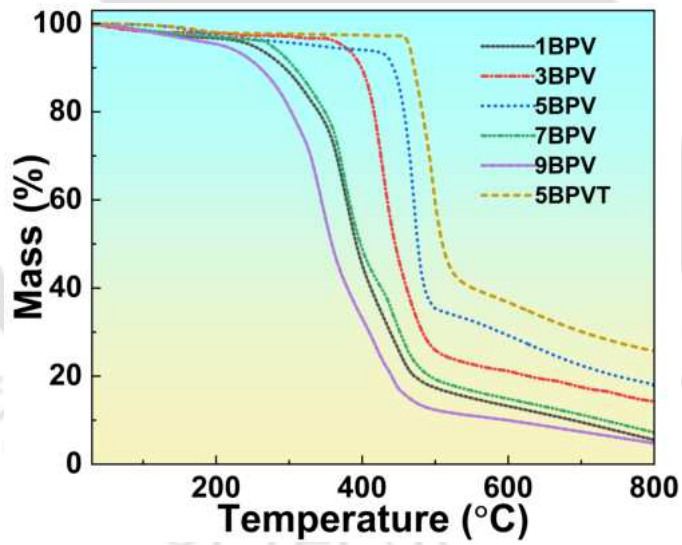

Fig. 6.7: TGA plots of composite samples.

6.4.5 UTM testing

The Young's modulus and tensile strength of composite films are calculated as presented in Fig. 6.8a. Points 1, 2, 3, 4, 5, 6, and 7 in Fig. 6.8b represent samples PV, 1BPV, 3BPV, 5BPV, 7BPV, 9BPV, and 5BPVT respectively. BMP reinforcement enhanced the Young's modulus and tensile strength of composites. The increment in mechanical properties is caused by the interac-

Table 6.3: List of TGA parameters for composite samples.

Sample	T_{onset} (°C)	m_r (%)
1BPV	431	8.9
3BPV	436	14.5
5BPV	474	18.6
7BPV	270	7.2
9BPV	232	4.8
5BPVT	488	25.7

tion between BMP and PVDF matrix, leading to an overall increase in strength of composites. Samples PV, 1BPV, 3BPV, 5BPV, 7BPV, and 9BPV, and 5BPVT displayed Young's modulus of 687.85±30.25, 731.2±35.43, 914.19±39.23, 883.52±46.67, 775.21±53.67, and 1071.47±41.23 MPa respectively. Sample 5BPV exhibited the highest tensile strength and Young's modulus among the untreated samples. It is likely that up to 5 wt.% of BMP loading, loaded bamboo particles inside PVDF matrix interrupt the crack growth propagation causing restriction to crack flow. In turn, this leads to improved mechanical strength [152]. BMP starts agglomerating inside the PVDF matrix

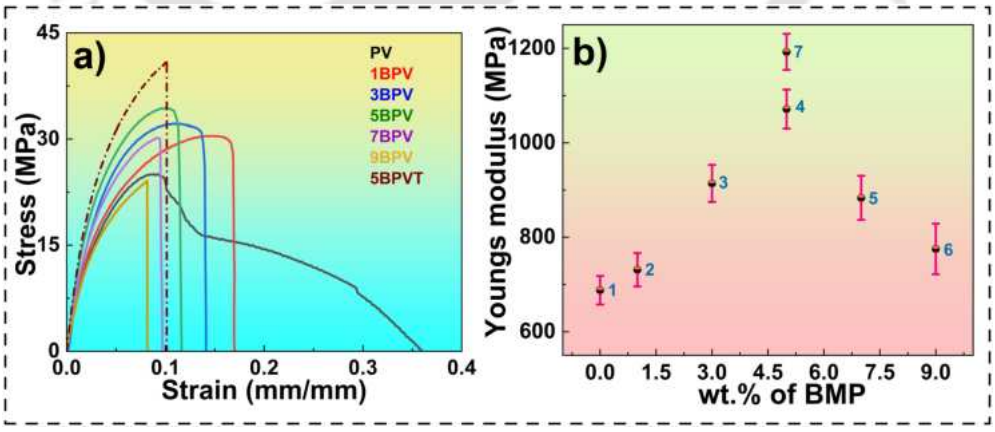

Fig. 6.8: a) Stress vs strain plot for pure PVDF and composite samples, b) variation of Young's modulus for test samples over BMP content.

when the loading quantity exceeds 5 wt.%, resulting in a drastic reduction in mechanical performance. Agglomerated particles tend to generate flaws and defects, which lead to stresses building

up inside composite materials causing reduction in Young's modulus and tensile strength [163]. Sample 5BPVT showed enhanced tensile strength and Young's modulus as compared to 5BPV. A 17% increment in tensile strength is observed for sample 5BPVT over 5BPV when NaOH-treated BMP are added to the PVDF matrix. Higher fraction of cellulose phase in the treated bamboo particles imparts higher tensile strength [164]. Furthermore, adding treated BMP to PVDF matrix increases the roughness of the composite films, improving bonding between filler and matrix materials and boosting mechanical strength.

6.4.6 Dielectric measurement

Dielectric properties of the fabricated composites over frequency range are presented in Fig. 6.9. BMP addition showed significant enhancement in dielectric constant values of PVDF matrix as shown in Fig. 6.9a. This increment is due to increase in number of space charge carriers at lower frequency values due to particle addition. Additionally, increased dipole-dipole interaction enhances the overall dielectric constant values. In lower frequency zone, value of dielectric constant is on higher side due to effect of various types of polarization mechanisms. But, as the frequency increases further, its value goes on reducing due to inability of electric dipoles to get aligned due to rapidly changing electric field [165]. The values of dielectric loss also increased on BMP addition as presented in Fig. 6.9b. The dielectric constant of sample 5BPVT is higher than that of sample 5BPV, however it is lower than that of sample 9BPV. The dielectric constant values are tabulated in Table 6.4.

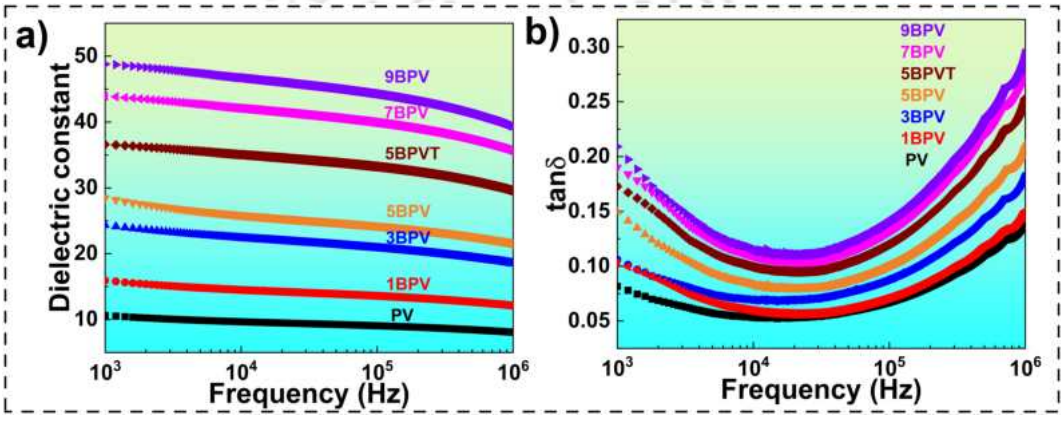

Fig. 6.9: a) Dielectric constant and b) dielectric loss of composite films.

Table 6.4: Dielectric constant values of PVDF based hybrid nanocomposites.

Sample name	ϵ
PV	10
1BPV	16
3BPV	24
5BPV	28
5BPVT	38
7BPV	45
10BPV	49

6.4.7 Energy harvesting performance

Before preparing the PENG devices to check its energy harvesting capabilities, the fabricated films of size 2.5 cm × 2.5 cm (see Fig. 6.10a) are subjected to thermal poling using DC power supply setup (50 kV, 5 mA, Ujwal Electronics). Poling process is performed in silicon oil to prevent electric arcing. A voltage of up to 3 kV is supplied in a step-wise manner for a total duration of 90 minutes. The poled sample is then covered on top and bottom side using PET tape to protect it from environmental noise and damage. Energy harvesting behaviour is assessed using manual palm tapping on the PENG device using hand. A fabricated PENG device for piezoelectric test is shown in Fig. 6.10b. Piezoelectric voltage and current are increased up to 5 wt.% of untreated BMP reinforcement and then are reduced at higher loadings as presented in Fig. 6.10c-d. Pure PVDF showed a voltage of 1.6 V and a current of 0.65 μA, whereas a PENG made up of 5BPV showed a voltage of 6.5 V and a current of 1.81 μA. A 300% increase in output voltage is observed for 5BPV samples compared to pure PVDF samples. The maximum voltage and current of 7.2 V and 2.18 μA are observed in sample 5BPVT due to the improved chemical bonding between BMP and the PVDF matrix. Additionally, NaOH treatment results in an enhanced fraction of cellulose β phase, thus increasing the piezo output voltage [154]. Thermal poling enhances the β phase of PVDF by maximizing the electric dipole alignment which is essential for piezoelectric behaviour.

BMP addition significantly enhances the piezo voltage and current values as compared to pure PVDF sample. O/p voltage and current values for the composite films are shown in Table 6.5. The comparison between fabricated PENG device and existing nanogenerators in the literature is shown in Table 6.6.

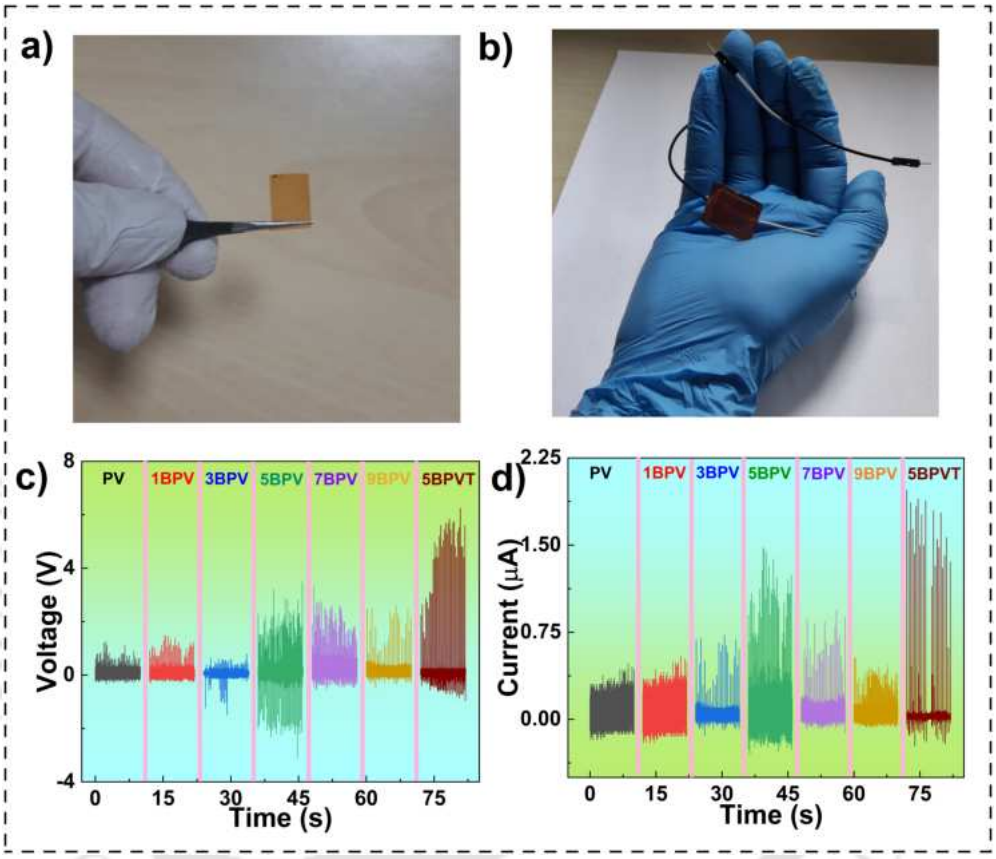

Fig. 6.10: a) Nanocomposite film used for PENG fabrication, b) PENG device used for piezo testing, c) Piezo voltage, d) current signals for BMP-PVDF composites.

6.5 COMPOSITES AS AN IMPACT SENSOR

An impact refers to a sudden application of force or shock within a brief timeframe. Impact sensors play a crucial role in structural health monitoring, ensuring integrity, quality control, and conducting failure analysis across various industries including aerospace, automotive, and process control. Impact sensors find common application in scenarios requiring monitoring of sudden motion changes or impacts, including automotive airbag systems, sports equipment, and industrial machinery. They operate by transforming mechanical force or acceleration into an electrical signal, which subsequently undergoes analysis to ascertain the impact's intensity, duration, and direction.

Table 6.5: Voltage and current values for composite films.

Sample	Voltage (V)	Current (μA)
PV	1.6	0.65
1BPV	1.73	0.75
3BPV	2.26	0.86
5BPV	6.5	1.81
7BPV	3.85	1.04
9BPV	3.1	0.58
5BPVT	7.2	2.18

Table 6.6: Comparison of piezoelectric performance of PVDF/BMP composite based PENG with existing nanogenerator devices in literature.

Material	Fabrication technique	V_{pp} (V)	Reference
PVDF/Cellulose	Electrospinning	6.3	[166]
Seagrass	Spray coating	288	[71]
Wood sponge	Delignification	0.7	[74]
Wood/ZnO	Hydrothermal growth of ZnO on delignified wood	1.5	[167]
Fish scale	Recycling with chemical treatment	4	[81]
PVDF/Coconut husk	Solvent casting	14	[75]
PVDF/cellulose	Electrospinning	3.5	[168]
PVDF/BMP	Solvent casting	7.2	**This work**

The damages inflicted by impact forces on composite structures, such as delaminations, are nearly impossible to detect through visual inspection alone. Consequently, this leads to substantial compromises in structural integrity and reliability. In recent times, various techniques have emerged for measuring impact forces, including optical fiber sensor systems [169], mechanoluminescence sensing [170], broadband wave-based acoustic sensors [171], and inertial mass coupled with a digitizer [172]. However, these methods necessitate advanced instrumentation, expert personnel, and

specialized setups, rendering them costly and somewhat inflexible. Polymer based piezoelectric thin films have garnered significant attention due to their outstanding properties, low fabrication cost, and numerous potential applications in sensor development. PVDF-BMP composite based PENG device is assessed for piezoresponse upon various impact loading conditions.

6.5.1 Experimental setup and formulation for Impact sensing

The 5BPVT sample is selected for impact sensor testing as it showed excellent mechanical properties with maximum piezoelectric response. A lab-made setup is developed to assess the effect of impact loading on test sample. For a better understanding, actual image and schematic representation of test setup is shown in Fig. 6.11. A piezoelectric sensor made of 5BPVT is fixed on a metallic base of a stand with sticky tape. Sensor wires are connected to DSO through the connecting probe. Weights of 5g (0.0221N), 10g (0.0443N), 15g (0.0687N), 20g (0.0781N) and 25g (0.1186N) are dropped through the top of hollow circular tube on test samples to check the impact loading response. Each load is tested for impact behavior 25 times. The dropping height is kept constant (9 cm) for all the readings. After collision, the initial potential energy will be transformed into kinetic energy.

$$mgH = \frac{1}{2}mv_{imp}^2 \tag{6.4}$$

where m = mass of the dead weight, H = drop height, g = acceleration due to gravity, and v_{imp} = velocity at impact. For ease of analysis, we have neglected air resistance to the dropping weights. On solving equation 6.4 further, v_{imp} is given by

$$v_{\text{imp}} = \sqrt{2gH} \tag{6.5}$$

Using work-energy principle, the net work done during impact is calculated as per equation 6.5:

$$W_{\text{net}} = \frac{1}{2}m\left[v_{\text{final}}^2 - v_{\text{initial}}^2\right] \tag{6.6}$$

v_{initial} will be zero and v_{final}= v_{imp} So, net work done will be equal to kinetic energy. At the end, the magnitude of impact force (F_{imp}) is calculated using equation 6.7:

$$F_{imp} = \frac{W_{net}}{h} = \frac{\frac{1}{2}mv_{imp}^2}{h} \tag{6.7}$$

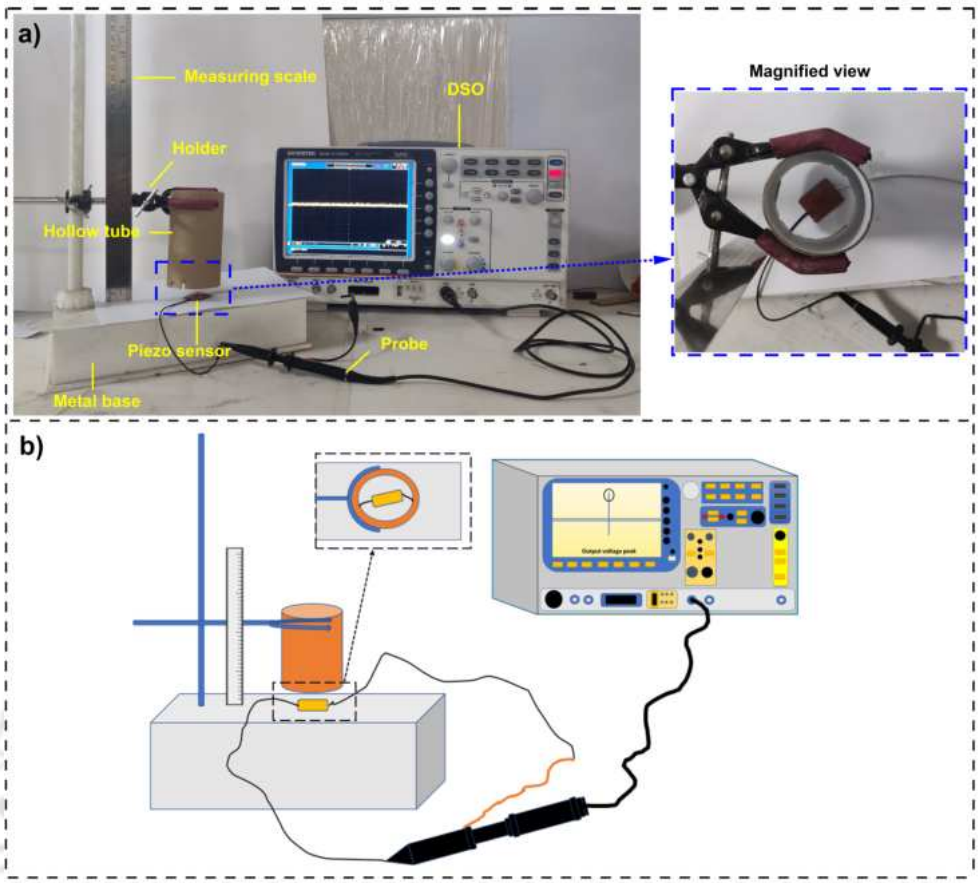

Fig. 6.11: a) Actual image of in house developed experimental setup for impact testing operation, b) Schematic diagram of the experimental setup.

The o/p voltage recorded by DSO on impact of test loads is shown in Fig. 6.12. Despite each test load being examined for impact loading 25 times, only one impact is shown here for each test load for the matter of convenience. The sharp voltage peaks in Fig. 6.12a-e (as shown in pink dotted circles) are the outcome of impacts by the test loads on the sensing area. The impact load is primarily determined by the mass of the test loads. The sensing area vibrates when test loads impact the sample. Vibrations result in the deformation of the composite film, resulting in a potential difference due to the piezoelectric effect. As a result, electrons flow between the top and bottom electrodes, generating a voltage signal. From the plots, it can be concluded that as the weight of the test load increases, the peak-to-peak value of the o/p voltage V_{pp} signal also increases. It can be attributed to increased vibration of the piezo sensing element caused by higher loads, resulting in higher strain generation, thus enhancing o/p voltage [173]. For each test load, the o/p voltages recorded showed variations. So, the obtained results are statistically analyzed

with the help of Weibull distribution model using Minitab 17 (student version) software. Equation 6.8 represents Weibull distribution model for impact testing analysis of composite sensor.

$$F_x = 1 - e^{-\left(\frac{x}{\eta}\right)^m} \tag{6.8}$$

where F_x is a failure probability for any continuous random variable x in any cumulative distribution function (CDF), η and m are scale and shape parameters respectively. The Weibull distribution

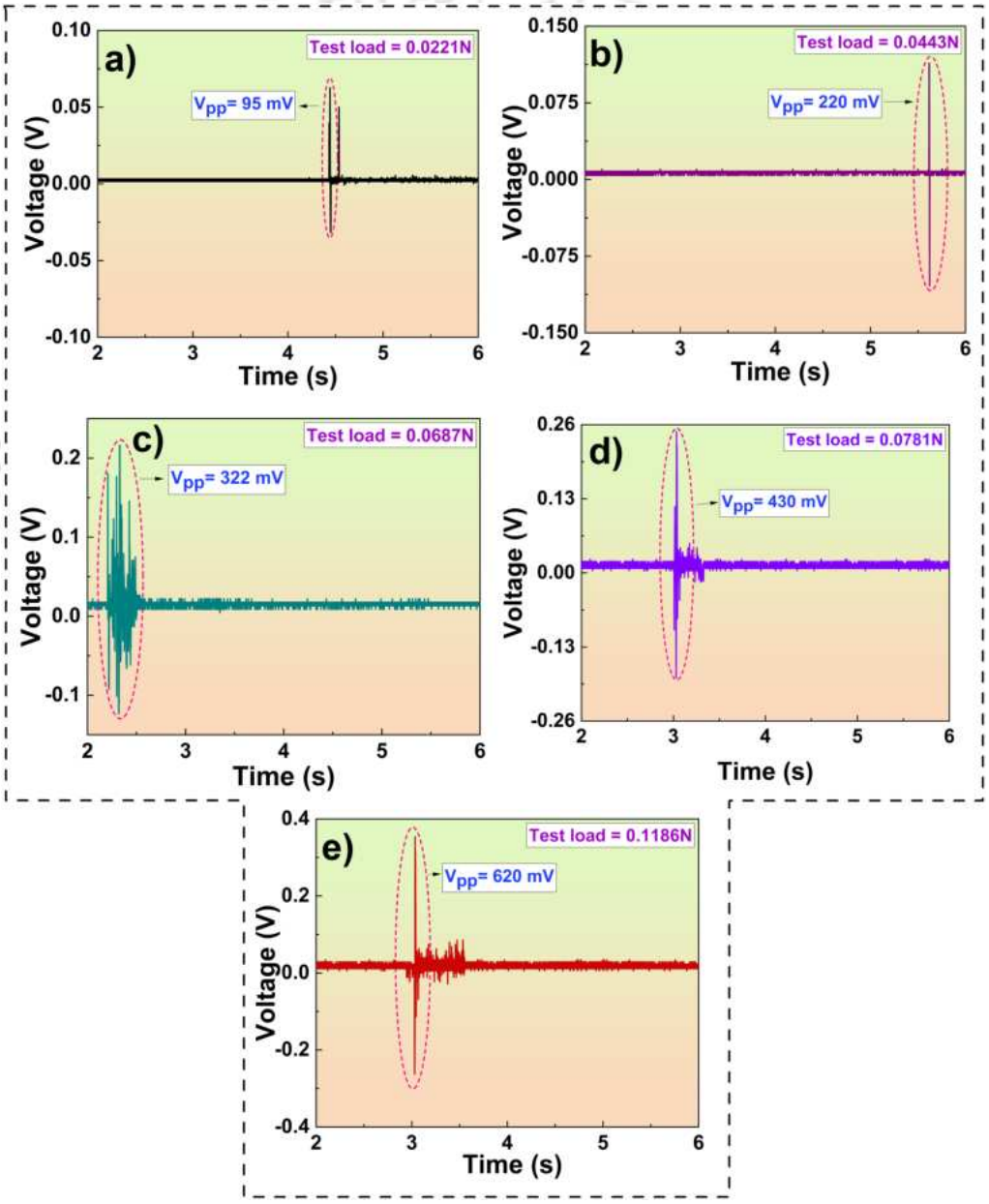

Fig. 6.12: O/p voltage peaks generated due to impact of test loads- a) 0.0221N, b) 0.0443N, c) 0.068N, d) 0.0781N, and e) 0.1186N.

results regarding output voltage of 5BPVT sample for different impact loading conditions is pre-

sented in Fig. 6.13. η and m are calculated using least square elimination technique (LS). The Weibull distribution shows a superior correlation with a correlation factor R^2 value in the range of 0.914–0.983 for various loading conditions. Furthermore, the investigative data is distributed evenly along the line and is correctly fitted. A good linear behaviour is observed between voltage obtained in response to impact loads for different loading conditions. A linear relationship function is obtained by fitting experimentally obtained points (R^2=0.978) as shown below in equation 6.9:

$$y = 5288x + 1.36 \tag{6.9}$$

where, y is voltage generated (mV) and x is impact load (N) acted on sensor. This shows that the fabricated sensor responds well to various impact loads with a sensitivity value of 5288 mV/N. The highly sensitive sensors developed can be utilized in applications requiring precise impact detection, such as structural health monitoring, smart packaging, and wearable devices for sports and healthcare. An impact sensor with the recorded sensitivity could be critical in scenarios where the accurate detection of minute impacts is necessary.

6.6 SUMMARY

This chapter is dedicated to the experimental investigation of sustainable composites reinforced with BMP in a PVDF matrix. Residual BMP sourced from local industries undergoes a thorough cleaning process and is utilized as a potential filler to augment the overall performance of PVDF. The BMP particles are treated with NaOH to enhance their bonding with PVDF. It is noted that composites containing treated BMP exhibit superior mechanical and dielectric performance in comparison to those with untreated BMP. Moreover, BMP particles increased thermal stability of PVDF matrix. The increased thermal stability of treated BMP composites is associated with covalent bonding of Na^+ ions with BMP. Through graft co-polymerization, the hydroxyl group and other hydrophilic functional groups of treated filler are replaced by Na grafted ionic groups, improving thermal stability. The incorporation of BMP improved the Young's modulus and tensile strength of the composites. This enhancement in mechanical properties stems from the interaction between BMP and the PVDF matrix, resulting in an overall strengthening effect on the composites.

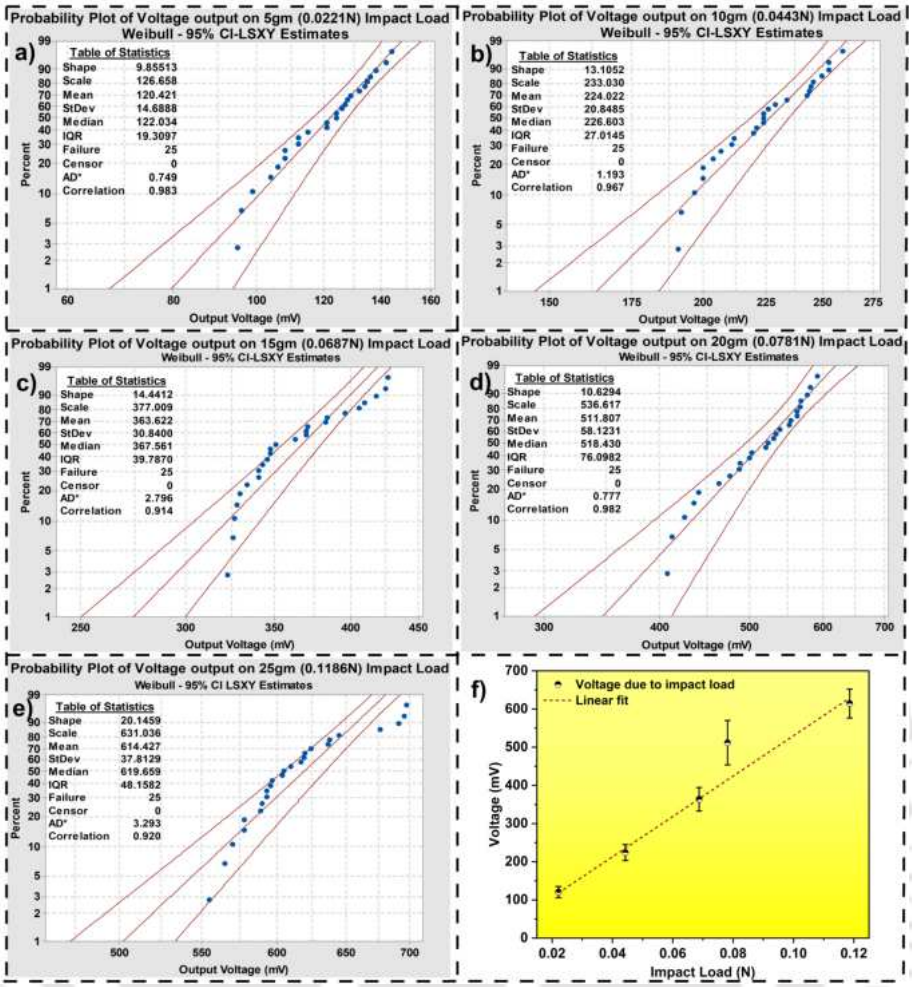

Fig. 6.13: Weibull distribution plot for different impact loading conditions a) 0.0221N, b) 0.0443N, c) 0.0687N, d) 0.0781N, e) 0.1186N, o/p voltage behaviour with respect to impact load (Linear fit).

It is probable that the incorporation of up to 5 wt.% of BMP loading, where bamboo particles are embedded within the PVDF matrix, hinders the propagation of crack growth, thereby restricting crack flow. Consequently, this contributes to enhanced mechanical strength. An increase of 17% in tensile strength is noted for sample 5BPVT compared to 5BPV when NaOH-treated BMP is incorporated into the PVDF matrix. The higher proportion of the cellulose phase in the treated BMP contributes to this elevated tensile strength. The enhanced hardness values upon addition of BMP into PVDF can be ascribed to the increased localized plastic strength and resistance to plastic deformation. However, a decrease in hardness values was noted at higher loadings, potentially stemming from inadequate bonding and the agglomeration of fillers within the PVDF matrix. The composite incorporating treated BMP is then employed to evaluate the voltage generation in

response to varying impact loads. The output voltage data, recorded in response to diverse impact loads, is subjected to statistical analysis using the Weibull distribution to calculate the sensitivity of the composite. Exhibiting an outstanding output voltage response across diverse applied impact loads, it demonstrated a sensitivity of 5288 mV/N. A highly responsive impact sensor of this caliber holds great potential for commercial applications. The findings of this research affirm the promising utility of PVDF-bamboo composites in the realms of sustainable energy harvesting and sensing applications.

Chapter 7

Piezoelectric performance assessment of fish scale based nanogenerators

7.1 INTRODUCTION

Energy scavenging from the living environment is an effective solution for developing battery-less self-powered sensors or nanogenerators. Researchers have been looking for sustainable and clean energy sources due to adverse effect of fossil fuels on environment. Chapter 7 delves into the use of PENGs made from leftover FS, emphasizing sustainable and eco-friendly materials derived from waste. This approach aligns with the broader goal of advancing environmentally friendly technologies. The selection of FS as a filler material is driven by its natural abundance, cost-effectiveness, and inherent piezoelectric properties, making it a promising option for PENG development. Many developing countries are looking for ways to create resources by recycling waste materials to reduce their environmental impact. Leftover fish scales (FS) in varying quantities (5, l0, 15, and 20 wt.%) are reinforced into a PVDF matrix to develop highly flexible PENGs to gauge their energy-harvesting capability. Sec.7.2 discusses preparation and characterization of FS particles. FS are processed before reinforcing them into PVDF matrix. Crystal structure and morphology of processed FS particles are then studied through FTIR, FESEM and XRD. After the FS particle characterization, PVDF-FS composite fabrication process is extensively discussed in this section. In sec.7.3, morphological, and structural characterization studies are discussed. Moreover, the different tests are also mentioned to assess the performance of PVDF-FS composites. Sec.7.4 describes the results of the various characterizations and test performed on FS based composites. Sample with 10% FS loading showed maximum values of UTS (37 MPa) and E (1192 MPa) respectively.

A 56% and 67% enhancement in ultimate tensile strength and Young's modulus values over pure PVDF matrix is recorded. PENGs are checked for their piezo response under various loading conditions using a human hand (finger tapping, palm tapping, film twisting, and wrist pressing). In sec.7.5, the potential of the PVDF-FS bio-composite as an impact sensor is examined. The device with maximum piezo response is assessed for potential impact sensing under different loading conditions. Test loads of 5g (0.0221N), 10g (0.0443N), 15g (0.0687N), 20g (0.0781N), and 25g (0.1186N) are released from the top of a hollow circular plastic tube onto the test samples to assess their response to impact loading. The recorded results are analyzed statistically using the Weibull distribution approach to cater to the o/p voltage variations for each test load. The potential for sustainability and circular economies is significantly expanded with a cost-effective, highly sensitive piezoelectric impact sensor fabricated from FS. The piezoelectric voltage generation capability for different PVDF devices is summarized in sec.7.6 At last, concise summary of the work is presented in sec.7.7.

7.2 EXPERIMENTAL

7.2.1 Materials

PVDF powder (molecular weight of 540,000), DMF (anhydrous, 99.8%) solvent are ordered from Sigma Aldrich, USA. Leftover FS are collected from the local hostel mess and canteen.

7.2.2 FS preparation

Leftover FS are subjected to several washings with DI water and NaOH. FS are then dried in an oven at 60 °C for 8 hrs. After complete drying, FS is subjected to ball milling to get it in powder form. To ensure uniform particle size, the FS powder undergoes a sieving process using sieve shaker equipment. Fig. 7.1a provides a comprehensive overview of the FS preparation process, while Fig. 7.1b-d depicts various forms of FS at different stages of its preparation. Varying quantities of these FS powders are then loaded into the PVDF matrix for composite fabrication.

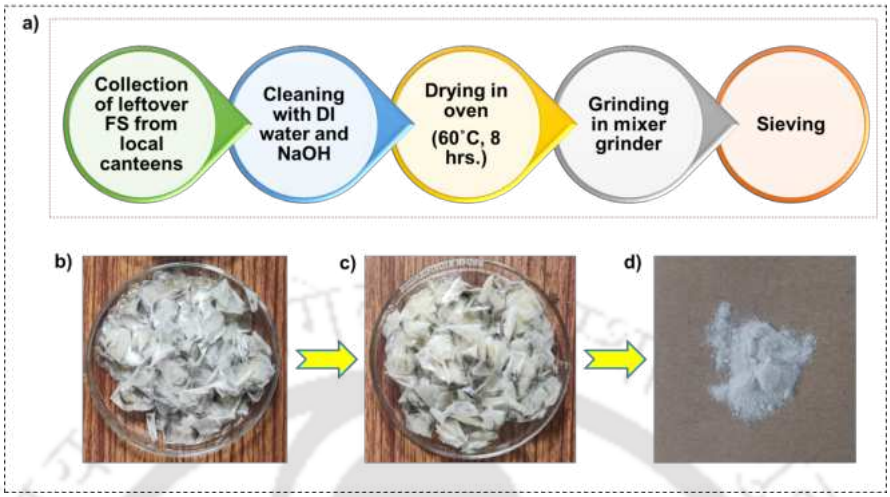

Fig. 7.1: a) FS preparation process, b) FS before treatment, c) FS after treatment, and d) FS in powder form.

7.2.3 Characterization of FS

FESEM image of FS powder is given in Fig. 7.2a. The presence of constituent elements in FS (C, O, Mg, N, P, and Ca) and its overall dispersion inside the FS matrix is given in Fig. 7.2b-c. XRD peaks observed at 28°, 32.4°, 48°, and 47° correspond to FS particles. FTIR of FS confirms the presence of the amide I band at 1633 cm^{-1}, amide II band at 1543 cm^{-1}, and amide III band around 1236 cm^{-1} because of C=O stretching/ hydrogen bonding coupled with COO-, N-H-bending (δ(N-H)) vibrations and N-H-bending (δ(N-H)) coupled with C-N stretching (ν(C-N)) respectively. The absorption peak at 1452 cm^{-1} belongs to CH_2 bending vibrations. In FS, the NH group of the peptide chain is engaged with a hydrogen bond corresponding to the amide A band. Amide B band is associated with vibrational bands observed at 2873 and 2929 cm^{-1} due to symmetrical ($\nu_s(CH_2)$) and CH_2 asymmetrical ($\nu_{as}(CH_2)$) vibrational modes respectively [174–179].

7.2.4 Composite fabrication process

A 2 g of PVDF powder is added to 15 ml of DMF and magnetically stirred (400 rpm, 60 °C) until PVDF is completely soluble in the solvent. A known quantity of FS is then added to 5 ml of DMF in a separate beaker and subjected to stirring for about 15 minutes. for uniform dispersion. Then, both the solutions are mixed and subjected to further stirring at around 60 °C for about 6

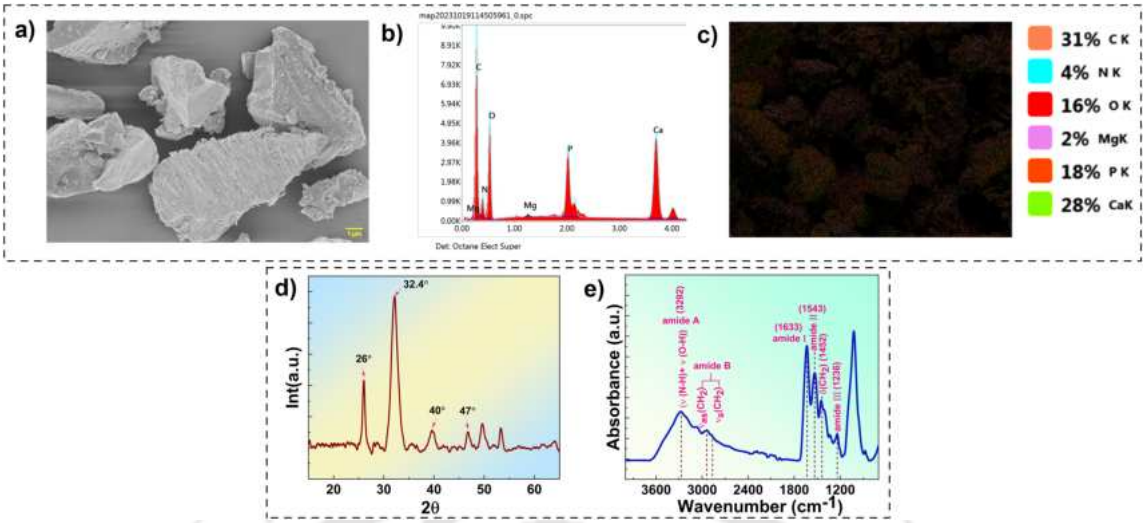

Fig. 7.2: Characterization of FS. a) SEM image, b) Elemental mapping, c) EDS plot with constituent elements, d) XRD plot, and e) FTIR spectra.

hours. The resulting mixture is then subjected to a vacuum desiccation process (45 minutes) to remove trapped air molecules if any to reduce porosity effects. The solution is then poured into a cleaned glass petri dish and kept for drying in a muffle furnace at 65 °C. Upon complete drying, free-standing flexible composite films are obtained. The films are then subjected to thermal poling (3 kV, 100 °C) to enhance their piezo response. For convenience, the composite samples created are designated with the following names: P (neat PVDF), P5FS (PVDF with 5% FS loading), P10FS (PVDF with 10% FS loading), P15FS (PVDF with 15% FS loading), and P20FS (PVDF with 20% FS loading). The schematic of synthesis of FS based composites is given in Fig. 7.3. The wt.% of FS can be obtained with the help of equation 7.1:

$$W_{FS} = \frac{W_{FS}}{W_{FS} + W_{PVDF}} \tag{7.1}$$

Where W_{FS} and W_{PVDF} are weights of FS and PVDF in g respectively. A list of the exact amounts of each mixture ratio is provided in Table 7.1.

7.3 CHARACTERIZATION

The detailed morphological and constitutive elemental study (EDS) of FS and PVDF-FS nanocomposite films is carried out using FESEM (make: Zeiss, model: GeminiSEM 500). Phase identifica-

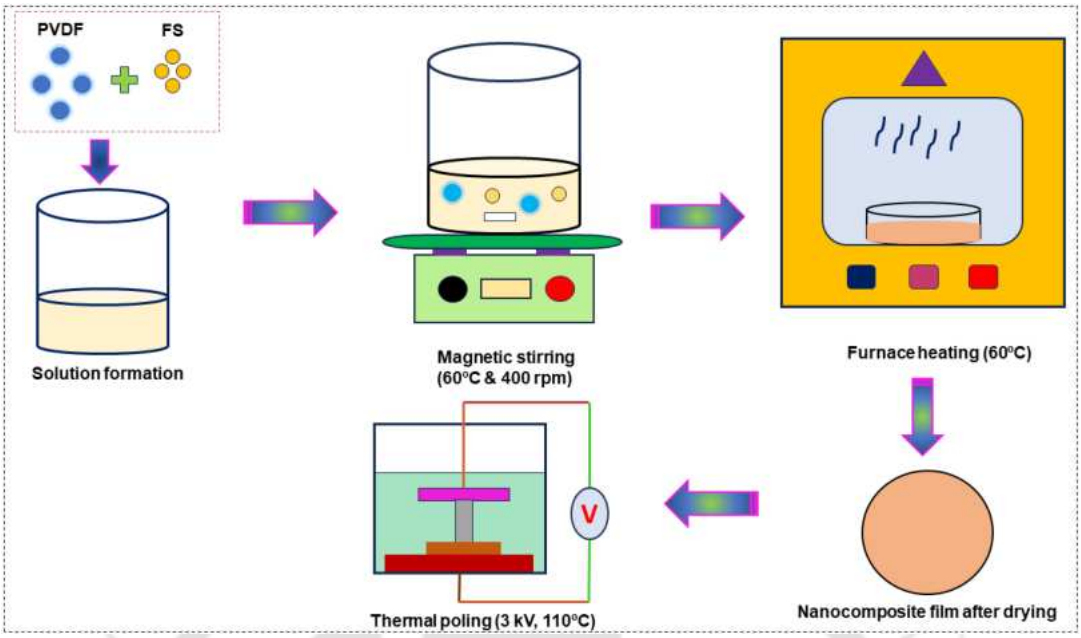

Fig. 7.3: Synthesis of FS-loaded composites through a solvent casting process.

Table 7.1: Weight percentages of different nanocomposite films.

Sample name	Weight of PVDF (g)	Weight of FS (g)	DMF volume (mL)
PVDF	2	-	20
PVDF-5T	2	0.105	20
PVDF-10T	2	0.223	20
PVDF-15T	2	0.353	20
PVDF-20T	2	0.5	20

tion of samples is performed using FTIR study (make: PerkinElmer, Singapore) for the wavelength range of 400-1700 cm^{-1} under ATR mode. XRD analysis of PV-FS composite films was conducted on an X-ray diffractometer from (make: Smartlab, Rigaku Technologies, Japan) utilizing Cu-kα rays. The scanning range for 2θ was set from 15 to 60° with a step size of 4°/min. Elastic modulus, toughness, and breaking strength of nanocomposites are calculated by performing tensile testing (make: Instron, model: dynamic 8801) at room temperature with 1 mm/min of velocity using specimen dimensions as per ASTM D882 standard. Micro-hardness values of nanocomposite films are recorded using a hardness tester with applied load and dwell period of 0.2 kgf and 20 s respectively

(make: Omni tech, model: MVH-II). Dielectric properties of each sample are measured through an LCR unit (make: Hioki, model: IM 3536 for the frequency span of 1 KHz to 1 MHz at room temperature conditions. The piezoelectric behavior of fabricated PENG devices is recorded using a DSO (make: GWInSTEK, model: GDS-2102A) instrument.

7.4 RESULTS AND DISCUSSION

7.4.1 XRD

The crystalline structure and phases of PVDF and its composites are examined using XRD as shown in Fig. 7.4a. It also aided in identifying the crystal structure's electroactive β phase. A characteristic peak at 18° corresponds to the α phase of PVDF, whereas a peak at 21° belongs to the β phase of PVDF. The peaks at 32° and 39° belong to that of FS particles. FS loading till 10% increases the intensity of the β phase resulting in enhanced piezoelectric behavior [104] (see Fig. 7.4b).

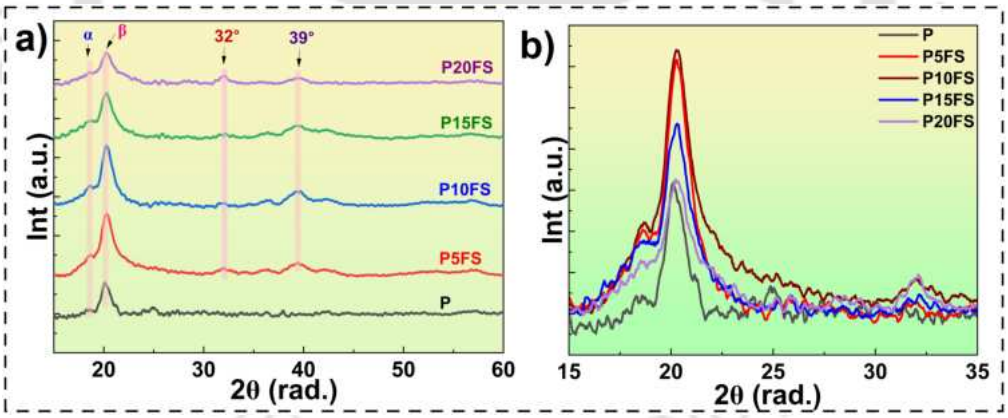

Fig. 7.4: a) XRD plot of pure PVDF and its composites, b) β phase enhancement of PVDF-FS composite films.

7.4.2 FTIR

FTIR plot of pure PVDF and its FS-loaded nanocomposite samples is presented in Fig. 7.5a FTIIR peaks corresponding to 763 (CF_2 and skeletal bending) belongs to the α phase of PVDF, whereas those at 841 (CF_2 stretching, CH_2 rocking, and skeletal C–C stretching), 1288 (Trans-band) and 1400 cm^{-1} (CH_2 scissoring) belongs to β phase of PVDF [180]. The electroactive β

phase content F(β) is calculated using equation 7.2:

$$F(\beta) = \frac{I_\alpha}{\left(\frac{K_\alpha}{K_\beta}\right) I_\alpha + I_\beta} = \frac{I_\alpha}{1.26 I_\alpha + I_\beta} \tag{7.2}$$

where and I_α and I_β are absorbance intensities at 841 and 763 cm^{-1} whereas K_β and K_α are absorption coefficient values for the corresponding wavenumber values, which correspond to 6.1 × 104 and 7.7 × 104 $cm^2.mol^{-1}$, respectively. The value of F(β) increases up to 10% FS loading and then reduces. A maximum F(β) value of 72% is recorded for sample P10FS, whereas P20FS showed the lowest F(β) value of 63%. An increase in electroactive phase content up to 10% was achieved through nanofiller addition, resulting in enhanced piezoelectric nature of nanocomposite films (see Fig. 7.5b). The reduction in F(β) may be due to the agglomeration of FS particles inside the PVDF matrix. The F(β) values of fabricated samples are presented in Table 7.2:

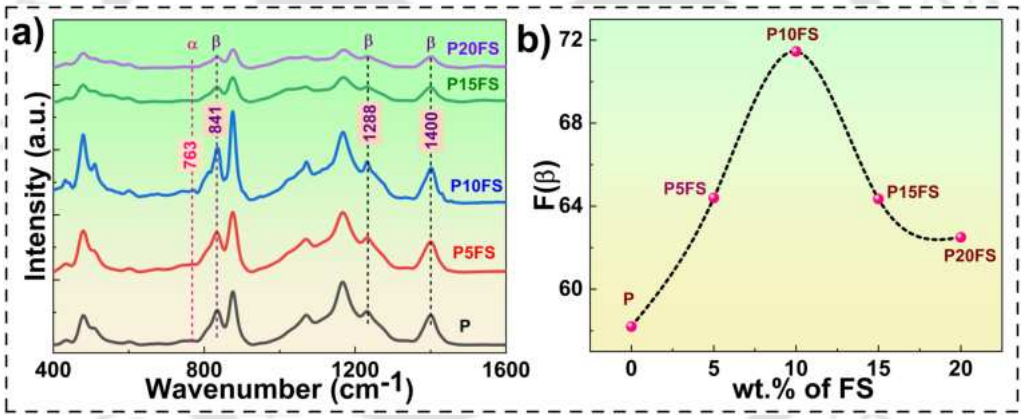

Fig. 7.5: a) FTIR spectra of PVDF and its composite films, b) variation of Fraction of electroactive phase content over FS content.

7.4.3 FESEM

Morphological characteristics and structure of the composite films is assessed through FESEM. In this study, five samples are analyzed. The uniform grain structure of PVDF is well observed in its microstructure (see Fig. 7.6a). Fig. 7.6b-c illustrates the uniform distribution of FS fillers in the PVDF without significant agglomeration, as indicated by the dotted cyan-colored circles. Upon exceeding a 10% loading of FS, the development of particle aggregation becomes apparent (refer to Fig. 7.6d), with a complete agglomeration of FS occurring at a loading of 20% (refer to

Table 7.2: Fraction of electroactive phase content values for different fabricated samples.

Sample name	F(β) %
P	58
P5FS	64
P10FS	72
P15FS	64
P20FS	62

Fig. 7.6e). The presence of Fluorine (F), Carbon (C), Oxygen (O), Calcium (Ca), Phosphorous (P), Magnesium (Mg), and Nitrogen (N) in the energy-dispersive X-ray Spectroscopy (EDS) confirms the formation of the PVDF-FS composite, as depicted in Fig. 7.6f. Fig. 7.6g shows elemental mapping spectra of P10FS confirming uniform dispersion of constituent elements in composite structure.

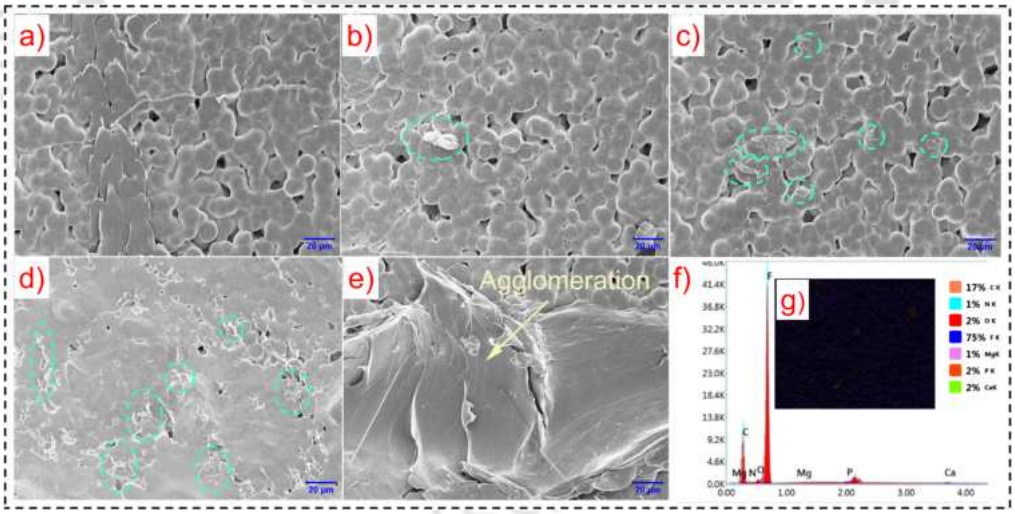

Fig. 7.6: SEM plots. a) P, b) P5FS, c) P10FS, d) P15FS, e) P20FS, f) EDS plot of P10FS, and g) elemental mapping of P20FS.

7.4.4 Mechanical testing

Flexibility and mechanical strength are one of the important criteria for developing smart and sustainable piezoelectric devices for sensing applications. The inner layer of collagen fibers serves as a resilient cushion for FS, demonstrating impressive tensile strength and shielding the fish's skin from the teeth of potential attackers [181]. Over millions of years of evolution, the scales

on the surface of fish skin have developed remarkable hierarchical structures. FS possessing a highly organized microstructure demonstrates a superb blend of mechanical strength and elastic modulus. The stress vs strain graph of pure PVDF and its composites are presented in Fig. 7.7a. The ultimate tensile stress (UTS) and elastic modulus (E) of films increase upon FS addition up to 10% of FS addition as shown in Fig. 7.7b-c. Sample P10FS showed maximum values of UTS (37 MPa) and E (1192 MPa) respectively. A 56% and 67% enhancement in UTS and E values over pure PVDF matrix is recorded for P10FS. FS particles upon loading restrict crack formation and its propagation leading to enhanced stress and modulus values. A ductile to brittle transformation takes place as the PVDF is reinforced with FS powder, causing a reduction in toughness values (see Fig. 7.7d). After 10% FS loading, E and UTS values start decreasing. This reduction can be attributed to the aggregation of FS particles inside the PVDF matrix causing flaws and defect generation leading to stress build-up inside nanocomposite films. This leads to a reduction in the mechanical performance of composites. The mechanical parameters of nanocomposite samples are mentioned in detail in Table 7.3.

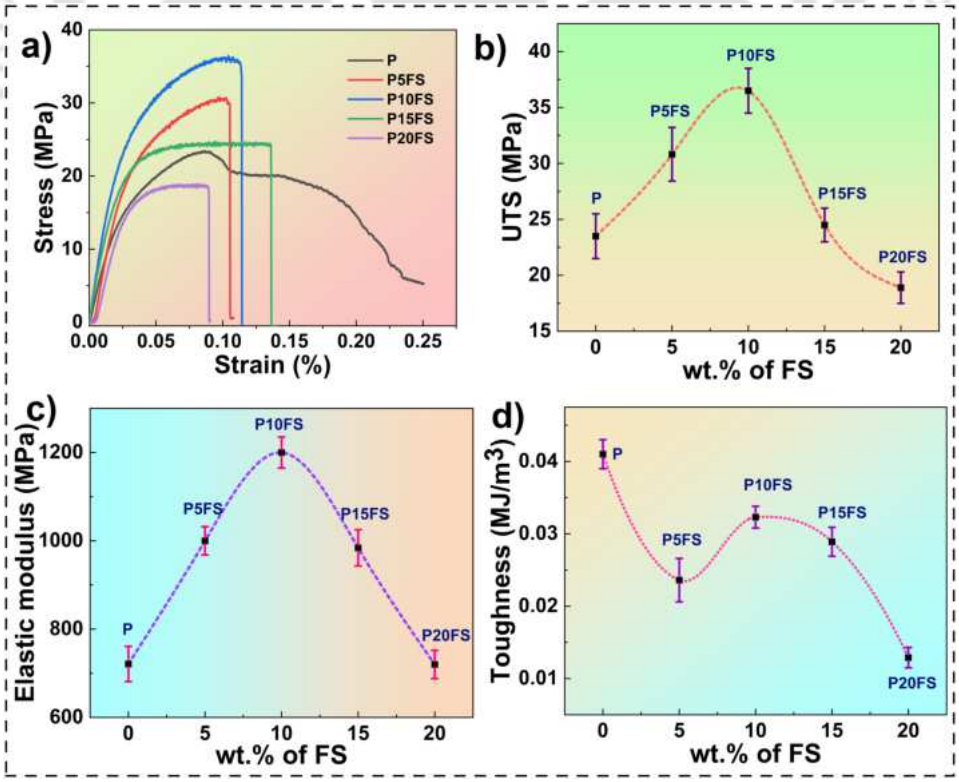

Fig. 7.7: a) Stress-strain plot, b) UTS, c) elastic modulus, and d) toughness of composites over different loading content of FS.

Table 7.3: Mechanical properties of PVDF and its composites.

Sample name	UTS (MPa)	E (MPa)	T (MJ/m^3)
P	23.5±2	721±40	0.041±0.002
P5FS	30.82±2.4	1000±32	0.023±0.0028
P10FS	37±2	1192±35	0.032±0.0015
P15FS	24.5±1.5	984±41	0.028±0.003
P20FS	18.9±1.3	720±34	0.012±0.0014

7.4.5 Hardness measurement

The hardness of composite films depends mainly on interfacial interactions between FS and PVDF matrix. The hardness values increased with the addition of FS particles until 10% loading was reached, followed by a decrease. Increased hardness values signify resistance to plastic deformation and more localized plastic strength. Sample P15FS showed a maximum hardness value of 23 which is about three times more than that of pure PVDF. Samples P, P5FS, P10FS, P15FS, and P20FS recorded hardness values of 7±0.45, 15±.6, 23±0.54, 19±.8 and 17±0.43 respectively (see Fig. 7.8a). Improper interfacial bonding and particle agglomeration results in decreased hardness values above 10% FS loading. This agrees well with tensile testing results which also conforms to the aggregation of FS particles. The hardness and dielectric constant values of composite samples are listed in Table 7.4.

7.4.6 Dielectric measurement

The dielectric behavior of FS-based composites is presented in Fig. 7.8b. Enhancement in ϵ is observed upon addition of FS powder. This increase is attributed to the rise in the number of space charge carriers at lower frequency values resulting from the addition of particles. The rise in ϵ value for lower frequency values is primarily driven by the entrapment of free charges existing within numerous interfaces among fibers and air pores, which predominantly form the collagen

Table 7.4: Hardness and dielectric values of nanocomposites.

Sample name	Hardness values (HV)	ϵ
P	7±0.45	9
P5FS	15±.6	15
P10FS	23±0.54	21
P15FS	19±.8	32
P20FS	17±0.43	43

networks in FS. This phenomenon is commonly referred to as the Maxwell–Wagner–Sillars (MWS) interfacial polarization effect. Additionally, secondary processes may contribute to this behavior, involving ionic movements and hydrogen bonds associated with the protein structure [81]. However, as the frequency continues to rise, its value decreases owing to the electric dipoles' inability to align rapidly with the changing electric field. Sample P20FS achieved a peak dielectric constant of 43, while sample P exhibited a ϵ of approximately 9 at 1 kHz. Around 378% increment in ϵ is observed by adding 20% FS powder in the PVDF matrix.

7.4.7 Piezoelectric voltage measurement

A PENG device is fabricated for o/p voltage measurement. Electrodes are made on either side of the film by painting silver paste. The device's packaging was made by encapsulating it into the PET elastomeric layer, providing high structural stability, including durability and robustness. A variety of physiological movements are tested on each fabricated PENG device, such as finger tapping, palm tapping, film twisting, and wrist pressing. The experimental setup used for recording o/p voltage for different human physiological conditions is shown in Fig. 7.9a. The actual PENG device which is used for the experimentation is shown in Fig. 7.9b. The piezoelectric output voltage of FS-based composites for different loading conditions, as recorded by DSO is presented in Fig. 7.9c-f. The piezoelectric voltage of sample P10FS is the highest, while sample P has the lowest value under each loading condition. Palm tapping criteria, however, record a maximum voltage of 15.4 V.

Higher output voltages are obtained with increasing FS content in the hybrid up to 10% FS loading. The enhancement of the piezoelectric response upon FS addition can be considered a cooperative electromechanical mutual interaction among the adjacent collagen nanofibrils [81]. An o/p voltage is reduced once FS loading exceeds 10% due to aggregation of FS particles. The detailed voltage values regarding different human hand-based loading conditions is presented in Table 7.5. The o/p voltage comparison of different biomaterials-based PENG devices with the existing one is presented in Table 7.6.

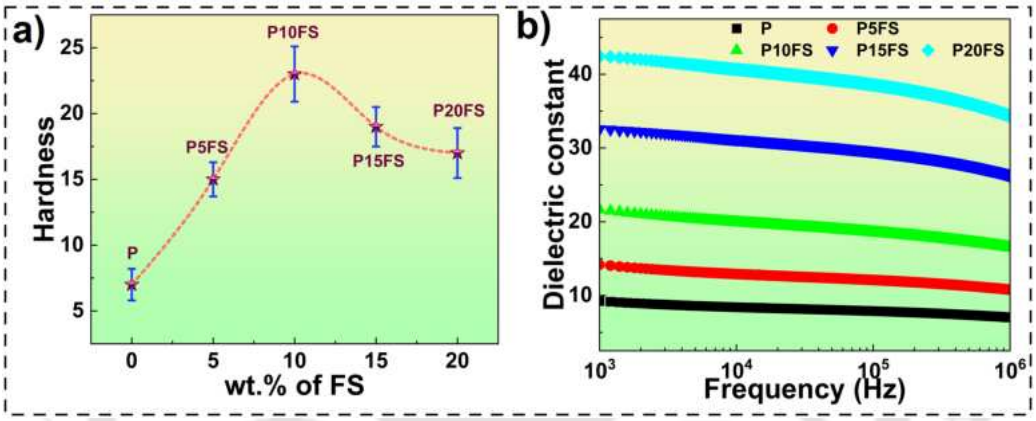

Fig. 7.8: Hardness values of nanocomposite films over varying FS content, b) variation of dielectric constant values over frequency range.

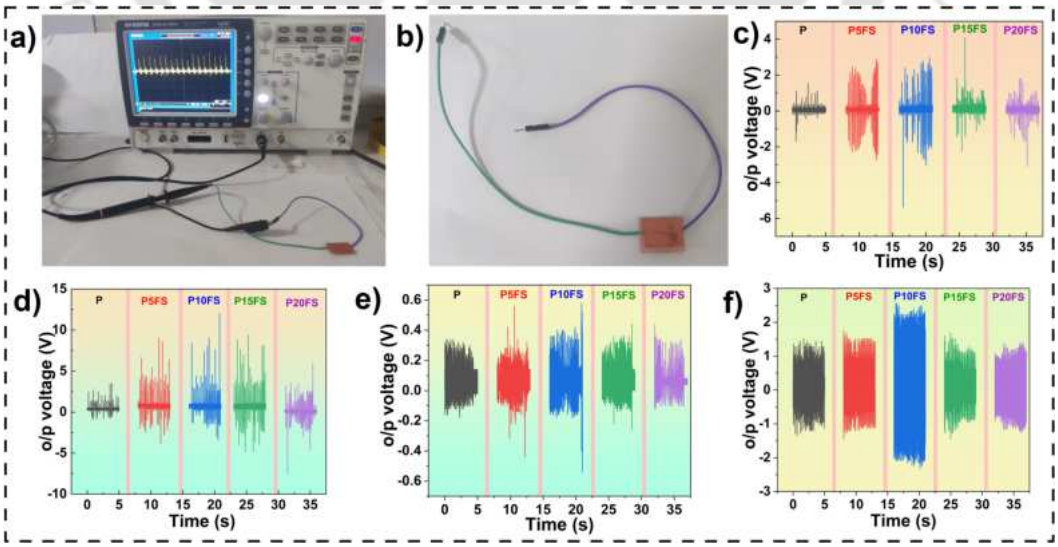

Fig. 7.9: Experimental setup for PENG voltage measurement, b) actual PENG device, o/p voltage recorded for c)finger tapping, d) palm tapping, e) film twisting, and f) wrist pressing conditions.

Table 7.5: Voltage values of different PENG devices for various human-based loading conditions.

Sample name	Voltage (V)			
	Finger tapping	Palm tapping	Film twisting	Wrist pressing
P	3.25	4.64	0.52	2.86
P5FS	5.62	12.81	0.99	3.19
P10FS	8.35	15.4	1.12	4.86
P15FS	6.33	14.15	0.7	3.15
P20FS	4.87	13.49	0.54	2.66

Table 7.6: Comparison of PVDF-FS based PENG device and comparing it with previously reported nanogenerator devices in the literature.

Materials used	Synthesis process	V_{pp} (V)	References
PVDF/coconut husk	Solvent casting	14	[75]
PVDF/cellulose	Electrospinning	3.5	[166]
Wood sponge	Delignification	0.7	[74]
Seagrass	Spray coating	288	[71]
Onion skin	Used as it is	18	[70]
Silk nanofibers	Electrospinning	6	[182]
Pomelo fruit	Drying	15	[183]
PVDF/FS	Solvent casting	15.4	**This work**

7.5 COMPOSITE AS AN IMPACT SENSOR

7.5.1 Experimental setup and formulation

A custom laboratory setup was created to investigate the impact loading effects on composite films (see Fig. 7.10). Sample P10FS has been chosen for an in-depth examination of its impact behavior due to its notable presence of the β phase content and a substantial piezo response. A piezoelectric sensor is affixed to a metallic base on a stand using adhesive tape, and the sensor wires are connected to a DSO via a connecting probe. Test loads of 5 g (0.0221 N), 10 g (0.0443 N), 15

g (0.0687 N), 20 g (0.0781 N), and 25 g (0.1186 N) are released from the top of a hollow circular plastic tube onto the test samples to assess their response to impact loading. Each load undergoes impact testing 25 times. The dropping height is maintained at a constant 9 cm for all readings. Following the collision, the initial potential energy is converted into kinetic energy as represented in equation 7.3:

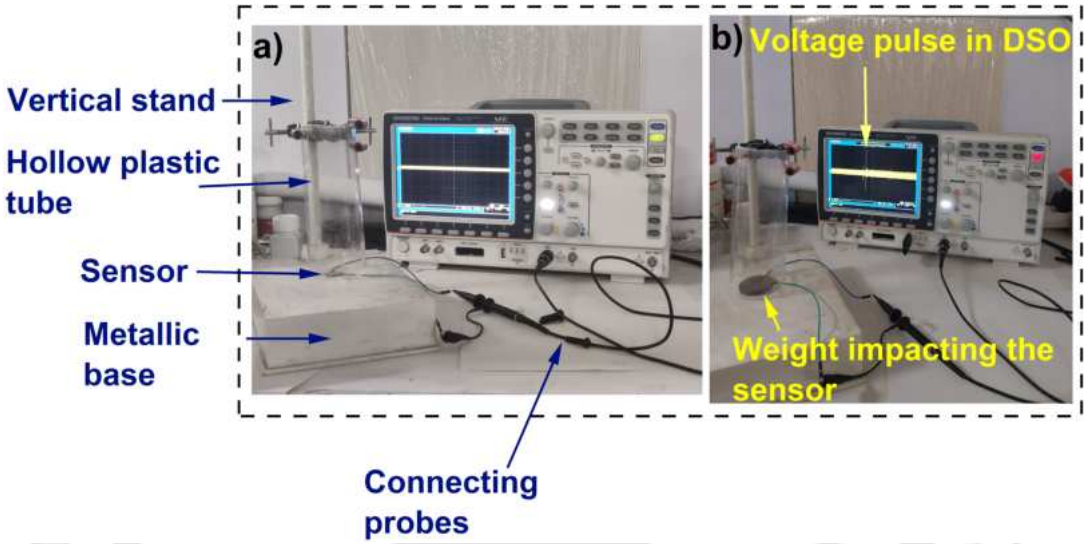

Fig. 7.10: Experimental setup. a) before the impact, b) after the dead weight impact.

$$mgH = \frac{1}{2}mV_i^2 \tag{7.3}$$

where m = mass of the weights used, H = dropping height, g = acceleration due to gravity, and V_{i} = impact velocity. To simplify the analysis, we have disregarded the influence of air resistance on the descending weights.

$$V_i = \sqrt{2gH} \tag{7.4}$$

Applying the work-energy principle, the determination of the net work done (W_{n}) during impact is conducted as given in 7.5:

$$W_n = \frac{1}{2}m\left[V^2 - V_0^2\right] \tag{7.5}$$

When V_0 is zero, and V equals V_{i}, the net work done becomes equivalent to kinetic energy. Finally, the magnitude of the impact force (F_{impact}) is computed using equation 7.6:

$$F_{\mathrm{impact}} = \frac{W_n}{h} \tag{7.6}$$

7.5.2 Impact loading test on the piezo sensor

Fig. 7.11 displays the output voltage recorded by the DSO in response to the impact of various test loads. Despite subjecting each test load to 25 impact examinations, only a single impact per test load is depicted in the figure for the sake of simplicity. The distinct voltage spikes in Fig. 7.11a-e, enclosed within pink dotted circles, signify the consequences of the test loads impacting the sensing area. The magnitude of the impact load is primarily dictated by the mass of the test loads. The sensing area undergoes vibrations upon the impact of test loads on the sample, leading to the deformation of the composite film. This deformation induces a potential difference owing to the piezoelectric effect. Consequently, there is an electron flow between the upper and lower electrodes, resulting in the generation of a voltage signal. Analysis of the plots reveals that, with

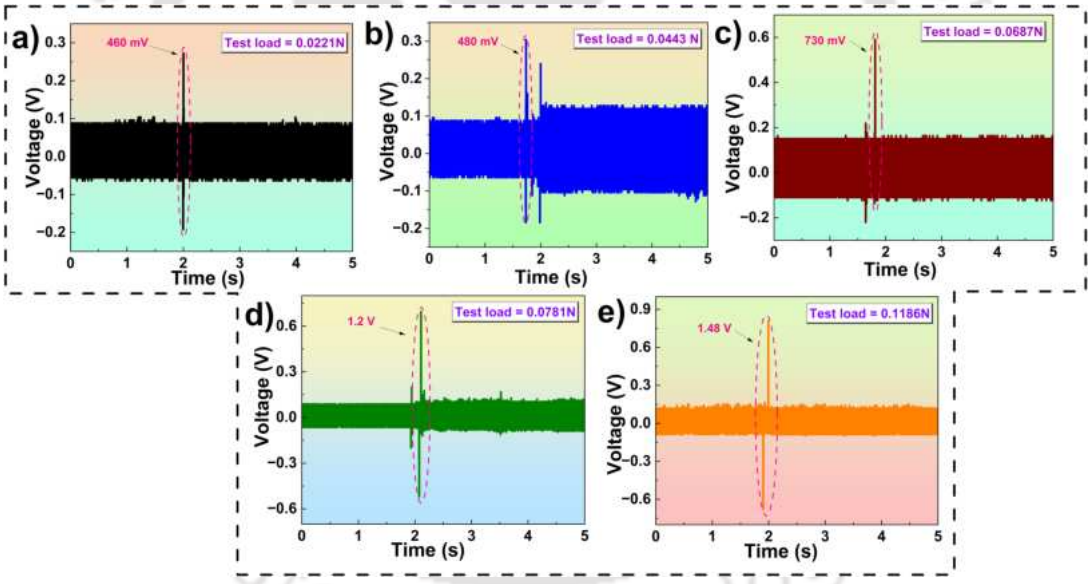

Fig. 7.11: Output voltage peaks due to the impact of test loads with the following values: a) 0.0221 N (5 g), b) 0.0443 N (10 g), c) 0.068 N (15 g), d) 0.0781 N (20 g), and e) 0.1186 N (25 g).

an increase in the weight of the test load, the peak-to-peak value of the output voltage signal also experiences an enhancement. This phenomenon can be ascribed to heightened vibrations of the piezo sensing element induced by heavier loads, causing an increase in strain generation and, consequently, enhancing the output voltage [173]. The output voltages recorded for each test load exhibited variations. Therefore, the obtained results underwent statistical analysis using the Weibull distribution model with the assistance of Minitab 17 (student version) software. Equation

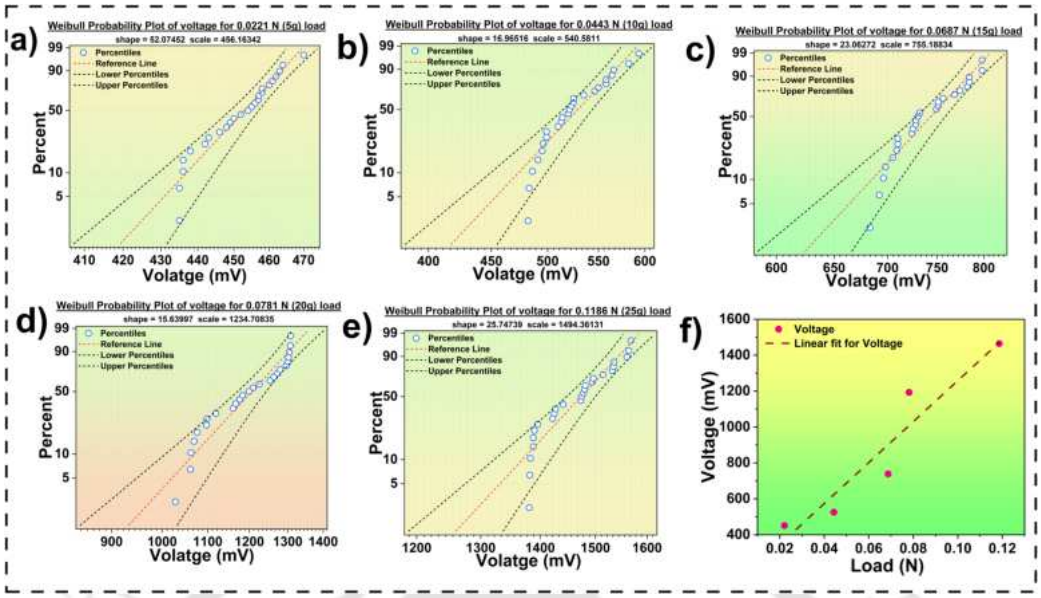

Fig. 7.12: Output voltage peaks due to the impact of test loads with the following values: a) 0.0221 N (5 g), b) 0.0443 N (10 g), c) 0.068 N (15 g), d) 0.0781 N (20 g), and e) 0.1186 N (25 g).

7.7 represents the Weibull distribution model employed for the analysis of impact testing on the composite sensor.

$$F_x = 1 - e^{-\left(\frac{x}{\eta}\right)^b} \tag{7.7}$$

The failure probability, denoted as F_x applies to any continuous random variable x within a cumulative distribution function (CDF), where η and b represent the scale and shape parameters, respectively. The outcomes of the Weibull distribution concerning the output voltage of the P10FS sample under various impact loading conditions are depicted in Fig. 7.12. The investigative data is evenly distributed along the line and accurately fitted. The voltage response to impact loads under various conditions displays a noteworthy linear behavior. Experimental points are fitted to obtain a linear relationship function, yielding an R^2 value of 0.90, as illustrated below in equation 7.8:

$$y = 11405x + 117 \tag{7.8}$$

In this context, with y representing the generated voltage (mV) and $x$denoting the applied impact load (N), it is evident that the fabricated sensor effectively responds to diverse impact loads, demonstrating a sensitivity value of 11405 mV/N. The prospects could be integrating energy harvesters based on FS into wearable devices, electronic gadgets, or larger-scale applications that have the potential to unlock innovative opportunities. This incorporation may pave the way for self-powered

electronic systems and contribute significantly to the advancement of energy-efficient technologies.

7.6 COMPARATIVE STUDY OF MAXIMUM OUTPUT VOLTAGE GENERATION IN VARIOUS PENG DEVICES

PVDF is extensively utilized in piezoelectric applications owing to its exceptional piezoelectric properties, chemical resistance, and mechanical flexibility. Introducing nanofillers into PVDF matrices can greatly enhance their piezoelectric performance, thereby increasing the efficiency of PVDF-based PENGs. In this comparative study, the output voltage generated by different PENG devices discussed in the subsequent chapters of the thesis is examined, as shown in Table 7.7. The PVDF/TiO_2/rGO nanocomposites, with an rGO loading of approximately 1 wt.%, demonstrated the highest output voltage. The synergistic effect created by combining PVDF with TiO_2 and rGO enhances interfacial polarization, significantly boosting the composite's overall piezoelectric properties. Conversely, the BTO-based composites exhibited a decrease in output voltage compared to the TiO_2-based PENG devices. This reduction can be attributed to factors such as interfacial compatibility, nanofiller dispersion, and polarization efficiency. Moreover, BMP and FS based sustainable composites fall short in piezoelectric performance and robustness compared to PVDF-TiO_2-rGO nanocomposites because of their intrinsic material limitations and difficulties in achieving optimal polarization and alignment.

Table 7.7: Comparison of maximum output voltage developed by different PENG devices.

PENG details	V_{pp} (V)
PVDF-10T	5.45
PTR1	10.2
ABC1.25	4.1
5BPVT	7.2
P10FS	8.35

7.7 SUMMARY

Fish scales, categorized as bio-waste, are composed of type I collagen reinforced by apatite, showcasing limited quantities of anisotropy and piezoelectric properties. This chapter summaries fabrication of biocompatible PENG devices consisting varying FS concentration in PVDF matrix. The remaining FS obtained from local food canteens are gathered and treated, then incorporated in different proportions into PVDF to create flexible composites via solvent casting. FS are then processed through multiple water and NaOH washings. FS particles are further characterised through FTIR, XRD, FESEM and EDS. Effect of FS loading on mechanical properties of PVDF matrix is investigated. The inner layer of collagen fibers serves as a resilient cushion for FS, demonstrating impressive tensile strength and shielding the fish's skin from the teeth of potential attackers. A well-organized microstructure in FS showcases an excellent combination of robust mechanical strength and elastic modulus. Enhancement in dielectric constant is observed upon addition of FS powder. This increase is attributed to the rise in the number of space charge carriers at lower frequency values resulting from the addition of particles. Enhanced piezoelectric performance is validated by assessing the output voltage of composite film-based PENG devices in reaction to diverse human physiological movements such as finger tapping, palm tapping, film twisting, and wrist pressing. The presence of hydrogen bonding motifs in FS (with polar uniaxial orientation) between the polypeptide chains behaves as molecular dipoles that result in spontaneous polarization and piezoelectric nature. Enhanced output voltages are achieved with an incremental FS content in the composite, reaching a peak at 10% FS loading. The palm tapping condition registers a maximum piezoelectric voltage of 15.4 V. Sample P10FS is further investigated for piezo performance for different impact loads ranging from 5 g to 20 g. An associated voltage peak is noted for each applied impact load. The analysis of voltage responses under diverse loading conditions is conducted using a Weibull distribution. The sensitivity of the P10FS specimen is computed and determined to be 11405 mV/N. The PENG device, utilizing a PVDF-FS composite, serves as a piezoelectric impact sensor, making it suitable for applications such as structural health monitoring of critical infrastructure like highways, bridges, and dams.

Chapter 8

CONCLUSIONS

8.1 CHAPTERWISE SYNOPTIC CONCLUSIONS FROM THE PRESENT WORK

This section summarizes the major outcomes of this research work and future research directions. The major conclusions are encapsulated below.

1. A detailed investigation on the role of TiO_2 nanofiller concentration on structural, mechanical, dielectric, piezoelectric and optical properties of PVDF is conducted. The following conclusions can be drawn from the present experimental results:

   (i) Highest fraction of β phase is obtained for PVDF-10T nanocomposite film. The crystallinity values and melting temperature of the nanocomposites are significantly improved.

   (ii) The dielectric and optical properties of PVDF-TiO_2 nanocomposite films are also improved on nanofiller addition.

   (iii) The strength and elastic modulus are enhanced up to 5wt.% of TiO_2 reinforcement. The increased piezo response was confirmed by increased remnant polarization value due to TiO_2 addition. In comparison to pure PVDF, PVDF-10T nanocomposite film showed maximum output voltage.

   (iv) These kind of flexible nanocomposite films prove to be ideal for mechanical energy harvesters used in sensing applications due to their excellent overall properties and good cost-performance balance.

2. A three phase PVDF-TiO_2-rGO based hybrid nanocomposite with fixed TiO_2 content and changing rGO concentration is fabricated. A MCDM based material selection and optimization technique called TODIM is applied, and a sensitivity study is performed to select the best material for mechanical energy harvesting applications. The following conclusions can be drawn from the above experimental investigation:

   (i) XRD, FTIR, and Raman spectroscopy tools confirmed the successful fabrication of hybrid nanocomposite. A detailed analysis of the role of rGO loading on mechanical, thermal, and structural properties of Pure PVDF and PVDF-TiO_2 based composites is carried out.

   (ii) The dielectric and optical properties of PVDF-TiO_2 nanocomposite films are also improved on nanofiller addition.

   (iii) Compared to pure PVDF and PVDF-TiO_2, PTR1 displayed maximum UTS, E, and hardness values, whereas PT displayed maximum toughness values. A PENG device made from sample PTR1 showed 390% and 85% increment in output voltage over pure PVDF and PVDF-TiO_2 based devices, respectively.

   (iv) A 438% and 207% enhancement in dielectric constant is recorded for sample PTR1.5 compared to pure PVDF and PVDF-TiO_2 composite, respectively.

   (v) TODIM technique is used for multi-critical decision-making for flexible electronics and energy harvesting applications in which S5 is selected as the best material and S1 as the poorest material.

3. A hybrid PVDF-BTO-rGO based nanocomposite with varying rGO loading is synthesized. The piezoelectric behaviour of solvent cast PVDF-BTO-rGO nanocomposites is enhanced by subsequent electrode poling. A thorough analysis on the role of rGO concentration on thermal, mechanical, and piezoelectric properties of PVDF-BTO composites is conducted. The following conclusions can be drawn from the results:

   (i) XRD and FTIR studies confirmed the existence and enhancement of β phase of PVDF

which is essential for piezoelectric behaviour. The values of Elastic modulus and tensile strength increased up to 1.25 wt.% of rGO loading, followed by drastic reduction at higher loading.

(ii) Sample ABC 1.25 displayed maximum viscosity and storage modulus as compared to pure PVDF. The dielectric constant and ac conductivity of the nanocomposite samples are considerably improved on nanofiller addition.

(iii) Piezo responses of poled and unpoled samples for different loading conditions were tested and compared. Electrode poled sample ABC 1.25 showed maximum V_{pp} value of 4.1 V for continuous finger tapping condition.

4. Bamboo reinforced PVDF based biocompatible piezoelectric sensors are developed and tested for different impact loading conditions. The results of the study lead to the following conclusions:

(i) 5BPV showed maximum structural, dielectric, and piezoelectric properties as compared to neat PVDF. A 300% increase in o/p voltage was observed for 5BPV compared to pure PVDF.

(ii) Alkaline treated bamboo particle reinforcement further enhanced o/p voltage and current values. Among all samples, sample 5BPVT showed maximum structural, mechanical, thermal, and piezoelectric properties.

(iii) A PENG device based on 5BPVT was further tested for its response to impact loads under different test conditions. With a sensitivity of 5288 mV/N, it showed excellent o/p voltage response for various applied impact loads.

(iv) A highly sensitive impact sensor like this could be the best bet for commercial applications. Our research outcomes confirm the promising applications of PVDF-bamboo composites in the domain of sustainable energy harvesting and sensing applications.

5. Energy harvesting performance of an efficient flexible bio-piezoelectric nanogenerator is demonstrated. The developed energy harvester acts as a sensor that interacts with human body

parts to monitor real-time physiological signals. The obtained experimental results suggest the following conclusions:

(i) The remaining FS obtained from local food canteens were gathered and treated, then incorporated in different proportions into PVDF to create flexible composites via solvent casting. Morphology, size, structure, and different phases of FS structures were examined through FESEM, XRD, and FTIR tools.

(ii) The effect of FS concentration on the mechanical properties of PVDF is assessed. Increment in tensile strength and elastic modulus was reported upon FS addition till 10% loading. Sample P10FS showed maximum values of UTS (37 MPa) and E (1192 MPa) respectively. A 56% and 67% enhancement in UTS and E values over pure PVDF matrix is recorded for P10FS.

(iii) Moreover, adding these FS into PVDF further enhances the piezo response of the overall composite sample. Increased piezoelectric behavior is confirmed by examining the o/p voltage of composite film-based PENG devices in response to various human physiological actions like finger tapping, palm tapping, film twisting, and wrist pressing.

(iv) Higher output voltages are obtained with increasing FS content in the hybrid up to 10% FS loading. A maximum piezo voltage of 15.4 V is recorded for the palm tapping condition.

(v) Sample P10FS is further investigated for piezo performance for different impact loads ranging from 5 g to 20 g. An associated voltage peak is noted for each applied impact load. The analysis of voltage responses under diverse loading conditions is conducted using a Weibull distribution. The sensitivity of the P10FS specimen is computed and determined to be 11405 mV/N.

8.2 FUTURE SCOPE

The future studies based on this work can be in the following aspects:

1. Signal conditioning of fabricated PENG devices:

   PENGs are devices that transform mechanical energy into electrical energy through the piezoelectric effect. To utilize the electrical signals produced by PENGs effectively, signal conditioning is crucial to ensure that the output is stable, accurate, and appropriate for further processing or application. The electrical output from a PENG device typically requires only basic conditioning, like rectification, Amplification and, filtering, which can be accomplished with minimal electronic components.

   - **Rectifier:** PENGs produce alternating current (AC) signals because of the oscillatory nature of mechanical stress. To make these signals usable, they must be converted into direct current (DC).
   - **Filtering:** To smooth the rectified DC signal and minimize noise and ripple.
   - **Amplification:** To boost the signal to a level appropriate for processing or interfacing with other electronic systems.

2. Integration of PENG into IoT devices for various applications such as smart cities, healthcare and industrial automation.

3. PENG device structure can be further improvised to facilitate the fabrication of wireless SAW devices, enabling the recording of strain and vibrations in remote or hard to reach locations. This versatility makes them valuable for monitoring the structural health of critical infrastructure such as bridges, buildings, and aircraft without requiring external power source.

4. Development of advanced fabrication techniques, such as 3D printing, for PENG device synthesis to improve the overall performance of piezoelectric sensory devices.

5. Explore the materials and principles for biological applications such as bone regeneration and tissue engineering.

6. Design and fabrication of the PENG devices for mass scale applications.

Bibliography

[1] Yongjin Ahn, Jun Young Lim, Soon Man Hong, Jaerock Lee, Jongwook Ha, Hyoung Jin Choi, and Yongsok Seo. Enhanced piezoelectric properties of electrospun poly (vinylidene fluoride)/multiwalled carbon nanotube composites due to high β-phase formation in poly (vinylidene fluoride). *The Journal of Physical Chemistry C*, 117(22):11791–11799, 2013.

[2] Shaul Katzir. The discovery of the piezoelectric effect. In *The beginnings of piezoelectricity: a study in mundane physics*, pages 15–64. Springer, 2006.

[3] S Mohith, Adithya R Upadhya, Karanth P Navin, SM Kulkarni, and Muralidhara Rao. Recent trends in piezoelectric actuators for precision motion and their applications: A review. *Smart Materials and Structures*, 30(1):013002, 2020.

[4] Suvrajyoti Mishra, Rajesh Sahoo, Lakshmi Unnikrishnan, Ananthakumar Ramadoss, Smita Mohanty, and Sanjay Kumar Nayak. Effect of multi-step processing on the structural, morphological and dielectric behaviour of PVDF films. *Ionics*, 26:6069–6081, 2020.

[5] Heiji Kawai. The piezoelectricity of poly (vinylidene fluoride). *Japanese Journal of Applied Physics*, 8(7):975, 1969.

[6] JG Bergman Jr, JH McFee, and GR Crane. Pyroelectricity and optical second harmonic generation in polyvinylidene fluoride films. *Applied Physics Letters*, 18(5):203–205, 1971.

[7] Jie Wu, Xiaoyu Sun, Shunjin Zhu, Jin Bai, Xuebin Zhu, Jianming Dai, Lihua Yin, Wenhai Song, and Yuping Sun. Magnetic field induced formation of ferroelectric β phase of poly (vinylidene fluoride). *Applied Physics A*, 126:1–6, 2020.

[8] Ali Salimi and Ali Akbar Yousefi. Analysis method: Ftir studies of β-phase crystal formation in stretched PVDF films. *Polymer Testing*, 22(6):699–704, 2003.

[9] S Naresh Kumar and Pawan Kumar. Dielectric and pyroelectric properties of ferroelectric SBN–PVDF composites prepared by hot-uniaxial press. *International Journal of Applied Ceramic Technology*, 10:E11–E17, 2013.

[10] Bo Lin, Zeng-Tian Li, Ying Yang, Ying Li, Jie-Ci Lin, Xu-Min Zheng, Fu-An He, and Kwok-Ho Lam. Enhanced dielectric permittivity in surface-modified graphene/PVDF composites prepared by an electrospinning-hot pressing method. *Composites Science and Technology*, 172:58–65, 2019.

[11] Kar Lai Ng, Helen Lai Wa Chan, and Chung Loong Choy. Piezoelectric and pyroelectric properties of PZT/P (VDF-TrFE) composites with constituent phases poled in parallel or antiparallel directions. *IEEE transactions on ultrasonics, ferroelectrics, and frequency control*, 47(6):1308–1315, 2000.

[12] Gwang Ho Kim, Soon Man Hong, and Yongsok Seo. Piezoelectric properties of poly (vinylidene fluoride) and carbon nanotube blends: β-phase development. *Physical chemistry chemical physics*, 11(44):10506–10512, 2009.

[13] Behzad Mohammadi, Ali Akbar Yousefi, and Samad Moemen Bellah. Effect of tensile strain rate and elongation on crystalline structure and piezoelectric properties of PVDF thin films. *Polymer testing*, 26(1):42–50, 2007.

[14] Suvrajyoti Mishra, Rajesh Sahoo, Lakshmi Unnikrishnan, Ananthakumar Ramadoss, Smita Mohanty, and Sanjay Kumar Nayak. Investigation of the electroactive phase content and dielectric behaviour of mechanically stretched PVDF-GO and PVDF-rGO composites. *Materials Research Bulletin*, 124:110732, 2020.

[15] Yizhi Liu, Yi Sun, and Fanlin Zeng. Ferroelectric performance, surface and mechanical properties of poled pvdf sheet with metal coating: Assessing through PFM, FTIR, and nanoindentation and nanoscratch. *Ferroelectrics*, 515(1):134–142, 2017.

[16] Suresha K Mahadeva, John Berring, Konrad Walus, and Boris Stoeber. Effect of poling time and grid voltage on phase transition and piezoelectricity of poly (vinyledene fluoride) thin films using corona poling. *Journal of physics D: applied physics*, 46(28):285305, 2013.

[17] Cheol Park, Zoubeida Ounaies, Kristopher E Wise, and Joycelyn S Harrison. In situ poling and imidization of amorphous piezoelectric polyimides. *Polymer*, 45(16):5417–5425, 2004.

[18] Chunyan Li, Pei-Ming Wu, Soohyun Lee, Andrew Gorton, Mark J Schulz, and Chong H Ahn. Flexible dome and bump shape piezoelectric tactile sensors using PVDF-TrFE copolymer. *Journal of Microelectromechanical Systems*, 17(2):334–341, 2008.

[19] Hoejin Kim, Fernando Torres, Md Tariqul Islam, Md Didarul Islam, Luis A Chavez, Carlos A Garcia Rosales, Bethany R Wilburn, Calvin M Stewart, Juan C Noveron, Tzu-Liang B Tseng, et al. Increased piezoelectric response in functional nanocomposites through multiwall carbon nanotube interface and fused-deposition modeling three-dimensional printing. *MRS Communications*, 7(4):960–966, 2017.

[20] CF Groner and MN Hirsh. Comparison of poling techniques for inducing piezoelectric behavior in PVF 2. In *1985 5th International Symposium on Electrets (ISE 5)*, pages 912–917. IEEE, 1985.

[21] ZA Weinberg, WC Johnson, and MA Lampert. High-field transport in SiO_2 on silicon induced by corona charging of the unmetallized surface. *Journal of Applied Physics*, 47(1):248–255, 1976.

[22] AN Arshad, MD Rozana, MHM Wahid, MK Mahmood, MN Sarip, Z Habibah, and M Rusop.

Enhanced dielectric and electrical properties of annealed PVDF thin film. In *AIP Conference Proceedings*, volume 1963. AIP Publishing, 2018.

[23] Liangke Wu, Zhaonan Jin, Yaolu Liu, Huiming Ning, Xuyang Liu, Alamusi, and Ning Hu. Recent advances in the preparation of PVDF-based piezoelectric materials. *Nanotechnology Reviews*, 11(1):1386–1407, 2022.

[24] Habibuddin Shaik, SN Rachith, KJ Rudresh, Abdul Sattar Sheik, KH Thulasi Raman, P Kondaiah, and G Mohan Rao. Towards β-phase formation probability in spin coated PVDF thin films. *Journal of Polymer Research*, 24:1–6, 2017.

[25] Zhengbao Yang, Shengxi Zhou, Jean Zu, and Daniel Inman. High-performance piezoelectric energy harvesters and their applications. *Joule*, 2(4):642–697, 2018.

[26] Jie Chen, Seung Kyu Oh, Noor Nabulsi, Heidi Johnson, Weijie Wang, and Jae-Hyun Ryou. Biocompatible and sustainable power supply for self-powered wearable and implantable electronics using III-nitride thin-film-based flexible piezoelectric generator. *Nano Energy*, 57: 670–679, 2019.

[27] Chunlong Fei, Xiangli Liu, Benpeng Zhu, Di Li, Xiaofei Yang, Yintang Yang, and Qifa Zhou. AlN piezoelectric thin films for energy harvesting and acoustic devices. *Nano Energy*, 51: 146–161, 2018.

[28] Hadi Madinei, H Haddad Khodaparast, Sondipon Adhikari, and MI Friswell. Design of MEMS piezoelectric harvesters with electrostatically adjustable resonance frequency. *Mechanical Systems and Signal Processing*, 81:360–374, 2016.

[29] Xinran Zhou, Kaushik Parida, Oded Halevi, Yizhi Liu, Jiaqing Xiong, Shlomo Magdassi, and Pooi See Lee. All 3D-printed stretchable piezoelectric nanogenerator with non-protruding kirigami structure. *Nano Energy*, 72:104676, 2020.

[30] Zhong Lin Wang and Jinhui Song. Piezoelectric nanogenerators based on zinc oxide nanowire arrays. *Science*, 312(5771):242–246, 2006.

[31] Kenneth J Loh and Donghee Chang. Zinc oxide nanoparticle-polymeric thin films for dynamic strain sensing. *Journal of Materials Science*, 46:228–237, 2011.

[32] S Jiansirisomboon, K Songsiri, A Watcharapasorn, and T Tunkasiri. Mechanical properties and crack growth behavior in poled ferroelectric PMN–PZT ceramics. *Current Applied Physics*, 6(3):299–302, 2006.

[33] Liang Huang, Shizhe Lin, Zisheng Xu, He Zhou, Jiangjiang Duan, Bin Hu, and Jun Zhou. Fiber-based energy conversion devices for human-body energy harvesting. *Advanced Materials*, 32(5):1902034, 2020.

[34] Chen Xu, Yu Song, Mengdi Han, and Haixia Zhang. Portable and wearable self-powered systems based on emerging energy harvesting technology. *Microsystems and nanoengineering*, 7(1):25, 2021.

[35] Yi Xin, Xiang Li, Hongying Tian, Chao Guo, Chenghui Qian, Shuhong Wang, and Cheng Wang. Shoes-equipped piezoelectric transducer for energy harvesting: A brief review. *Ferroelectrics*, 493(1):12–24, 2016.

[36] Laiming Jiang, Yang Yang, Ruimin Chen, Gengxi Lu, Runze Li, Di Li, Mark S Humayun, K Kirk Shung, Jianguo Zhu, Yong Chen, et al. Flexible piezoelectric ultrasonic energy harvester array for bio-implantable wireless generator. *Nano energy*, 56:216–224, 2019.

[37] Jaegyu Kim, Seoungwoo Byun, Sangryun Lee, Jeongjae Ryu, Seongwoo Cho, Chungik Oh, Hongjun Kim, Kwangsoo No, Seunghwa Ryu, Yong Min Lee, et al. Cost-effective and strongly integrated fabric-based wearable piezoelectric energy harvester. *Nano Energy*, 75:104992, 2020.

[38] Kyung-Eun Byun, Min-Hyun Lee, Yeonchoo Cho, Seung-Geol Nam, Hyeon-Jin Shin, and Seongjun Park. Potential role of motion for enhancing maximum output energy of triboelectric nanogenerator. *APL Materials*, 5(7), 2017.

[39] Haipeng Peng, Ye Tian, Jürgen Kurths, Lixiang Li, Yixian Yang, and Daoshun Wang. Secure and energy-efficient data transmission system based on chaotic compressive sensing in body-to-body networks. *IEEE transactions on biomedical circuits and systems*, 11(3):558–573, 2017.

[40] N Izyumskaya, Y-I Alivov, S-J Cho, H Morkoç, Howard Lee, and Y-S Kang. Processing, structure, properties, and applications of PZT thin films. *Critical reviews in solid state and materials sciences*, 32(3-4):111–202, 2007.

[41] Liao Qiao, Guo Li, Hong Tao, Jiagang Wu, Zhuo Xu, and Fei Li. Full characterization for material constants of a promising KNN-based lead-free piezoelectric ceramic. *Ceramics International*, 46(5):5641–5644, 2020.

[42] Huaxiang Fu and L Bellaiche. First-principles determination of electromechanical responses of solids under finite electric fields. *Physical review letters*, 91(5):057601, 2003.

[43] Chih-Yen Chen, Guang Zhu, Youfan Hu, Jeng-Wei Yu, Jinghui Song, Kai-Yuan Cheng, Lung-Han Peng, Li-Jen Chou, and Zhong Lin Wang. Gallium nitride nanowire based nanogenerators and light-emitting diodes. *ACS nano*, 6(6):5687–5692, 2012.

[44] Yi-Feng Lin, Jinhui Song, Yong Ding, Shih-Yuan Lu, and Zhong Lin Wang. Piezoelectric nanogenerator using CdS nanowires. *Applied Physics Letters*, 92(2), 2008.

[45] Xin Chen, Xu Han, and Qun-Dong Shen. PVDF-based ferroelectric polymers in modern flexible electronics. *Advanced Electronic Materials*, 3(5):1600460, 2017.

[46] Md Mehebub Alam, Ayesha Sultana, and Dipankar Mandal. Biomechanical and acoustic en-

ergy harvesting from TiO_2 nanoparticle modulated PVDF nanofiber made high performance nanogenerator. *ACS Applied Energy Materials*, 1(7):3103–3112, 2018.

[47] Humaira Razzaq, Hifza Nawaz, Asima Siddiq, M Siddiq, and S Qaisara. A brief review on nano composites based on pvdf with nanostructured TiO_2 as filler. *Madridge Journal of Nanotechnology and Nanoscience*, 1:22–28, 2016.

[48] WC Gan and WH Abd Majid. Effect of TiO_2 on enhanced pyroelectric activity of pvdf composite. *Smart Materials and Structures*, 23(4):045026, 2014.

[49] Md Mehebub Alam, Ayesha Sultana, Debabrata Sarkar, and Dipankar Mandal. Electroactive β-crystalline phase inclusion and photoluminescence response of a heat-controlled spin-coated PVDF/TiO_2 free-standing nanocomposite film for a nanogenerator and an active nanosensor. *Nanotechnology*, 28(36):365401, 2017.

[50] Jianfeng Zhu, Hongshuai Sun, Yang Xu, Tao Liu, Tianyuan Hou, Lishuang Liu, Yongchao Li, Tingting Lin, and Yi Xin. Preparation of PVDF/TiO_2 nanofibers with enhanced piezoelectric properties for geophone applications. *Smart Materials and Structures*, 28(8):085006, 2019.

[51] Mehdi Haji Abdolrasouli, Hossein Abdollahi, and Ali Samadi. PVDF nanofibers containing GO-supported TiO_2–Fe_3O_4 nanoparticle-nanosheets: piezoelectric and electromagnetic sensitivity. *Journal of Materials Science: Materials in Electronics*, 33(8):5970–5982, 2022.

[52] Lulu Liu, Wenyi Fu, Lili Wang, Haigang Tian, and Xiaobiao Shan. Piezoelectricity of PVDF composite film doped with dopamine coated nano-TiO_2. *Journal of Alloys and Compounds*, 885:160829, 2021.

[53] J Arunguvai and P Lakshmi. Influence of ZrO_2 and TiO_2 nano particles in P (VDF-TrFE) composite for energy harvesting application. *Journal of Materials Science. Materials in Electronics*, 32(9):12223–12231, 2021.

[54] Renjun Liu, Qing Liu, Dan He, Guoxing Sun, Zongjin Li, and Yu Zhu. Enhancement of the piezoelectric property of polyvinylidene fluoride through electroactive phase enrichment and the application in piezoelectric generators. *ACS Applied Electronic Materials*, 3(4):1804–1812, 2021.

[55] Pornsawan Kum-Onsa, Narong Chanlek, and Prasit Thongbai. Largely enhanced dielectric properties of TiO_2-nanorods/poly(vinylidene fluoride) nanocomposites driven by enhanced interfacial areas. *Nanocomposites*, 7(1):123–131, 2021.

[56] Usman Yaqoob and Gwiy-Sang Chung. Effect of surface treated MWCNTs and $BaTiO_3$ nanoparticles on the dielectric properties of a P(VDF-TrFE) matrix. *Journal of Alloys and Compounds*, 695:1231–1236, 2017.

[57] Kwi-Il Park, Chang Kyu Jeong, Na Kyung Kim, and Keon Jae Lee. Stretchable piezoelectric nanocomposite generator. *Nano Convergence*, 3(1):1–12, 2016.

[58] Aisha Al-Saygh, Deepalekshmi Ponnamma, Mariam AlAli AlMaadeed, Poornima Vijayan P, Alamgir Karim, and Mohammad K Hassan. Flexible pressure sensor based on pvdf nanocomposites containing reduced graphene oxide-titania hybrid nanolayers. *Polymers*, 9(2):33, 2017.

[59] Saira Ishaq, Farah Kanwal, Shahid Atiq, Mahmoud Moussa, Umar Azhar, and Dusan Losic. Dielectric properties of graphene/titania/polyvinylidene fluoride (G/TiO_2/PVDF) nanocomposites. *Materials*, 13(1):205, 2020.

[60] Deepalekshmi Ponnamma, Solleti Goutham, Kishor Kumar Sadasivuni, Kalagadda Venkateswara Rao, John John Cabibihan, and Mariam Al Ali Al-Maadeed. Controlling the sensing performance of rGO filled pvdf nanocomposite with the addition of secondary nanofillers. *Synthetic Metals*, 243:34–43, 2018.

[61] Zine Ghemari, Salah Belkhiri, and Salah Saad. Improvement of the relative sensitivity for

obtaining a high performance piezoelectric sensor. *IEEE Instrumentation and Measurement Magazine*, 26(4):49–56, 2023.

[62] Usman Yaqoob and Gwiy-Sang Chung. Effect of reduced graphene oxide on the energy harvesting performance of P(VDF-TrFE)-$BaTiO_3$ nanocomposite devices. *Smart Materials and Structures*, 26(9):095060, 2017.

[63] Usman Yaqoob, ASM Iftekhar Uddin, and Gwiy-Sang Chung. A novel tri-layer flexible piezoelectric nanogenerator based on surface-modified graphene and PVDF-$BaTiO_3$ nanocomposites. *Applied Surface Science*, 405:420–426, 2017.

[64] Kunming Shi, Bin Sun, Xingyi Huang, and Pingkai Jiang. Synergistic effect of graphene nanosheet and $BaTiO_3$ nanoparticles on performance enhancement of electrospun pvdf nanofiber mat for flexible piezoelectric nanogenerators. *Nano Energy*, 52:153–162, 2018.

[65] Elyani Abu Bakar, Mohd Ambri Mohamed, Poh Choon Ooi, MF Mohd Razip Wee, Chang Fu Dee, and Burhanuddin Yeop Majlis. Fabrication of indium-tin-oxide free, all-solution-processed flexible nanogenerator device using nanocomposite of barium titanate and graphene quantum dots in polyvinylidene fluoride polymer matrix. *Organic Electronics*, 61:289–295, 2018.

[66] Jiaqing Luo, Libing Zhang, Ting Wu, Haijun Song, Chengli Tang, Fengli Huang, and Chuncheng Zuo. Flexible electronic skin with high performance pressure sensing based on PVDF/rGO/$BaTiO_3$ composite thin film. *Organic Electronics*, 98:106296, 2021.

[67] Yinhui Li, Jianqiang Tan, Kun Liang, Yong Li, Jiaojiao Sun, Hulin Zhang, Cuixian Luo, Pengwei Li, Jianle Xu, Huabei Jiang, et al. Enhanced piezoelectric performance of multi-layered flexible polyvinylidene fluoride–$BaTiO_3$–rGO films for monitoring human body motions. *Journal of Materials Science: Materials in Electronics*, pages 1–14, 2022.

[68] Sumanta Kumar Karan, Sandip Maiti, Anand Kumar Agrawal, Amit Kmar Das, Anirban Maitra, Sarbaranjan Paria, Aswini Bera, Ranadip Bera, Lopamudra Halder, Avnish Kumar Mishra, et al. Designing high energy conversion efficient bio-inspired vitamin assisted single-structured based self-powered piezoelectric/wind/acoustic multi-energy harvester with remarkable power density. *Nano Energy*, 59:169–183, 2019.

[69] Sachin Kumar Singh, Piyush Kumar, Rushikesh Magdum, Utkarsh Khandelwal, Swati Deswal, Yogeshwar More, Subas Muduli, Ramamoorthy Boomishankar, Sagar Pandit, and Satishchandra Ogale. Seed power: natural seed and electrospun poly (vinyl difluoride)(PVDF) nanofiber based triboelectric nanogenerators with high output power density. *ACS Applied Bio Materials*, 2(8):3164–3170, 2019.

[70] Sandip Maiti, Sumanta Kumar Karan, Juhyun Lee, Avnish Kumar Mishra, Bhanu Bhusan Khatua, and Jin Kon Kim. Bio-waste onion skin as an innovative nature-driven piezoelectric material with high energy conversion efficiency. *Nano Energy*, 42:282–293, 2017.

[71] Qazi Muhammad Saqib, Mahesh Y Chougale, Muhammad Umair Khan, Rayyan Ali Shaukat, Jungmin Kim, Jinho Bae, Hyung Woo Lee, Jung-Im Park, Myung Sook Kim, and Byung Gul Lee. Natural seagrass tribopositive material based spray coatable triboelectric nanogenerator. *Nano Energy*, 89:106458, 2021.

[72] Qazi Muhammad Saqib, Muhammad Umair Khan, Hyunjae Song, Mahesh Y Chougale, Rayyan Ali Shaukat, Jungmin Kim, Jinho Bae, Min Joo Choi, Seong Chan Kim, Ohbin Kwon, et al. Natural hierarchically structured highly porous tomato peel based tribo-and piezo-electric nanogenerator for efficient energy harvesting. *Advanced Sustainable Systems*, 5 (7):2100066, 2021.

[73] Simadri Badatya, Dhiraj Kumar Bharti, Avanish Kumar Srivastava, and Manoj Kumar Gupta. Solution processed high performance piezoelectric eggshell membrane–PVDF layer

composite nanogenerator via tuning the interfacial polarization. *Journal of Alloys and Compounds*, 863:158406, 2021.

[74] Jianguo Sun, Hengyu Guo, Javier Ribera, Changsheng Wu, Kunkun Tu, Marco Binelli, Guido Panzarasa, Francis WMR Schwarze, Zhong Lin Wang, and Ingo Burgert. Sustainable and biodegradable wood sponge piezoelectric nanogenerator for sensing and energy harvesting applications. *ACS nano*, 14(11):14665–14674, 2020.

[75] Manisha Sahu, Sugato Hajra, Sagar Jadhav, Basanta Kumar Panigrahi, Deepak Dubal, and Hoe Joon Kim. Bio-waste composites for cost-effective self-powered breathing patterns monitoring: An insight into energy harvesting and storage properties. *Sustainable Materials and Technologies*, 32:e00396, 2022.

[76] Eiichi Fukada. Piezoelectricity as a fundamental property of wood. *Wood Science and Technology*, 2:299–307, 1968.

[77] Eiichi Fukada. Piezoelectricity of wood. *Journal of the Physical Society of Japan*, 10(2): 149–154, 1955.

[78] Eiichi Fukada. Piezoelectricity of natural biomaterials. *Ferroelectrics*, 60(1):285–296, 1984.

[79] Fereidoon Shahidi. Proteins from seafood processing discards. *Seafood proteins*, pages 171–193, 1994.

[80] Shan Sun, Tongxin Kou, and Hesun Zhu. A study on bioelectret collagen. *Journal of applied polymer science*, 64(2):267–271, 1997.

[81] Sujoy Kumar Ghosh and Dipankar Mandal. High-performance bio-piezoelectric nanogenerator made with fish scale. *Applied Physics Letters*, 109(10), 2016.

[82] Sujoy Kumar Ghosh and Dipankar Mandal. Sustainable energy generation from piezoelectric

biomaterial for noninvasive physiological signal monitoring. *ACS Sustainable Chemistry and Engineering*, 5(10):8836–8843, 2017.

[83] M Marimuthu, S Ganesan, and A Ravi Kumar. Fishery waste-driven piezo-capacitor as unprecedented energy conversion and storage for real-time monitoring device. *Journal of Energy Storage*, 78:110121, 2024.

[84] Chandan Kumar, Anupama Gaur, Shivam Tiwari, Arpan Biswas, Sanjay Kumar Rai, and Pralay Maiti. Bio-waste polymer hybrid as induced piezoelectric material with high energy harvesting efficiency. *Composites Communications*, 11:56–61, 2019.

[85] Ajay Vasudeo Rane, Krishnan Kanny, VK Abitha, and Sabu Thomas. Methods for synthesis of nanoparticles and fabrication of nanocomposites. In *Synthesis of inorganic nanomaterials*, pages 121–139. Elsevier, 2018.

[86] Yu-Chih Hu, Ching-Liang Dai, and Cheng-Chih Hsu. Titanium dioxide nanoparticle humidity microsensors integrated with circuitry on-a-chip. *Sensors*, 14(3):4177–4188, 2014.

[87] M El Achaby, FZ Arrakhiz, S Vaudreuil, EM Essassi, and A Qaiss. Piezoelectric β-polymorph formation and properties enhancement in graphene oxide–PVDF nanocomposite films. *Applied Surface Science*, 258(19):7668–7677, 2012.

[88] IM Joni, L Nulhakim, and C Panatarani. Characteristics of TiO_2 particles prepared by simple solution method using $TiCl_3$ precursor. In *Journal of Physics: Conference Series*, volume 1080, page 012042. IOP Science, 2018.

[89] Duo Mao, Bruce E Gnade, and Manuel A Quevedo-Lopez. Ferroelectric properties and polarization switching kinetic of poly (vinylidene fluoride-trifluoroethylene) copolymer. *Ferroelectrics-Physical Effects*, pages 78–100, 2011.

[90] Xiaomei Cai, Tingping Lei, Daoheng Sun, and Liwei Lin. A critical analysis of the α, β and γ phases in poly (vinylidene fluoride) using FTIR. *RSC Advances*, 7(25):15382–15389, 2017.

[91] Nick A Shepelin, Alexey M Glushenkov, Vanessa C Lussini, Phillip J Fox, Greg W Dicinoski, Joseph G Shapter, and Amanda V Ellis. New developments in composites, copolymer technologies and processing techniques for flexible fluoropolymer piezoelectric generators for efficient energy harvesting. *Energy and Environmental Science*, 12(4):1143–1176, 2019.

[92] Bilal Zaarour, Lei Zhu, Chen Huang, and Xiangyu Jin. Enhanced piezoelectric properties of randomly oriented and aligned electrospun PVDF fibers by regulating the surface morphology. *Journal of Applied Polymer Science*, 136(6):47049, 2019.

[93] K Madhusudan Reddy, CV Gopal Reddy, and SV Manorama. Preparation, characterization, and spectral studies on nanocrystalline anatase TiO_2. *Journal of Solid State Chemistry*, 158 (2):180–186, 2001.

[94] K Madhusudan Reddy, Sunkara V Manorama, and A Ramachandra Reddy. Bandgap studies on anatase titanium dioxide nanoparticles. *Materials Chemistry and Physics*, 78(1):239–245, 2003.

[95] C Joseph Mathai, S Saravanan, MR Anantharaman, S Venkitachalam, and S Jayalekshmi. Effect of iodine doping on the bandgap of plasma polymerized aniline thin films. *Journal of Physics D: Applied Physics*, 35(17):2206, 2002.

[96] Marcel Benz and William B Euler. Determination of the crystalline phases of poly (vinylidene fluoride) under different preparation conditions using differential scanning calorimetry and infrared spectroscopy. *Journal of Applied Polymer Science*, 89(4):1093–1100, 2003.

[97] Dorian AH Hanaor and Charles C Sorrell. Review of the anatase to rutile phase transformation. *Journal of Materials science*, 46:855–874, 2011.

[98] Sumanta Kumar Karan, Dipankar Mandal, and Bhanu Bhusan Khatua. Self-powered flexible Fe-doped RGO/PVDF nanocomposite: an excellent material for a piezoelectric energy harvester. *Nanoscale*, 7(24):10655–10666, 2015.

[99] Fang-Chyou Chiu. Comparisons of phase morphology and physical properties of PVDF nanocomposites filled with organoclay and/or multi-walled carbon nanotubes. *Materials Chemistry and Physics*, 143(2):681–692, 2014.

[100] Ram Jeewan Sengwa, Shobhna Choudhary, and Priyanka Dhatarwal. Nonlinear optical and dielectric properties of TiO_2 nanoparticles incorporated PEO/PVP blend matrix based multifunctional polymer nanocomposites. *Journal of Materials Science: Materials in Electronics*, 30:12275–12294, 2019.

[101] S Vinoth, G Kanimozhi, Harish Kumar, ES Srinadhu, and N Satyanarayana. High conducting nanocomposite electrospun PVDF-HFP/TiO_2 quasi-solid electrolyte for dye-sensitized solar cell. *Journal of Materials Science: Materials in Electronics*, 30:1199–1213, 2019.

[102] Toshikatsu Tanaka and Alun S Vaughan. *Tailoring of nanocomposite dielectrics: from fundamentals to devices and applications*. CRC Press, 2016.

[103] Fan Mao, Zhicheng Shi, Jing Wang, Chao Zhang, Chaoqiang Yang, and Minghua Huang. Improved dielectric permittivity and retained low loss in layer-structured films via controlling interfaces. *Advanced Composites and Hybrid Materials*, 1:548–557, 2018.

[104] Abhishek Anand, Deshraj Meena, Kajal Kumar Dey, and Mukesh Chander Bhatnagar. Enhanced piezoelectricity properties of reduced graphene oxide (RGO) loaded polyvinylidene fluoride (PVDF) nanocomposite films for nanogenerator application. *Journal of Polymer Research*, 27:1–11, 2020.

[105] Prateek, Ritamay Bhunia, Shahil Siddiqui, Ashish Garg, and Raju Kumar Gupta. Significantly enhanced energy density by tailoring the interface in hierarchically structured TiO_2–

$BaTiO_3$–TiO_2 nanofillers in pvdf-based thin-film polymer nanocomposites. *ACS applied materials and interfaces*, 11(15):14329–14339, 2019.

[106] Yunxiang Zhang, Min Zuo, Yihu Song, Xueping Yan, and Qiang Zheng. Dynamic rheology and dielectric relaxation of poly (vinylidene fluoride)/poly (methyl methacrylate) blends. *Composites Science and Technology*, 106:39–46, 2015.

[107] Dinesh Patidar, Sonalika Agrawal, and NS Saxena. Storage modulus and glass transition behaviour of CdS/PMMA nanocomposites. *Journal of Experimental Nanoscience*, 6(4):441–449, 2011.

[108] Li-Yun Yu, Hong-Mei Shen, and Zhen-Liang Xu. Pvdf–TiO_2 composite hollow fiber ultrafiltration membranes prepared by TiO_2 sol–gel method and blending method. *Journal of Applied Polymer Science*, 113(3):1763–1772, 2009.

[109] Wei Li, Hong Li, and Yong-Ming Zhang. Preparation and investigation of PVDF/PMMA/TiO_2 composite film. *Journal of Materials Science*, 44:2977–2984, 2009.

[110] Joao Gomes, J Serrado Nunes, Vitor Sencadas, and Senentxu Lanceros-Méndez. Influence of the β-phase content and degree of crystallinity on the piezo-and ferroelectric properties of poly (vinylidene fluoride). *Smart Materials and Structures*, 19(6):065010, 2010.

[111] Marcel Benz, William B Euler, and Otto J Gregory. The role of solution phase water on the deposition of thin films of poly (vinylidene fluoride). *Macromolecules*, 35(7):2682–2688, 2002.

[112] Rajni Verma, Jitendra Gangwar, and Avanish K Srivastava. Multiphase TiO_2 nanostructures: A review of efficient synthesis, growth mechanism, probing capabilities, and applications in bio-safety and health. *RSC advances*, 7(70):44199–44224, 2017.

[113] Yanan Yang and Peng Wang. Preparation and characterizations of a new PS/TiO_2 hybrid membranes by sol–gel process. *Polymer*, 47(8):2683–2688, 2006.

[114] Lucas Galhardo Pimenta Tienne, Ludmila da Silva Candido, Barbara de Salles Macena da Cruz, Fernanda Fabbri Gondim, Matheus Pereira Ribeiro, Renata Antoun Simao, Maria de Fátima Vieira Marques, and Sergio Neves Monteiro. Reduced graphene oxide synthesized by a new modified hummer's method for enhancing thermal and crystallinity properties of poly (vinylidene fluoride). *journal of materials research and technology*, 18:4871–4893, 2022.

[115] Weikang Li, Anthony Dichiara, and Jinbo Bai. Carbon nanotube–graphene nanoplatelet hybrids as high-performance multifunctional reinforcements in epoxy composites. *Composites Science and Technology*, 74:221–227, 2013.

[116] MM Shokrieh, MR Hosseinkhani, MR Naimi-Jamal, and HJPT Tourani. Nanoindentation and nanoscratch investigations on graphene-based nanocomposites. *Polymer Testing*, 32(1): 45–51, 2013.

[117] Jingshi Wang, Min Yi, Zhigang Shen, Lei Liu, Xiaojing Zhang, and Shulin Ma. Enhanced thermal and mechanical properties of poly (vinylidene fluoride) nanocomposites reinforced by liquid-exfoliated graphene. *Journal of Macromolecular Science, Part A*, 56(7):733–740, 2019.

[118] Jinglei Yang, Zhong Zhang, Klaus Friedrich, and Alois K Schlarb. Creep resistant polymer nanocomposites reinforced with multiwalled carbon nanotubes. *Macromolecular rapid communications*, 28(8):955–961, 2007.

[119] Abhinav Bhatt, Vishal Singh, Priyanka Bamola, Deepali Aswal, Saurabh Rawat, Shilpa Rana, Charu Dwivedi, Bharti Singh, and Himani Sharma. Enhanced piezoelectric response using TiO_2/MoS_2 heterostructure nanofillers in PVDF based nanogenerators. *Journal of Alloys and Compounds*, 960:170664, 2023.

[120] Ajeet Kumar, Satish Jaiswal, Rita Joshi, Siddharth Yadav, Anshu Dubey, Divyam Sharma, Debrupa Lahiri, and Indranil Lahiri. Energy harvesting by piezoelectric polyvinylidene fluo-

ride/zinc oxide/carbon nanotubes composite under cyclic uniaxial tensile deformation. *Polymer Composites*, 44(8):4746–4756, 2023.

[121] Mukesh Kumar and Poonam Kumari. Design and fabrication of self-powered flexible P (VDF-TrFE)/ZnO/ TiO_2 fiber mats as nanogenerator for wearable applications. *Materials Science in Semiconductor Processing*, 160:107429, 2023.

[122] Mohd Faraz, Huidrom Hemojit Singh, and Neeraj Khare. A progressive strategy for harvesting mechanical energy using flexible PVDF-rGO-MoS_2 nanocomposites film-based piezoelectric nanogenerator. *Journal of Alloys and Compounds*, 890:161840, 2022.

[123] Sakti P Muduli, Sabyasachi Parida, Sanjay K Behura, Shailendra Rajput, Sanjeeb K Rout, and Shweta Sareen. Synergistic effect of graphene on dielectric and piezoelectric characteristic of PVDF-(BZT-BCT) composite for energy harvesting applications. *Polymers for Advanced Technologies*, 33(10):3628–3642, 2022.

[124] Sakti Prasanna Muduli, Loree Lipsa, Abhisek Choudhary, Shailendra Rajput, and Sabyasachi Parida. Modulation of electrical characteristics of polymer–ceramic–graphene hybrid composite for piezoelectric energy harvesting. *ACS Applied Electronic Materials*, 2023.

[125] Huidrom Hemojit Singh, Simrjit Singh, and Neeraj Khare. Design of flexible PVDF/$NaNbO_3$/RGO nanogenerator and understanding the role of nanofillers in the output voltage signal. *Composites Science and Technology*, 149:127–133, 2017.

[126] Mahdi Hasanzadeh, Mohammad Reza Ghahhari, and Seyed Mansour Bidoki. Enhanced piezoelectric performance of PVDF-based electrospun nanofibers by utilizing in situ synthesized graphene-ZnO nanocomposites. *Journal of Materials Science: Materials in Electronics*, 32 (12):15789–15800, 2021.

[127] Qi Wu, Huiling Guo, Huajun Sun, Xiaofang Liu, Huiting Sui, and Fang Wang. Flexible piezoelectric energy harvesters with graphene oxide nanosheets and PZT-incorporated P (VDF-

TrFE) matrix for mechanical energy harvesting. *Ceramics International*, 47(14):19614–19621, 2021.

[128] Rezgar Hasanzadeh, Parisa Mojaver, Shahram Khalilarya, and Taher Azdast. Air co-gasification process of LDPE/HDPE waste based on thermodynamic modeling: Hybrid multi-criteria decision-making techniques with sensitivity analysis. *International Journal of Hydrogen Energy*, 48(6):2145–2160, 2023.

[129] Rezgar Hasanzadeh, Parisa Mojaver, Taher Azdast, Shahram Khalilarya, Ata Chitsaz, and Marc A Rosen. Decision analysis for plastic waste gasification considering energy, exergy, and environmental criteria using topsis and grey relational analysis. *Process Safety and Environmental Protection*, 174:414–423, 2023.

[130] Maxim Nikiforov, Haiqing Liu, Harold Craighead, and Dawn Bonnell. Polarization controlled transport in PANI-$BaTiO_3$ nanofibers. *Nano Letters*, 6(5):896–900, 2006.

[131] J Arunguvai and P Lakshmi. Flexible nano-vibration energy harvester using three-phase polymer composites. *Journal of Materials Science: Materials in Electronics*, 31:8283–8290, 2020.

[132] Hiromichi Hayashi, Takashi Nakamura, and Takeo Ebina. In-situ raman spectroscopy of $BaTiO_3$ particles for tetragonal–cubic transformation. *Journal of Physics and Chemistry of Solids*, 74(7):957–962, 2013.

[133] Pavel Kaspar, Dinara Sobola, Klára Částková, Rashid Dallaev, Eva Št'astná, Petr Sedlák, Alexandr Knápek, Tomáš Trčka, and Vladimír Holcman. Case study of polyvinylidene fluoride doping by carbon nanotubes. *Materials*, 14(6):1428, 2021.

[134] Sejung Kim, Youngjun Song, Michael J Heller, et al. Influence of mwcnts on β-phase PVDF and triboelectric properties. *Journal of Nanomaterials*, 2017, 2017.

[135] Rahul Naik et al. Self-powered flexible piezoelectric nanogenerator made of poly (vinylidene fluoride)/zirconium oxide nanocomposite. *Materials Research Express*, 6(11):115330, 2019.

[136] Deepankar Sri Gyan and Akansha Dwivedi. Structural and electrical characterization of $NaMbO_3$ -PVDF nanocomposites fabricated using cold sintering synthesis route. *Journal of Applied Physics*, 125(2), 2019.

[137] Merve Zeyrek Ongun, Sibel Oguzlar, Eyyup Can Doluel, Ugur Kartal, and Metin Yurddaskal. Enhancement of piezoelectric energy-harvesting capacity of electrospun β-pvdf nanogenerators by adding GO and rGO. *Journal of Materials Science: Materials in Electronics*, 31: 1960–1968, 2020.

[138] Rama K Layek, Sanjoy Samanta, Dhruba P Chatterjee, and Arun K Nandi. Physical and mechanical properties of poly (methyl methacrylate)-functionalized graphene/poly (vinylidine fluoride) nanocomposites: Piezoelectric β polymorph formation. *Polymer*, 51(24):5846–5856, 2010.

[139] Ravinder Sharma, Rupinder Singh, and Ajay Batish. Study on barium titanate and graphene reinforced PVDF matrix for 4D applications. *Journal of Thermoplastic Composite Materials*, 34(9):1234–1253, 2021.

[140] Bingcheng Luo, Xiaohui Wang, Yueping Wang, and Longtu Li. Fabrication, characterization, properties and theoretical analysis of ceramic/PVDF composite flexible films with high dielectric constant and low dielectric loss. *Journal of Materials Chemistry A*, 2(2):510–519, 2014.

[141] Usman Yaqoob, ASM Iftekhar Uddin, and Gwiy-Sang Chung. The effect of reduced graphene oxide on the dielectric and ferroelectric properties of PVDF–$BaTiO_3$ nanocomposites. *RSC advances*, 6(36):30747–30754, 2016.

[142] AK Bledzki, H-P Fink, and K Specht. Unidirectional hemp and flax EP-and PP-composites: Influence of defined fiber treatments. *Journal of Applied Polymer Science*, 93(5):2150–2156, 2004.

[143] Abir Saha and Poonam Kumari. Effect of alkaline treatment on physical, structural, mechanical and thermal properties of bambusa tulda (northeast indian species) based sustainable green composites. *Polymer Composites*, 44(4):2449–2473, 2023.

[144] Naruemon Sumrith, Laongdaw Techawinyutham, MR Sanjay, Rapeephun Dangtungee, and Suchart Siengchin. Characterization of alkaline and silane treated fibers of 'water hyacinth plants' and reinforcement of 'water hyacinth fibers' with bioepoxy to develop fully biobased sustainable ecofriendly composites. *Journal of Polymers and the Environment*, 28:2749–2760, 2020.

[145] G Rajeshkumar, V Hariharan, S Indran, MR Sanjay, Suchart Siengchin, J Prakash Maran, Naif Abdullah Al-Dhabi, and Ponmurugan Karuppiah. Influence of sodium hydroxide (NaOH) treatment on mechanical properties and morphological behaviour of phoenix sp. fiber/epoxy composites. *Journal of Polymers and the Environment*, 29:765–774, 2021.

[146] P Madhu, MR Sanjay, Mohammad Jawaid, Suchart Siengchin, Anish Khan, and Catalin Iulian Pruncu. A new study on effect of various chemical treatments on agave americana fiber for composite reinforcement: Physico-chemical, thermal, mechanical and morphological properties. *Polymer Testing*, 85:106437, 2020.

[147] Lifang Liu, Qianli Wang, Longdi Cheng, Jingfang Qian, and Jianyong Yu. Modification of natural bamboo fibers for textile applications. *Fibers and Polymers*, 12:95–103, 2011.

[148] A Vinod, MR Sanjay, Suchart Siengchin, and Steffen Fischer. Fully bio-based agro-waste soy stem fiber reinforced bio-epoxy composites for lightweight structural applications: influence of surface modification techniques. *Construction and Building Materials*, 303:124509, 2021.

[149] Susheel Kalia, BS Kaith, and Inderjeet Kaur. *Cellulose fibers: bio-and nano-polymer composites: green chemistry and technology*. Springer Science and Business Media, 2011.

[150] Gautam Basu, Leena Mishra, and Ashis Kumar Samanta. Investigation of structure and property of indian cocos nucifera l. fibre. *Journal of The Institution of Engineers (India): Series E*, 98:135–140, 2017.

[151] Hsuan-Hao Chiu and Wen-Bin Young. The longitudinal and transverse tensile properties of unidirectional and bidirectional bamboo fiber reinforced composites. *Fibers and Polymers*, 21:2938–2948, 2020.

[152] Rahul Kumar, Kaushik Kumar, Sumit Bhowmik, and Gautam Sarkhel. Tailoring the performance of bamboo filler reinforced epoxy composite: insights into fracture properties and fracture mechanism. *Journal of Polymer Research*, 26:1–15, 2019.

[153] Abir Saha, Santosh Kumar, and Avinash Kumar. Influence of pineapple leaf particulate on mechanical, thermal and biodegradation characteristics of pineapple leaf fiber reinforced polymer composite. *Journal of Polymer Research*, 28:1–23, 2021.

[154] Santosh Kumar and Abir Saha. Graphene nanoplatelets/organic wood dust hybrid composites: physical, mechanical and thermal characterization. *Iranian Polymer Journal*, 30(9): 935–951, 2021.

[155] Ehsan Behazin, Manjusri Misra, and Amar K Mohanty. Sustainable biocarbon from pyrolyzed perennial grasses and their effects on impact modified polypropylene biocomposites. *Composites Part B: Engineering*, 118:116–124, 2017.

[156] Ahmed Belaadi, Abderrezak Bezazi, Mostefa Bourchak, Fabrizio Scarpa, and Chenchen Zhu. Thermochemical and statistical mechanical properties of natural sisal fibres. *Composites Part B: Engineering*, 67:481–489, 2014.

[157] Salah Amroune, Abderrezak Bezazi, Alain Dufresne, Fabrizio Scarpa, and Abdellatif Imad. Investigation of the date palm fiber for green composites reinforcement: thermo-physical and mechanical properties of the fiber. *Journal of Natural Fibers*, 18(5):717–734, 2021.

[158] Huidrom Hemojit Singh, Simrjit Singh, and Neeraj Khare. Enhanced β-phase in PVDF polymer nanocomposite and its application for nanogenerator. *Polymers for Advanced Technologies*, 29(1):143–150, 2018.

[159] Miles C Rehwoldt, Yujie Wang, Feiyu Xu, Pankaj Ghildiyal, and Michael R Zachariah. High-temperature interactions of metal oxides and a PVDF binder. *ACS Applied Materials and Interfaces*, 14(7):8938–8946, 2022.

[160] Sergio N Monteiro, Veronica Calado, Ruben Jesus S Rodriguez, and Frederico M Margem. Thermogravimetric behavior of natural fibers reinforced polymer composites—an overview. *Materials Science and Engineering: A*, 557:17–28, 2012.

[161] Manish Kumar Lila, Gaurav Kumar Saini, M Kannan, and Inderdeep Singh. Effect of fiber type on thermal and mechanical behavior of epoxy based composites. *Fibers and Polymers*, 18:806–810, 2017.

[162] Manish Kumar Lila, Ujendra Kumar Komal, Yashvir Singh, and Inderdeep Singh. Extraction and characterization of munja fibers and its potential in the biocomposites. *Journal of Natural Fibers*, 19(7):2675–2693, 2022.

[163] Mukesh Kumar and Poonam Kumari. P(VDF-TrFE)/ZnO nanocomposite synthesized by electrospinning: effect of ZnO nanofiller on physical, mechanical, thermal, rheological and piezoelectric properties. *Polymer Bulletin*, 20:1–20, 2022.

[164] Abir Saha and Poonam Kumari. Functional fibers from bambusa tulda (northeast indian species) and their potential for reinforcing biocomposites. *Materials Today Communications*, 31:103800, 2022.

[165] Krishna Auromun, Sugato Hajra, RNP Choudhary, and Banarji Behera. Structural and electrical properties of 0.7(BiSmxFe1-xO$_3$)–0.3(PbTiO$_3$) composites. *Applied Physics A*, 125: 1–11, 2019.

[166] Hossein Fashandi, Mohammad Mahdi Abolhasani, Parastoo Sandoghdar, Nima Zohdi, Quanxiang Li, and Minoo Naebe. Morphological changes towards enhancing piezoelectric properties of pvdf electrical generators using cellulose nanocrystals. *Cellulose*, 23:3625–3637, 2016.

[167] Ying Gao, Farsa Ram, Bin Chen, Jonas Garemark, Lars Berglund, Hongqi Dai, and Yuanyuan Li. Scalable hierarchical wood/zno nanohybrids for efficient mechanical energy conversion. *Materials and Design*, 226:111665, 2023.

[168] Hamouda M Mousa, Hanan S Fahmy, Ragab Abouzeid, GT Abdel-Jaber, and WY Ali. Polyvinylidene fluoride-cellulose nanocrystals hybrid nanofiber membrane for energy harvesting and oil-water separation applications. *Materials Letters*, 306:130965, 2022.

[169] Chia-Chen Chang and James S Sirkis. Design of fiber optic sensor systems for low velocity impact detection. *Smart Materials and Structures*, 7(2):166, 1998.

[170] BP Chandra, VK Chandra, SK Mahobia, P Jha, R Tiwari, and B Haldar. Real-time mechanoluminescence sensing of the amplitude and duration of impact stress. *Sensors and Actuators A: Physical*, 173(1):9–16, 2012.

[171] AC Okafor, AW Otieno, A Dutta, and VS Rao. Detection and characterization of high-velocity impact damage in advanced composite plates using multi-sensing techniques. *Composite Structures*, 54(2-3):289–297, 2001.

[172] Yusaku Fujii and JDR Valera. Impact force measurement using an inertial mass and a digitizer. *Measurement Science and Technology*, 17(4):863, 2006.

[173] Sudeep Joshi, GM Hegde, MM Nayak, and K Rajanna. A novel piezoelectric thin film impact sensor: Application in non-destructive material discrimination. *Sensors and Actuators A: Physical*, 199:272–282, 2013.

[174] Toshiyuki Ikoma, Hisatoshi Kobayashi, Junzo Tanaka, Dominic Walsh, and Stephen Mann. Microstructure, mechanical, and biomimetic properties of fish scales from pagrus major. *Journal of structural biology*, 142(3):327–333, 2003.

[175] Fernando G Torres, Omar P Troncoso, and Evelin Amaya. The effect of water on the thermal transitions of fish scales from arapaima gigas. *Materials Science and Engineering: C*, 32(8): 2212–2214, 2012.

[176] Lin Wang, Qiufang Liang, Tingting Chen, Zhenbin Wang, Junmin Xu, and Haile Ma. Characterization of collagen from the skin of amur sturgeon (acipenser schrenckii). *Food Hydrocolloids*, 38:104–109, 2014.

[177] JH Muyonga, CGB Cole, and KG Duodu. Characterisation of acid soluble collagen from skins of young and adult nile perch (lates niloticus). *Food chemistry*, 85(1):81–89, 2004.

[178] Onouma Kaewdang, Soottawat Benjakul, Thammarat Kaewmanee, and Hideki Kishimura. Characteristics of collagens from the swim bladders of yellowfin tuna (thunnus albacares). *Food Chemistry*, 155:264–270, 2014.

[179] Falguni Pati, Basudam Adhikari, and Santanu Dhara. Isolation and characterization of fish scale collagen of higher thermal stability. *Bioresource technology*, 101(10):3737–3742, 2010.

[180] Yijun Fu, Yue Cheng, Chi Chen, Dawei Li, and Wei Zhang. Study on preparation process and enhanced piezoelectric performance of pine-needle-like ZnO@ PVDF composite nanofibers. *Polymer Testing*, 108:107513, 2022.

[181] Di Qin, Shichao Bi, Xinguo You, Mengyang Wang, Xin Cong, Congshan Yuan, Miao Yu,

Xiaojie Cheng, and Xi-Guang Chen. Development and application of fish scale wastes as versatile natural biomaterials. *Chemical Engineering Journal*, 428:131102, 2022.

[182] Changwan Sohn, Hyunseung Kim, Jihoon Han, Ki-Tae Lee, Andris Šutka, and Chang Kyu Jeong. Generating electricity from molecular bonding-correlated piezoresponse of biodegradable silk nanofibers. *Nano Energy*, 103:107844, 2022.

[183] Satyaranjan Bairagi, Saikat Ghosh, and S Wazed Ali. A fully sustainable, self-poled, biowaste based piezoelectric nanogenerator: Electricity generation from pomelo fruit membrane. *Scientific Reports*, 10(1):12121, 2020.

Appendix A

A.1 COST ANALYSIS OF PENG DEVICES

The highest and lowest cost PENG devices have been analyzed, considering raw material and processing costs. The highest cost was incurred for the PVDF-TiO_2-rGO-based PENG device, referred to as Device 1, while the lowest cost was for the PVDF-FS-based PENG device, referred to as Device 2. The analysis reveals that Device 1 is more expensive than Device 2. However, for commercialization, Device 1 is more suitable. This conclusion is based on the following observations:

1. Higher mechanical and piezoelectric performance
2. Low initial investment compared to device 2
3. Ease of processing

A summary of the findings is provided below:

Device 1 (Highest cost):

Table 1: Raw material cost for PENG device.

Raw material	Quantity	Unit cost	Total cost
PVDF	2 g	₹0.2/g	₹0.4
TiO_2	0.36 g	₹400/g	₹144
rGO powder	0.02 g	₹2600/g	₹52
DMF solvent	25 ml	₹12/ml	₹300
PET film substrate	$30 \times 30 \times 0.1$ (mm^3)	2.10	0.0134
		Total	₹536

Table 2: Material processing cost for PENG device.

Type of energy used	Unit cost	Total
Energy Cost (Solvent Evaporation)	10 hours @ ₹22.5/hour	₹225
Energy Cost (Thermal Poling)	₹6/kWh × 3.5 kW × 6 hours	₹126/batch
Desiccation Energy cost/batch	₹6/kWh × 0.06 kW × 4 hours	₹1.44/batch

Total cost for fabricating device 1 = Raw materials cost + Material processing cost= ₹889/-

Device 2 (Lowest cost):

Table 3: Raw Material Cost for PENG device.

Raw Material	Quantity	Unit Cost	Total Cost
PVDF	2 g	₹0.2g	₹0.4
FS particles	0.223 g	-	-
NaOH solution	30 ml	₹2.2/ml	₹66
DI water	30 ml	₹0.05/ml	₹1.5
DMF solvent	25 ml	₹12 /ml	₹300
PET film substrate	30 × 30 × 0.1 (mm^3)	₹0.45/mm^3	₹40
		Total	₹408

Table 4: Material Processing Cost for PENG device.

Type of energy used	Unit cost	Total
Energy Cost (Solvent Evaporation)	10 hours @ ₹22.5/hour	₹225
Energy Cost (Thermal Poling)	₹6/kWh × 3.5 kW × 6 hours	₹126/batch
Desiccation Energy cost per batch	₹6/kWh × 0.06 kW × 4 hours	₹1.44/batch

Brief biodata of the author

Nikhil Dilip Kulkarni

Senior Research Fellow

Department of Mechanical Engineering

Indian Institute of Technology Guwahati, Assam, India

Education:

Ph.D. (Mechanical Engineering), IIT Guwahati, India **July, 2019-present**

(CPI-7.67/10)

MTech (Nanoscience & Technology), IIT Patna **July 2017-2019**

(CPI-8.8/10)

BE (Mechanical Engineering), Sinhgad College of Engineering, Pune University **July 2011-2015**

61.8%

Internship:

- One Month **Internship** at **Mazagon Dock Shipbuilders Limited**, Mumbai, India

Software proficiency:

SOLIDWORKS, COMSOL Multiphysics, Origin Pro, MS Excel, MS Word, MS PPT, KLayout, ABAQUS

Academic Achievements:

- Received NEW GENERATION INNOVATION AND ENTREPRENEURSHIP DEVELOPMENT CENTRE (NewGen IEDC) 2021-22 **prototype development funding** (up to 2.5 lakhs).
- Received **CSIR International travel grant** to attend ICMAT-2023 conference held at Singapore from 26 June to 30 June, 2023.
- Coordinator, Inauguration and Cultural committee, ACMFMS-2022 conference, IIT Guwahati. (Dec. 2022)
- Treasurer, Research scholar forum, Department of Mechanical Engineering, IIT Guwahati **April 2023- present**
- Peer reviewer for **Journal of Materials Science**
- Peer reviewer for **Journal of Applied Polymer Science (twice)**

List of Publications from the Thesis

Publications in SCI journals

1. Kulkarni, N. D., Kumari, P., 2023. Development of highly flexible PVDF-TiO_2 nanocomposites for piezoelectric nanogenerator applications. Materials Research Bulletin, 157: 112039. DOI:10.1016/j.materresbull.2022.112039

2. Kulkarni, N. D., Saha, A. Kumari, P., 2023. Role of rGO on mechanical, thermal, and piezoelectric behavior of PVDF-BTO nanocomposites for energy harvesting applications. Journal of Polymer Research 30.2: 79. DOI:10.1007/s10965-023-03449-4

3. Kulkarni, N. D., Saha, A. Kumari, P., 2023. The development of a low-cost, sustainable bamboo-based flexible bio composite for impact sensing and mechanical energy harvesting applications. Journal of Applied Polymer Science, e54040. DOI:10.1002/app.54040

4. Kulkarni, N. D., Saha, A. Kumari, P. Utilizing multi criteria decision making approach for material selection in hybrid polymer nanocomposites for energy harvesting applications. Polymer Composites. DOI:10.1002/pc.28194

5. Kulkarni, N. D., Saha, A. Kumari, P. (*Submitted*). Fabrication and testing of PVDF-Fish scales based sustainable piezoelectric impact sensor. Journal of Materials Chemistry and Physics.

International Conference Publications

1. Kulkarni, N. D., Kumar, M. Kumari, P., 2022. PVDF/RGO based piezoelectric nanocomposite films for enhanced mechanical and dielectric properties. *International Conference on Advances in Chemical and Materials Sciences (ACMS-2022)*, February 24-26, 2022 Virtually at HIT Kolkata, India, Materials Today: Proceedings (2022).

2. Kulkarni, N. D., Kumari, P., 2023. Design and Development of Highly Flexible Piezoelectric PVDF-$BaTiO_3$ Nanocomposites Films for Sensing Applications. *International Conference on Materials for Advanced Technologies (ICMAT-2023)*, June 26-30, 2023 at Suntec, Singapore.

3. Kulkarni. N. D., Kumar, M., Kumari, P., 2023. Development of flexible PVDF-Graphene piezoelectric nanocomposites for smart sensing applications. *International Conference on Graphene, Semiconductors and 2D Materials (Graphene 2023)*, March 20-21, 2023 City Seasons Hotel, Dubai, UAE.

4. Kumar, M., **Kulkarni, N. D.**, Kumari, P., 2022. Fabrication and characterization of PVDF/$BaTiO_3$ nanocomposite for energy harvesting application. *1st International Conference on Advances in Mechanical Engineering and Material Science (ICAMEMS-22)*, January 22-24, 2022 Virtually at VIT AP, India, Materials Today: Proceedings 56 (2022): 1151-1155.

5. Kulkarni, N. D., Saha, A., Kumari, P., 2024. Development of biocompatible fish scales based biocompatible piezoelectric sensors. *International Conference on Sustainable Materials for Engineering Applications (ICSMEA 2024)*, February 1-3, 2024, IIT Madras, India,